# Applying Single-Molecule Localisation Microscopy to Achieve Virtual Optical Sectioning and Study T-Cell Activation

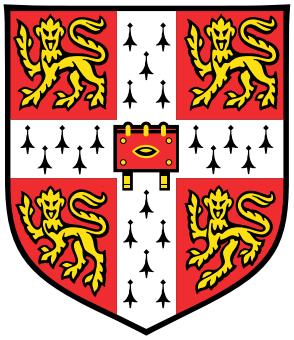

**Matthieu Grégoire Simon Palayret**

Department of Chemistry

University of Cambridge

This dissertation is submitted for the degree of

*Doctor of Philosophy*

Gonville & Caius College

2015

To my beloved family, heroes who built the hull.
To the joyful crew of friends, fellows of a life-long cruise.

"Le savant n'étudie pas la nature parce que cela est utile ; il l'étudie parce qu'il y prend plaisir et il y prend plaisir parce qu'elle est belle. (...) nous nous complairons tantôt à suivre la course gigantesque des astres, tantôt à scruter avec le microscope cette prodigieuse petitesse qui est aussi une grandeur..."
*Science et méthode, H. Poincaré, 1908.*

("The scientist does not study nature because doing so is useful; he studies it because he enjoys doing so and he enjoys doing so because nature is beautiful. (...) we may sometimes revel in tracing the gigantic course of the stars, sometimes in scrutinizing, through a microscope, this prodigious littleness, which is grand too...")

# Declaration

This dissertation summarises research carried out in the laboratory of Professor David Klenerman at the Department of Chemistry, University of Cambridge, between October 2011 and February 2015. The work described in the dissertation is my own. When work was performed in collaboration with others, it has been explicitly specified in the text: any experiments and protocols performed by others are denoted in the methods sections and/or relevant chapters and any data provided by others is noted in the relevant chapters and figure legends. This thesis has not, either in part or as a whole, been submitted for a degree, diploma, or other qualification at any other university. The length of this dissertation does not exceed the word limit of the degree committee (60,000 words), including appendices, bibliography, footnotes, tables and equations.

Matthieu Grégoire Simon Palayret
2015

# Acknowledgements

Although a statement of originality must precede any PhD thesis, this work would have been an impossible achievement without the support I received over the past three years.

First of all, I would like to thank my supervisor, *Professor David Klenerman*: Dave, your humble, positive and proactive attitude to tackle scientific challenges and ideas have inspired this work. I am deeply grateful for your generosity in support, encouragement and ever-flowing ideas that have continuously fuelled and channelled my scientific curiosity.

All the T cell work in this thesis was done in close collaboration with the lab of *Professor Simon Davis* at the University of Oxford: Simon, I would like to thank you for your communicative enthusiasm that never despaired. I am also grateful for the biological focus you brought to my work and your financial support during the last months of my PhD.

Many ideas in this thesis originated and were discussed during regular meetings with the labs of *Professor Ernest Laue* at the Department of Biochemistry and *Professor Anthony Carr* at the University of Sussex. These meetings were precious opportunities to get external feedback and extend my curiosity to different perspective and exciting research. I would like to thank you both to have maintained such a collaborative dynamic.

The *Wellcome Trust* must be thanked for both its generous funding without which this work could not have been undertaken, but also for giving me the opportunity to briefly explore three research topics in immunology and get priceless experience in T cell biology and mathematical modelling before starting my PhD.

This work has truly benefited from the knowledge and the abilities of many scientists I had the pleasure to work with over the past three years in Cambridge:

*Dr Steven Lee*: Steve, from my very first day in the lab I tried to follow your successful steps in the windings of the basement. Many thanks for the infinite time you patiently spent building Arabidopsis with me. This may not be the first thesis of the Lee lab, may it be its first thèse!

*Dr Kristina Ganzinger*: Kristina, I could not decide where your name would fit best in this list of acknowledgements. You truly deserve my deepest thanks for your unconditional support, both scientific and emotional, from the beginning until the very end of this adventure. You are both a precious colleague and a critical friend. Thank you for your advice, the many coffees and discussions we had, the travels we shared and your final proofreading. I wish you the very best of luck on the next step of your journey!

*Meike Aßmann*: Meike, working with you on CD28 super-agonism has been intellectually motivating and rewarding. I really enjoyed constructively confronting ideas and planning focussed experiments with you. Although I will leave Cambridge, super-agonism and the kinetic-segregation model will keep populating my thoughts at night! Thanks for careful proofreading.

*Elizabeth Huang*: Thank you for your continual help with the TCR project, through its many iterations!

*Dr James McColl*: James, thanks for your cheerful welcome in the Klenerman group and your foolproof patience with my countless questions.

*Dr Julien Godet*: Many thanks for your discreet but efficient work on the light-sheet. I must also thank you for your career advice which are leading me to Bordeaux. I have been very honoured to share my nickname with such another 'Frenchman'.

There is not enough room here to thank all the *members of the Klenerman group* that I would like to personally thank. Countless lunches and coffees, lab discussions, code debugging and instrument troubleshooting, have put rhythm and motivation in my life in the dark labs in the last three years. Particular thanks to Rohan, Kristina and Laura who cosseted me during the writing-up, and to the members of the lab fine dining society.

The end of this work coincides with the end of my time in Cambridge. Looking back at the last four years, I realise how lucky I have been to cross the path of so many (new) friends. A heartfelt thank you to:

*Ana* for our first awkward meeting and the inseparable four years that followed; *Maddie & Ross* for enduring my chaotic presence in St Andrews Road; *Daniel, Roeland, Elsa & Marius, Jude & Tom, Daniel, Ben, Mike, Olga & Matteusz, Emma, Lala, Adèle, ...* and the mysterious M* for long nights, friendship with style and trips to Andorra and Corsica; *Dr John Casey* for intense and rich debates, fine dinners and precious friendship;

*Ro'*, because your British irony and Rohan's dynamics are *terra incognita* in Bordeaux; because you are a rare example of unpretentious precision; because these three years changed an indecisive 'vous' into a definite 'tu'; (and thanks for proofreading!)

*Benoît* and *Jérôme* for bridging Cambridge to Paris; *Delphine* and *Élise* for the provisions of motivating chocolate; *Clémence, Pierre* and *Charles* for their constancy and fidelity; *Thierry Hubert* for his joyful example.

The final thanks are reserved to my dearest family: my parents, *Anne* and *Laurent*, for their attentive, constant and strong support for all my projects; my siblings, *Basile* for his enthusiasm when I come back, *Madeleine* for frequently taking news and taking me abroad, *Ambroise* for sharing his joys and sorrows, *Julie* and *her whole family* which expanded three times during this work to my greatest delight.

# Abstract

Single-molecule localisation microscopy (SMLM) allows imaging of fluorescently-tagged proteins in live cells with a precision well below that of the diffraction limit. As a single-molecule technique, it has also introduced a new quantitative approach to fluorescence microscopy.

In the Part A of this thesis, the design and building of three SMLM instruments, the implementation of a custom-developed image analysis package and the characterisation of the photo-physical properties of the photo-activable fluorescent protein used in this thesis (mEos), are discussed. Then, a new post-processing method for SMLM analysis is characterised: axial optical sectioning of SMLM images is demonstrated by thresholding fitted localisations using their fitted width and amplitude to reject fluorophores that emit from above or below a virtual 'light-sheet', a thin volume centred on the focal plane of the microscope. This method provides qualitative and quantitative improvements to SMLM.

In the Part B of this thesis, SMLM is applied to study T cell activation. Although the T cell receptor plays a key role in immunity, its stoichiometry in the membrane of resting T cells is still a matter of debate. Here, single-molecule counting methods are implemented to compare the stoichiometry of TCRs fused with mEos2 in resting T cells to monomeric and dimeric controls. However, because of the stochasticity of mEos2 photo-physics, results are inconclusive and new counting techniques based on structural imaging are discussed. In addition to TCR triggering, T cells require the co-stimulatory triggering of the CD28 transmembrane receptor to become fully activated. However, some immobilised anti-CD28 antibodies, referred to as super-agonists (SA), can directly activate T cells without triggering the TCR. In this thesis, single-molecule tracking techniques are used to investigate the molecular mechanism of CD28 super-agonism in live T cells. The results indicate that the diffusion of CD28 is slowed by SA binding. This effect is further discussed in light of the kinetic-segregation model proposed for TCR triggering.

Quantitative SMLM as implemented and further developed in this work offers new tools to investigate the molecular mechanisms initiating T cell activation, ultimately facilitating the discovery of novel approaches to target these pathways for therapeutic purposes.

# Contents

# Abbreviations

**Acronyms / Abbreviations**

| | |
|---|---|
| $K_D$ | Dissociation constant |
| $n_a$ | Numerical aperture (of an objective lens) |
| 2D | Two dimensional $(x, y)$ |
| 3D | Three dimensional $(x, y, z)$ |
| *E. coli* | *Escherichia coli* |
| *S. pombe* | *Schizosaccharomyces pombe* |
| Ab | Antibody |
| APC | Antigen-presenting cell |
| ATP | Adenosine triphosphate |
| BALM | Binding-activated localisation microscopy |
| CA | Conventional antibody |
| CBC | Coordinate-based co-localisation |
| CD | Cluster of differenciation |
| cSMAC | Central SMAC |
| CTLA-4 | Cytotoxic T-lymphocyte-associated protein 4 |
| DBSCAN | Density-based spatial clustering of applications with noise algorithm |

| | |
|---|---|
| DH-PSF | Double-helix PSF |
| DNA | Deoxyribonucleic acid |
| dSMAC | Distal SMAC |
| dSTORM | Direct STORM |
| DySCo | Dynamic single-molecule co-localisation |
| EMCCD | Electron-multiplying charge-coupled device |
| eYFP | Enhanced yellow fluorescent protein |
| F-actin | Filamentous actin |
| Fab | Fragment antigen-binding region of an antibody |
| Fc region | Fragment crystallisable region |
| FLIM | Fluorescence lifetime imaging microscopy |
| fPALM | Fluorescence PALM |
| FRET | Förster resonance energy transfer |
| FWHM | Full width at half maximum |
| GFP | Green fluorescent protein |
| HILO | Highly inclined and laminated optical sheet |
| hsPALM | High-speed PALM |
| ICAM-1 | Intercellular adhesion molecule 1 |
| ICOS | Inducible T-cell costimulator |
| IgG | Immunoglobulin G |
| IL-2 | Interleukin 2 |
| iPALM | Interferometric PALM |
| ITAM | Immunoreceptor tyrosine-based activation motifs |

| | |
|---|---|
| JD | Jump-distance |
| KS | Kinetic-segregation |
| LAT | Linker of activated T cells |
| LFA | Lymphocyte function-associated antigen |
| mAb | Monoclonal antibody |
| MAP | Mitogen-associated protein |
| MBIC | Membrane-bound immune complex |
| MHC | Major histocompatibility complex |
| MHC | Major histocompatibility complex |
| MSD | Mean square displacement |
| NeNA | Nearest-neighbour-based approach |
| PA-mCherry1 | Photo-activable mCherry 1 |
| PAINT | Point accumulation imaging in nanoscale topography |
| PALM | Photo-activated localisation microscopy |
| PBS | Phosphate-buffered saline solution |
| PC-PALM | Pair-correlation PALM |
| PD-1 | Programmed cell-death protein 1 |
| PDMS | Polydimethylsiloxane |
| PKC$\theta$ | Protein kinase C $\theta$ |
| pMHC | Complex formed of a peptide presented in the groove of an MHC |
| PSCFP2 | Photo-switchable cyon fluorescent protein 2 |
| PSF | Point-spread function |
| pSMAC | Peripheral SMAC |

| | |
|---|---|
| RESOLF | Reversible saturable optical fluorescence transitions |
| RNA | Ribonucleic acid |
| SA | Super-agonist antibody |
| sCMOS | Scientific complementary metal-oxide semi-conductor |
| SDS-PAGE | Sodium-dodecyl-sulfate polyacrylamide-gel electrophoresis |
| SIM | Structured illumination microscopy |
| SMAC | Supra-molecular activation complex |
| SMACM | Single-molecule active control microscopy |
| SMLM | Single molecule localisation microscopy |
| SNR | Signal to noise ratio |
| SPIM | Selective plane illumination microscopy |
| sptPALM | Single particle tracking PALM |
| SSIM | Saturating SIM |
| STED | Stimulated emission depletion microscopy |
| STORM | Stochastic optical reconstruction microscopy |
| TCCD | Two-colour co-localisation detection |
| TCR | T cell receptor complex |
| TEM | Transmission electron microscopy |
| TIRF | Total internal reflection fluorescence |
| TMR | Tetramethylrhodamine (orange dye) |
| uPAINT | Universal PAINT |
| UV | Ultraviolet |
| vls | Virtual ‘light-sheet’ |
| ZAP-70 | $\zeta$-chain-associated protein 70 |

# Chapter 1

# Thesis overview

Single-molecule localisation microscopy (SMLM) allows imaging of fluorescently-tagged proteins in live cells with a precision well below that of the diffraction limit. It has also introduced a new quantitative approach to fluorescence microscopy by enabling the tracking and counting of single molecules.

In the first part of this thesis (**Part A**), the design and building of three SMLM instruments, the implementation of a coherent custom-developed image analysis package and the characterisation of the photo-physical properties of the photo-activable fluorescent protein used in this thesis, *i.e.* mEos, are discussed (Chapter 3).

Then, in Chapter 4, a new post-processing method for SMLM analysis is developed and characterised. Axial optical sectioning of SMLM images is demonstrated by making use of fitting information that is usually discarded to reject fluorophores that emit from above or below a virtual 'light-sheet' (vls), a thin volume centred on the focal plane of the microscope. A universal easy-to-use ImageJ plug-in is implemented to quickly analyse a calibration sample to define and use such a vls. This optical sectioning of super-resolution images is achieved by applying well-characterised width and amplitude thresholds to diffraction-limited spots that can be used to tune the thickness of the vls. This allows qualitative and quantitative imaging improvements: by rejecting out-of-focus fluorophores, the super-resolution image gains contrast and local features may be revealed; by retaining only fluorophores close to the focal plane, vlsSMLM improves the probability that all emitting fluorophores will be detected, fitted and quantitatively evaluated.

In the second part of this thesis (**Part B**), SMLM is applied to study T cell activation. The human body is constantly challenged with ever-mutating pathogens. The complex and well-balanced capacity of the adaptive immune system to distinguish self from non-self is

crucial for survival. One key player in this recognition mechanism is the T cell receptor (TCR). The exact mechanism of TCR triggering, from the binding of the TCR ligand, to the transduction of the signal across the plasma membrane, is however still an object of controversy. Three main non-exclusive models have been proposed: aggregation, segregation and conformational change of the TCR. In light of the aggregation model, the natural organisation of TCRs at the membrane of the resting T cell has been widely discussed. Therefore, in Chapter 6, single-molecule counting methods are developed to try to determine the stoichiometry of TCRs fused to mEos2 and expressed at low levels on a resting T cell fixed in solution. Monomeric and dimeric proteins are expressed in both yeast and T cell models as quantitative controls. Although a variety of analyses are investigated, results are not conclusive: the photo-physical properties of mEos2 are too stochastic for single-molecule counting by sequential and irreversible photo-activation. New counting techniques based on structural imaging methods are discussed to further study the natural state of the TCR, before its triggering.

In addition to TCR triggering, T cells require a co-stimulatory signal to become fully activated. This second signal is initially delivered by a transmembrane receptor, CD28, expressed on the T cell. CD28 can also directly activate T cells without requiring TCR triggering: resting T cells incubated with defined anti-CD28 monoclonal antibodies, referred to as super-agonists (SAs), and immobilised on a surface, proliferate and release IL-2. In 2006, a tragic clinical trial also dramatically revealed the potency of CD28 SA in vivo. This super-agonism effect is specific to antibodies directed against epitopes of the receptor close to the plasma membrane. In Chapter 7, single-molecule tracking techniques are used, in parallel with functional IL-2 assays, to investigate the mechanism of CD28 super-agonism at the single-molecule level in live T cells. Results indicate a specific slowing down of CD28 upon SA binding. Although critical, antibody cross-linking does not fully account for this SA-specific slowing down effect. The possibility that avidity of the SA is increased by geometric constraints imposed by its epitope location is discussed. Finally, simultaneous imaging of both CD28 and the large phosphatase CD45 could suggest some size-dependent segregation at the membrane of the T cell. Additional experiments are proposed to challenge a CD28 triggering model inspired by the kinetic-segregation model proposed for TCR triggering.

Finally, in the last part of this thesis (**C**), material and methods used for all experiments presented in this work are summarised.

# PART A

# Chapter 2

# Introduction to single-molecule localisation microscopy

This chapter provides the technical context for the work presented in this thesis, and especially in the next two chapters (Chapters 3 and 4), by introducing fluorescence microscopy and its physical limit in terms of resolution, single-molecule localisation microscopy (SMLM) as a successful method to overcome it, and the new quantitative approach that SMLM enables. This chapter was partially published as a review [1] and an introductory article written for the special imaging issue of the Physiology News of Summer 2014 [2].

## 2.1 Fluorescence microscopy

### 2.1.1 Fluorescence and Stokes' shift

First described by Stokes in 1852, fluorescence describes the emission of a photon of light when an electron of a molecule relaxes from an excited high-energy state $S_1$ to a lower-energy ground state $S_0$ with a temporal probability well-modelled by an exponential decay and a characteristic fluorescence lifetime $\tau$ on the order of nanoseconds [3]. The energy loss $E$ during this event is converted in a photon of wavelength $\lambda_{em} = h \cdot c/E$ (where $h = 6.62 \cdot 10^{-34}\,\mathrm{J{\cdot}s}$ is Planck's constant, and $c = 2.998 \cdot 10^{8}\,\mathrm{m{\cdot}s^{-1}}$, the speed of light in a vacuum) (*cf.* general Jablonski diagram in Figure 2.1).

In most applications, electrons in fluorescent molecules (also called fluorophores) are pumped in their first excited singlet state $S_1$ by absorption of a photon. This excitation photon has a shorter wavelength $\lambda_{ex}$ than the emitted photon: because of the second law of thermodynamics, no energy is created but rather dissipated between the time when the

excitation photon is absorbed and when fluorescence is emitted (in terms of energies of both photons: $h \cdot c/\lambda_{ex} \geq h \cdot c/\lambda_{em}$). Mechanistically, during relaxation, some non-radiative (*i.e.* non-fluorescent) energy is transferred by heat to the solvent, and lost: (1) the excitation photon generally populates a high vibrational energy level of the excited state $S_1$ which quickly relaxes to the lowest vibrational energy level of $S_1$ before emission of the fluorescence. (2) The electron also often relaxes to a higher vibrational energy level of the ground state $S_0$, emitting a photon and further relaxing to the ground state by a non-radiative way.

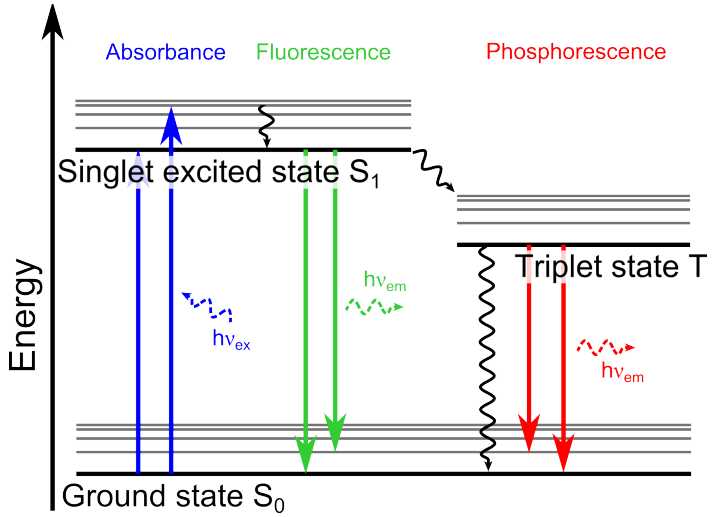


Figure 2.1 *General Jablonski energy diagram of a fluorophore.* Under illumination at a wavelength $\lambda_{ex}$, an orbital electron of the fluorophore can be excited by a photon of energy $h\nu_{ex}$ and leave its ground state $S_0$ to a singlet excited state $S_1$ (Absorbance). The electron then relaxes to the lowest vibrational energy level of $S_1$ in a non-radiative way, dissipating heat in solution. The electron can either relax to its ground state $S_0$ by emitting a photon of light of energy $h\nu_{em}$ (Fluorescence) or transition to other states, such as a triplet state $T$ in a non-radiative way. Generally, the electron finally relaxes from the triplet state $T$ to its ground state $S_0$ by radiative (Phosphorescence) or non-radiative ways.

This spectral shift between excitation and emission light is called the Stokes' shift of a fluorophore. Magnitudes of Stokes' shifts differ from fluorophore to fluorophore for sometimes complex reasons. The Stokes' shift also depends on the local environment of the fluorophore (*e.g.* Förster resonance energy transfer (FRET) uses the close proximity of a donor and an acceptor fluorophores to dramatically increase the spectral shift of the donor). However, fluorophores with large Stokes' shifts enable the optical separation of their absorbance and emission spectra by use of beamsplitters. This explains the successful advent of fluorescence microscopy that uses fluorophores to tag a specific target in the sample: the fluorescent signal can then be collected without being convolved with the reflected illumination light.

One drawback of fluorescence imaging, especially when single molecules are observed

is the inherent stochasticity of fluorescence (as ensemble averaging masks individual stochastic behaviours). This is, moreover, usually convolved with a multitude of competing energy paths by which the excited fluorophore can relax to its ground energy state. Thus, a fluorophore under constant excitation light will stochastically take radiative and non-radiatives pathways, through different intermediary energy states. The probabilities or kinetics associated to each pathway determine the quantum yield and photo-blinking (transient entry in a dark state, *i.e.* cycling in non-radiative paths) propensity of a fluorophore.

### 2.1.2 Abbe's diffraction limit

Microscopes, like telescopes, have been aiming at increasing their magnification in order to see deeper into the infinitely small or the infinitely large. However, both optical tools are limited in this goal by the physical diffraction limit as described by Abbe [4]: all imaging systems are limited in their frequency space by a high-frequency cut-off corresponding to $\lambda/(2\,n_a)$ (where $\lambda$ is the wavelength of the collected light, and $n_a$ the numerical aperture of the lens of optical device being used). The function that convolves a point-emitter imaged through an optical system is called the point-spread function (PSF) of the system.

Abbe's limit results in the fact that the PSF of a typical objective lens corresponds to an Airy disk that is well approximated with a 2D-Gaussian for emitters close to the focal plane. The width $\sigma_{Gaussian}$ of the corresponding PSF approximation is proportional to the wavelength as follows [5]:

$$\sigma_{Gaussian} = \frac{1.323\,\lambda}{2\,\pi\,n_a} \tag{2.1}$$

In this thesis (as it is common in the field of single-molecule microscopy), the PSF of a fluorophore refers to the image of the specific fluorophore through the objective lens of the microscope, *i.e.* the convolution of the PSF of the instrument with the position and intensity of the fluorophore of interest (*cf.* Figure 2.2, C for an illustration).

Equation 2.1 reveals the restriction imposed by Abbe's diffraction limit on optical resolution (typically limiting the resolution of modern fluorescence microscopes to $\sim 250$ nm): two fluorophores closer than 250 nm from each other will hardly be distinguished as their PSFs will overlap. They cannot be directly resolved optically. Electron microscopy solves this issue by using much smaller wavelengths ($10^{-10}$ instead of $10^{-7}$ m). It however requires fixation of the sample, both altering the sample and preventing live cell imaging.

However, the imaged PSF of a fluorophore can be thought of as a probability distribution function of the position of the point-emitter. Therefore, through determination of the centre of an individual PSF, the Abbe diffraction limit can be overcome and the emitter can be

localised with greater precision. The calculation of the centre of the PSF and consequently the precision of the localisation depends on two main variables: the number $N$ of collected photons, via $1/\sqrt{N}$, and the pixel size of the detector (*cf.* Equation 3.13) [6].

### 2.1.3 An overview of far-field optical super-resolution techniques

New methods, collectively grouped under the term super-resolution microscopy, have been developed to overcome the physical limit of diffraction, gaining over two orders of magnitude in precision [7], and allowing direct observation of processes at spatial scales much more compatible with the regime that biomolecular interactions take place on. Different approaches have so far been proposed, including: (1) limiting spontaneous fluorescence emission of the sample to spatial regions smaller than the diffraction limit or frequency domains overpassing Abbe's limit (targeted switching and readout), (2) or stochastically separating single fluorophores in time to gain resolution in space (stochastic switching and readout). Various other techniques, such as the recent radically-innovative expanding microscopy [8], are still emerging and may present complementary advantages which could be precious to orthogonally validate controversial observations.

#### Structured illumination microscopy

Targeted switching and readout includes structured illumination microscopy (SIM) [9] and stimulated emission depletion (STED) microscopy [10, 11]. Both techniques use specific illumination geometries to gain sub-diffraction information. By only illuminating a grating pattern and imaging the Moiré pattern resulting from its interference with the sample, SIM enables a two-fold gain in resolution due to more precise information obtained in specific domains of the Fourier transform of the recorded image. To fully compute and rebuild the frequency domain of the sample, though, multiple frames needs to be recorded while varying independently both the orientation and the phase of the sine illumination pattern. The super-resolved figure is obtained by finally computing the reverse Fourier transform of the recombined frequency domain of the sample.

Although fast, conventional SIM can only improve the resolution two fold. However, in a similar strategy to STED, saturating SIM (SSIM) [12] uses non-linear optical saturation of the sample to overpass this limitation: schematically, the saturation of the sample enables to limit the size of the non-illuminated domains of the sample to specific sub-diffraction values. Saturation induces a series of high-order harmonics in the frequency domain of the imaged sample which analysis translates into sub-diffraction resolutions (*e.g.* 50 nm). SIM

and SSIM present the advantage of being fast and generally compatible with all conventional fluorophores. They are, however, less precise than other methods such as STED.

### Stimulated emission depletion microscopy

Similarly to SSIM, STED uses non-linear optical saturation to overpass Abbe's limit, but the optical saturation here concerns fluorescence depletion in a configuration reminiscent of scanning confocal microscopy. In STED, a traditional confocal illumination beam is aligned with a 'doughnut'-shaped depletion beam designed such as to overlap a zero-intensity spot with the excitation focal spot. The illumination beam excites the fluorophores in the confocal volume and the powerful depletion beam depletes almost instantaneously the excited states of the fluorophores located in the zone illuminated by the doughnut, through stimulated emission.

Using high-power depletion beams, saturation of the depletion is reached for all the fluorophores around the focal diffraction-limited excitation spot, thus limiting the spontaneous fluorescence emission to a sub-diffraction area (*i.e.* all fluorophores further than a distance $r$ (<250 nm) from the centre of the illumination beams are trapped in their ground dark state $S_0$). The radius $r$ of the emission area can directly be modulated by the intensity of the depletion bead. As in confocal microscopy, the aligned beams are then scanned through the sample to rebuild the final super-resolved figure.

The resolution achieved by STED microscopy, equal to the width $2r$ of the scanned of spontaneous fluorescence emission area, is theoretically only limited by the power of the depletion beam, but practically by the quality and precision of the alignment of both excitation and depletion beams. Another important drawback of the technique is the requirement for high-power illumination which makes live cell imaging challenging. However, the generalisation of STED to the concept of reversible saturable optical fluorescence transitions (RESOLFT) dramatically reduces the amount of required illumination, thus potentially increasing its compatibility with live cell imaging [13, 14].

The other important drawback of STED microscopy is its time resolution which is inversely proportional to the area of the region of interest that is imaged and limited by the scanning speed and the mean time of the duty cycle of the fluorophore. For very small regions of interest ($\sim 1\ \mu m^2$) though, STED has so far been the fastest of all super-resolution methods (up to 80 frames per second for diffusing beads [15], or 28 frames per second in living cells [16]). Interestingly, parallelisation of the illumination pattern dramatically improves its speed and combines STED with SSIM: two orthogonal SIM-like interference patterns were designed to produce an array of more than 100,000 doughnut-shaped deple-

tion beams that only need to scan a tiny fraction of the sample [17]. Finally, an advantage of the traditional implementation of STED with pulsed illumination is its compatibility with lifetime measurements, adding another dimension to the data (as spectrally separating proteins tagged with different fluorophore is technically challenging in STED microscopy).

#### Single-molecule localisation microscopy

The second approach (stochastic switching and readout) was independently demonstrated by three different groups in 2006: photo-activated localisation microscopy (PALM) [18], stochastic optical reconstruction microscopy (STORM) [19], and fluorescence photo-activation localisation microscopy (fPALM) [20]. These techniques, grouped under the name of single-molecule localisation microscopy (SMLM), or single-molecule active control microscopy (SMACM), allow the imaging of single molecules which cannot only be precisely localised, but also followed through time and quantified. The next sections focus on this 'pointillism-based' super-resolution imaging[1].

## 2.2 Single-molecule localisation microscopy

### 2.2.1 Principle: spreading spatial density in time

The concept behind SMLM is that the position of an object can be known with greater precision than its size. The size of a table is on the order of meters, but its position can be easily known with a precision of centimetres. This is similar with fluorophores. Although they are observed as 250 nm wide PSFs, each PSF can be very accurately fitted with a 2D-Gaussian and its centre localised with great precision. The localisation precision mainly depends on the pixel size of the camera and is inversely proportional to the square root of the number of collected photons above the background (*cf.* Section 3.4.3) [6].

However, this strategy can only be applied if PSFs are distinguishable and separated from each other. If the density of labelled proteins brings the fluorophores closer than the diffraction limit (*e.g.* protein complexes), their PSFs merge and determining the number of PSFs and the positions of their centres becomes almost impossible. This is made additionally complicated by the fact that the intensity of a fluorophore considerably varies both in a deterministic and non-deterministic way, depending on its position, its orientation and its excitation. This means that a PSF twice brighter than another one cannot be inferred to be the image of twice as many labels.

[1] Good extensive reviews for STED and SIM methods can be found in refs. [21] and [22], resp..

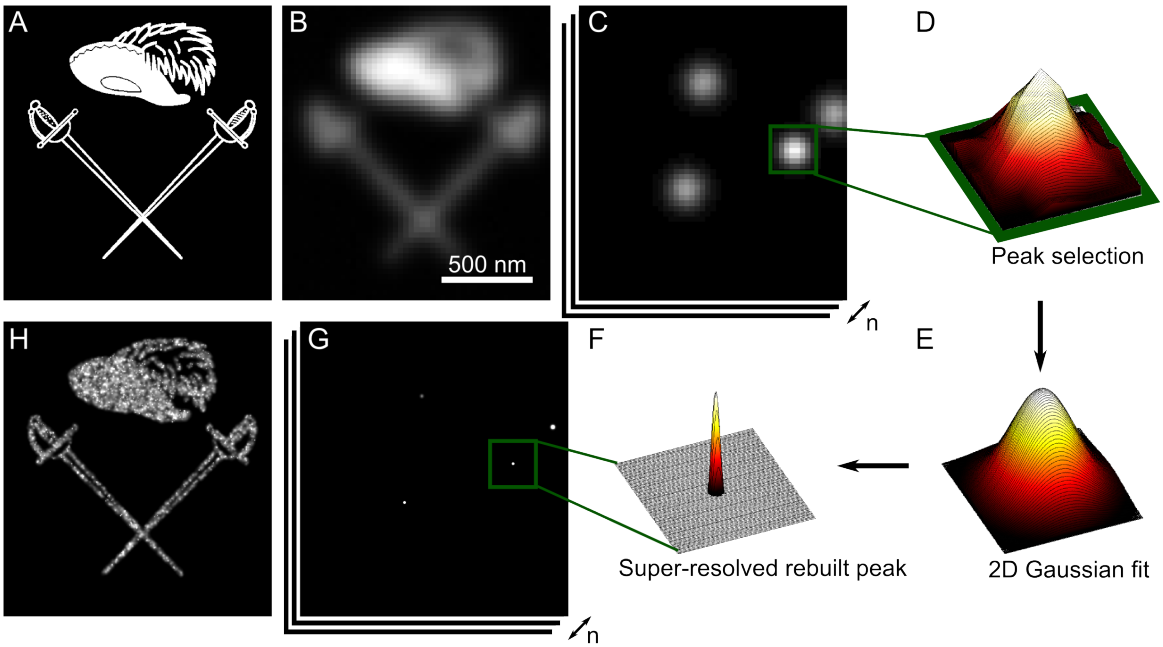


Figure 2.2 *Concept of single-molecule localisation microscopy.* A musketeer coat of arms structure was simulated (**A**) from which 10,000 fluorophores were stochastically activated. A few fluorophores only are activated in each frame (**C**). Each PSF is then fitted (**D-H**) and re-plotted as a 2D-Gaussian which width corresponds to the precision of the localisation (**F-G**). Many frames allow the rebuilding of a super-resolved picture (**E**) which is much more precise than the diffraction limited one (**B**).

To circumvent this density issue, the essential step leading to pointillism-based super-resolution microscopy was the ability to control the activation of point-emitters to stochastically separate them in time, so that only a few PSFs appear in each single frame. Thus, a SMLM experiment consists in imaging thousands of frames, each of which only showing sparse separated PSFs that are fitted with 2D-Gaussians and whose positions and precisions are plotted in a final super-resolved figure (*cf.* Figure 2.2).

The various SMLM techniques now distinguish themselves based on how the emitters are spatially isolated: although Betzig originally proposed to separate emitters spectrally [23], dense fluorophores are now commonly separated by using a population of dark fluorophores (*i.e.* initially non-fluorescent or pumped into a non-fluorescent state) and stochastically turning a few of them in their fluorescent state, thanks to photo-blinking, photo-activation or binding interactions (*cf.* Section 2.2.2). Thus, very few fluorophores are imaged at the same time, statistically allowing their spatial separation through time.

### 2.2.2 Single-molecule photo-switching

To separate dense fluorophores through time, SMLM requires methods for switching fluorophores 'On' and 'Off'. Many solutions to this exist. Here, three popular mechanisms used in biological imaging are highlighted: exploiting the innate photo-physics of fluorophores, chemical/spectral structural modification, and finally diffusion.

#### Photo-physical manipulation

When pumped in its first singlet excited state, a fluorophore usually relaxes to its ground state by emitting fluorescence within nanoseconds. However, inter-system crossing to non-fluorescent states, such as triplet states may also occur, and when in such states, the fluorophores are unable to rapidly relax and enter further excitation-emission cycles; here the fluorescence lifetime is typically on the order of micro- to milliseconds. This leads to the molecules undergoing fluorescence intermittently, so-called blinking, as they cycle into and out of the 'dark' state. Unfortunately, population of these dark states can often be part of the photo-bleaching pathway, and so the number of switching cycles is limited.

However, this blinking can still be used to temporally separate the emitters, and therefore allow for SMLM imaging [24–26]. This process is also observed in genetically encodable fluorescent proteins, for example enhanced yellow fluorescent protein (eYFP), which has been shown to undergo power-dependent blinking under irradiation of 515 nm laser excitation. This has been used to study super-resolved spatial distributions of proteins in bacterial models [27, 28].

Photo-blinking has also successfully been used to resolve close quantum dots [29]. However, quantum dot photo-blinking is difficult to control and spatial separation of single quantum dots is often impossible in dense labelled samples. An alternative strategy described by Hoyer *et al.* consists in using quantum dot 'blueing' to further separate a smaller fraction of blinking quantum dots as their emission spectrum switches towards the blue under photo-induced oxidation [30].

#### Chemical modification

In standard fluorescence microscopy, various methods have been employed to circumvent the effect of photo-bleaching. Because of its triplet state, oxygen has the most understood role in inducing photo-bleaching [31]. Thus, means to remove molecular oxygen from the imaging buffer, for example by simple degassing, or through addition of enzymatic oxygen scavenger systems, are commonly used in fluorescence microscopy [32–34]. However, re-

moval of molecular oxygen simultaneously increases of the lifetime of the triplet state, and consequently enhances the photo-blinking behaviour of the fluorophore.

This oxygen-depletion-induced photo-blinking could be directly used for SMLM imaging, but its poor tunability makes it hard to adjust the blinking rate to the density of fluorophores to be separated. Thus, addition of triplet state quenchers at various concentrations (*i.e.* micro- to millimolar concentrations of reducing and oxidizing agents) to the oxygen-depleted buffer enables a finer control over the proportion of fluorophores in their triplet dark state as they are able to relax the fluorophore back to its ground energy state[2] [35–37].

By varying the buffer composition (*i.e.* the concentrations of the oxidizing and reducing agents), long-lasting dark states can be generated, therefore allowing for SMLM imaging [38–40]. The dark state generally exists as a reduced form of the chromophore, which absorbs at shorter wavelengths. Hydrogenated fluorophores can also act as dark states (by addition of sodium borohydrate for example) which can be depopulated upon 405 nm illumination [41, 42]. Such dark states can thus be depopulated through irradiation with a 405 nm illumination yielding the on-state of the dye once again. Although in direct STORM (dSTORM − a generalisation of STORM to standard dyes) excitation at this wavelength is achieved directly by irradiation at 350-550 nm [26, 43], STORM originally used a reporter-activator dye pair, or cyanine switch (*e.g.* Cy5-Cy3), where the close proximity of the two dyes leads to the on-switching of the reporter by illumination at a lower wavelength [19, 44].

Globally, this chemically-induced photo-switching has now been successfully implemented with a very wide variety of cyanine, rhodamine and oxazine dyes [45, 46]. Finally, Uno *et al.* recently proposed a strategy to avoid the use of buffers hardly compatible with live imaging and designed dyes which spontaneously blink at physiological pH [47].

### Diffusion

In addition to photo-switchable fluorophores, techniques that rely on fluorophores being transiently bound to the protein of interest have been developed. Fluorophores freely diffusing in solution are not observed as their PSFs are blurred by their rapid sub-frame diffusion. However, when a fluorophore temporally binds to a protein of interest, its diffusion drastically decreases and its PSF is detected over the diffusing and out-of-focus background. In point accumulation for imaging in nanoscale topography (PAINT) [48] and universal PAINT (uPAINT) [49], fluorophores temporarily bind to surfaces, such as membranes, and are lo-

[2]Triplet state quenchers were initially rather used to deplete the triplet state, thus the photo-blinking of the fluorophore in order to increase its quantum yield. They were later used at lower concentrations to control the population of fluorophores in the dark triplet state.

calised one-by-one allowing for SMLM imaging. Binding-activated localisation microscopy (BALM) has been used to generate super-resolved figures of DNA, using the intercalating dye YOYO-1, the quantum yield of which increases threefold upon binding to DNA [50].

### 2.2.3 Fluorophores for SMLM imaging

#### Fluorescent dyes and proteins

Although photo-switching was mostly presented and discussed for conventional organic (cyanine, rhodamine and oxazine) dyes in the previous sections, other photo-switching fluorophores have been used in SMLM experiments. Quantum dots have the advantage of high brightness and little if any photo-bleaching, but are neither photo-activable nor cell-permeable, present some cytotoxicity and are prone to aggregation. Thus their use in SMLM has been limited to the tracking of low density of membrane proteins using their photo-blinking behaviour [29, 51, 52].

Light-inducible control of the spectroscopic properties of fluorescent proteins enabled their use in SMLM imaging. Fluorescent proteins are genetically encoded and thus present the advantages of high specificity, stoichiometric and intracellular labelling, and compatibility with live imaging. They, however, are usually less bright and photo-stable than organic dyes, although brighter fluorescent proteins have now been described, some providing a photon budget comparable to popular organic dyes (*e.g.* the different versions of the bright and popular mEos − *cf.* Section 3.3).

Many different fluorescent proteins have been described; however, they all consist of a single polypeptide chain of about 230 amino acids in length, each containing an 11-stranded beta-barrel, which has a single distorted helix spiralling down its centre and contains three amino acids that form the chromophore [53]. The chromophore engages in a wide-range of interactions with surrounding amino acids and solvent environments, and single mutations in the non-chromophore amino acids can strongly influence the spectroscopic properties of the protein, shifting its absorption and emission spectra, or even leading to it becoming non-fluorescent [54]. Some mutations induce remarkable photo-switching properties of the fluorescent proteins which can be distinguished in two general categories of fluorophores: reversible photo-switchable and irreversible photo-activable fluorophores. Both categories and their distinction are discussed in next section.

Fluorescent proteins directly tag the protein of interest as a genetic fusion protein. In terms of label size (critical for accurate SMLM measurements − *cf.* Section 3.4.3), fluorescent dyes ($\leq$1 nm) are smaller than quantum dots ($\sim$2-10 nm) and fluorescent proteins

(cylindrical shape of diameter ∼2.8 nm and length ∼4 nm). However, to specifically label a protein, most dyes need to be covalently attached to an antibody, making the total tag actually larger (∼14 nm in their largest dimension). Nevertheless, means to limit the total size of the tag (*e.g.* nanobodies − small single-domain antibodies from camelids or cartilaginous fish [7, 55, 56] −, small target molecules like phalloidin [37] or the intercalating dye YOYO-1 [50], 'click' chemistry strategy [57, 58]) or to get the specificity of fluorescent proteins (by retro-engineering enzyme tags, *e.g.* the HaloTag [59] of the Snap-tag [60]) have been proposed to optimise sample labelling and get the best of both organic dyes and fluorescent proteins.

### Reversible and irreversible photo-switching

Photo-switchable fluorophores can be separated in two categories[3]:

**Reversibly photo-switchable fluorophores.** The photo-switching methods described in the previous section involve reversible dark states. A wide range of fluorescent proteins also displays a light-induced, reversible transition between a fluorescent and non-fluorescent state [61–64]. Some of them present a very high contrast, good thermal reversibility and high thermal stability (*e.g.* Dronpa [65], rsTagRFP [66], or mGeos [67]). This type of photo-switching usually involves a transition to the off-state after irradiation with the same wavelength that induces fluorescent emission, while irradiation with UV light leads to recovery of the on-state.

**Irreversibly photo-activable fluorophores.** Although organic dyes are mostly used as reversible photo-switching fluorophores in SMLM experiments, some methods were developed to use dyes in an irreversible photo-activation scheme. The dye is made non-fluorescent by covalently either adding a hybrid anion *in situ* [68] or replacing an amine group by an azide [69], both of which disturb the $\pi$-bonded network responsible for the fluorescence properties of the chromophore. The $\pi$ network of these so-called caged dyes or fluorogens is released during imaging by a light-induced chemical reaction which irreversibly photo-activate the dark molecule.

Fluorescent proteins can also display irreversible light-induced changes, either consisting of an off-state to on-state conversion (*e.g.* PA-GFP [70], PS-CFP [71], and

[3]Incorrectly, but as a practical convention, the acronym 'PALM' is often used to refer to an experiment using irreversibly photo-activable fluorophores and 'STORM' to an experiment that involves reversibly photo-switchable fluorophores. However, the distinction sometimes rather refer to the use of fluorescent proteins ('PALM') as opposed to organic dyes ('STORM').

PAmCherry [72]), or a conversion from shorter to longer wavelength emission (green to red) (*e.g.* Kaede [73], EosFP [74] and its monomeric/tandem variants, Dendra2 [75]), when irradiated with near-UV light. The green to red photo-conversion is a result of the conjugated system in the chromophore being extended due to cleavage of a histidine side-chain [76, 77].

The major advantage of the latter type of fluorophores is that they allow single-molecule counting as they are activated only once and thus each single burst of fluorescence theoretically corresponds to one fluorophore (*cf.* next section and the introduction of Chapter 6). Single-molecule counting is one of the various quantitative approaches that SMLM brings, together with improved resolution, to the field of fluorescence microscopy.

## 2.3 A quantitative approach to microscopy

One of the least known but major advantage of SMLM is the quantification it brings to the microscopy field. Instead of the $N$ (*e.g.* 512x512) pixel intensity values obtained in any other bulk method, an SMLM experiment gives as primary results a multi-dimensional matrix composed of >10,000 rows (*i.e.* the list of fitted localisations) and >10 columns (frame of first appearance, $(x, y)$ position, amplitude, width of the PSF, ellipticity, number of re-appearances, *etc.*). These data require careful statistical and sometimes complex analysis, but provide precious quantitative information about the sample.

### 2.3.1 Local diffusion analysis and detection of rare events

As a proportion of fluorophores does not photo-bleach in a single frame, a natural extension of SMLM in live cells is to follow a single activated fluorophore over a few consecutive frames. This proportion is dependent on the illumination power which can be lowered to increase the average time that the fluorophores are imaged for before photo-bleaching. Bridging SMLM and single particle tracking [78] (in single particle tracking PALM − spt-PALM [79]) gives access to local diffusion maps [49] and to the precise description of single-molecule kinetic states [80].

In this respect, at the core of SMLM is the ability to track and study low probability events. This is illustrated by the American school bus problem: when looking from the space at the Earth, looking specifically at the American school busses in average over a day (as in bulk imaging), an observer would see them aligned in car parks, static and aggregated. This observation would not help the observer to understand the function of such a device

on Earth. However, if the observer could follow only a few busses over one day, he would realise that they leave their static state and very regularly visit the same schools. These tracks would help understand the very functionality of the school busses. This metaphor highlights the help SMLM provides in understanding the functionality of rare events compared to conventional fluorescence bulk imaging.

### 2.3.2 Single-molecule counting and cluster analysis

Another natural extension of SMLM, especially when using irreversibly photo-activable fluorophores, is to consider single-molecule counting. Indeed, although most fluorophores used in SMLM enter multiple times in a dark state and photo-blink, some fluorophores such as caged dyes or the fluorescent protein mEos can be photo-activated once and imaged until they bleach. Such fluorophores thus promise the possibility of counting the precise number of labelled molecules in a cell, a cluster or a protein complex. The technique is still at its beginning and faces major over- and under-counting challenges, but innovative methods begin to propose partial solutions to tackle them and unravel the stoichiometry of protein complexes *in vivo* (*cf.* the introduction of Chapter 6 for a complete description of the field).

The stoichiometry of a protein complex can also be determined by localising each of its proteins with higher precision than the size of the complex. A remarkable example is the repeated observation of the 8-fold symmetry of the nucleopore complex by different groups [7]. Because of the reproducibility of the sample preparation and the robust stoichiometry of the nucleopore complex, it has even recently become a molecular ruler for both localisation and counting precision [81].

Finally, in a larger scale, the positions of the fitted localisations can be statistically analysed in pair-correlation PALM (PC-PALM) [82, 83] to quantitatively study the size and population of a distribution of clusters.

### 2.3.3 Single-molecule multi-dimensional imaging

Beyond the initial two spatial dimensions collected in SMLM, additional single-molecule information can be collected on each imaged single emitter such as its axial position, its lifetime, its spectral distribution or its orientation. Concerning continuous structures such as membrane domains or vesicles, information about their evolution over time in live cells can also add a further dimension to the SMLM experiment.

### 3D imaging

As most biological processes happen in three dimensions, observing their 2D projection is not always relevant or convincing to study specific phenomena. Several methods were developed to code the information about the axial position of the fluorophore in some deformation of the shape of its PSF. This additional feature is implemented by the addition of different optical components in the imaging path, allowing it to be compatible with all SMLM methods. Four main methods have been developed, enumerated here in the order of their ease of implementation and use (or, in the reverse order, on their axial localisation precision) [84, 85]: biplane microscopy [86], astigmatism [87], the double-helix PSF (DH-PSF) [88] and interferometric PALM (iPALM) [89] (a detailed review of the four strategies can be found in ref. [1]).

All four methods however share the same drawbacks: the axial position is gained to the detriment of both precision and resolution. Indeed, adding extra optical elements, dilating the PSF over more pixels or the increase in out-of-focus noise automatically decreases the signal-to-noise ratio which is inversely correlated to the precision (*cf.* Section 3.4.3). Similarly, since a volume is observed, more labelled proteins have to be separated, and an increased sampling is necessary to prevent a decrease of resolution in the final super-resolved picture.

### Video-rate imaging

If the movement of the process observed is an order of magnitude slower than the time required to acquire enough frames to sufficiently sample the structure of interest, SMLM can be compatible with live cell imaging. Hence, a super-resolved video or time-lapse of the phenomenon can be rebuilt: a moving time-window may be used to rebuild the final video as a way to balance sampling and fluidity of the final super-resolved movie. Until very recently this technique was limited by the acquisition rate of the highly-sensitive cameras required for SMLM imaging (electron multiplying charged-coupled devices – EMCCDs – have a typical minimal exposure of 33 ms).

Thanks to the subtle adaptation of the localisation fitting algorithms to the noise characteristics of scientific complementary metal-oxide semiconductor (sCMOS) cameras, much higher frame rates are reachable (on the order of the millisecond over the same area) [90]. This makes the new limiting factor the physical photo-physics of the fluorophore, such as its lifetime decay, its photon budget or its absorption cross-section. Indeed, in order to keep a high signal-to-noise ratio, a constant number of photons is required per fluorophore and per

frame. Thus decreasing the exposure amounts to increase the illumination power if the fluorophore is not saturated. An increase in illumination power might also prove to be cytotoxic which can be problematic when imaging live samples.

Although these limitations are challenging, one could propose to bridge SMLM with fluorescence lifetime imaging microscopy (FLIM), recording the fluorescence lifetime of each single fluorophore. Single-molecule FLIM is commercially available and proof of concept of wide-field FLIM imaging [91] and combination of TIRF illumination and FLIM (TIRFLIM) [92] were demonstrated, but together with the saturation of the fluorophores and the cytotoxicity of the illumination, new design of cameras are required [93].

**A nano-world in five dimension?**

As for conventional fluorescence microscopy, spectrally-separated fluorophores can be used to simultaneously label various proteins of interests [72, 94, 95]. Interestingly, emission spectra of the fluorophores can overlap or be similar if the photo-induced activation involves separated wavelength ranges [44]. Another strategy for fixed samples, so-called exchange-PAINT, consists in using the transient binding of the fluorophores in uPAINT to wash the labels from the samples at the end of acquisition and replace them with labels targeting another proteins tagged with the same colour [96].

Instead of considering discretely separated spectra, single-molecule spectroscopy can also be associated with SMLM (spectral-PAINT, developed by Godet *et al.*, article in preparation): for each bright fluorophore, both its spatial position and its spectrum are recovered thanks to the simultaneous imaging of both zero and first interference orders through a diffraction grid.

Finally, other more exotic but complementary dimensions, such as fluorescence anisotropy [97] that gives information about the rotational mobility or the orientation of each single emitter [98, 99], have also successfully been explored and coupled to SMLM imaging protocols.

Thus, by active control of the switching of fluorophores, the physical limit of diffraction can be overcome: using SMLM, biological samples have been imaged with sub-diffraction precision on the nanometer scale. Multiple mechanisms to separate dense fluorophores through time have been described, and numerous dyes and fluorescent proteins have successfully been used in SMLM. By localising single fluorophores one-at-a-time, SMLM provides rich quantitative information about the sample and has inspired the development of new statistical methods for data analysis.

# Chapter 3

# Building and characterising a single-molecule super-resolution platform

Building of the three super-resolution platforms was the work of M. Palayret. They were designed in collaboration with Dr S.F. Lee. Dr J. Godet helped with setting up the light-sheet on the double-helix instrument. All algorithms were designed and written by M. Palayret. All data presented here were also imaged and analysed by M. Palayret. The experiment described in Section 3.5 are published in ref. [100].

## Aim of this chapter

This chapter sums up the considerations about the design, building, and characterisation of three single-molecule super-resolution microscopes: two similar 2D platforms differing mostly in the wavelengths available for illumination (Figure 3.1 describes the first microscope built, the second one offering additional 514 nm, 594 nm and 730 nm laser lines), and a 3D two-colour double-helix platform (Figure 3.2). These instruments are now heavily used by many users on a variety of projects ranging from the study of the aggregation of pathogenic proteins in neuro-degenerative disorders to early T cell triggering, to DNA replication and repair in live fission yeast [101].

This chapter first describes the two parts of a microscopes, and their specific requirements for SMLM: the illumination and the imaging paths. It then characterises the photophysical properties of mEos, the fluorescent protein used in this thesis. Following, the

bespoke algorithms developed to process SMLM data is described. Finally, an example of a 'smart' automated imaging protocol is presented, and advantages of automation are discussed.

## 3.1 Illumination path

In fluorescence microscopy, to measure signal from a sample, the fluorophores need to be excited at a wavelength resonant to their absorption peak. In SMLM, since signals from single fluorophores are recorded, both excitation of the fluorophores and collection of their emitted signal are critical. First, the specific requirements of the illumination for single-molecule imaging are described and discussed.

A single dye or fluorescent protein typically emits 1,000-10,000 photons per acquisition frame ($\sim$50 ms). Because of the limited numerical aperture of the lens collecting the fluorescent signal, and the imperfect optical elements used in the imaging path (that absorbs and reflects part of the signal), $\sim$100-1,000 photons are detected above the background at the plane of the detector. However, this signal is spread over typically nine pixels on the camera chip [6], following a 2D-Gaussian distribution. This spread decreases the signal-to-noise ratio (SNR), since each pixel of the EMCCD reads a similar electronic noise [103, 104]. As discussed in Section 3.4.3, the localisation precision of each fluorophore is inversely proportional to the square-root of the SNR (Equation 3.13). Thus, optimising the SNR of the technique is not only necessary to be able to detect single fluorophores but also to localise them with precision below the diffraction-limit of the light.

A main source of noise in microscopy is the detection of photons coming from out-of-focus fluorophores: since in epifluorescence microscopy (Figure 3.3, A-B,D) the entire field of view is illuminated, all fluorophores emit photons, both those at the focal plane of the imaging lens and those below or above it. The bright contrasted signal coming from the focal plane is consequently noised by the diffused light coming from out-of-focus fluorophores. Confocal microscopy increases the resolution of epifluorescence microscopy by limiting both the illumination of the sample to a small single confocal volume (which can be approximated to a 3D-Gaussian of standard deviation $\sim$230 nm laterally and $\sim$650 nm axially for a 1.49-$n_a$ oil-immersion objective at $\lambda$ =680 nm), and the collection of the emitted fluorescent light to a similar volume (with a pinhole of diameter around one Airy unit, *i.e.* 33.5 µm).

Other methods, compatible with wide-field imaging, have been described to limit the illumination of the sample to the focal plane and drastically reduce the out-of-focus noise

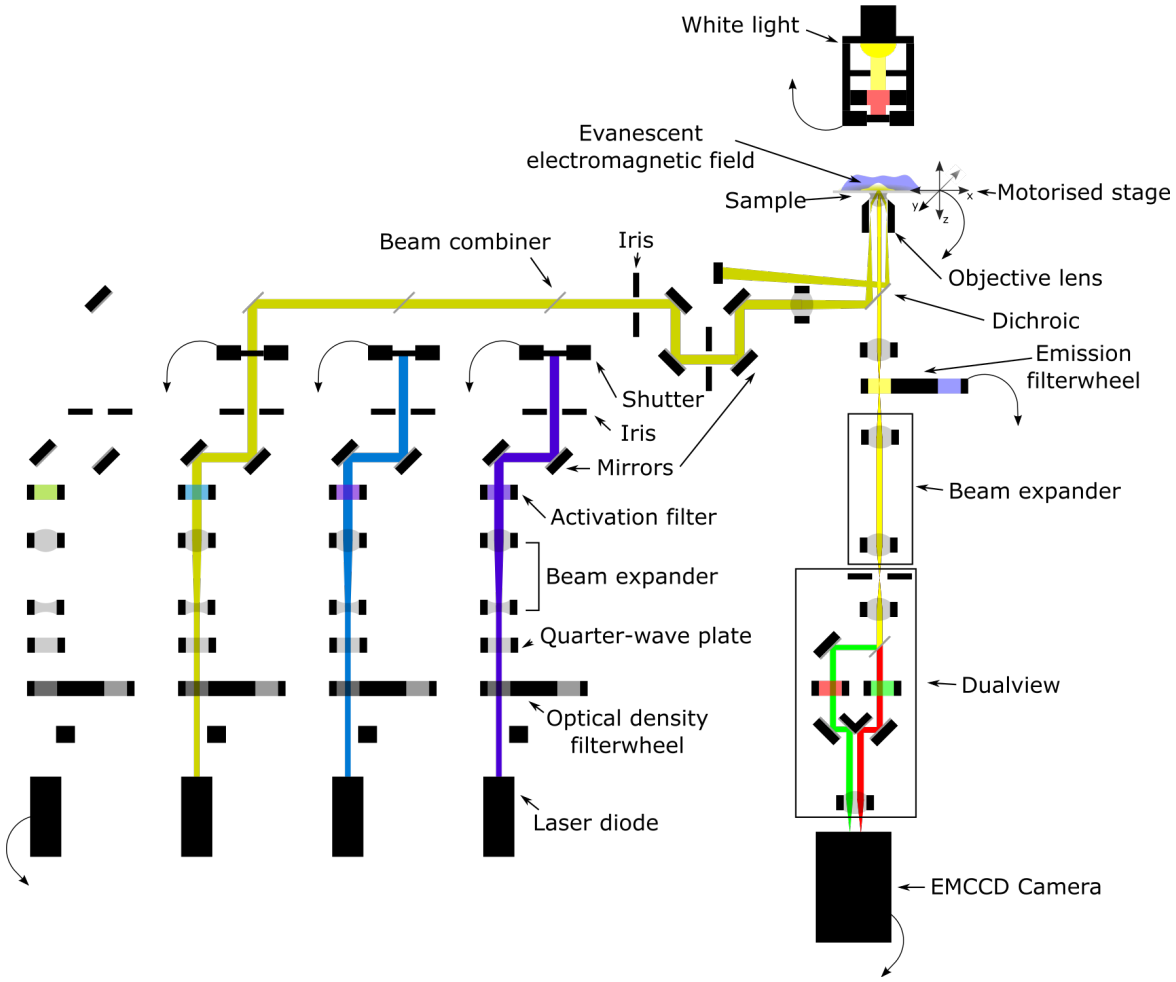


Figure 3.1 *Scheme of one of the two 2D single-molecule localisation microscope built in this thesis.* The illumination path is composed of four laser-lines (640, 561, 488 and 405 nm from left to right) that are prepared and aligned to illuminate a sample under TIRF. For clarity, only the 561 nm illumination is shown. The fluorescence signal emitted by the sample is collected by the objective lens, filtered and spectrally separated in a dualview before being projected on the EMCCD.
Legend: Curved arrows indicate direct hardware control by the MicroManager piece of software [102]. The 640 nm diode laser (left) was controlled through MicroManager and thus directly acts as a computer-controlled shutter. Actual shutters were required for the three other laser lines.

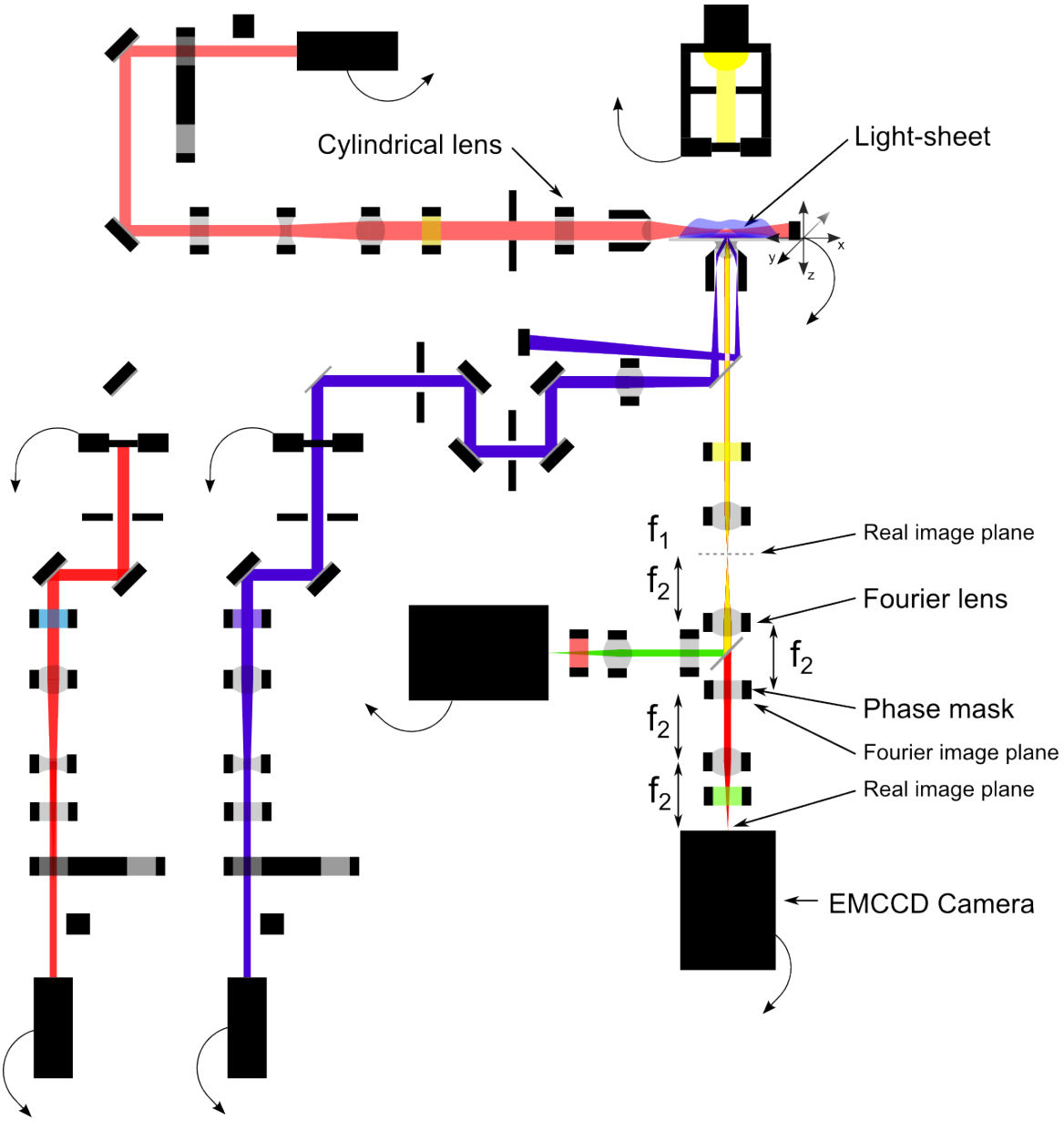


Figure 3.2 *Scheme of the 3D two-colour double-helix microscope built in this thesis.* The illumination path is composed of two laser-lines (640 and 405 nm from left to right) that are prepared and aligned to illuminate a sample under TIRF, and one laser-line (640 nm) that illuminates the sample with a thin sheet of light. The light-sheet is created by focussing the laser beam in a single direction at the back aperture of an objective lens thanks to a cylindrical lens: an 'extended 1D confocal volume' is thus created, perpendicular to the optical axis of the imaging objective. For clarity, only the 405 nm TIRF illumination and the 640 nm light-sheet are shown. The fluorescence signal emitted by the sample is collected by the imaging objective, filtered and conjugated in a $4f$ system. The signal is spectrally separated by a dichroic mirror after the first Fourier lens. A phase mask adapted to the wavelength of the collected signal is placed at each Fourier image plane. Finally, the second Fourier lens of each channel focusses the resulting signal on the chip of an EMCCD camera.
Legend: Curved arrows indicate direct hardware control by the MicroManager piece of software [102].

(Figure 3.3, A):

- Total internal reflection fluorescence (TIRF) uses the difference of refractive index at the surface between the glass coverslip and the water-based imaging buffer to totally reflect the illumination beam[1]. A non-propagating evanescent wave is locally created. The intensity of the TIR wave decreases exponentially along the optical path, typically limiting the illumination of the sample up to $\sim$100 nm above the coverslip (Figure 3.3, A,F);

- Highly inclined and laminated optical sheet (HILO) [105], also referred to as "near-TIRF", is based on a similar optical geometry than TIRF illumination. However, the angle of the illuminating beam with the coverslip is kept below the critical angle to prevent its total reflection. As a consequence, a collimated beam illuminates the sample. But because the incident angle is very close to the critical angle, the refracted beam, following Snell's law, is almost parallel to the coverslip, thus illuminating a thin inclined sheet of the sample above the coverslip. Nevertheless, an inconvenience of HILO is the non uniformity of the illumination as the HILO sheet is not perpendicular to the optical axis (Figure 3.3, A,E);

- Selective plane illumination microscopy (SPIM) [106], or commonly called light-sheet microscopy, conversely to both previous methods, usually uses two different lenses for illumination and imaging (a very recent and elegant method, single objective-SPIM, has been proposed by the group of Dr J.B. Sibarita[2] to combine both lenses and avoid the complex geometrical issue of bringing two high-numerical aperture objectives at 90° and very close from each other). The collimated illumination beam is focussed horizontally at the back focal plane of the illumination lens thanks to a cylindrical lens in order to focus the illumination beam in a line, similar to a confocal volume extended in one dimension. This 'focussed line' acts locally as a 2D-sheet of light which is aligned with the focal plane of the imaging lens (the axes of the two objectives being perpendicular to each other) (Figure 3.3, A,C).

[1]The refractive index of the oil or the glass is $n_e = 1.52$, higher than the average refractive index of living cells $n_e = 1.35$ or water, allowing total internal reflection if the angle of incidence is higher than the critical angle.

[2]Dr J.B. Sibarita gave a convincing presentation about this technique at the Single-Molecule Localisation Microscopy Symposium organised at King's College, London in August 2014. The title of the talk was: "Single-objective Selective Plane Illumination for 3D high- and super-resolution imaging of biological structures".

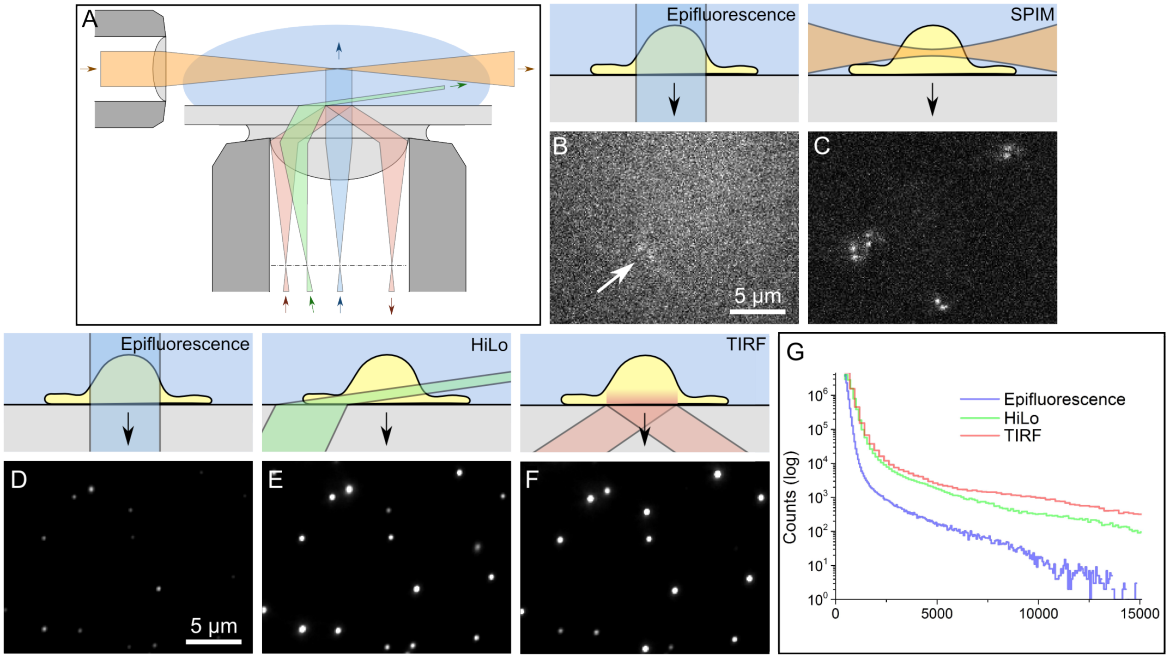


Figure 3.3 *Effect of varying illumination geometries on the imaging contrast.* Different illumination geometries have been proposed to increase the signal-to-noise ratio in large-field microscopy. **A**: Scheme of four commonly used illumination strategies: epifluorescence (blue), HILO (green), TIRF (red) and SPIM (orange). **B-C**: Diffusing sub-diffraction fluorescent beads were imaged a few micrometers above the coverslip under either epifluorescence (B) or SPIM (C) illumination in the double-helix PSF (DH-PSF) configuration of the microscope (*cf.* Section 3.2.2). The arrow in (B) indicates the possible DH-PSF of one bead. **D-F**: Similar carboxylated beads were fixed on the surface of a poly-lysine-coated coverslip and the same field of view was imaged under either epifluorescence (D), HILO (E) or TIRF (F). The contrast of images D-F is fixed to the same value. **G**: Histograms of the pixel intensities of each sample shown in D-F (A.U.: arbitrary unit – *y* axis: log scale).

Figure 3.3 shows the experimental difference of contrast obtained when imaging fluorescent beads in solution with either epifluorescence (Figure 3.3, B) or light-sheet (Figure 3.3, C) illumination. The latter dramatically increases the contrast as only a plane is illuminated: although four diffusing beads are distinctly observed in panel C[3], only one bead might be observed when the whole depth of the sample is illuminated (white arrow, Figure 3.3, B).

Immobilised beads were imaged under epifluorescence, HILO or TIRF illumination (Figure 3.3, D-F, resp.). Interestingly, the signal-to-noise ratio increases strikingly for HILO and TIRF illuminations, as observed in Figure 3.3, D-F shown with the same contrast. The background noise does not increase significantly, as opposed to the signal (Figure 3.3, G, higher intensities). Furthermore, beads slightly out-of-focus and visible under epifluorescence or HILO illuminations disappear under TIRF illumination (Figure 3.3, F).

The sub-diffraction axial width of the TIRF field makes it the best illumination technique to limit out-of-focus fluorescence emission. However, the main drawback is that TIRF can only illuminate the part of the sample close to the coverslip. It is the perfect method to image receptors at the plasma membrane of a cell forming a contact with the coverslip; but to observe resting receptors on the top of a cell, or the organisation of the nuclei of living yeast or stem cells, a HILO or a light-sheet illumination will be preferred. In this thesis, TIRF illumination is used in Chapters 4-7, HILO illumination in the Section 3.5 of this chapter, and a 4 µm-wide light-sheet is combined with 3D double-helix imaging in Section 3.2 of this chapter.

## 3.2 Imaging path

When illuminated, the sample emits a fluorescence signal that is collected by the imaging lens and focussed by the tube lens onto the detector. This imaging path is very sensitive to any external instability and noise as the collected single-molecule signal over the background is on the order of magnitude of the limit of detection of the camera (10-100 photons/PSF). The signal can also be optically modified to get more information about the single-emitter: changing its wavefront allows to additionally obtain the axial position of the fluorophore; spectrally separating the signal in two channels allows simultaneous imaging of two spectrally-separated fluorophores.

[3] *Cf.* Section 3.2.2 for more details about the shape of the PSFs.

### 3.2.1 Stability of the frame

Since SMLM allows to image single-emitters with a sub-diffraction precision typically on the order of 50 nm, the stability of the imaging path, *i.e.* the variation of the relative position of the sample to the camera, has to be an order of magnitude lower, or corrected for. To prevent any major variation, each microscope was built on a heavy optic table supported by vibration-isolator legs in a temperature-controlled environment (air conditioned at 20°C). Solid, heavy sample holders made of mild steel were designed to fit in nm-precise piezo-electric microscope stages. To prevent any drift due to the dragging induced by oil after a stage displacement, samples were maintained on the sample holder by small rare-earth magnets.

In order to evaluate the stability of the microscopes and their resistance to different external noise, fluorescent beads were immobilised on a coverslip and imaged for multiple frames. Their trajectories were rebuilt (*cf.* Section 3.4) and their standard deviation analysed as a metric for stability or drift of the microscope (Figure 3.4). It is worthy to notice that this metric is a lower bound for the stability, as even for high SNR, the standard deviation of the trajectory of a bead is the convolution of the stability of the instrument, the movement of the bead and the precision of localisation of the bead. In optimal conditions, under high illumination, the distribution of standard deviations peaked at 6-7 nm (Figure 3.4, C), about 6-8-fold lower than the typical precision obtained for SMLM experiments (40-60 nm). Although opening of the door or switching off the air condition during the course of the experiment did not affect the stability (E), any perturbation of the imaging path, either of the optic table or of the camera, induced major displacement of the sample (F), even impeding correct analysis of the trajectories of the beads in extreme cases. Two different microscopic frames (Olympus IX71 and IX73) were tested and, under similar illumination and with the same imaging optical path the new frame IX73, although offering more access to the optical path in infinity space at its base, was repeatably slightly more stable than the previous IX71 frame (6 nm *vs.* 7 nm, Figure 3.4, A-C).

As a control, the effect of a ten-fold decrease in illumination was observed (D). As expected from Equation 3.13, the SNR decreased and the standard deviation of the trajectories increased from 6 nm to 11.5 nm for the IX73 frame. If illumination and signal were linearly correlated, the precision should have varied of a factor $\sqrt{10} = 3.2$. The observed difference results from the non linearity of the relation between illumination power and emitted signal and from the convolution of the stability of the instrument with both long-term drift and localisation precision which worsen the latter for high illumination power.

Long-term drift (in time scales of minutes) is harder to avoid as it involves many phe-

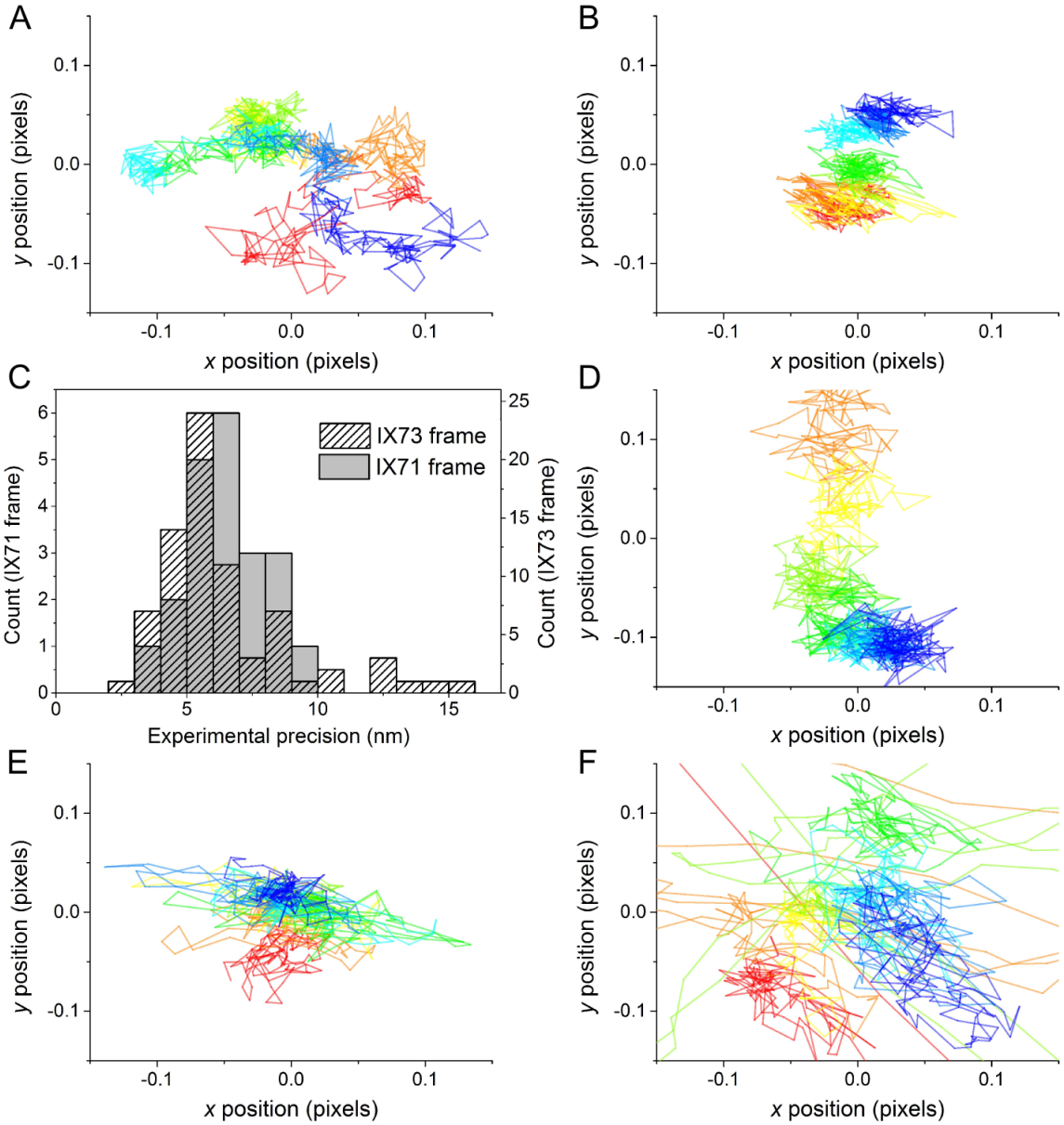


Figure 3.4 *Stability of the microscopes.* Sub-diffraction carboxylated fluorescent beads were fixed on poly-lysine-coated coverslips and imaged under TIRF illumination. Trajectories of single separated beads were tracked and an average trajectory was calculated to measure the global translational $(xy)$ drift of the sample. **A**: Average trajectory, *i.e.* drift, of beads from a sample mounted on a microscope frame IX71. **B**: Drift of the same sample under similar activation, on a microscope frame IX73. **C**: Comparison of the distribution of experimental precisions (*i.e.* the standard deviation of the trajectory of fixed fiducial markers, *cf.* Section 3.4.3) for both frames IX71 (A, grey bars) and IX73 (B, hatched bars). **D**: Same experiment as panel B, under a ten-times lower illumination. **E-F**: Same experiment as panel B, some perturbations are introduced: in **E**, the door of the room was closed; in **F**, the optic table was perturbed.
Legend: In panels A-B and D-F, positions are given in pixels. The colour of the trajectories codes for the time of the experiment (*i.e.* the frame of the SMLM movie) to which the position corresponds (from red, to yellow, to green, to blue). In panel C, the experimental precision is in nm.

nomena such as thermal local variations or mechanical relaxations [107, 108]. It is however easy to correct for lateral drift thanks to fixed bright fiducial beads or markers [18]. Then, the coordinates of the fitted localisations can be measured relative to the average position of the markers over time. The main difficulty here is to properly and stochastically immobilise a few markers in each field of view. The brighter and the more immobile the markers are, the better their positions are known and the less precision is lost in each localisation by such correction. However, consistently correcting for axial, or focus, drift requires some deep understanding about the axial variation of the PSF and robust real-time algorithms to prevent losing the signal of the single fluorophore as it leaves the focal plane of the objective [109]. Correcting the varying distance between the objective lens and the bottom of the coverslip by either monitoring the position of the reflected TIR beam or using a closed-loop piezo-electric actuator proves to globally correct for only half of the focus drift (personal communication from Dr E. Drier).

### 3.2.2 The double-helix point-spread function

The double-helix PSF (DH-PSF) is an optical method allowing to gain axial information about the position of an imaged single molecule thanks to the deformation of its 2D-PSF. Its principle resides in a phase change of the Fourier transform of the imaged PSF. In order to explain how the Fourier decomposition of a 2D image can be obtained and modified optically, some basic theoretical concepts, such as the spherical-plane wave duality, will be approached in this section, followed by experimental optical calculations of a Fourier decomposition. Then, the specific implementation of the DH-PSF will be described, and preliminary results presented.

In classical optics, a point emitter located at the origin $\vec{r}_0$ uniformly radiates light in all directions. The sine electromagnetic wave of wavelength $\lambda$ that propagates through the transparent medium of refractive index $n$ at any point $\vec{r}$ and any time $t$ can be described as:

$$\begin{aligned} f(\vec{r},t) &= \tfrac{A}{r}\,\sin(k\,r-\omega\,t) \\ &= \Im\left(\tfrac{A}{r}\,e^{\imath\,k\,r}\,e^{-\imath\,\omega\,t}\right) \end{aligned} \tag{3.1}$$

where $r = \|\vec{r}\|$, $k = 2\,\pi/\lambda$ and $\omega = k\,c/n$ (with $c$ the speed of light in vacuum). The total intensity of the spheric wave for any spherical surface centred at the source,

$$\iiint |f(\vec{r},t)|^2\,r^2\,\sin(\theta)\,\mathrm{d}\theta\,\mathrm{d}\varphi\,\mathrm{d}t = 4\pi\,A^2 \tag{3.2}$$

in spherical coordinates $(r,\theta,\varphi)$ originating from the origin $\vec{r}_0$, is constant over time and

independent from the distance $r$ from the source, which is consistent with the law of conservation of energy. For calculus simplification, the wave function is often defined as the imaginary part of a complex function (Equation 3.1). Also, when working with a single wavelength $\lambda$, the dependence in time $e^{-\imath\,\omega t}$ is similar for all propagating waves and can be eliminated to study the geometry of a wavelength. The simplified complex wave function is thus:

$$\phi(\vec{r}) = \frac{A}{r}\, e^{\imath\, k\, r} \tag{3.3}$$

If the point emitter $\vec{r_0}$ is far from the point of observation $\vec{r}$, *i.e.* $r \gg \lambda$, the wave fronts can be approximated with parallel planes. The simplified complex wave function of a plane wave of constant amplitude $\left|B(\vec{k})\right|$ and vector of propagation $\vec{k} = k\,\vec{e_\perp}$ is:

$$\phi(\vec{r}) = B(\vec{k})\, e^{\imath\, \vec{k}\cdot\vec{r}} \tag{3.4}$$

Interestingly, an optical lens of focal length $f$ transforms a spherical wave originating from a point emitter $\vec{r_0} = (x_0, y_0, -f)$ in its object plane to a plane wave of vector of propagation:

$$\begin{aligned} \vec{k} &= k\,\left[\cos(\theta_x)\,\cos(\theta_y)\vec{e_z} + \sin(\theta_x)\vec{e_x} + \cos(\theta_x)\,\sin(\theta_y)\vec{e_y}\right] \\ &= \tfrac{2\pi}{\lambda}\,\left[\vec{e_z} - \tfrac{x_0}{f}\vec{e_x} - \tfrac{y_0}{f}\vec{e_y}\right] \\ &\qquad \text{in the approximation of small angles } (x_0 \ll f \text{ and } y_0 \ll f). \end{aligned} \tag{3.5}$$

Conversely, and following Helmholtz reciprocity principle, the lens transforms a plane wave of vector of propagation $\vec{k}$ to a spherical wave converging to a single point in its image plane which coordinates are:

$$\begin{pmatrix} x \\ y \\ f \end{pmatrix} = \begin{pmatrix} f\,\frac{\tan(\theta_x)}{\cos(\theta_y)} \\ f\tan(\theta_y) \\ f \end{pmatrix} = f \begin{pmatrix} \theta_x \\ \theta_y \\ 1 \end{pmatrix} = f \begin{pmatrix} \frac{k_x}{k_z} \\ \frac{k_y}{k_z} \\ 1 \end{pmatrix} \tag{3.6}$$

Both Figures 3.5 C and D are two interpretations of the same physical phenomenon. In Figure 3.5 C, the complex 2D electromagnetic wave from the object plane is interpreted in the Huygens sense as a superposition of spherical waves originating from a continuum of point emitters. Each spherical wave is collimated by the lens and forms a plane wave of specific vector of propagation (*cf.* Equation 3.5). So each point $(x, y, f)$ of the image plane

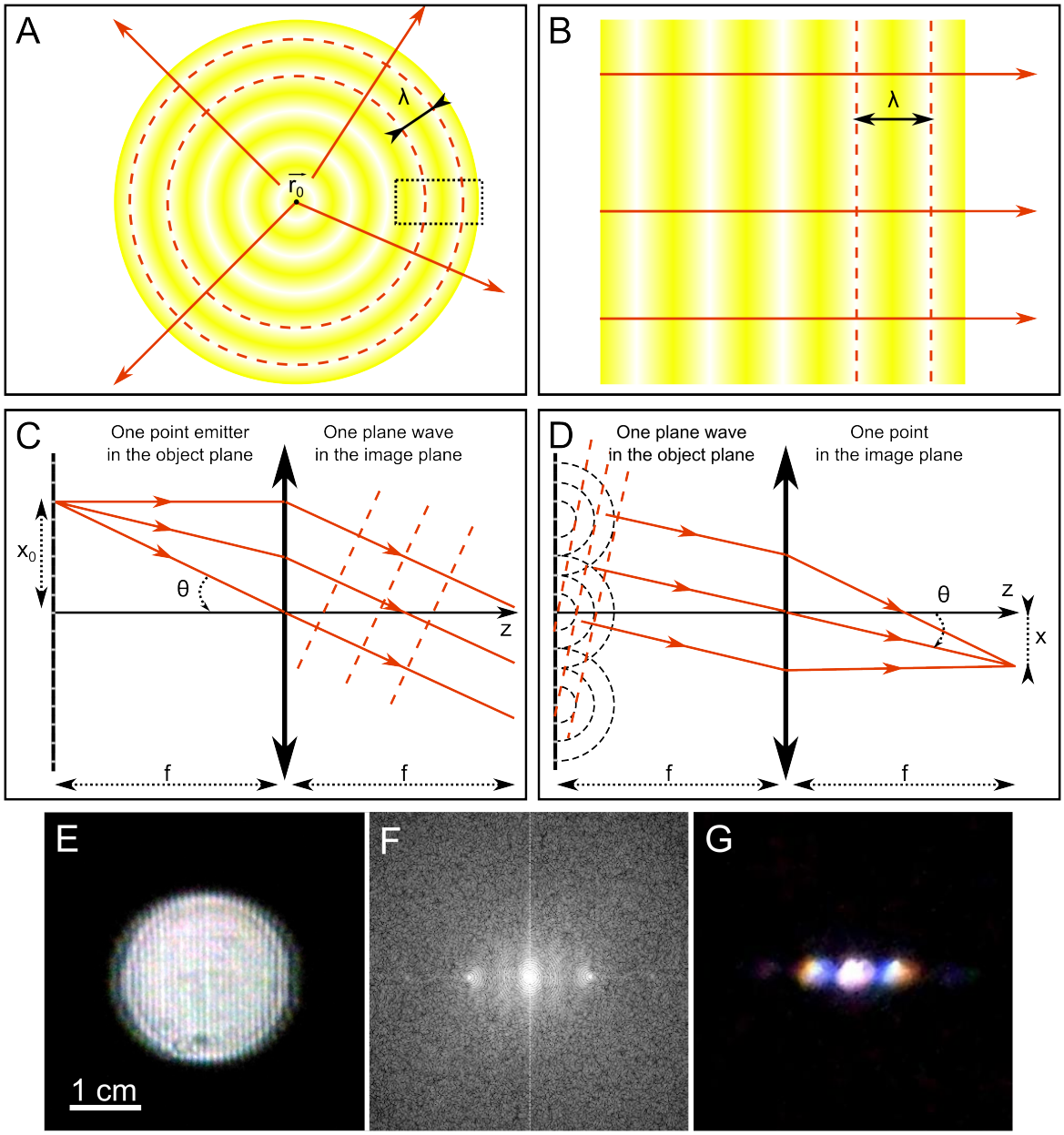


Figure 3.5 *A lens is an optical Fourier transformer.* A point-emitter emits light uniformly in all directions, producing a spherical wave of wavelength $\lambda$ (**A**). Looking from afar ($\|\vec{r}\| >> \lambda$, *e.g.* in the boxed region), the spherical wave is approximated with a plane wave (**B**). Examples of wavefronts and light rays are resp. shown as dotted red lines and red arrows. An optical lens, by conjugating a spherical waves originating from its object plane to plane waves (**C**) and vice versa (**D**), acts as an optical Fourier transformer. Indeed, an image in the object plane can be seen as a superposition of point emitters or of plane waves corresponding to its decomposition. Experimentally, the image of a grating was focused on the object plane of a lens (**E**). The Fourier transform of (E), calculated *in silico*, (**F**) is observed at the image plane of the lens (**G**).

receives a superposition of plane waves corresponding to point sources in the object plane:

$$\begin{aligned}
\phi(x,y,f) &\propto \iint B(\vec{k})\, e^{\imath\, \vec{k}\cdot\vec{r}}\, \mathrm{d}\vec{k} && \text{from Equation 3.4} \\
&\propto \iint B(x_0,y_0)\, e^{-2\pi\imath\left(\frac{x_0}{\lambda f}x+\frac{y_0}{\lambda f}y\right)}\, \mathrm{d}x_0\, \mathrm{d}y_0 && \text{from Equation 3.5} - \textit{cf.}\ \text{note}\ [4]
\end{aligned} \tag{3.7}$$

In Figure 3.5 D, the complex 2D electromagnetic wave from the object plane is interpreted in the Fourier sense as a superposition of plane waves interfering in the object plane (each plane wave representing a 2D spatial frequency). Each plane wave is focussed on a single point of the image plane. So each point $(x,y,f)$ of the image plane receives all the energy that departed from the object plane at the spatial frequency $\vec{k} = k_x\vec{e}_x + k_y\vec{e}_y + k_z\vec{e}_z$:

$$\begin{aligned}
\phi(x,y,f) &\propto T_{\text{Fourier}}((x_0,y_0) \in \text{object plane})(\vec{k}) \\
&\propto \iint \phi(x_0,y_0,-f) e^{\imath\left(x_0\, k_x + y_0\, k_y\right)}\, \mathrm{d}x_0\, \mathrm{d}y_0 && \textit{cf.}\ \text{note}\ [5] \\
&\propto \iint \phi(x_0,y_0,-f) e^{-\frac{2\pi\imath}{\lambda}\left(x_0\frac{x}{f}+y_0\frac{y}{f}\right)}\, \mathrm{d}x_0\, \mathrm{d}y_0 && \text{from Equation 3.6}
\end{aligned} \tag{3.8}$$

Experimentally, a Ronchi ruling slide (Figure 3.5 E), a grating of parallel lines, was placed at the focal plane of the microscope. A lens of focal length $f = 20$ cm was aligned in the imaging path of the microscope, at a distance $f$ from the image plane of the microscope. The camera of a smartphone was placed at the image plane of the lens and the image in Figure 3.5 G was recorded. The 2D Fourier transform of Figure 3.5 E was performed *in silico* and its 2D intensity is shown in Figure 3.5 F. As the image of the grating can be approximated with a sine wave, the Fourier transform shows three components: the average intensity of the image at the centre (order 0) and the positive and negative symmetric spatial frequencies of the sine (first order). A very similar geometry can be appreciated after the optical transformation through the lens. Interestingly, the first order is more shifted for red wavelengths compared to shorter ones. Indeed, the image of the grating in the image plane of the microscope is diffraction-limited, smoothing the square signal of the grating into an approximated sine wave. But diffraction is intrinsically achromatic, and the size of

[4] After simplification of the constant term $e^{2\pi\imath\,\frac{f}{\lambda}}$ in the multiplicative factor.

[5] After simplification of the constant term $e^{\imath\, f\, k_z}$ in the multiplicative factor, in the approximation of small angles $\left(k_z \sim \frac{2\pi}{\lambda} = \left\|\vec{k}\right\| \text{ for } \theta \ll 1\right)$.

the diffraction pattern, or of the PSF, is inversely proportional to the wavelength of the light (Equation 2.1). Thus, the red signal will be observed in the image plane of the microscope as a wider sine, which is translated in the Fourier domain as a shift of the first order away from the order 0.

The DH-PSF method consists in modifying the phase of the emitted light in the Fourier domain in order to change the 3D-PSF of the instrument in the real domain. Indeed, phase cannot be directly recorded on an EMCCD, although it carries additional axial information to amplitude about the position of the observed fluorophore. A phase mask was engineered by Pavani *et al.* to change the diffraction-limited PSF of the emitter into two diffraction-limited spots which angle with the lateral axes is proportional to the axial position of the emitter (Figure 3.6 C-E) [88]. The phase mask is applied at the Fourier plane of a $4f$ system, *i.e.* two collimated lenses of focal length $f$ (Figure 3.6 A-B). Introduction of the phase mask induces a modification of the PSF of the instrument in the plane of the camera chip.

Immobilised fluorescent beads were imaged at different axial positions in order to calibrate the microscope set-up (Figure 3.6 D-F). As a proof of principle to show that the trajectories of sub-diffraction particles could be followed in three dimensions, freely diffusing beads were also imaged in water (Figure 3.6 G).

Other methods have been implemented to follow sub-diffraction particles in 3D (*cf.* Section 2.3.3). The DH-PSF method has the main advantage of presenting uniform axial and lateral precisions over its depth of field (Figure 3.6 F, bottom panels), compared to bi-plane microscopy or astigmatism. Compared to iPALM, it is also easier to implement and allows imaging of thicker samples as DH-PSF does not require dual-objective imaging. However, iPALM has better lateral and axial precisions and collects more signal from the single emitters[6].

### 3.2.3 Two-colour imaging: registration of two channels

#### Pairing fluorescent beads

In order to simultaneously image two different proteins, two spectrally-separated fluorophores can be used in a dual-labelling strategy (*cf.* Section 3.3). Under the illumination of two aligned lasers, the fluorescence signal of both fluorophores is spectrally separated by a dichroic mirror which reflects signal of all wavelengths above a characteristic value,

[6] In DH-PSF, the photons collected by the objective is separated in two lobes that both needs to be detected with high precision when in iPALM, the photons are collected by two objectives and divided between three cameras.

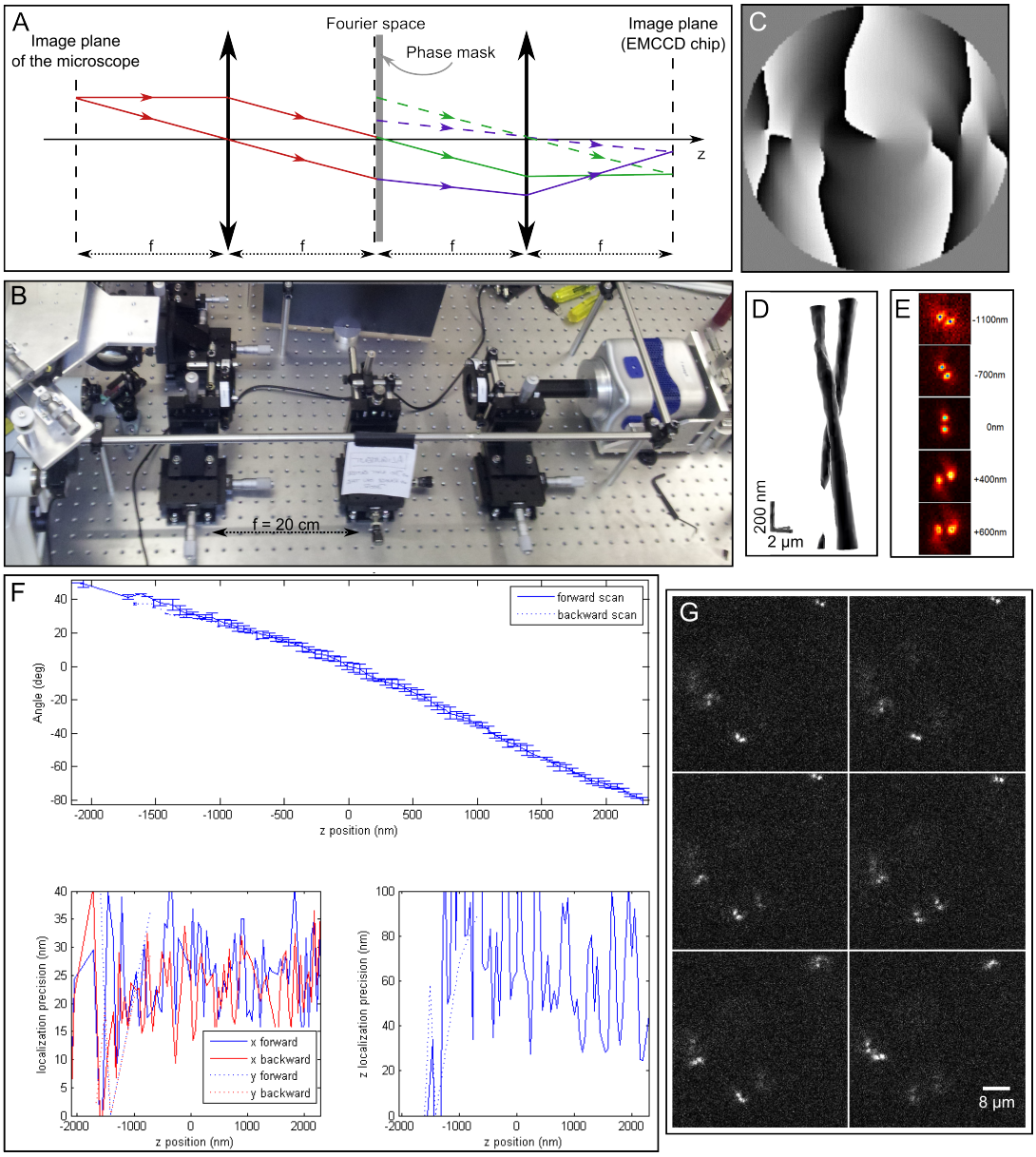


Figure 3.6 *The double-helix point-spread function allows three-dimensional localisation of diffraction-limited particles.* A $4f$ optical system is composed of two conjugated lenses (**A**) and allows the modification of the phase of the relayed image from the object plane of the first lens in the Fourier domain. A $4f$ system was implemented to relay the image plane of a microscope to the chip of an EMCCD (**B**). In the Fourier plane, the DH-PSF phase mask (**C**, diameter: 7.25 mm) was aligned with the optical axis, optically modifying the PSF of the microscope to two lobes forming a double-helix (**D**) which rotation angle is proportional with the axial localisation of the emitter (**E**, and top graph in **F**). Fluorescent sub-diffraction fixed beads were imaged at different axial position to calibrate the set-up. Uniform localisation lateral and axial precisions of resp. ∼30 and ∼80 nm were achieved over a depth of field of 4 µm (**F**). Freely diffusing fluorescent beads in solution were also imaged to test the possibility of 3D trajectory analysis (**G**, montage of a small field of view, from left to right, then top to bottom, every 60 ms).

and transmits all other wavelengths (Figure A.1). Each separated channel can be independently handled and focussed on two different cameras (Figure 3.2) or focussed back on the two halves of a single camera. The latter technique is referred to as dualview imaging (Figure 3.7, A).

To compare the localisation of the proteins from both channels, the channels have to be optically aligned, computationally registered and the precision of their alignment has to be assessed. Because new optical elements are added (lenses, mirrors, dichroic mirror as in Figure 3.7, A), the channels need to be finely aligned by using an alignment sample such as a regular grid of gold dots deposited on a glass coverslip, or separated dual-coloured fluorescent beads (Figure 3.7, B) [110–113]. However, due to chromatic aberrations and fine sub-diffraction translation and rotation which are difficult to assess and correct by eye, a further correction step is calculated and corrected for *in silico*.

To do so, immobilised dual-coloured separated fluorescent beads are simultaneously imaged in both channels (Figure 3.7, B-C). Intensity maxima in each channel are fitted with 2D-Gaussians thanks to a SMLM routine (see Section 3.4). The localisations of the beads detected in one channel are paired with their nearest neighbours in the other channel in order to match the positions of the same beads in both channels. Remarkably, for this step to work, a relatively good initial optical alignment is necessary. Also, to prevent the miss-match of close miss-aligned beads, a localisation $A_i$ is paired with its nearest-neighbour in the other channel $B$ *only if* their distance is smaller than a fraction (here, 0.3) of the distance separating $A_i$ from its nearest neighbour in the original channel $A$. This pairing process can be repeated for more than one field of view to increase the density of paired localisations, *i.e.* the sampling, and consequently the precision of the registration without increasing the density of the imaged beads (Figure 3.7, D).

### A global linear geometric correction

In geometry, any 2D affine transformation can be sequentially decomposed in a translation, a uniform scaling and a rotation. The calculation and determination of each of these consecutive steps of the transformation which moves any point from channel $A$ to channel $B$ is described next. First, the respective barycentres ($\Omega$ and O) of the paired localisations $(A_i,\ B_i)$ in each channel are calculated:

$$\Omega = \frac{1}{N}\sum_{i=0}^{N}(\mathrm{A}_i) \qquad \text{and } \mathrm{O} = \frac{1}{N}\sum_{i=0}^{N}(\mathrm{B}_i)$$

The translation $\overrightarrow{T} = \overrightarrow{\Omega O}$ (Figure 3.7, G) is then applied to all localisations of channel $A$: $\mathrm{A}'_i = \mathrm{A}_i + \overrightarrow{\Omega O}$.

The scale factor is calculated as the following mean (Figure 3.7, H):

$$h = \frac{1}{N} \sum_{i=0}^{N} \frac{\mathrm{OB}_i}{\mathrm{OA}'_i}$$

The uniform scaling is then applied to the localisations of channel $A'$: $\mathrm{OA}''_i = h\,\mathrm{OA}'_i$. The angle of the rotation is calculated as the mean angle between $\overrightarrow{\mathrm{OA}''_i}$ and $\overrightarrow{\mathrm{OB}_i}$ (Figure 3.7, I):

$$\theta = \frac{1}{N} \sum_{i=0}^{N} \sin^{-1} \frac{\left\| \overrightarrow{\mathrm{OA}''_i} \wedge \overrightarrow{\mathrm{OB}_i} \right\|}{{\mathrm{OB}_i}^2}$$

The rotation is finally applied to the localisations of channel $A''$:

$$\overrightarrow{\mathrm{OA}'''_i} = \begin{bmatrix} \cos\theta & -\sin\theta \\ \sin\theta & \cos\theta \end{bmatrix} \overrightarrow{\mathrm{OA}''_i}$$

Both channel $B$ and the corrected channel $A'''$ are plotted in Figure 3.7, E. The registration process allows a significant increase in co-localisation position (Figure 3.7, J): the distance between localisations of each pairs after correction is greatly reduced (blue histogram, compared to the orange one). The precision of registration is defined as the value at the peak of the histogram in Figure 3.7, J.

Such registration correction allows sub-pixel registration precisions of typically $\sim$55 nm. It successfully corrects geometrical miss-alignment of the fluorescence signals, but it is limited by non-linear achromatic distortions between the two channels.

### A locally-weighted mean of linear transformation correction

To obtain a finer registration and account for the small non-linear distortions (due to non-linear achromatism) that cannot be dealt with thanks to the previous global geometrical method, a method originating from image processing to register two images of the same objects taken from different angles and detectors (tilted, rotated, scaled, with different intensity values, *etc.*) was implemented [114, 115].

For each pair of calibration localisations $(A_i,\ B_i)$, the $n$ nearest neighbours of $A_i$ are selected and used to build two separate polynomials $(P^{\mathrm{x}}_{A_i},\ P^{\mathrm{y}}_{A_i})$ of degree $d$ that interpolate the distance between both channels at these $(n+1)$ points, projected on each coordinate

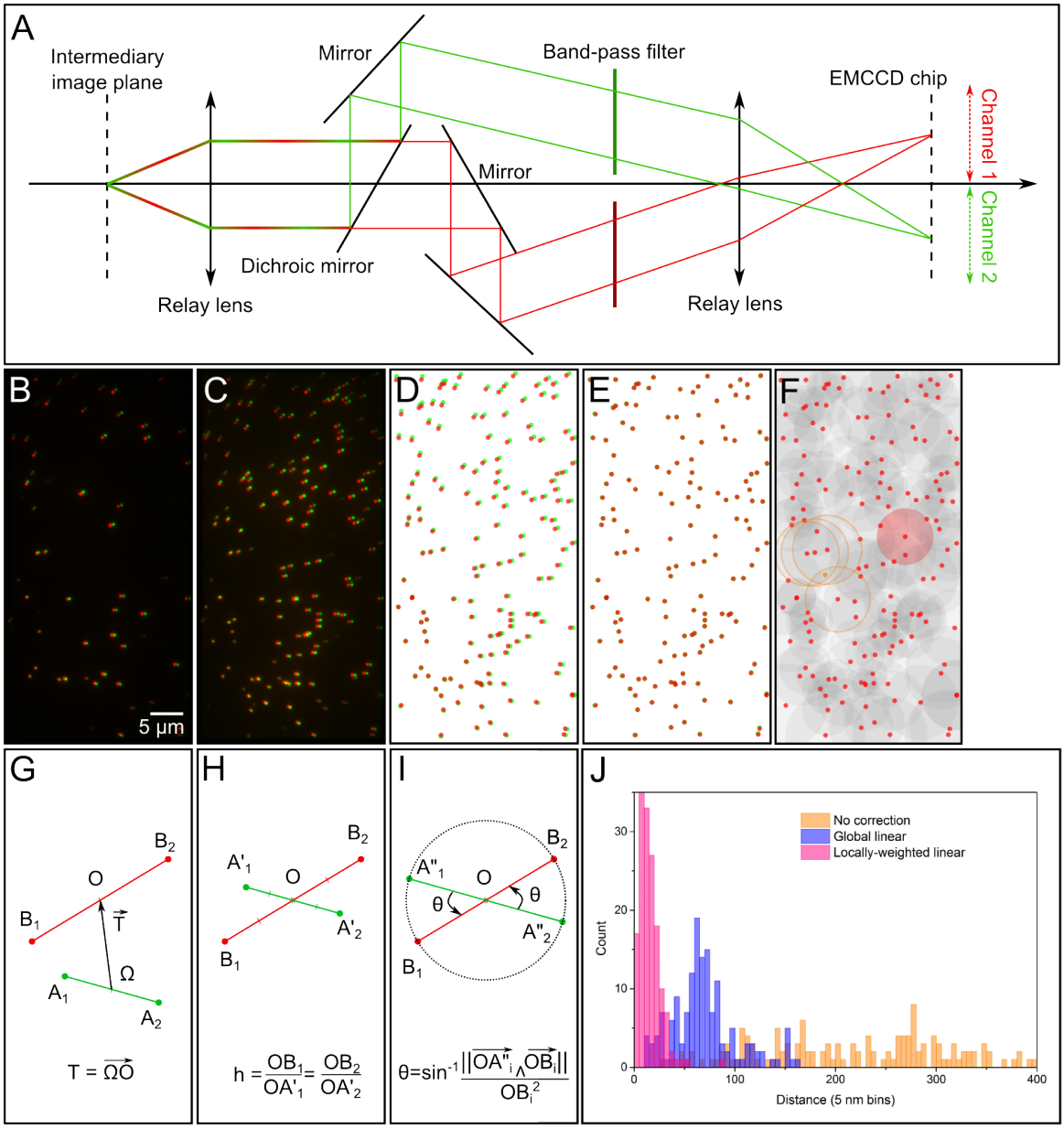


Figure 3.7 *Two channel imaging requires registration for co-localisation studies.* A dualview system, made of a dichroic mirror spectrally separates the fluorescent signal into two channels that are projected on both halves of the camera (**A**). After manual alignment of the dualview channels, multiple fields of view of fixed separated dual-coloured beads fixed on a coverslip are simultaneously imaged in both channels (**B**, one field of view; **C**, the superposition of three fields of view; long wavelength channel in red, short wavelength channel in green). For each field of view and each channels, each intensity maximum is fitted with a 2D-Gaussian and paired with its nearest neighbour in the other corresponding channel. All successful pairs of localisations for the three fields of view in (**C**) are plotted as coloured circles in (**D**). A geometrical combination of a translation (**G**), a scaling transformation (**H**) and a rotation (**I**) are calculated to match the green localisations with the red ones. A locally-weighted mean of linear transformation is also calculated for the same purpose (**F**, *cf.* text for details). As a result of the corrections applied to the green channel, the distribution of the distance separating the localisations in each channel is thinned and its centre is displaced to a lower value (**J**, orange before correction; blue after global linear correction; pink after locally-weighted linear correction). The average precision of registration achieved was 12 and 55 nm, resp.

axis:

$$\forall j \in [\![0,\ n]\!],\quad P^{\mathrm{x}}_{A_i}(x_j, y_j) = x'_j - x_j \tag{3.9}$$
$$\text{and}\quad n = \frac{(d+1)(d+2)}{2} - 1$$

where $(x_j,\ y_j)$ is the $j$-th nearest neighbour of $A_i$ ($A_i$ being its 0-th nearest neighbour), and $(x'_j,\ y'_j)$ its corresponding localisation in channel $B$. The range of both polynomes is defined as the circle centred on $A_i$ and of radius $R_{A_i}$ corresponding to the distance to its $n$-th nearest neighbour (*e.g.* Figure 3.7, F, red circle, $n = 4$).

Once the calibration step is done, for each new position $(x,\ y)$ from channel $A$, a corrected position $(x',\ y')$ is calculated as the weighted sum of all the $T$ polynomials that it intersects in channel $A$ (*e.g.* Figure 3.7, F, orange dot intersecting four orange circles):

$$x' = x + \frac{\sum_{j=0}^{T} W(j,\ x,\ y) P^{\mathrm{x}}_{A_j}(x,\ y)}{\sum_{j=0}^{T} W(j,\ x,\ y)} \tag{3.10}$$
$$\text{with}\quad W(j,\ x,\ y) = 1 - 3R^2 + 2R^3 \quad \text{and} \quad R = \frac{d(A_j,\ (x,\ y))}{R_{A_j}}$$

The weight function $W$ was chosen so that (1) the weight is null outside of the range $R_{A_j}$ of its polynomial $P_{A_j}$; (2) it increases up to a value of 1 at its centre $A_j$; and (3) its derivative is null in its centre and at the limit of its range, allowing the transformation to be continuous and smooth on all points of the surface.

If the position to correct does not intersect any range of any polynomial, a pair of interpolating polynomials $(P^{\mathrm{x}},\ P^{\mathrm{y}})$ is calculated with its $(n+1)$ nearest neighbours, and their values at the position $(x,\ y)$ determines the correction to apply.

The precision of the registration is estimated and calculated by imaging $m$ separate calibration fields of view: $(m-1)$ fields are used to build polynomials, and the last $i$-th field of view is used as a control measurement, which corrected positions from channel $A$ are compared to the real positions of the corresponding beads in channel $B$. This is repeated for all fields of view $i \in [\![1,\ m]\!]$. At the end of the calibration, all fields of view are used to build the final set of polynomials that are used for correction of experimental data. Thus, the precision calculated is a worse estimate of the real registration precision.

Interpolation polynomials are calculated with a quick orthogonal polynomial method as described in ref. [115]. Quadratic polynomials ($d = 2$) allow a better precision than linear ones ($d = 1$), but induce high distorting fluctuations out of the convex envelope of the calibration localisations. Linear polynomials were thus preferred in this thesis.

Finally, to tackle loose interpolations due to colinear nearest neighbours, two extra nearest neighbours are used than what is theoretically needed for an exact interpolation ($n' = n + 2$, Figure 3.7, F, $d = 1$ and $n' = 4$). Strictly speaking, such polynomials are not exact interpolators but good local approximators. This is also a very good way to make the method robust to outliers due to miss-paired calibration localisations. Lastly, it increases the range of the polynomials, *i.e.* the cover of the surface that can be corrected with this method.

Such registration method allows registration precisions almost five-fold better than the global linear method (typically $\sim$12 nm, Figure 3.7, J), *i.e.* less than the average localisation precision of typical SMLM experiments. Furthermore, compared to the global linear method, neither the calibration nor the correction steps noticeably slowed the analysis. This method is adapted to SMLM imaging as it calculates smooth corrections for discrete localisations [112, 116]. For all these reasons, it was chosen for registration of any single-molecule dual-colour experiments in this thesis.

#### Conclusion

The registration corrections presented here allow sub-pixel registration precisions[7] ($\sim$55 nm in the case of a global linear transformation, $\sim$12 nm in the case of a locally-weighted mean of linear transformations). Although these methods correct for both misalignment (global linear transformation) and lateral achromatism (locally-weigthed mean transformation), they do not correct for axial achromatism that affects dualview imaging: the microscope imaging lenses have slightly different focal planes for different wavelengths. If each channel is projected on different cameras, axial achromatism is easily accommodated for by axially adapting the camera position. However, as both channels share a similar camera in the dualview geometry, a small correcting lens can be added in one channel to correct the mismatched focal planes.

## 3.3 Which labelling strategy?

The possibility to precisely tag proteins with fluorophores in many different ways enables the use of SMLM in biology: genetically, immunologically and chemically. This allows to image non-naturally-fluorescent proteins with single-molecule precision and high accuracy.

[7] To get the squared precision of the co-localisation, the squared registration precision needs to be added to the squared precisions of localisation of both co-localised fluorophores (*cf.* Section 3.4) [107, 117].

### 3.3.1 Labelling requirements and strategy

The labelling strategy in SMLM is critical to the precision, the resolution and the accuracy of the localisations (*cf.* Section 3.4.3). Good reviews extensively reference existing labelling methods in fixed [45, 52] and live [118] cell SMLM experiments, and compare photo-transformable fluorescent proteins [119]. Here, seven characteristics of the labelling strategy that require consideration are distinguished:

1. Size of the label: the protein of interest is not directly imaged but the fluorophore that labels it. The *accuracy* of the measured position is thus decreased with the distance separating the label to the protein. Antigen-binding fragments (Fab) of antibodies or nanobodies [120] should thus be favoured over full antibodies. The use of noncanonical amino acid and 'click' chemistry, although genetically heavy to use, is the best approach limiting the size of the label described so far [57, 58].

2. Specificity: as for classical fluorescence microscopy, specificity of the fluorescent label to the protein of interest is critical for *accuracy* of the detection. Antibodies with very low dissociation constants are thus required. Also, genetically-encoded fluorescent proteins (*e.g.* mEos [121], PA-mCherry [122]) or enzyme-based tags (*e.g.* Snaptags [60], HaloTags [59]) have the advantage of the genetic control and specificity of the tagging.

3. Perturbation: the addition of a label to a protein can perturbate its function, its folding, its expression or its cellular localisation. This is particularly known for fluorescent proteins that tend to self-aggregate, especially at high densities [123]. Most of them indeed are monomeric mutants of tetrameric proteins. This characteristic is critical, as it has led to extensive studies of aggregation and miss-localisation artefacts in fluorescence microscopy [121, 123, 124].

4. Density: the labelling density directly affects the *resolution* (*i.e.* the sampling) of the experiment (*cf.* Section 3.4.3). A high density is usually restrained by sterical hindrance of dense labels (*e.g.* for labelled antibodies, or fluorescent proteins in virus particles), or the expression levels reachable for fluorescently-tagged proteins [125]. In the latter case of fluorescent proteins, the folding efficiencies of the protein, of the tag and of the fluorophore are three factors limiting the final density of proteins that can be imaged. The aim of a labelling strategy, especially if counting is at stake, is to label each protein of interest with exactly one and only one fluorophore. Over-

labelling is also frequent, when antibodies targeting the protein of interest are used and labelled with dyes through their lysines.

5. Activation control: in SMLM, fluorophores are observed one by one. To reach super-resolution, dense fluorophores are successively and stochastically switched to their fluorescent states. Fluorophores are required to be activable or switchable in some way (chemically, optically, or through thermodynamic binding events). In the case of photo-activable fluorescent proteins, the activation efficiency is intrinsically limited [126]. Furthermore, in general, precise switching of the dye is not entirely controllable. This is particularly the case in two-colour imaging, when two different fluorophores present at different concentrations are to be switched independently at different rates, in an orthogonal manner. Over- or under-switching limits the *resolution* of the experiment by decreasing the number of detected localisations (because of overlapping PSFs or of under-sampling, resp.).

6. Brightness: because in an SMLM experiment single molecules are imaged one by one (single molecule detection requires high signal-to-noise ratios), and since the localisation *precision* is inversely correlated with the number of collected photons (Equation 3.13), high photon-flux fluorophores are required. Quantum dots and organic dyes, compared to fluorescent proteins, are generally brighter and more photostable. The HaloTags and Snap-tags combine the advantages of both the specificity of a genetically-encoded tag and the brightness of organic dyes, but also the drawbacks of limited folding efficiency and target accessibility of the tag to the organic dye.

   Moreover, the brightness of fluorophores can be increased in specific buffer conditions. For instance, the fluorescence quantum yield (*i.e.* the probability that a photon is emitted for each excitation photon) of far-red fluorophores is typically low; however, non-radiative decay routes can be selectively turned off through the use of deuterated (heavy) water based buffers, leading to an increase in the quantum yield by over 200%. This has been shown in multiple common classes of dyes, including oxazines and cyanines [127, 128].

7. Live-cell compatibility: the last characteristic specifically concerns live-cell imaging. Not only some fluorophores are cytotoxic (*e.g.* quantum dots) but most dSTORM buffers, required to control the blinking of organic fluorophores, are too. Additionally, if the protein of interest lives inside the cell, cell-permeable fluorophores are required. Intracellular live-cell labelling with organic dyes or quantum dots is still a

real challenge in SMLM. The compatibility of photo-activable or -switchable fluorescent proteins with intracellular labelling and live-cell imaging makes these convenient to use.

Because fluorescent proteins are compatible with live-cell intracellular imaging, and are highly specific labels of moderate size, mEos was chosen as the main fluorophore for the experiments presented in this thesis. Indeed, mEos is an efficient photo-activable fluorophore [74, 123], and the brightest described so far [18, 46, 94, 129]. Although early constructs (mEos, mEos2) tended to dimerise at high concentration, true monomeric mEos proteins (mEos3.1 and mEos3.2) were engineered [121], making mEos the most used photo-activable fluorescent protein in SMLM applications [101, 123, 130, 131]. The choice of an irreversibly photo-activable fluorophore is also important for the quantitative PALM approach investigated in Chapter 6 [132].

However, mEos occupies a large space in the wavelength domain [52]: it is activated by 405 nm illumination; its green inactivated form absorbs around 488 nm and emits in the yellow domain; its red activated form absorbs around 561 nm and emits in the red domain. Thus, if the distribution of a second protein of interest needs to be simultaneously observed, a photo-switchable fluorophore absorbing and emitting in the far red needs to be found. In this domain, no bright fluorescent proteins allowing single-molecule detection are known [119]. Thus, in this thesis, labelling with a second colour is obtained by Fabs targeting the protein of interest and labelled with Atto655. This dye has the advantage of not being affected by the 405 nm illumination required for mEos activation, but also the advantage of naturally blinking under 640 nm illumination [25, 133, 134]. Atto655 photo-blinking is also increased in 40 µM ascorbic acid (*i.e.* vitamin C) buffer, which is compatible with live-cell imaging[8] [37, 139, 140]. Thus, the control of both Atto655 and mEos activations are deconvolved and orthogonal, enabling the optimisation of the densities of both activated fluorophores that are imaged during acquisition.

### 3.3.2 Ensemble characterisation of the dark states of mEos

Since most experiments of this thesis involve mEos as the fluorophore of choice for single-molecule experiments, some initial characterisation of its single-molecule photo-physical

[8] Ascorbic acid is naturally and abundantly present in cells at concentrations of 0.1 to 0.4 mM [135]. Although millimolar concentrations of ascorbic acid are known to affect cell viability, the sub-millimolar concentrations used to induce Atto655 blinking failed to exhibit any cytotoxic effect after 24 h exposure for various cell lines [136–138].

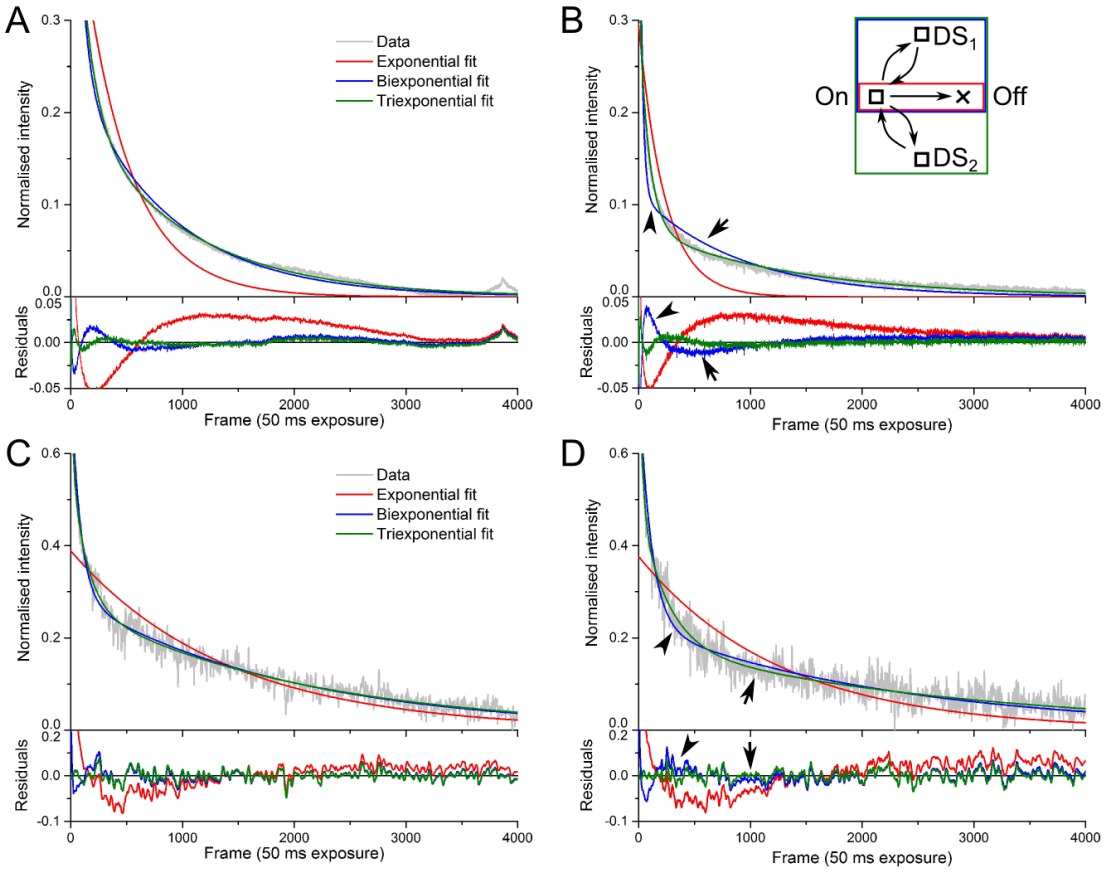


Figure 3.8 *Ensemble photo-physics of mEos.* Purified mEos2 (**A-B**) and mEos3.1 (**C-D**) proteins were activated by a pulse of 405 nm laser beam and imaged under 561 nm only (**A and C**) or both 561 and 405 nm (**B and D**) illumination. The normalised intensity over 4,000 frames are plotted (grey) and linear combinations of one (red), two (blue) and three (green) exponential decays were fitted. The residuals for each fit are also plotted. **Arrows**: region poorly described by a biexponential decay. **Inset**: two- (ref), three- (blue) and four-state (green) models for mEos fluorescence. The 405 nm-activated red-emitting fraction of mEos ('On') is photo-bleached ('Off') over time, but could also be, under constant illumination, in equilibrium with one ('$DS_1$') or two ('$DS_1$' and '$DS_2$') dark states.

properties were investigated. Indeed, although bulk experiments had been originally published [123], very little was known about the molecular behaviours of this new fluorescent protein.

mEos2 and mEos3.1[9] [121] proteins were expressed in *E. coli* and purified by Dr A. Watson. After dilution in a gelatin gel, each protein was imaged in bulk concentration after activation with a pulse of 405 nm laser (5 s; 66.3 mW), under either only 561 nm (227 mW) illumination or both 561 nm and 405 nm (162 µW) illuminations. The variations of the mean intensities over 4,000 frames (50 ms exposure) were analysed with models of one, two or three exponential decays (Figure 3.8, with (B, D) or without (A, C) 405 nm illumination).

Consistently with the supplementary figures of ref. [123], the photo-bleaching curve of the red form of mEos2 is not well fitted to a simple exponential decay. Instead, both mEos2 and mEos3.1 are well and parsimoniously described by three or two exponential decays, depending on whether the proteins are continuously illuminated with a 405 nm laser beam or not, respectively. Remarkably, both fluorescent proteins present quantitatively similar photo-bleaching lifetimes (Table 3.1).

Table 3.1 *Models of mEos photo-bleaching.* (Values are given ± one standard deviation of the mean for two fields of view and two biological repeats.)

| | **mEos2** | | **mEos3.1** | |
|---|---|---|---|---|
| No 405 nm illumination<br>$f(t) = A\,e^{-\frac{t}{\tau_1}} + B\,e^{-\frac{t}{\tau_2}}$ | $\tau_1 = 116$<br>$\tau_2 = 9,600$ | ± 46 s<br>± 8,200 s | $\tau_1 = 135$<br>$\tau_2 = 10,600$ | ± 18 s<br>± 400 s |
| Continuous 405 nm illumination<br>$f(t) = A\,e^{-\frac{t}{\tau_1}} + B\,e^{-\frac{t}{\tau_2}} + C\,e^{-\frac{t}{\tau_3}}$ | $\tau_1 = 42$<br>$\tau_2 = 360$<br>$\tau_3 = 10,800$ | ± 27 s<br>± 60 s<br>± 3,900 s | $\tau_1 = 26$<br>$\tau_2 = 310$<br>$\tau_3 = 7,100$ | ± 11 s<br>± 110 s<br>± 1,300 s |

The different exponential models can be interpreted as Jablonski diagrams of the fluorescent protein with different numbers of non-fluorescent states [141]: the simple exponential decay characterises a two-state model, for which a initially populated visible 'On' state (the activated red form of mEos) is depleted with a fixed rate (*i.e.* photo-bleached) over time (Figure 3.8, inset in B, red rectangle); the addition of a dark state ($DS_1$, blue rectangle) in equilibrium with the 'On' state induces a biexponential decay of the occupation of the fluorescent state; and a second dark state ($DS_2$, green rectangle) is manifested by the 'On' state population following a linear combination of three exponential decays [142].

[9] Since mEos2 partially dimerises at high concentrations, mEos3.1 or mEos3.2 were preferred when the constructs were designed after the publication of mEos3.1 and mEos3.2 sequences in ref. [123], mostly in Chapter 7.

Although a linear combination of two exponential decays describes well the occupancy of the red fluorescent form of both mEos2 and mEos3.1 in the absence of 405 nm illumination (Figure 3.8, A,C), the addition of a third exponential decay is necessary to properly fit this population when illuminated by both a 405 and a 561 nm beams (B,D − black arrows indicate specific regions that the biexponential decay does not satisfactorily account for). This 405 nm-dependence could be explained by the 405 nm-induced additional photo-activation of mEos that re-populates the red fluorescent form of mEos ('On' population) from the green-emitting non-activated pool of mEos acting as a dark state 'DS2' under 561 nm excitation. The fitted values of the amplitudes and exponential time constants of the combination of the two or three exponential decays are given in Tables 3.1 and A.1.

In order to validate this working model of a single dark state, experiments to directly study the photo-physical properties of separated single-fluorophore were designed and performed.

### 3.3.3 Single-molecule characterisation of the dark states of mEos

Purified mEos2 and mEos3.1 were diluted in a gelatin gel so that they could be imaged as spatially separated PSFs under constant 561 nm (227 mW) and 405 nm (power varying from 7 to 910 µW) illuminations. PSFs were fitted (*cf.* Section 3.4) and spatially grouped in trajectories (all localisations closer than 150 nm from each other). The distributions of the 'on' and 'off' times ($t_{ON}$: number of consecutive frames for which a PSF is detected, and $t_{OFF}$: number of frames separating the last detection of a PSF and its next detection in a non-consecutive frame, respectively) were calculated for thousands of trajectories (Figure 3.9).

Each distribution was then approximated by a linear combination of one or two exponential decays (Figure 3.9, red and blue, respectively − in A-B, for the white histogram). Although a single exponential approximated well the 'on' time distributions (A,C − in C, the biexponential fit did not converge), the combination of two exponential functions were required to correctly account for the shapes of the $t_{OFF}$ histograms (B,D − values of the extracted amplitudes and exponential time constants are summed up in Tables 3.2 and A.2).

In accordance with previous work on the photo-physics of Dronpa [143] and mEos2 [144, 145], the biexponential decay of the 'off' time distributions reveals the existence of two dark states in addition to the irreversible photo-bleached state[10]. The single exponen-

[10]The 'off' time histogram can be seen as the evolution of a global dark state initially populated and in equilibrium with the 'on' state over time. The biexponential decay indicates two different activation energies or kinetic mechanisms linking the global dark state and the fluorescent state. Since a usual hypothesis for fluorescent proteins is that there is a single fluorescent state, two activation energies would reveal the existence

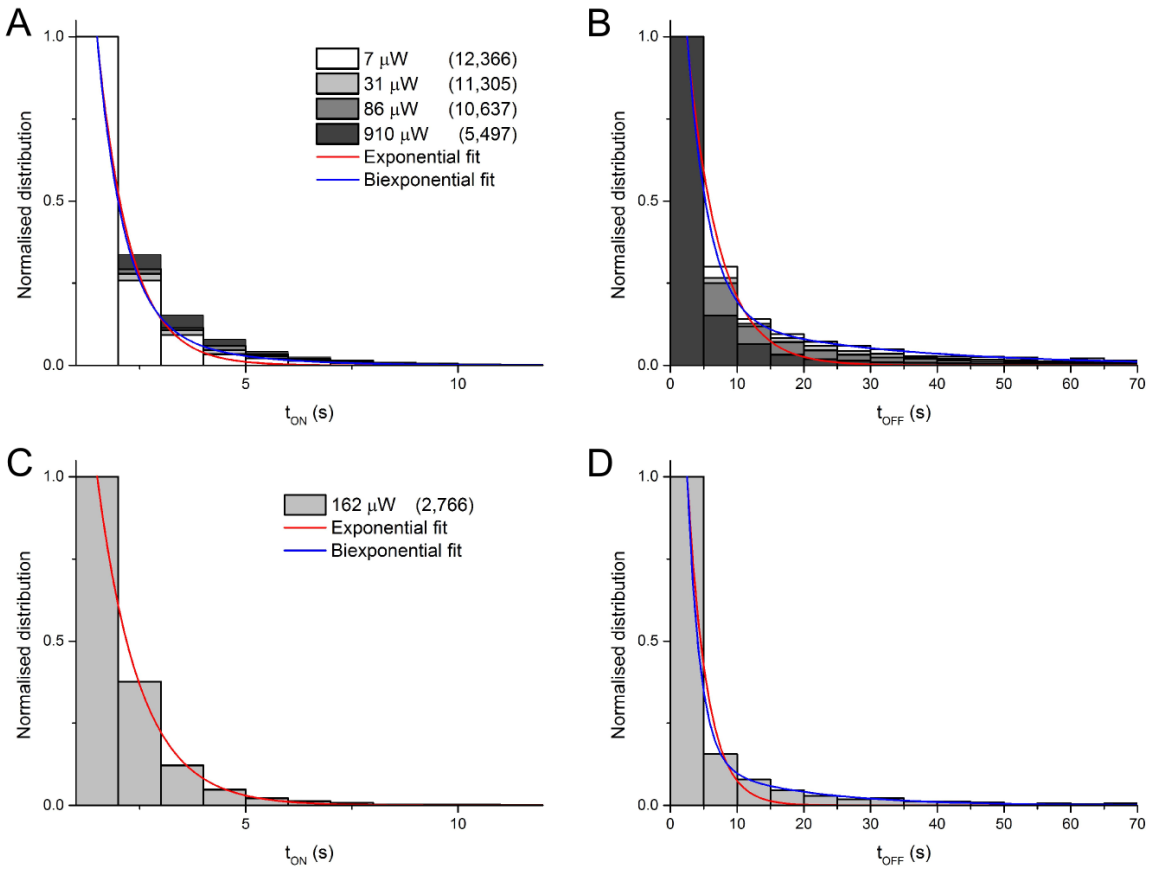


Figure 3.9 *Single-molecule photo-physics of mEos.* Distribution of 'On' (**A and C**) and 'Off' (**B and D**) times of trajectories of spatially-separated purified mEos2 (**A-B**) and mEos3.1 (**C-D**) proteins immobilised in a gelatin gel under both constant 561 nm and varying 405 nm illumination. **A,C**: normalised distribution of the number of consecutive frames (of 50 ms) for which single mEos proteins were detected. **B,D**: normalised distribution of the time spent by single mEos proteins in a non-fluorescent state between two following fluorescent detections. Experiments were done at different 405 nm illumination power: varying from 7 to 910 µW for mEos2 (from white to dark grey, A-B) and at 162 µW for mEos3.1 (C-D). The number of trajectories recorded for each distribution is indicated in parentheses in the legends. Distributions (white in A-B, grey in C-D) were fitted with both a single exponential decay (red) or a combination of two exponential decays (blue).

Table 3.2 *Models of mEos photo-physics.* Exponential time constants $\tau$ of the exponential decays fitted to the distributions of 'on' and 'off' times as described in Figure 3.9 under different 405 nm activation powers. Values are given for the fit of a single exponential decay for $t_{ON}$, and a linear combination of two exponential decays for $t_{OFF}$.

| **mEos2** | | | **mEos3.1** | | |
|---|---|---|---|---|---|
| 405 nm | $t_{ON}$ | $t_{OFF}$ | 405 nm | $t_{ON}$ | $t_{OFF}$ |
| 7 µW | $\tau_1 = 0.77$ s | $\tau_1 = 3.20$ s<br>$\tau_2 = 26.1$ s | 162 µW | $\tau_1 = 1.00$ s | $\tau_1 = 1.88$ s<br>$\tau_2 = 14.6$ s |
| 31 µW | $\tau_1 = 0.83$ s | $\tau_1 = 2.79$ s<br>$\tau_2 = 20.0$ s | | | |
| 86 µW | $\tau_1 = 0.87$ s | $\tau_1 = 2.62$ s<br>$\tau_2 = 15.6$ s | | | |
| 910 µW | $\tau_1 = 1.01$ s | $\tau_1 = 1.91$ s<br>$\tau_2 = 10.9$ s | | | |

tial decay fitting the 'on' time distributions can be explained by three scenarios: (1) not enough trajectories were recorded to precisely detect a more complex shape of the distribution; (2) direct depopulation of the fluorescent state by both dark states, together with the photo-bleached state, have indistinguishable activation energies; (3) the fluorescent state is depopulated by the single short-lived dark state that is further depopulated in either the second dark state, the fluorescent state or the photo-bleached state.

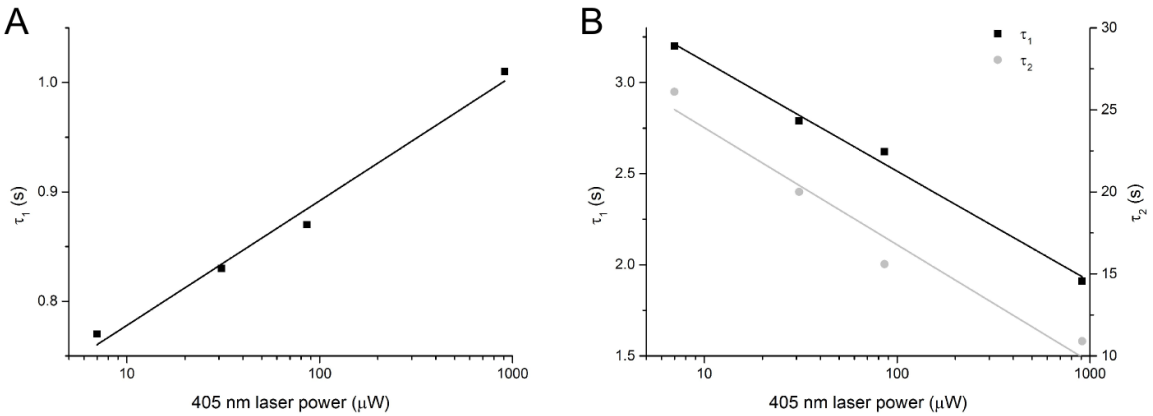


Figure 3.10 *Lifetimes of the fluorescent and dark states of mEos2.* The exponential time constants of the 'on' (**A**) and 'off' (**B**) time distributions of mEos2 plotted in Figure 3.9, A-B and summed up in Table 3.2 are plotted in function of the 405 nm illumination power (log scale). For each lifetime, a linear regression (in the log scale of the *x* axis) is shown.

of two different dark states composing the global dark state. It has to be underlined that the photo-bleached state does not appear in the diagram as if photo-bleached, the protein never re-enters the 'on' state, which is necessary to calculate an 'off' time.

Lifetimes of the fluorescent and dark states varied with the power of 405 nm illumination (Table 3.2). The lifetime $\tau_1$ of the fluorescent state increased exponentially with the 405 nm laser power ($R^2 = 0.981$) whereas the lifetimes $\tau_1$ and $\tau_2$ of the dark states decreased exponentially ($R^2 = 0.989$ and 0.941, resp.) (Figure 3.10). These observations are consistent with a 405 nm-induced depletion of one dark state [62, 143, 144], inducing longer 'on' times and shorter 'off' times of the fluorescent protein.

To refine the Jablonski diagram of mEos, more experiments would be required. However, these experiments justify the use of a low continuous 405 nm activation during PALM imaging [146], as opposed to pulses of activation [100], especially when counting, and not localising, is at stake. Indeed, depletion of one of the dark states induces less photo-blinking (or re-activation) of the same single fluorescent protein, preventing initial over-counting. Also, an important result is the very similar photo-physical behaviour of mEos3.1 compared to mEos2. Both are thus used indifferently in this thesis.

### 3.3.4 Optimisation of mEos photo-activation

The concept of SMLM is based on the idea of stochastically separating in time fluorophores that are spatially closer from each other than the diffraction limit. In PALM, this is achieved by turning the fluorescent protein from a dark state (here, the native green form of mEos) to a fluorescent state (the red form of mEos) with near-UV illumination. The photo-activation efficiency (*i.e.* the combination of the folding efficiency of the protein and of the fluorophore, and the photo-conversion efficiency from the dark to the fluorescent state) of the most used fluorescent proteins were recently measured [126]: only 61 and 41% of expressed mEos2 and mEos3.2 (resp.) are actually activated and can be observed during a PALM experiment. This intrinsically limits the accuracy of both localisation (lowering the labelling density) and counting (inducing under-counting that needs to be accounted for) in PALM. This is a main drawback of PALM imaging.

In order to optimise the photo-activation of mEos during a PALM experiment, the power of the 405 nm illumination needs to be adapted so that a similar density of fluorophores gets activated in each frame of the experiment, theoretically equal to the number of photobleaching events per frame. As densities of non-activated fluorophores are high at the beginning of an experiment, a low 405 nm illumination is required so that the probability of activating one fluorophore stays low; however, at the end of the experiment, very few fluorophores are left and, in order to optimise the time of the experiment and activate all activable fluorophores by the end of it, the power of the activation beam should be increased.

This optimisation is of critical importance when counting single molecules is at stake, to prevent both initial under-counting by activating too many fluorophores at once, and late over-counting by imaging no fluorophore in most of the final frames but single-molecule-like background noise.

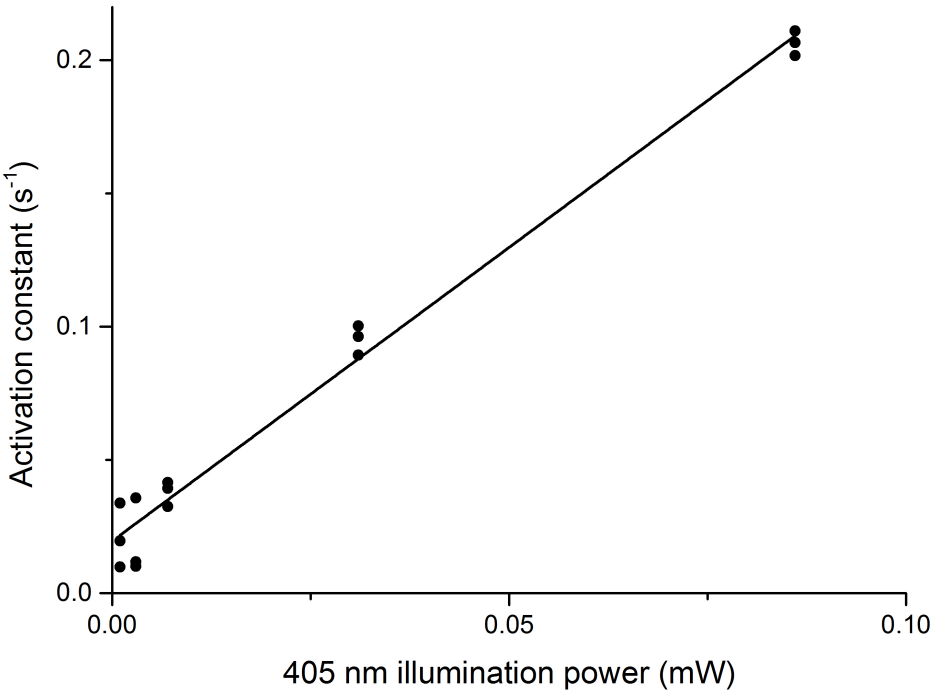


Figure 3.11 *Activation rate of mEos2.* Purified mEos2 proteins were immobilised in a gelatin gel and imaged under 561 (200 mW) and 405 nm (powers as indicated) illumination. For each detected trace of the red form of mEos, the time of its first appearance was calculated. Their distributions for three repeats and four different 405 nm illumination powers were fitted with an exponential decay. The corresponding exponential rates (or activation constants) are plotted. A linear regression is shown ($R^2 = 0.983$).

Lee *et al.* describe a Fermi activation curve that activates a constant number of fluorophores during an entire SMLM experiment [145]. Such an imaging protocol also optimises the imaging time, and consequently the size of the data to be stored and analysed. In order to apply this shape of activation, the calibration curve of the effect of the activation power on the activation rate was measured (Figure 3.11). Consistently with supplementary data from ref. [145], a linear correlation between the activation rate $k_a$ of mEos2 and the 405 nm illumination power ($R^2 = 0.983$) was observed. This enabled the optimisation of mEos photo-activation in counting experiments (*cf.* Chapter 6), varying the power of the 405 nm

illumination over time using the following formula (Equation 5 from ref. [145]):

$$k_a(t) = \frac{1}{T}\frac{e^{-(t-t_F)/T}}{[1+e^{-(t-t_F)/T}]\log[1+e^{-(t-t_F)/T}]} \tag{3.11}$$

with $T$ the fall-off time of the Fermi function, and $t_F$ its half-time.

## 3.4 Analysis

Because of the wave nature of the light, the distribution of photons emitted by a single fluorophore interferes with itself. This mathematical description of the propagation of a light ray as a wave explains the diffraction patterns of the intensity of a single fluorophore recorded on a detector: the point-like fluorophore is observed through any focussed optical system as a blurred spot, or point-spread function (PSF), of width $\sim$200 nm (Equation 2.1, for visible wavelengths). In order to localise the position of the fluorophore in the imaging plane with greater precision than the observed blur, each PSF needs to be detected and can be fitted with a model PSF. This section describes and discusses the algorithm used for SMLM processing in this analysis, and the post-processing tools that were developed to further analyse the list of localisations obtained into trajectories or clusters, or to compare the localisations of two differently-labelled proteins.

### 3.4.1 Fitting routine

The concept of SMLM relies on separation of fluorophores in time. Thus, multiple frames are recorded to rebuild one single super-resolved picture. In each frame, a sub-set of fluorophores are activated and visible as separated PSFs. A fitting routine is used to find and fit each PSF with a 2D-Gaussian and store its precise lateral position. Good reviews describe and compare existing algorithms [147, 148]. Below, two routines are described and compared: a bespoke piece of software that was first written to analyse data and understand the challenges and limitations of fitting; and a quick and efficient fitting routine called Peak Fit and developed by Dr Alex Herbert at the University of Sussex [149] that was later used and incorporated in all further post-processing scripts for convenience and rapidity reasons. All results in this dissertation have been analysed with Peak Fit, using the parameters listed in Table A.3. Both routines are written as ImageJ [150] plugins and follow a very similar sequential approach (Figure 3.13, A): each frame is first filtered through a Gaussian band-pass filter in order to detect local maxima; the position of each maxima is then used as an initial guess to fit a PSF function to the original non-filtered data.

Table 3.3 *Differences between home-made and Peak Fit fitting routines.*

| | **Home-made** | **Peak Fit** |
|---|---|---|
| Algorithm | Simplex optimiser | Levenberg Marquardt |
| Method | Maximising log-likelihood | Minimising non-linear least square error |
| Parameters | $\Theta_{1-5,7}$ ($\Theta_6 = 0$) | $\Theta_{1-7}$ |
| Bounds | All positive parameters, $(x,y)$ in fitting box | Positive intensity |
| Fit check | None | Position shift, signal strength and width |
| Stop decision | All selected maxima | When 10 successive fits failed |

- Gaussian band-pass filtering: two copies of each frame (Figure 3.13, C) are made, and each copy is respectively convolved with a 2D-Gaussian kernel smaller than the expected width of the PSF to get rid of high-frequency electrical noise, or with a 2D-Gaussian kernel larger than the width of the largest expected PSF (Figure 3.13, D). The latter is subtracted from the former in order to remove low-frequency biological noise, giving a filtered frame as shown in Figure 3.13, E. This convolution process amounts filtering the Fourier transform of the frame with a Gaussian band-pass filter, but runs faster than calculating two Fast Fourier transforms for small kernels [151].

- Maxima selection: local maxima of the filtered frame are listed (Figure 3.13, F). Two different strategies followed: in the home-made routine, local maxima were rejected if they were below an empirically-defined threshold ($1.2\ \mu_{\text{Background}} + 5\ \sigma_{\text{Background}}$, where μ is the mean background of the frame and $\sigma$, the standard deviation of the frame); in Peak Fit, local maxima are ranked by their intensity value.

- Fitting routine: for each local maximum, a region of the unfiltered initial data around the maximum was selected and further fitted with a theoretical PSF. Although an Airy disc PSF can be used, fitting a Gaussian PSF is quicker while it gives similar results [152], and was thus preferred (Figure 3.13, G):

$$\text{PSF}_{\Theta_{1-6}}(x,y) = \frac{\Theta_5}{2\pi\ \Theta_3\ \Theta_4} e^{-\frac{(x'-\Theta_1)^2}{2\ \Theta_3^2} - \frac{(y'-\Theta_2)^2}{2\ \Theta_4^2}} \tag{3.12}$$

$$\text{with} \begin{pmatrix} x' \\ y' \end{pmatrix} = \begin{pmatrix} \cos\Theta_6 & \sin\Theta_6 \\ -\sin\Theta_6 & \cos\Theta_6 \end{pmatrix} \begin{pmatrix} x \\ y \end{pmatrix}$$

where ($\Theta_1$, $\Theta_2$) is the centre of the PSF, ($\Theta_3$, $\Theta_4$), its two elliptical half-widths, $\Theta_6$,

the rotation angle between its two perpendicular axes and the $(xy)$ axes, and $\Theta_5$, its integrated intensity. For the home-made routine, $\Theta_6$ was fixed to 0, limiting the number of parameters to fit. The background noise, or offset of the Gaussian function, is added as a last additive fitted parameter in Equation 3.12 in Peak Fit. Then, the least squared error between the estimated Gaussian function and the data is minimised by a Levenberg Marquardt algorithm. Differently, the home-made routine makes the hypothesis that the background noise is Poissonian and consequently incorporates it in the log-likelihood estimator described by Abraham *et al.* [152], which is maximised by a Simplex optimiser. The log-likelihood estimator theoretically allows a more precise estimation of the positions [152] but requires a good model of the noise of the camera.

A last difference between the two fitting algorithms resides in the decision of which maxima to fit. The home-made routine *a priori* selects the maxima thanks to an empirical threshold before fitting them all. Peak Fit orders the maxima by intensity and fit them until ten successive fits fail. A fail is defined by empirical thresholds on different parameters such as the signal-to-noise ratio, the width, or the displacement of the position of the PSF after fitting (see Table A.3 for the thresholds that were used in this thesis).

Finally, both fitting plug-ins output a list of fit positions and parameters to be post-processed (*e.g.* Figure 3.13, H), before rebuilding the final super-resolved picture.

### 3.4.2 Post-processing

Once the SMLM data has been processed, the list of localisations usually requires some post-processing: localisations can be linked in trajectories to determine their diffusion behaviour, or grouped in clusters to spatially compare effects of different conditions. If two proteins labelled with two different fluorophores are simultaneously imaged, determining how much co-localised they are is also commonly expected, although not well-defined.

#### Single particle tracking

Single particle tracking is of key importance for quantitative analysis of live-cell SMLM data [49, 79, 153, 154]. Many algorithms, varying in (1) how they detect particles and (2) how they link the particles from different frames in trajectories, have been proposed (compared and reviewed in ref. [78]). Comparison of the different existing methods reveals that the choice of the tracking algorithm is critical when the signal-to-noise ratio (SNR, defined in [78] as SNR $= (I_0 - I_b)/\sqrt{I_0}$, $I_0$ denoting the amplitude of the PSF and $I_b$, the

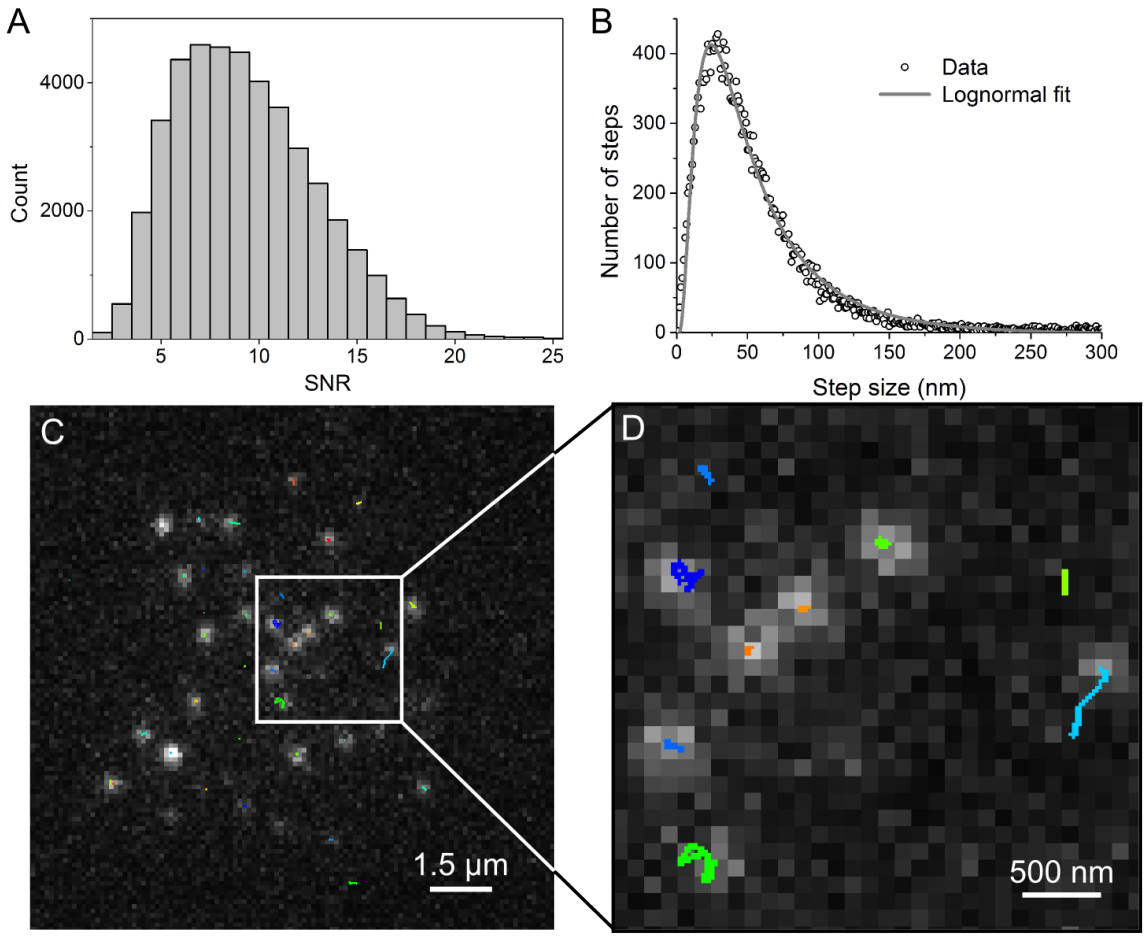


Figure 3.12 *Single-particle tracking algorithm.* The three validating steps of the single-particle tracking analysis used in this thesis are shown for data from one representative experiment (from Chapter 7). **A**: Distribution of the signal-to-noise ratios (SNR $= (I_0 - I_b)/\sqrt{I_0}$, $I_0$ denoting the amplitude of the PSF and $I_b$, the mean background intensity) for all localisations fitted in the SMLM experiment. **B**: Distribution of the step sizes of all built trajectories (○). A characteristic lognormal distribution was fitted to the data (grey line, $R^2 = 0.988$). **C**: One representative frame of the SMLM time-lapse experiment with several activated but separated mEos proteins. The trajectories of all localisations detected in the frame are plotted (one colour per trajectory). Trajectories are shown up to the frame shown. **D**: Zoom-in of the white square in C. All the 1,555 frames are available in Movie B.1.

mean background intensity) is lower than 4. In the experiments of this thesis, SNR $\geq 7$ (Figure 3.12, A), thus a simple tracking algorithm was chosen, in which localisations in successive frames are linked in a trajectory if a localisation in one frame falls within some maximum distance (here, 300 nm) of a localisation in the previous frame (as described in ref. [154]).

The low density of the localisations in the SMLM experiments, together with the slow diffusion of the transmembrane proteins of interest (*cf.* Chapter 7, for which measured diffusion coefficients fall below 0.08 $\mu m^2/s$), makes also the choice of a complex algorithm based on prior knowledge of the data less relevant. The choice of the trajectory radius (300 nm, less than the dimension of three pixels of the camera) was confirmed *a posteriori* by examining the resultant step distribution, which could always be fitted with a log-normal distribution ($R^2 \geq 0.95$, Figure 3.12, B). Furthermore, the trajectory radius was chosen to allow the detection of diffusion coefficients up to 0.1 $\mu m^2/s$ (at a frame rate of 20 Hz), which is in the upper range of the diffusion coefficients of membrane receptors [79].

More specifically, trajectories were defined as follows (Figure 3.13, B): for each localisation, all $n$ localisations within 300 nm from its positions in the previous frame were identified; then, three cases were found: (1) if $n = 0$ (no localisation detected in the previous frame), the process was repeated with the second previous frame (up to four frames of memory, to allow for short blinking of the fluorophore and partial efficiency of the fitting algorithm); (2) if $n = 1$, the localisation was linked to the single localisation detected in the previous frame; (3) if $n > 1$ (*i.e.* the tracks merge), the localisation was linked to all detected localisations from the previous frame and all the corresponding trajectories were terminated to avoid artefacts. A characteristic example of CD28-mEos tracks is given in Figure 3.12, C-D and Movie B.1.

### Cluster grouping

Once a SMLM experiment is analysed, the list of localisations can be plotted in a super-resolved picture or quantitatively analysed: a cluster analysis of the distribution of localisations is often essential, either to group multiple occurrences of a single emitter (PC-PALM) [82, 155], or to compare the aggregation or multimeric states of proteins in different conditions. Such algorithms are based on either:

1. the iterative search and grouping of all localisations within a defined distance $d$ (Figure 3.13, K − around an iterative weighted mean position of the grouped localisations [130, 131, 145, 155, 156], or by coalescing all localisations closer to at least one

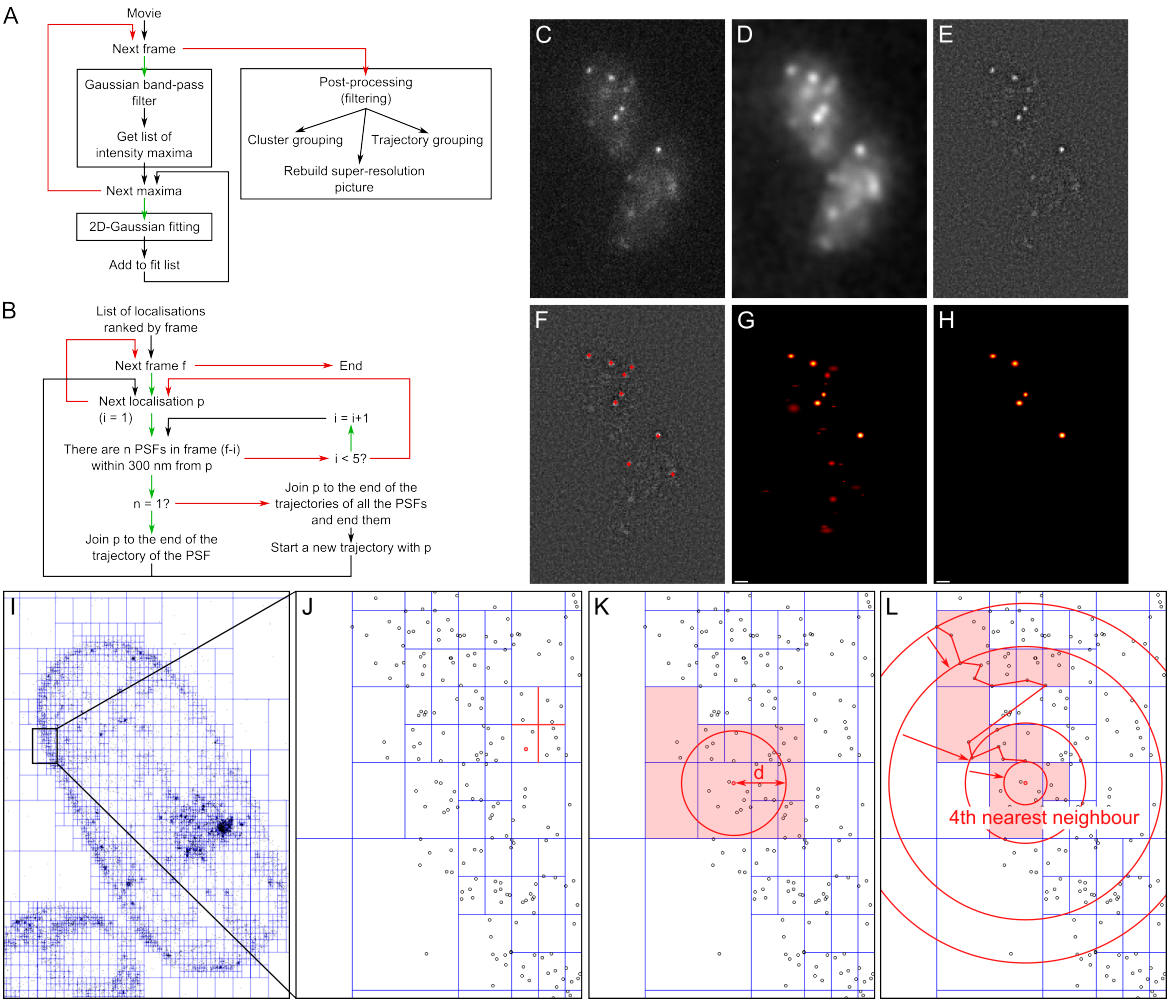


Figure 3.13 *Single molecule experiments require intensive data processing for any data analysis.* In SMLM, a fitting routine is used to extract the positions of single blinking fluorophores from a diffraction-limited movie (**A**, flow chart of the fitting process used in this thesis): the background (**D**) of each diffraction-limited frame (**C**) is filtered out (**E**) for its local maxima to be detected (**F**, local maxima represented as red crosses). Each local maximum is then fitted with a 2D-Gaussian (**G**, fitted 2D-Gaussians). Finally, the output localisations are post-processed (**H**, fitted 2D-Gaussians after amplitude and width thresholding). Together with rebuilding the final super-resolution picture, post-processing can require tracking fluorophores that appears in successive frames (**B**, flow chart of the simple but robust algorithm used in this thesis) or grouping fluorophores in clusters. For such latter analysis, efficient representation of the sometimes very large data (> 100, 000 localisations) is necessary: a QuadTree representation of the data (**I**, close-up of the squared region in **J**) was developed. This allowed fast grouping of localisations within a defined distance (**K**) or fast searching of $k^{th}$ nearest neighbour (**L**) (speed in $N \ln N$ instead of $N^2$).
*Legend:* green arrows in A-B, path if true; red arrows, path if false; transparent red rectangles in K-L, sub-regions explored by the algorithm; red line in L, path followed by the algorithm.

localisation of the group than $d$ [146, 157]);

2. or on a nearest-neighbour density approach (Figure 3.13, L). This was described in a density-based spatial clustering of applications with noise algorithm (DBSCAN) [158] which uses the distance of a point $p$ to its $k^{\text{th}}$ nearest-neighbour to decide whether $p$ is part of a cluster, or part of the data noise. This is a robust, fast, size-, density- and shape-independent clustering method.

For either approach, a brute force algorithm exploring and comparing the distance between each pair of $N$ localisations has a complexity, and speed, varying in $O(N^2)$. For small dataset, such speed is manageable but when the list of localisations increases ($N > 100,000$), clustering can take a few hours up to days. A way to increase the speed of the analysis is to re-organise the sparse data using its spatial information. In this thesis, a quad tree [159, 160] or Q-tree approach is proposed to efficiently represent the data and to speed the spatial clustering analysis up to a complexity in $O(N \ln N)$.

A quad tree consists of a tree whose leaves contain between 0 and $m$ localisations. Each branch of the tree divides itself in four branches or leaves that correspond to four spatial quadrants (north-west, north-east, south-east and south-west). Each branch of a quad tree is represented in Figure 3.13, I-J as a blue cross dividing the branch it is rooted in, in four. The last branches, or leaves, contain the localisations (up to $m = 10$ black circles). The value of the size $m$ of the leaf is a compromise between a fast memory-consuming ordered tree ($m = 1$) and a slow list-like tree-leaf ($m \geq N$); in this thesis, $m$ was fixed to 10.

When a new localisation $l$ is inserted, its leaf is quickly found ($O(\ln N)$, *i.e.* the average depth of the tree) by following, from the root of the tree, the consecutive branch it spatially belongs to until the algorithm finds a leaf. If the leaf contains less then $m$ localisations, the new localisation $l$ is added to the leaf. Otherwise, the leaf becomes a branch and spatially splits into four new leaves, re-arranging the $(m+1)$ localisations it previously contained (Figure 3.13, J).

Searching for all localisations closer than $d$ from a localisation $l$ consists in measuring the distance between all localisations in the leaves which spatially intersect the circle of centre $l$ and radius $d$ (Figure 3.13, K). All branches and their subsequent nodes and leaves that do not intersect this circle can be rejected as the quad tree is visited from its root up to its leaves. Such grouping has a complexity in $O(d \ln N)$ per localisation to be grouped.

Querying the $k^{\text{th}}$ nearest-neighbour of a localisation $l$ can be seen as the search for all localisations closer than a *varying* distance $d$: initially, $d = +\infty$ and the first $k$ visited localisations are stored in a circular buffer; for each new localisation $l'$ closer than $d$ from $l$, $l'$ is

inserted in place of the localisation $l_{\text{furthest}}$ in the buffer that is the furthest from $l$, and $d$ is modified to $d(l, l_{\text{furthest}})$. This algorithm allows a dramatic decrease in the number of localisations (or the spatial surface) explored: only the nine red leaves are explored in Figure 3.13, L (the red path underlines the consecutive localisations $l_{\text{furthest}}$ that actualised the distance $d$), instead of the whole plane composed of more than 48 leaves. Consequently, instead of visiting the $N$ localisations, such algorithm only visits an average of $O(k \ln N \ln(\ln N))$ localisations per nearest-neighbour query.

### Coordinate-based co-localisation

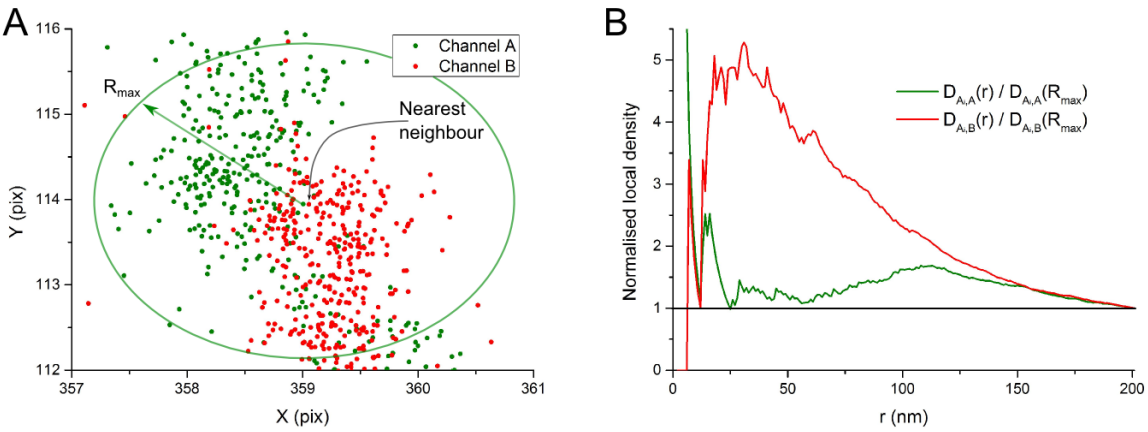


Figure 3.14 *Coordinate-based co-localisation.* After registration of two channels $A$ and $B$, SMLM analysis outputs a list of localisations (**A**, green and red, resp.). For each localisation $A_i$ from channel $A$, the local densities $D_{A_i,\,A}(r)$ and $D_{A_i,\,B}(r)$ in either channel within a radius $r \leq R_{max}$ of $A_i$ are computed. Both densities are normalised to their values at $r = R_{max}$ (**B**). Spearson's correlation coefficient between them is calculated (0.129) and weighted by the distance of the point $A_i$ to its nearest neighbour in the other channel $B$ (**A**, distance of 5.37 nm in the example shown). This final value is defined as the coordinate-based co-localisation (CBC) value of the point $A_i$ with respect to the channel $B$ (here, 0.125).

SMLM is inherently different from classical microscopy or confocal techniques (*e.g.* STED, SIM): it outputs spatially sparse and discrete data, a list of localisations (*i.e.* 0-dimensional points in a multi-dimensional continuous space). To further analyse SMLM data, methods that are specifically designed for such types of datasets have to be used [132]. A good example is found for two-colour co-localisation analysis: the super-resolved figure rebuilt from the list of fitted localisations cannot be used as the input for classical co-localisation methods (*e.g.* conventional coefficient calculation by pixel-per-pixel overlay, or intensity correlation analysis) because the way localisations are rebuilt would importantly affect their co-localisation [52]. Conceptually, it makes more sense to keep a coordinate-based approach for the entire analysis, as proposed by Malkush *et al.* [116].

Although co-localisation techniques have been extensively used in multi-colour fluorescence microscopy to gain functional insights from the comparison of the distribution of various proteins, the concept of co-localisation can reach its limit in super-resolution microscopy: at the molecular scale, two bound proteins that can be localised with an infinite precision are not superposed but are located at different positions. Thus, in SMLM, when localisation precisions reach tens of nanometers (*i.e.*, the size of a large molecular complex), interacting molecules may not be observed as co-localised. Then, a nearest-neighbour approach may be more valuable than a direct co-localisation analysis. Furthermore, co-localisation studies are also affected at this molecular scale by the sampling, the size and position of the label on the protein of interest, its localisation precision and its sub-frame diffusion [107]. This is why a specific implementation to study the spatial correlation of dual-colour SMLM data, as proposed by Malkush *et al.* [116] is required. By extension and analogy to the bulk microscopy concept, this algorithm is called 'coordinate-based co-localisation' (CBC) in this thesis."

For each localisation $A_i$ of the channel of reference $A$, the local densities $D_{A_i,\,A}(r)$ and $D_{A_i,\,B}(r)$ of the localisations of each channel, within an increasing radius $r \leq R_{max}$, are calculated and normalised to their values at $r = R_{max}$ (Figure 3.14). Spearman's correlation coefficient $S_{A_i}$ between both normalised densities is computed and weighted with a coefficient $e^{-E_{A_i,\,B}/R_{max}}$ ($E_{A_i,\,B}$ being the distance between $A_i$ and its nearest neighbour in channel B) to prevent false positive co-colocalisations if the local density in the channel $B$ is null.

Through the weighting factor, $R_{max}$ defines the resolution of the CBC analysis, especially for low-density data for which the nearest neighbour of the other species could be potentially far away for many localisations. Therefore, its value should be chosen to reflect the average localisation precision of both channels and their registration precision (see Section 3.4.3), giving an overall expected CBC resolution.

The final weighted correlation coefficient, taking values between $-1$ (anti-correlated distributions), through 0 (non correlated distributions), to $+1$ (perfectly correlated distributions), is defined as the CBC value of the localisation $A_i$ with respect to channel $B$. This allows to affect a co-localisation value for each super-resolved localisation separately, for each channel. Moreover, this co-localisation value is independent of the representation of the single-molecule data.

### 3.4.3 What is precision

The purpose of SMLM is to image structures with a precision better than the diffraction limit of visible light. A clear definition of precision is worth being carefully discussed, together with its limits and its common misuses. The precision of a localisation is experimentally accessed by imaging a fiducial marker multiple times. Because of the electrical noise of the detector, the PSF is fitted slightly differently in each frame, inducing a variation in the estimation of its localisation, which is by definition the precision of the localisation. The position of the localisation is usually assumed to be normally distributed (Figure 3.15, A). Although in part of the literature a full-width-at-half-maximum (FWHM) is sometimes used, in this thesis the precision $\sigma$ of a localisation refers to the standard deviation of the distribution of its fitted position. In case of a normal distribution, however, $\text{FWHM} = 2\sqrt{2\ln 2}\,\sigma \sim 2.35\,\sigma$.

Importantly, the precision of a localisation has to be distinguished with the fitting error: although both depends on the intensity of the fluorophore and the background noise, the fitting error depends on the estimator that is maximised (*e.g.* least squared error, likelihood) and on the number of degrees of freedom of the fitting function (*e.g.* symmetric, or asymmetric Gaussian). A high number of fitting parameters can lead to some over-fitting of the fluorescent signal. In this scenario, the fitting error will be very low, but will not represent any physical precision.

However, since a high signal-to-noise ratio is required in SMLM and because most experiments have a time-constraint, the position of each single fluorophore cannot be assessed in enough consecutive frames to get a distribution of localisation positions: (1) in fixed PALM or STORM experiments, the aim is to record a full duty cycle in a single frame to limit the noise accumulated on each frame recorded by the EMCCD; (2) in sptPALM, live STORM or uPAINT, each diffusive fluorophore is imaged for a few frames, but because of its diffusion, the position of the fluorophore changes over time. Therefore, a theoretical formula which, from one single localisation, describes the statistical distribution it originates from and gives its precision from accessible parameters is essential. Mortensen *et al.* developed such a formula summarised in the following equation [149, 161]:

$$\sigma_{th}^2 = 1.83\,\frac{\tilde{\sigma}^2}{N}\left(\frac{16}{9} + \frac{8\pi\,\tilde{\sigma}^2 b^2}{N a^2}\right) \tag{3.13}$$

where $\tilde{\sigma}$ is a length constant defined as:

$$\tilde{\sigma}^2 = \sigma_x\,\sigma_y + \frac{a^2}{12}$$

and

$$N = \frac{\text{Amplitude} \cdot 2\,\pi\,\sigma_x\,\sigma_y}{\text{Gain}}$$

Interestingly, the precision $\sigma_{\text{th}}$ is inversely correlated with the total integrated intensity $N$ and correlated with the noise of the background $b$. Indeed, the more detected photons above the background, the better the distribution of the PSF is evaluated and the better the position of the localisation can be known. The dependence on the pixel size $a$, *i.e.* the physical size of the conjugated image of one pixel of the camera in the focus plane, reveals the existence of an optimal pixel size ($\sigma_{th}$ diverges when $a \to 0$ and $a \to +\infty$): physically, if the pixel size $a$ is too large, the whole PSF of the single fluorophore will fall into a single pixel and no information above the background noise will be available to determine the sub-pixel localisation of the centre of the PSF; inversely, if the pixel size is too small, the whole PSF will be divided between a large number of pixels which will only receive a low number of photons. If this number is too low, it will quickly fall below the constant background noise observed per pixel and no spatial information will be available to localise the sub-pixel position of the centre of the PSF.

Ober *et al.* [162] demonstrate that the optimal pixel size is ∼100 nm/pixel (corresponding to a magnification of 50x for pixels of 5 µm) for a GFP-like emitter observed through a 1.4-$n_a$ objective lens. Although the objective lens used in this thesis has a slightly higher numerical aperture ($n_a = 1.49$), the optimal pixel size, which varies similarly than the width of the PSF of the instrument (*cf.* Equation 2.1), will not differ significantly. Since the physical size of the pixels of the EMCCD cameras in this thesis is 16 µm, with the magnification of the 60x objective only, the pixel size would be 267 nm/pixel. Adding a 2.5x beam expander leads to an optimised pixel size of 107 nm/pixel (110 nm/pixel as measured with a Ronchi slide).

Nevertheless, Equation 3.13 is an estimate of the best theoretically accessible precision. Although this equation is used as such in many publications to calculate super-resolved precisions (*e.g.* in PC-PALM), it seems important to compare it to actual data and possibly adapt it to the characteristics of the imperfect optics of the microscope. Diffraction-limited beads labelled with fluorophores were imaged for several consecutive frames under constant excitation. After PSF fitting and grouping the localisations of the fixed fiducials, the standard deviations of the successive positions of each bead were plotted against their average fitted intensity (Figure 3.15, B, black dots).

As expected, this experimental precision follows a similar curve than the theoretical precision, calculated with Equation 3.13 for the average fitted intensity, noise and PSF width of each trajectory (grey dots). Both precisions are well fitted and described by a function

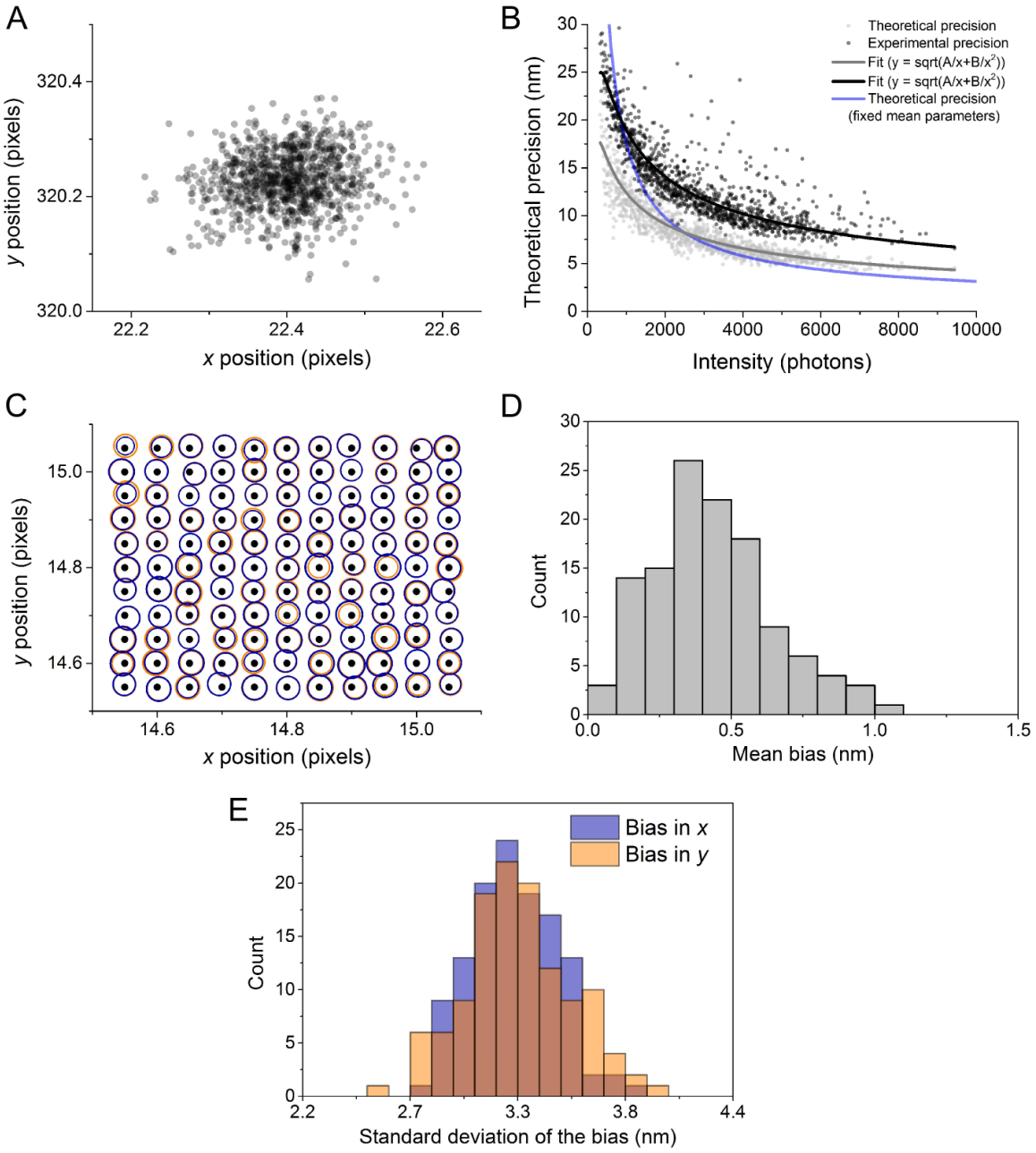


Figure 3.15 *Experimental localisation precision and bias of the fitting algorithm.* Separated fluorescent sub-diffraction carboxylated beads were fixed on a poly-lysine coated coverslip and imaged for 1,000 frames (33 ms exposure) under varying 561 nm illumination (**A-B**). **A**: All localisations of one fiducial marker, originating from the 1.000 frames of one experiment, are plotted (•). **B**: Localisations for each experiments were spatially grouped in trajectories (all localisations within 110 nm from each other). For each trajectory, a theoretical precision (**grey dots**) was calculated using Equation 3.13 and the average intensity, width and noise of all the localisations of the trajectory. The experimental precision (**black dots**) was also calculated as the standard deviation of the successive positions of all localisations of the trajectory. Both precisions were fitted with the following function: $y = \sqrt{A/x + B/x^2}$ (**grey and black lines**, resp.). Finally, Equation 3.13 is also plotted for the average value of intensity, width and noise of all plotted trajectories (**blue line**).
Fluorophores were simulated 100 times *in silico* at the positions of a 11x11 square grid sampling a quarter of a pixel, in order to test the fitting algorithm for its sub-pixel accuracy and possible structural bias. **C**: Simulated positions are plotted as **black dots** (ground truth). **Blue and orange circles** are centred on the average position of the corresponding fitted localisations and their radii are proportional to the standard deviations (on the $x$ and $y$ axes, resp.) of the fitted positions. **D**: Distribution of the distance between the ground truth and the average fitted position for all 121 simulated positions. **E**: Distributions of the standard deviations (or bias) of the fitted positions.

with same dependencies on the intensity than the previous equation: $\sigma = \sqrt{A/N + B/N^2}$ (black and grey lines, resp.). Thus, the fitted function describing the experimental precision in function of the number of collected photons could be used instead of the theoretical estimate for all SMLM data taken on a similar microscope.

However, although used to determine the theoretical precision for each trajectory independently, Equation 3.13 does not describe either theoretical or experimental precisions if plotted as function of the intensity $N$ only ($\sigma = f(N)$, blue line) with fixed background noise and PSF width (fixed as the average value over all trajectories). This reveals the importance of both noise and PSF width variables, critical in this equation. Noticeably, the fitted experimental function does not take into account these dependencies. Thus, in this thesis, the localisation precision was defined as the theoretical precision. Although under-estimating the error in the localisation, it describes precisely the main dependencies of the localisation precision on the parameters of the PSF fit. Moreover, with the calibration curve presented here (Figure 3.15, B), an estimation of the error made with this approximation of the localisation precision with the theoretical precision can be determined: an under-estimation of $\sim$ 5-10 nm is made.

Experimentally, the localisation precision can also be affected by different parameters such as diffusion blurring [163] if the sample is not fixed, or the dipole orientation of the fluorophore [98] if it does not rotate freely. Additionally, if the positions of localisations in two different channels are compared, the square of the precision of the registration of both channels needs to be added to the squares of the localisation precisions of both fluorophores (*cf.* Section 3.2.3) [107].

Finally and importantly, distinction between sometimes confused concepts needs to be clarified [52, 164, 165]:

1. The localisation *precision* concerns how *reproducible* the repeated localisation of a fluorophore is (it depends on the number of collected photons, on how they are spread on the detector and on the background noise);

2. The *resolution* of an experiment concerns the size of the smaller structures or features observed in the final rebuilt super-resolved figure (it depends on both the precision and the *density* of the localisations [121]). Fourier ring correlation analysis, inspired from a common method in electron microscopy, is a robust way to estimate the resolution of an experiment [166].

3. The *accuracy* of an SMLM experiment concerns the mean distance between the estimated localisation and the *ground truth*, *i.e.* the position of the protein of interest,

and measures *inherent bias* of the method (it depends on both the size of the label and its linker to the protein of interest, and systematic bias of the fitting localisation estimator).

These three parameters are important in an SMLM experiment and should be kept in mind.

The accuracy of the fitting localisation estimator was briefly studied: fluorophores were estimated at varying positions on a 11x11 square grid spanning a quarter of a pixel of the camera (Figure 3.15, C). At each position, 100 frames were simulated, then fitted with Peak Fit (*cf.* Section 3.4.1). No symmetric bias was observed in either the average localisation position or its distribution (Figure 3.15, C). A symmetric error would be a marker for a systematic intrinsic error induced by the symmetric fitting estimator. An estimation of the average error made (Figure 3.15, D, less than 1 nm) and of its spread (Figure 3.15, E, distribution of the standard deviations of the $x$ and $y$ errors for all simulated positions, peak at $\sim$ 3.2 nm) reveals that the systemic bias of the algorithm is negligible compared to the typical localisation precision of SMLM experiments presented in this thesis (on the order of 30-40 nm).

To conclude, in this thesis, the localisation precision is defined as the theoretical precision $\sigma_{th}$ (Equation 3.13). The precision of an SMLM experiment is the value at the peak of the histogram of $\sigma_{th}$ for all localisations. However, when possible, the distribution of theoretical precision is compared to the distribution of the standard deviations of trajectories of fixed fluorophores (*i.e.* an estimation of the experimental precision). An interesting new approach has recently been proposed by Endesfelder *et al.* [167]: the nearest-neighbour-based approach (NeNA). Because of time constraint, this direct, robust and useful method, with no need for calibration or prior knowledge of the sample or fluorophores, was not implemented in this thesis. This would be, however, an important tool to use in further experiments.

## 3.5 Automation

One major improvement allowed by SMLM over classical microscopy is the possibility to observe rare behaviours of molecules that would otherwise be missed in the ensemble averaging of the entire population. However, a major drawback of SMLM compared to conventional fluorescence microscopy is that very few cells are imaged as each acquisition takes much longer. For each imaged cell, much more data is recorded and must be stored. Also, since magnifications are higher, fields of view are usually much smaller. Therefore, as distributions of proteins in a single cell can be observed more precisely, separating each single behaviour, the variation of these behaviours in a population of cells, which is required

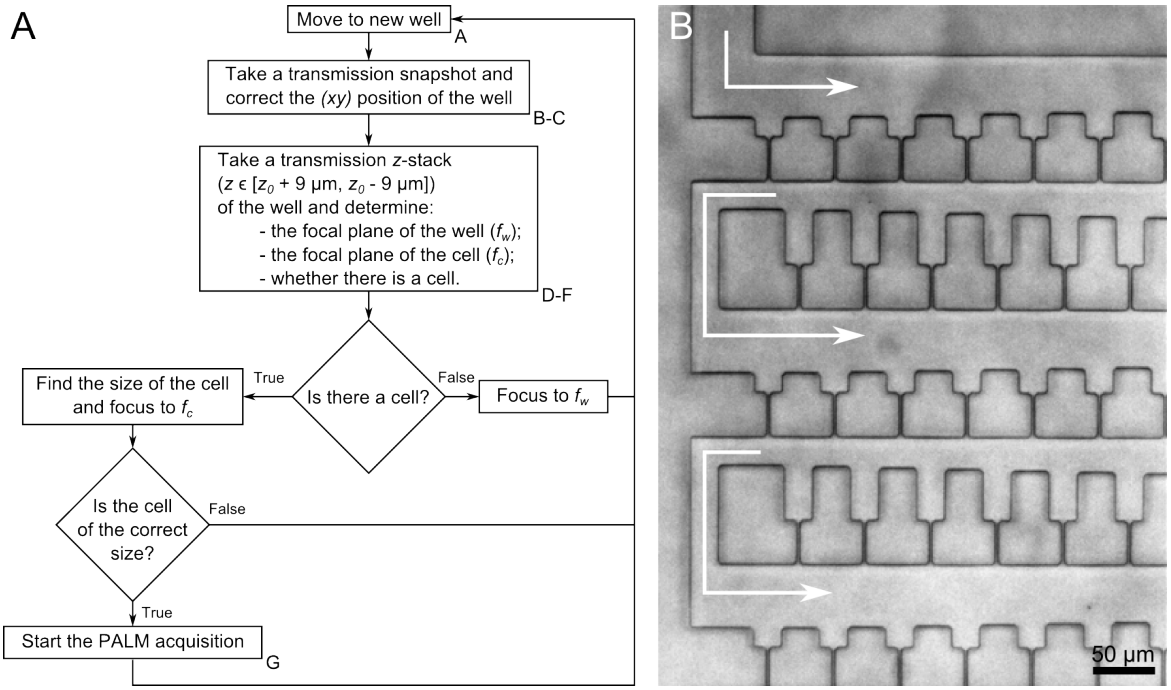


Figure 3.16 *Designing an automated imaging procedure.* **A**: Flow chart of the automation algorithm designed for 'smart' large-scale data acquisition (Software B.3). Capital letters indicate the corresponding panels in Figure 3.17. $f_w$, $f_c$: Focal planes of the well and of the cell, resp.. **B**: White-light transmission snapshot of part of a micro-fluidic device with five rows of trapping sites. Direction of the flow is shown by white arrows. Scale bar: 50 µm

to draw any conclusion, proves to be a real challenge, especially if the cellular population of interest is itself rare in the general population of cells that is observed.

This is the case of yeast cells in SMLM live imaging. Yeast cells are usually mounted between an agarose pad and the glass coverlips, to immobilise and image them live [130, 168, 169]. However, when interested in a specific phase of cell division, one needs to manually find and select such cells one by one (the division phases of *S. pombe* cells are strongly correlated with a specific cell size [170]) and acquisition cannot be automated.

An important evolution in the method was the design and introduction of a micro-fluidic device through which separated yeast cells can be flown until they get individually trapped at specific positions where they grow while they can be imaged [100]. By knowing the positions of the discreet sites where cells can be trapped, an automated microscope stage can visit and thus allows to image many trapped cells. The aim of the algorithm described in this section (Software B.3) is, once initially focussed on the first well in the first row of the device, to visit each trapping site, determine whether a cell is trapped and if so, whether it has a pre-determined length of interest (*i.e.* whether it is in a specific phase of the cell cycle) (Figure 3.16, A). If this is the case, then the cell can be imaged in a PALM experiment.

To account for the fact that both (1) the position of the trap site within the well varies along a row (Figure 3.16, B, the depth of the sites varies in each row to keep a same trapping pressure in each site) and (2) the axis of the trapping device may be at a slight angle relative to the detector (*e.g.* Figure 3.17, A-C), moving from one well to the next is done in two consecutive steps: firstly the $(xy)$ stage moves to the theoretical place of the next well; then a white-light transmission snapshot (to prevent any pre-activation of the fluorophores from light of wavelength below 610 nm, a long-pass filter is used, Figure 3.17, A) is taken and binarised to detect the main characteristics of the well (four horizontal lines and one vertical one, Figure 3.17, B); the position of the $(xy)$ stage is finally adjusted to precisely place the centre of the trap in the centre of the camera chip (Figure 3.17, C). In this way individual *S. pombe* cells always appear in the centre of the field of view independently of the trap the cell happens to be trapped in.

For various reasons (stability of the optical components of the PALM platform, temperature or oil drift, non-orthogonal sample mounting, *etc.*), the focus can repeatedly drift on large spatial scales (typically over more than five to ten wells). An autofocus function was thus added to the algorithm to correct for this instability: a transmission $z$-scan (Figure 3.17, D-E) is taken to define the focal plane of the well and, if a cell is present, of the cell (which usually differs from the former, since the cell can be trapped at slightly different axial planes in the trapping site). The autofocus analysis is based on contrast maximisation on

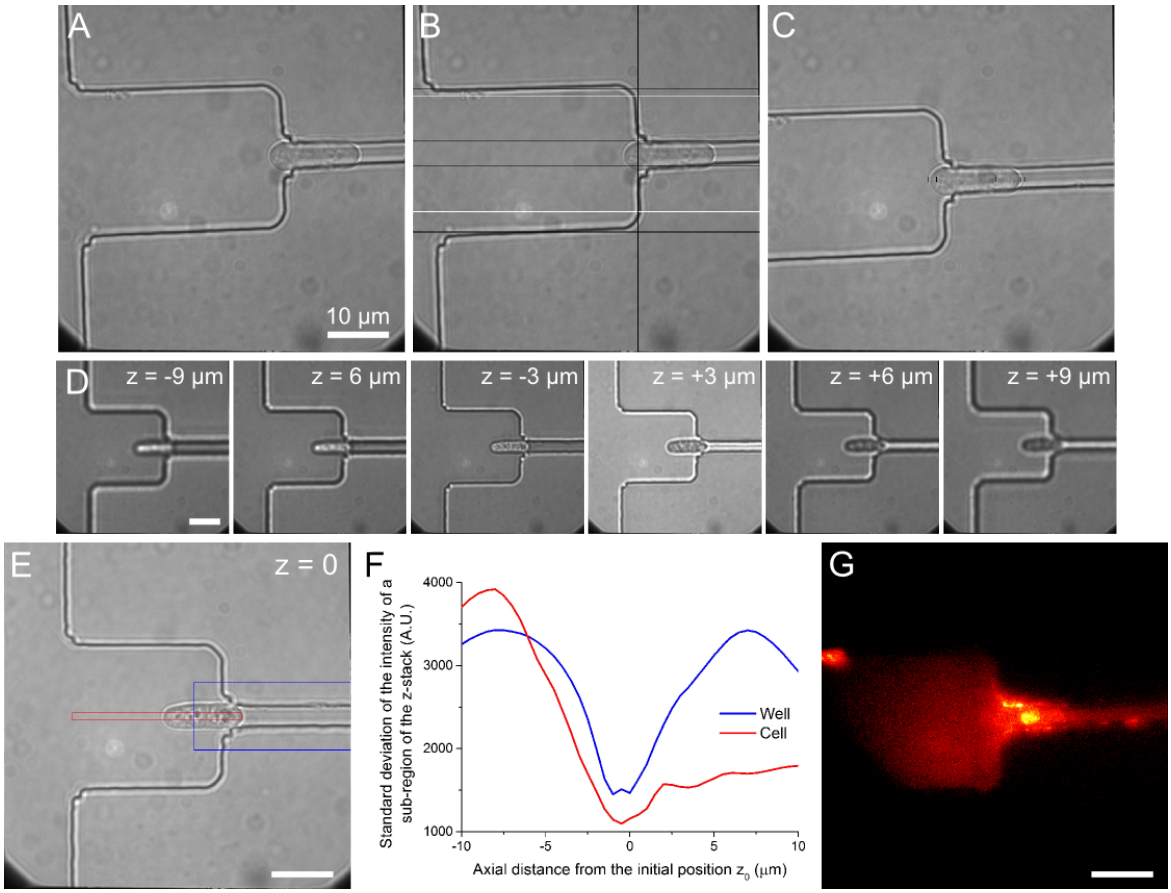


Figure 3.17 *Automated imaging of live yeast cells.* Live yeast cells were trapped in several sites of a microfluidic device. The different stages of the the automation algorithm are described with one representative cycle observed during the course of an experiment. For each cycle, the $(xy)$ computer-controlled microscope stage moves to the theoretical position of the new well, takes a transmitted light snapshot (**A**), analyses it by recognising characteristics of the borders of the well shown as fine lines (**B**) and adjusts the $(xy)$ position of the stage to move the centre of the trap to the centre of the field of view and therefore the camera sensor (**C**). A transmitted light $z$-stack is then taken (**D-E**), allowing the determination of both focal planes of the well and the possible cell by minimising the contrast (**F**) of both sub-regions of the well (blue rectangle, E) and of the potential cell (red rectangle). This analysis determines whether a cell has been trapped in the centre of the well and, if so, the length of the cell is calculated. Then, in the case of the detection of a cell, the algorithm focuses the microscope on the focal plane of the cell and starts a PALM acquisition (**G**: standard deviation projection of 50 frames). Otherwise, it focuses on the focal plane of the well before moving to the next well. Movie B.2 displays the visit of four consecutive trapping sites in real-time. Scale bars: 10 µm.

sub-regions of the field of view over 9 µm above and below the initial $z_0$ plane (Figure 3.17, E-F) [171]. A trapped cell is detected if the contrast variation of the sub-region of the area of interest is greater than 1.5.

Then, if a cell has been detected, its width and total length are measured. Finally, if the cell has the specific size of interest (corresponding, for example, to the important but short-lived phase G2 of the yeast division cycle [130]), PALM acquisition is started (Figure 3.17, G). This 'smart' automation algorithm allows one to 'search out' and image a specific sub-population of cells from a large sample while optimising acquisition time, computer memory use and analysis computing time (Movie B.2).

This section describes a relatively simple and specific SMLM experiment for which an automated design increases the size of the data that can be collected per sample by more than an order of magnitude and decreases requirements in term of resources (number of samples to prepare, data storage, time). This is a single example to underline the importance of automation in SMLM. Bridging single-molecule techniques and high-throughput automation [102, 172, 173] will allow to gain a deep and quantified understanding of rare molecular events on the scale of cell populations, while avoiding two of the major drawbacks of current microscopy: the user bias in selecting cells to image and the low-throughput of the technique [174]. Moreover, with the coming of faster and faster algorithms [149, 175, 176], an on-the-go SMLM analysis is almost presently available, opening the door to decision-making algorithms that will decide when to stop imaging (when local densities of localisations reach a determined value) [177], how to adapt, in real time, the laser powers of the activation and illumination beams in order to activate an optimal fraction of fluorophores and track them for a given number of frames (*cf.* Section 3.3.4), *etc.*

However, such an automation procedure requires the efficient positioning of tens of cells in known sites or wells. The design of such wells is itself a complex field of research, especially in the case of mammalian cells. Indeed, contrarily to yeast cells, mammalian cells present a wide variation of sizes and shapes, and develop strong, diverse and complex interactions with the surfaces they meet. These two separate reasons explain why this automation step, although demonstrated here in the case of yeast cell imaging, was not further used in this thesis which focusses on applications of SMLM to T-cell biology. Nevertheless, were a device available for efficiently positioning T cells without activating them (*cf.* Section 6.2.3), this automation procedure would greatly benefit the results of Chapters 6 and 7.

# Chapter 4

# The virtual-‘light-sheet’

Most data from this chapter has been published in PLOS ONE as an article entitled "Virtual-‘Light-Sheet’ Single-Molecule Localisation Microscopy Enables Quantitative Optical Sectioning for Super-Resolution Imaging" [2]. The original idea was from Dr S.F. Lee. All experimental design, data analysis, and code writing was undertaken by the author of this thesis. Dr S.F. Lee and M. Palayret designed and built the super-resolution instrument used in this chapter. H. Armes imaged the *S. pombe* cells made by Dr A.T. Watson and presented in Figure 4.8. Dr S. Basu imaged the stem cell presented in Figure 4.9. Dr U. Endesfelder and T.J. Etheridge took some of the calibration $z$-scans analysed in Figure 4.6. Dr S.F. Lee imaged the Tau-labelled monomers analysed in Figure 4.2, B. All other experiments were done by M. Palayret. Finally, Dr A. Herbert gave precious advice in algorithm optimisation, and M. Tracey is responsible for the final design of Figure 4.1, A and 4.9, B.

## 4.1 Introduction

Two limiting factors have driven technical developments in fluorescence microscopy: contrast optimisation and precision. Both innovative illumination and emission techniques have been developed to increase the signal-to-noise ratio of the image: restricting the illumination to a strict portion of the in-focus sample imaged by the detector (*e.g.* confocal illumination, TIRF, HILO, SPIM) decreases collection of light originating from out-of-focus emitters; secondly, spatially restricting the fluorescence signal to reject all light originating from above or below the focal plane thanks to a pinhole or a slit placed in the image plane of the microscope (confocal detection) drastically increases the signal-to-noise ratio. Contrast optimisation has become a main challenge with the observation of ever-smaller biological structures, down to single-molecule tracking and imaging: structures with fewer proteins

of interests are tagged with fewer fluorophores which results in lower signals for similar background noise.

Interest in smaller biological structures was challenged by the second limiting factor of fluorescence microscopy: the Abbe diffraction-limit of the light (*cf.* Section 2.1.2). The resolution, and the precision, of a microscope is intimately linked to the Abbe limit as two objects cannot be separated and distinguished if their relative distance is smaller than the width of their PSF, up to a prefactor (2.90 for the Rayleigh criterion, 1.44 for the Sparrow criterion, *cf.* Section 3.4.3). One of the successful techniques developed to bypass the Abbe limit is to sequentially image the single emitters one at a time in SMLM (*cf.* Section 2.2.1).

However, in SMLM, optimising the signal-to-noise ratio is essential for any substantial increase in precision (the precision is inversely proportional to the square-root of the signal above background − Equation 3.13). To improve it, restricting the sample illumination is necessary (TIRF, HILO or SPIM). But as SMLM is a wide-field technique, a pinhole cannot be used in the emission path[1].

In this chapter, a method that enables 3D sectioning with SMLM is demonstrated that uses fitting information that is usually discarded to reject fluorophores that emit from above or below a virtual-'light-sheet' (vls), a thin volume centred on the focal plane of the microscope. An easy-to-use routine (implemented as an open-source ImageJ plug-in) is described that quickly analyses a calibration sample to define and use such a vls. In addition, the plug-in is easily applicable on almost any existing 2D super-resolution instrumentation. This optical sectioning of super-resolution images is achieved by applying well-characterised width and amplitude thresholds to diffraction-limited spots that can be used to tune the thickness of the vls. This allows qualitative and quantitative imaging improvements: by rejecting out-of-focus fluorophores, the super-resolution image gains contrast and local features may be revealed; by retaining only fluorophores close to the focal plane, vlsSMLM improves the probability that all emitting fluorophores will be detected, fitted and quantitatively evaluated.

[1]This is theoretically possible but impracticable since the separation of dense fluorophores in time that is needed for SMLM would make the method extensively slow if additional confocal scanning was required, multiplying the duration of an experiment by the number of confocal volumes to visit.

## 4.2 Results

### 4.2.1 Axial variations of the point-spread function

In geometrical optics, a point-emitter in the object plane of the objective lens is conjugated with a point on the plane of the detector located in the image plane of the tube lens (green rays, Figure 4.1, A). Conversely, a point-emitter located above or below the object plane of the objective lens, is conjugated with a point located respectively in front of or behind the plane of the detector (red rays). The image recorded on the detector is consequently larger and dimmer (for the same number of emitted photons, as they are distributed over a larger surface on the detector). Because of the diffraction of the light, images of both the in-focus and out-of-focus emitters are further 'blurred': *e.g.* the image of the in-focus single-emitter is recorded as a blurred spot, or PSF, rather than a mathematical point (Figure 4.1, D). The diffracted image of a point-emitter located at an axial position $z$ through a microscope is defined as the PSF($z$) of the microscope.

In order to measure the 3D shape of the PSF of the instrument, sub-diffraction green-fluorescent beads were imaged in axial steps of 10 nm (Figure 4.1, B). As expected, both the width and the amplitude of the PSF dramatically vary in $z$: the PSF of an in-focus bead is both thin (Figure 4.1, D, left panel, contrast-adjusted $(xy)$ plane) and bright (right panel, intensity plot), whereas the PSF of the same bead located 500 nm above or below the focal plane is broader and dimmer (Figure 4.1, C and E). The 2D shape of the PSF of an object therefore holds axial information. Bi-plane microscopy [86], a technique that compares the widths of the PSFs of single emitters simultaneously imaged at two different axial positions, is based on this same conclusion.

Most SMLM analyses fit each detected single PSF with a 2D-Gaussian function. This means that characteristics of the PSF such as the width or the amplitude are *de facto* usually extracted, although not quantitatively further used. This chapter offers to quantitatively study the axial dependence of such parameters in order to increase contrast of the super-resolved image by rejecting out-of-focus emitters.

An in-focus thin plane, or virtual-'light-sheet' (vls), is defined as an arbitrary volume around the focal plane. The focal plane is itself defined here as the plane for which the integrated intensity of a box drawn around the 2D-PSF of each imaged bead is maximal. Due to the axial variations of most high-numerical aperture super-resolution microscopes, the height of the vls will typically be of $\sim$600 nm (full width at half maximum $-$ FWHM

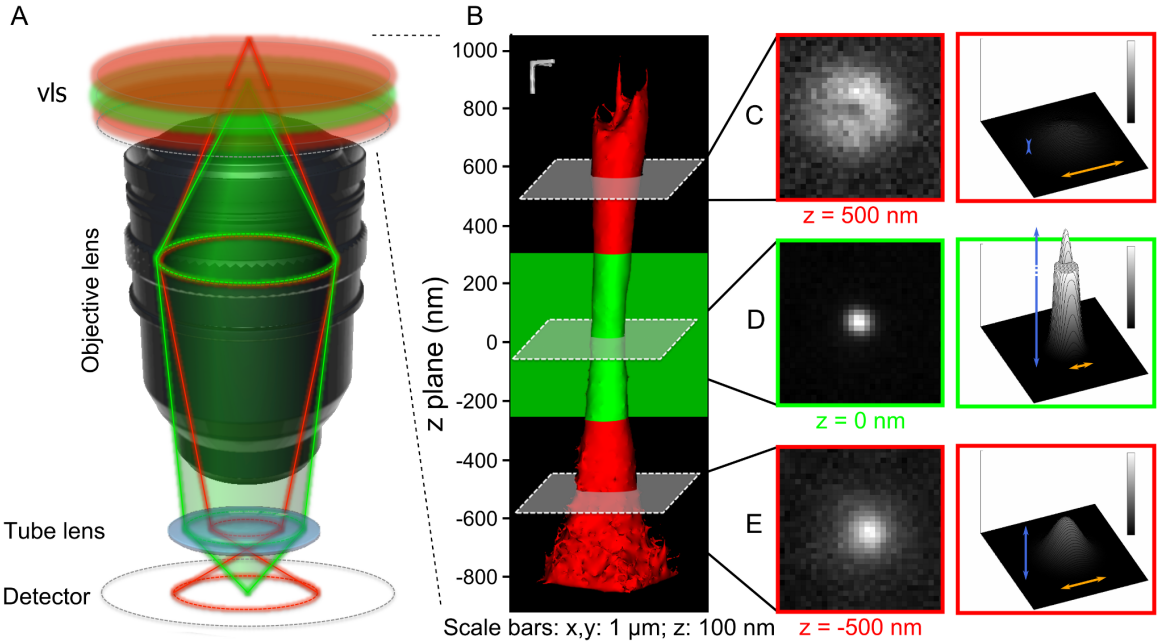


Figure 4.1 *The point-spread function of a SMLM instrument varies axially.* In geometrical optics, an in-focus point-emitter is conjugated with a point on the plane of the detector (**A, green rays**) whereas the light coming from an out-of-focus emitter focusses in front of or behind the same plane, distributing the same intensity on a larger surface (**A, red rays**); it is therefore imaged as a dimmer and larger spot. Imaging a z-scan of separated 40 nm diameter 505 nm emitting beads confirms this conclusion: the 3D intensity image of 28 beads were superposed and rendered (**B**, the contrast of each plane being adjusted) to obtain a finer model of the 3D-PSF. Close-ups of the section of the 3D-PSF are given for the focal plane ($z = 0$, **D**) and symmetric out-of-focus planes ($z = \pm 500$ nm, **C and E**). Left panels (**C-E**) present the contrast adjusted intensity image (1pixel $= 110$ nm); right panels show the intensity surface plot of the same $-$though non contrast-adjusted$-$ data.

*Legend:* (Average) width $\sigma = (\Theta_3 + \Theta_4)/2$ of the PSF as fitted in Equation 3.12; Integrated intensity $\Theta_5$; Amplitude $\Theta_5/(2\pi\,\Theta_3\,\Theta_4)$; Signal to noise ratio defined as the amplitude over the noise of the background $b$; Ellipticity defined as the ratio of $\max(\Theta_3, \Theta_4)/\min(\Theta_3, \Theta_4)$; Precision $\sigma_{th}$ defined as in Equation 3.13.

−, corresponding to a Gaussian standard deviation $\sigma = 255$ nm[2]); in the experiments described in this chapter, with a 1.49-$n_a$ oil-immersion objective, the variation of the integrated intensity of the 2D-PSF along the optical axis was fitted with a Gaussian function ($\sigma = 283$ nm; FWHM = 666 nm). However, the width of the vls is highly dependent on −and anti-correlated with− the numerical aperture (NA) of the objective lens used [178]: in Figure 4.6, a calibration $z$-scan of beads was imaged with a 1.2-$n_a$ water-immersion lens; the thickness of the vls was consequently adjusted to 2,000 nm.

### 4.2.2 Sub-diffraction beads under low illumination mimic idealised single fluorophores

To build the vls, a $z$-scan of single emitters is needed to calibrate the effect of width and amplitude thresholding on typical localisations located at different $z$ positions. A common way to measure the PSF of a microscope in fluorescence microscopy is to use sub-diffraction fluorescently-labelled beads as is done in deconvolution microscopy [179–182]. Conversely to isolated fluorophores, they are photostable for many excitation/emission cycles (the same multi-labelled beads can be sampled many times at different $z$ positions without photo-blinking and photo-bleaching), cheap and commercially available.

In order to validate this hypothesis, additional experiments were performed by purifying the photo-activable fluorescent protein mEos3.1 from *S. pombe*, which was immobilised on a glass coverslip and imaged in PBS. Similarly, single TMR* fluorophores were adsorbed on a coverslip and imaged. Since it is impossible to repeatedly image a single dye (under SMLM conditions) at many different axial positions, the protocol was adapted: a high density of fluorescent protein was immobilised on the coverslip but very low irradiance activation light was used in order to image only a few separated fluorophores per frame. Therefore, different fluorophores were imaged at each axial position of the stage. After fitting each detected 2D-PSF, the width *vs.* amplitude parameter plot was computed for the localisations detected in the vls (Figure 4.2 A, purified mEos3.1 in green, TMR* in orange). Separated sub-diffraction beads (40 nm in diameter) were also imaged under low illumination so that the beads were excited to yield a similar photon count as single fluorophores (between 500 and 1,500 photons detected per frame) [45]. The beads were imaged at different axial positions and, after PSF fitting, their localisations were plotted in the same width *vs.* amplitude parameter plot (navy blue). The distributions of localisations of the single fluorophores and of the bead in the parameter plot are indeed very similar, confirming the

[2] FWHM $= 2\sqrt{2\ln 2}\sigma = 2.35\sigma$

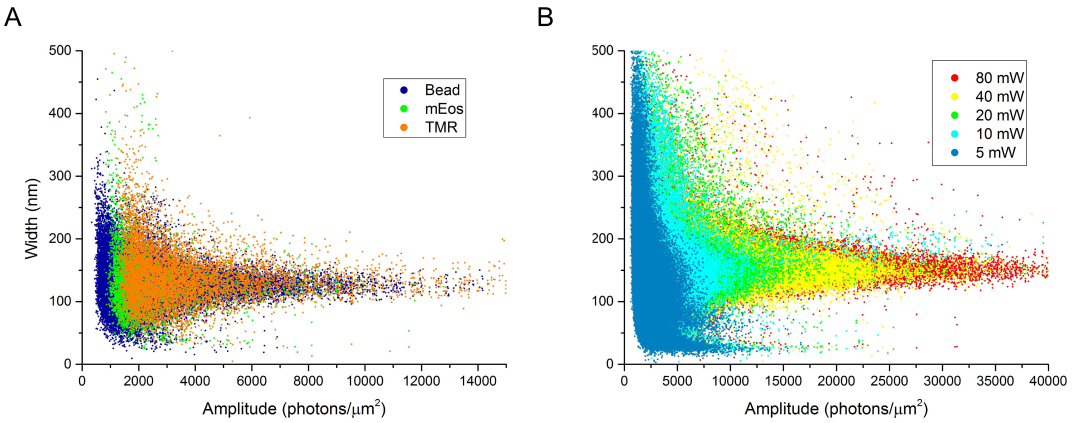


Figure 4.2 *Images of single sub-diffraction beads under adapted low illumination have similar widths to those of single fluorophores.* **A**: Single fluorophores (purified mEos3.1 in green, TMR* in orange) were immobilised on poly-lysine-coated coverslips and imaged under 561 nm illumination. Additional very low 405 nm irradiance was used to activate a few separated fluorophores in each frame. 40 nm-diameter 505 nm emitting beads (navy blue) were also immobilised on a similar coverslip and imaged under low 488 nm illumination to obtain similar signal-to-noise levels as for the single fluorophores. For each sample, ten frames were imaged every 10 nm axially. After fitting, each localisation was plotted in a width *vs.* amplitude parameter plot. **B**: Separated fixed Alexa-647-labelled Tau monomers were imaged in focus until they photo-bleached under different illumination powers. After fitting, each localisation was plotted in a similar parameter plot.

use of beads as idealised single fluorophores in such low illumination conditions.

A fitting artefact is observed in Figure 4.2 at small width values: a line of localisations of various amplitudes but of very similar width (∼30 nm) reveals the fitting of high frequency noise or 'hot' pixels (one pixel corresponds to 110 nm). This observation points out the permissive width threshold value used in Peak Fit to allow further informative post-processing during vlsSMLM (*cf.* 'Width Factor' in Table A.3).

The effect of illumination power was also investigated: another sample (separated and immobilised Alexa647-labelled Tau monomers) was imaged until total photo-bleaching under illumination powers varying from 5 to 80 mW (corresponding to 0.430 to 10.9 mW measured at the objective). For illuminations higher than 5 mW, the distribution of localisations in the width *vs.* amplitude plot was similar to the distribution previously obtained with beads (Figure 4.2, B). The distribution contracted on the amplitude axis when the illumination decreased, indicating that the illumination did not saturate the fluorophore. At the lowest illumination power (5 mW), the single fluorophores could only be qualitatively guessed after averaging multiple frames. Thus, this last imaging condition does not represent an illumination that can be used in an SMLM experiment.

Furthermore, a simple simulation confirms that the sub-diffraction bead can have a diameter of up to 100 nm without increasing the width of its PSF by more than 2.10 nm: in an

array of 512x512 pixels (1 pixel = 110 nm), disks of different diameters (1, 40 and 100 nm) of constant intensity −as a crude model of a fluorescent bead− were convolved with a 2D-Gaussian of width $\sigma_{\text{Gaussian}} = 71.36$ nm corresponding to the theoretical approximation of the in-focus PSF of a 505 nm emitting point-emitter (Equation 2.1). These simulations of the PSF of the beads were fitted with a Gaussian function and their widths and $R^2$ values stored in Table 4.1. Interestingly, the simulated width of the PSF of the largest nano-object (100 nm diameter) is only 2.10 nm wider than the theoretical width of the PSF of a point-emitter. This difference is negligible when compared with the experimental variation of the widths of the fitted PSFs (*e.g.* the in-focus ∼50 nm-thick band in Figure 4.2, A-B).

Table 4.1 *Effect of the diameter of sub-diffracted emitters on the width of their image.*

| **Disk diameter (nm)** | $\sigma_{\text{fitted}}$ **(nm)** | $R^2$ |
|---|---|---|
| 0 (theoretical point-emitter) | 71.36 | N/A |
| 1 | 71.40 | 1.0000 |
| 40 | 71.49 | 1.0000 |
| 100 | 72.46 | 1.0000 |

However, as described by Equation 2.1, the width of the PSF of an emitter depends on the wavelength of its emitted photons. Table 4.2 gives the expected width of the PSF of a point-emitter for three typical wavelengths. Although a 10 nm chromatic variation of the width of the PSF between 505 nm emitting beads and 580 nm emitting mEos proteins is predicted, Figure 4.2 reveals that this variation is experimentally not a limiting factor. The pixilation of the camera, chromatic imperfections of the lenses, background noise and the fitting algorithm are all factors that can introduce additional variation of the width of the PSF above the theoretical value given by Equation 2.1. However, whenever possible, the spectrum of the beads should be matched to the spectrum of the single emitters that they are mimicking.

Table 4.2 *Effect of the wavelength of sub-diffraction emitters on the width of their image.*

| **Wavelength $\lambda$ (nm)** | $\sigma_{\text{theoretical}}$ **(nm)** |
|---|---|
| 510 | 72.07 |
| 580 | 81.96 |
| 670 | 94.68 |

### 4.2.3 Building of the virtual-'light-sheet'

In order to calibrate and build the vls, separated idealised single fluorophores, *i.e.* sub-diffraction fluorescent beads, were immobilised on a poly-lysine coated coverslip and successively imaged at different axial positions. The axial and lateral variations of different fitted parameters that characterise the shape of the PSF were plotted in Figure 4.3. The three parameters which vary the most in the axial direction are the amplitude, the width and the theoretical precision of the localisations. The variations of these parameters at a given plane are much smaller than their axial variations. This validates the possibility of rejecting out-of-focus localisations via thresholding some specific parameters.

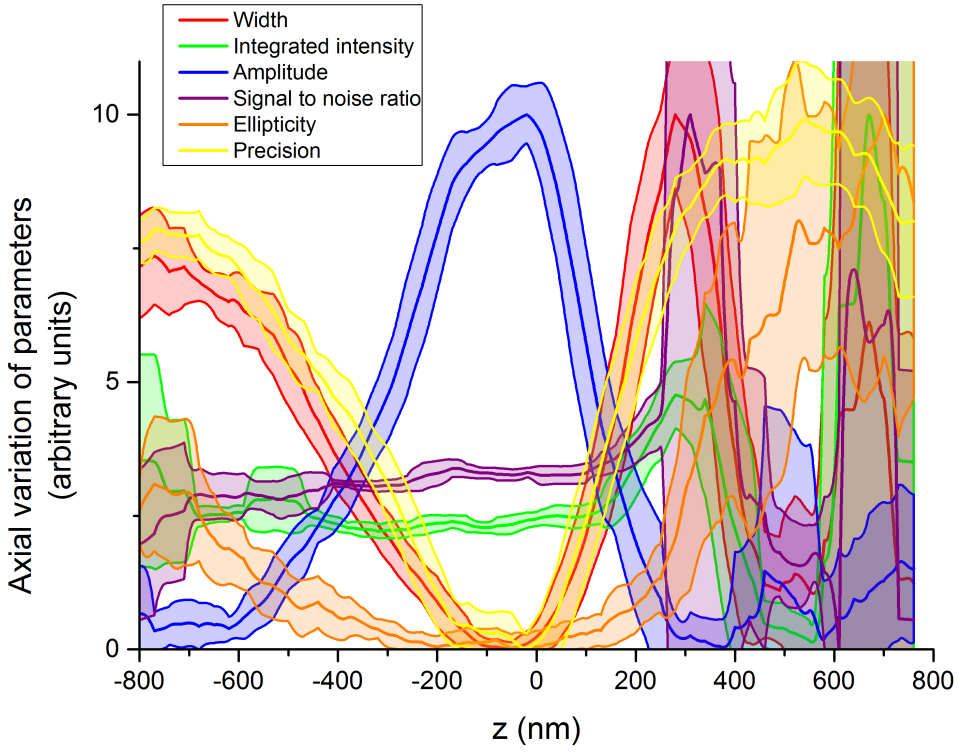


Figure 4.3 *Axial variations of the PSF.* Separated idealised single fluorophores were immobilised on a coverslip and imaged at different axial positions. After SMLM fitting, the axial variations of different fitted parameters (width, amplitude) or commonly-used metrics (integrated intensity, signal to noise ratio, ellipticity, precision) were compared. The variation of each parameter at a given axial plane $z$ is represented as a shaded region (mean $\pm$ standard deviation of the mean).

In principle, multi-parameter vlsSMLM thresholding is possible. However, the precision is not a parameter which is directly fitted, and is calculated using both amplitude and width parameters (Equation 3.13). The calculated precision is therefore mathematically correlated

to both width and amplitude, and cannot be independently thresholded. Thus, the width and amplitude are the best suited parameters for thresholding in vlsSMLM.

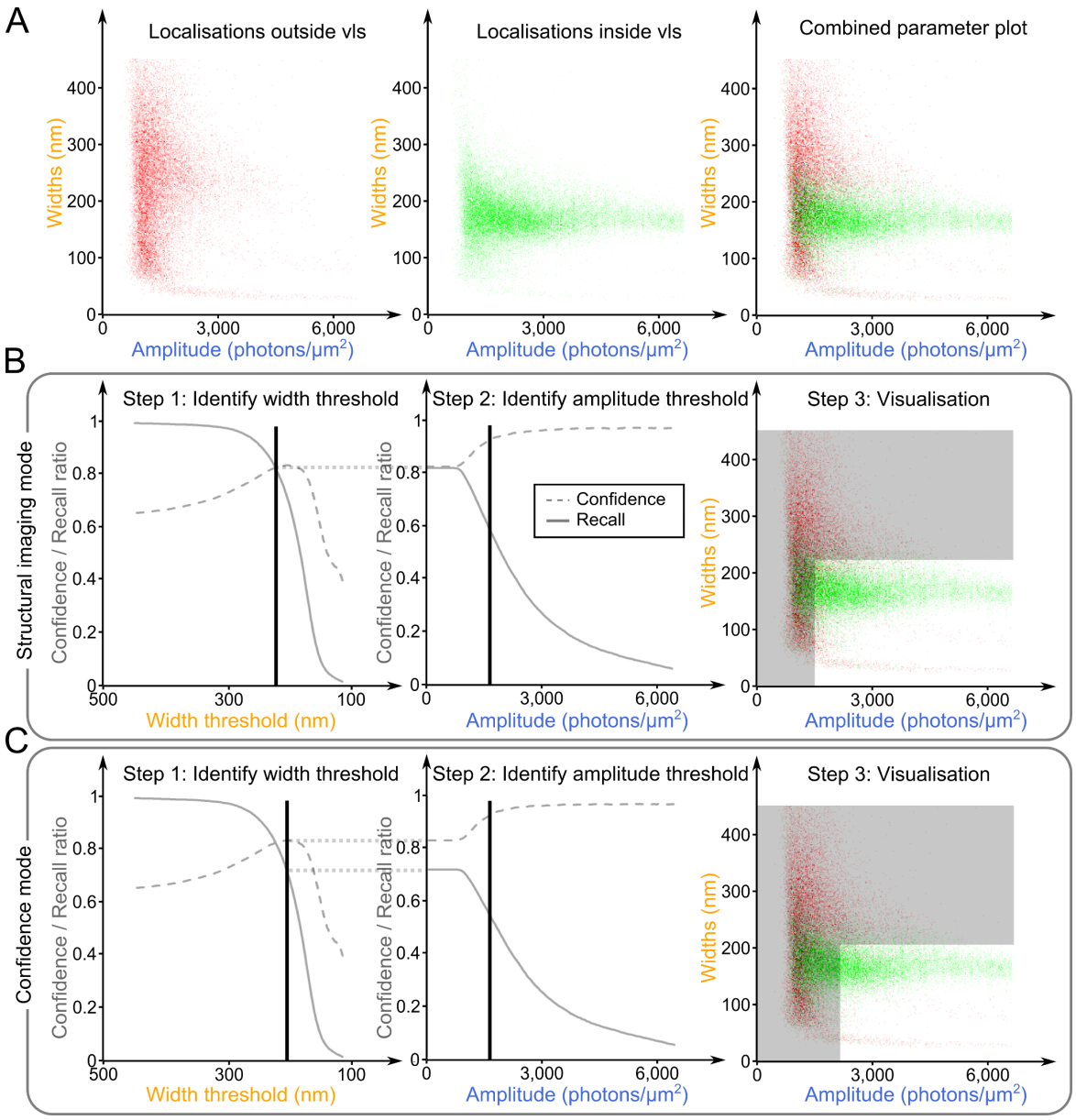


Figure 4.4 *Building the vls.* A calibration $z$-scan of separated and immobile idealised single fluorophores is imaged. After SMLM fitting, all localisations are plotted in a width *vs.* amplitude parameter plots (**A**), in red if they originate from a plane outside of the vls (left and right panels); in green otherwise (middle and right panels). vlsSMLM consists of successively applying an upper width and lower amplitude thresholds (**B-C**, respectively left and middle panels). The value of each threshold is chosen as a compromise between the confidence (**plain grey line**) and the recall (**dashed**) ratios. The effect of thresholding can be seen in the original parameter plot (**B-C**, right panels: localisations from greyed areas are rejected). **B and C** are two different sets of vlsSMLM thresholds for two different applications: structural imaging and confidence modes as defined and used in Section 4.2.5.

To visualise the axial variations of the width and amplitude, localisations were plotted in a width *vs.* amplitude parameter plot, in green when imaged in the defined vls (Section 4.2.1), otherwise in red (Figure 4.4, A). The vlsSMLM strategy can here be seen as selecting the region of the parameter plot that contains most green localisations and the fewest red ones. To quantitatively measure the effect of thresholding, confidence and recall ratios were defined as follow:

$$\begin{cases} \text{confidence} &= \dfrac{\text{TP}}{\text{TP} + \text{FP}} \\ \\ \text{recall} &= \dfrac{\text{TP}}{\text{TP} + \text{FN}} \end{cases} \tag{4.1}$$

where TP represents the true positives (green localisations kept after thresholding), FP, the false positives (red localisations kept after thresholding), and FN, the false negatives (green localisations that are thresholded out). The confidence ratio is the probability that a localisation that has been kept after thresholding actually comes from the vls. The recall ratio measures the fraction of emitters from the vls that are kept after thresholding.

First, the effect of applying a width threshold to the localisations was studied. A threshold eliminating all localisations whose widths were larger than a value varying from 500 to 100 nm was applied and the corresponding confidence and recall ratios were calculated (Figure 4.4, B-C, left panels). As the threshold increases, more and more localisations are rejected and the recall ratio drops (solid line). However, at thresholds $\geq$ 206 nm, most of the rejected localisations come from outside the vls; thus the confidence ratio increases until a maximum is reached (dashed line). In order to choose a width threshold, a compromise needs to be made between high confidence (to increase the contrast of the final rebuilt picture) and a high enough recall to correctly sample the structure of interest.

Once the first width threshold is defined, the confidence and recall ratios are calculated for different amplitude thresholds (Figure 4.4, B-C, middle panels). Again, the amplitude threshold is adjusted to obtain a high confidence ratio together with a high enough recall rate (depending on the sampling required for the considered applications). Since the beads were imaged under conditions at which their intensities were similar to the intensities of single fluorophores in SMLM experiments (Section 4.2.2), similar thresholds can be used for the analysis of SMLM experiments.

Finally, the result of the applied thresholds can be schematically observed in the parameter plot (Figure 4.4, B-C, right panels). The aim of vlsSMLM is to select a large fraction of green localisations with widths of $\sim$175 nm (for the 505 nm emitting beads), while rejecting

most of the red localisations.

### 4.2.4 Robustness of the calibration

The robustness of the calibration was then tested: (1) its sampling, both in the number of detected localisations per plane and in the number of axial planes to be imaged; (2) its robustness over different calibration samples and instruments; (3) finally, the effect of different fitting algorithms.

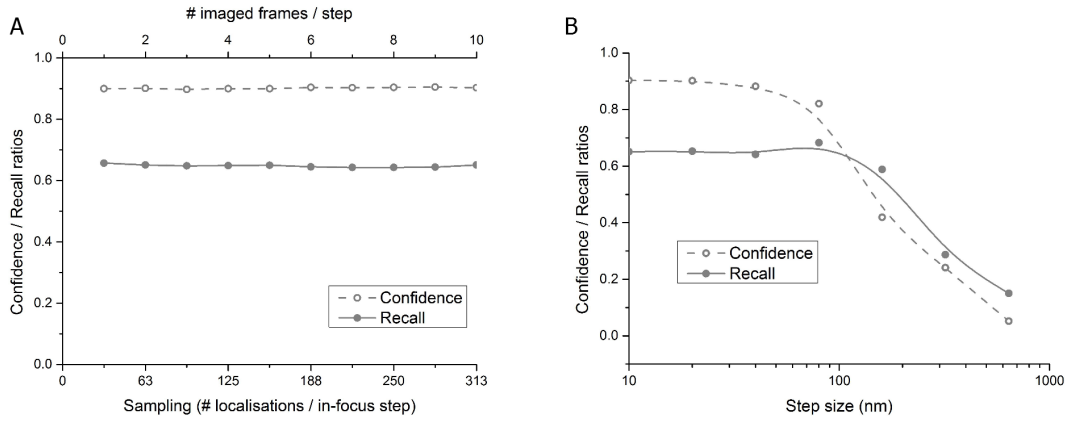


Figure 4.5 *Optimisation of the vls calibration sampling.* Ten frames of 32 fixed and separated idealised single fluorophores were recorded every 10 nm axially. **A**: Varying *in silico* the number of frames taken into account in the vlsSMLM analysis (top horizontal axis) was used as a metric to vary the sampling −the total number of imaged physical fiducial markers− of the calibration data (bottom horizontal axis). **B**: The effect of the variation of the axial sampling was studied by varying *in silico* the size of the $z$-steps used in the vlsSMLM analysis. The values of both confidence and recall ratios for the threshold values corresponding to the structural imaging mode (width threshold: 223 nm; amplitude threshold: 1,502 photons/$\mu m^2$) were monitored (**A-B**).

Since both confidence and recall ratios are statistical metrics, the effect of the number of detected localisations on their value was analysed. A calibration $z$-scan was imaged, recording ten frames of the same region for each axial positions. As 32 beads were imaged ten times in the field of view, an average of 31.5 beads were detected at the focal plane. Selecting only one to ten frames per axial positions *in silico* (from the ten recorded), the sampling of detected localisations was consequently varied and its effect on both ratios observed (Figure 4.5, A). As few as 32 beads (or one frame per axial step) were sufficient to characterise both confidence and recall ratios.

A similar analysis was used to assess the importance of axial sampling of the calibration. A calibration $z$-scan was imaged, stepping every 10 nm. Calibration $z$-scans stepping every 20, 40, 80, 160, 320 and 640 nm were computationally extracted from the $z$-scan and the

confidence and recall ratios calculated for each of them (Figure 4.5, B). As expected, and since the height of the vls is ∼600 nm ($\sigma = 283$ nm, Section 4.2.1), the size of the step of the $z$-scan has a strong impact on the calibration efficiency: the confidence rate (dashed line) dropped significantly as soon as the sampling involved $z$-steps of more than 40 nm. The recall rate (plain line) was flatter, but also dropped for $z$-steps of 80 nm or higher. It is therefore recommended to sample ∼35 beads at least every 40 nm along the optical axis; this can be achieved in multiple ways including piezo, mechanical or even manual positioning.

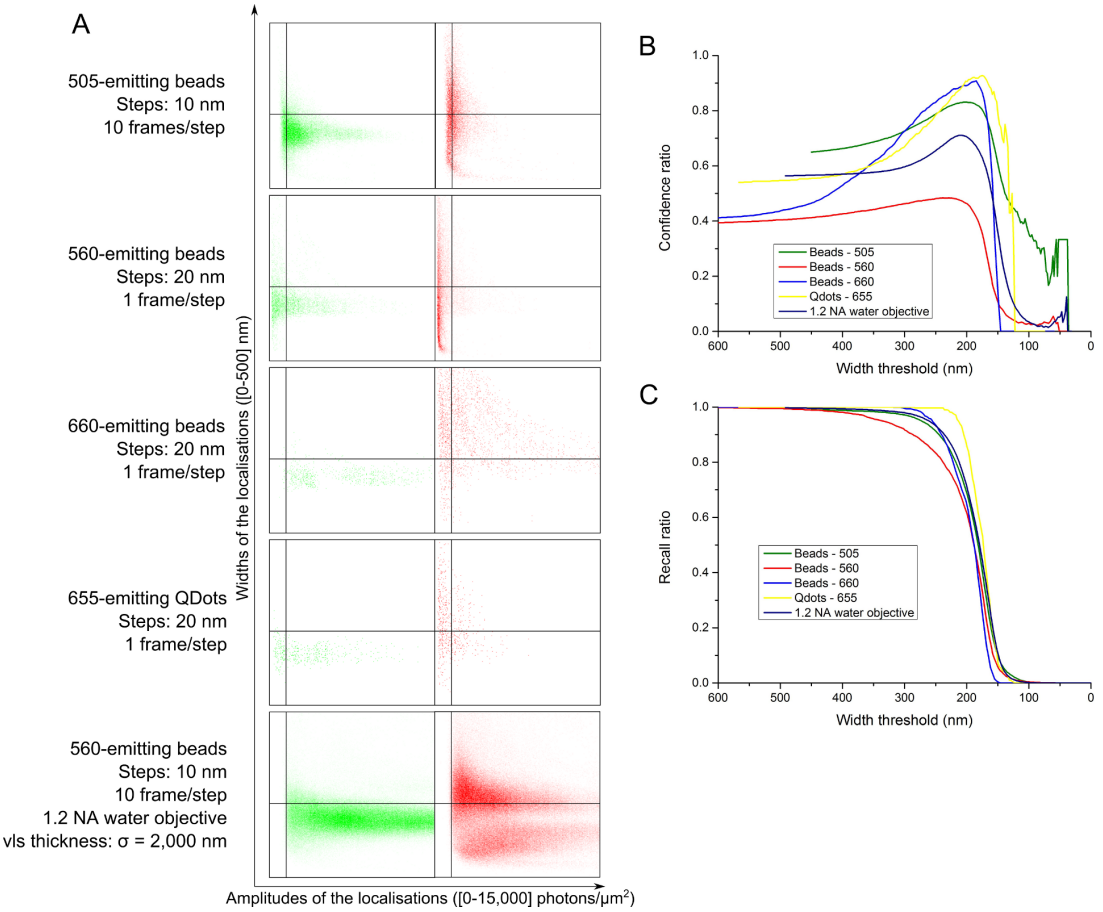


Figure 4.6 *Robustness of the vlsSMLM calibration to different samples and instruments.* Independent $z$-scans of different isolated fluorescent particles were imaged following various protocols on different SMLM nanoscopes to test the robustness of the vlsSMLM calibration. Analyses of five experiments were compared: their in-vls (green) and out-of-vls (red) parameter plots are drawn in **A**. The vlsSMLM thresholds corresponding to the structural imaging mode (223 nm, 1,502 photons/µm$^2$) are respectively plotted as black horizontal and vertical lines. The confidence (**B**) and recall (**C**) curves for width thresholding are also plotted and compared.

To test the robustness of the vls calibration to different SMLM instruments and different protocols, Dr U. Endesfelder and T.J. Etheridge immobilised diffraction-limited fluorescent fiducial markers (*i.e.* fluorescent photo-stable particles of diameter smaller than the width

of the PSF of the microscope at the same wavelength) on a coverslip and record a $z$-scan on their own SMLM instruments. Calibration using beads emitting at different wavelengths, or quantum dots, with different frame and $z$-step samplings, on different TIRF instruments, were analysed (Figure 4.6, A-C). Since all microscopes tested had a 1.4-$n_a$ oil-immersion objective lens, a calibration $z$-scan was also performed with a radically different 1.2-$n_a$ water-immersion lens, leading to the definition of a 'thicker' vls ($\sigma = 2,000$ nm instead of 283 nm − see Section 4.2.1). The parameter plots (Figure 4.6, A) look relatively similar, although they vary in density; the localisations located in the vls are remarkably denser below the 223 nm width threshold (black horizontal line). The variations of the confidence (Figure 4.6, B) and recall (Figure 4.6, C) ratios for width thresholding qualitatively follow a similar shape. They however peak (Figure 4.6, B) and drop (Figure 4.6, C) at slightly different threshold values depending on both the wavelength of the fluorescent particles and on the specific instrument (Section 4.2.2). A calibration on the same microscope used for the SMLM experiment of interest, with fiducial markers whose spectrum is matched with the spectrum of the fluorophores used in the SMLM experiment is therefore recommended. Interestingly, the confidence ratio for 560 nm emitting beads is globally lower. This is due to some diffusing beads in solution which are out of the vls but are considered in it during the calibration. Finally, the noticeable shift of the ratio curves for quantum dots may be linked to the very small sampling in terms of the number of fiducial markers (only one frame was imaged every 20 nm and the field of view only allowed the imaging of 8 quantum dots).

As vlsSMLM is a post-processing method, the effect of different fitting algorithms has to be assessed. Five commonly-used algorithms (Peak Fit [149], QuickPALM [183], rapidSTORM [156], ThunderSTORM [184] and M2LE [185]) were used to fit the same calibration data. The resulting list of localisations was then analysed with the vlsSMLM plugin described here. Their difference is reflected in the parameter plots shown in panel A of Figure 4.7. However, localisations of fluorophores within the vls (green) are mostly found just below the 223 nm width threshold (black horizontal line). The confidence (Figure 4.7, B) and recall (Figure 4.7, C) curves for the width threshold follow a similar shape. They however peak (Figure 4.7, B) and drop (Figure 4.7, C) at different values, underlining the importance of processing the calibration $z$-scan in the same way as the SMLM data, using the same fitting routine with the same parameters. Outlier behaviour is noticeable for QuickPALM. This could be explained by the imprecise fitting of localisation widths by QuickPALM.

Each fitting algorithms uses slightly various 2D-Gaussian PSF models defined by different numbers of parameters. To increase the speed of the analysis, rapidSTORM only fits

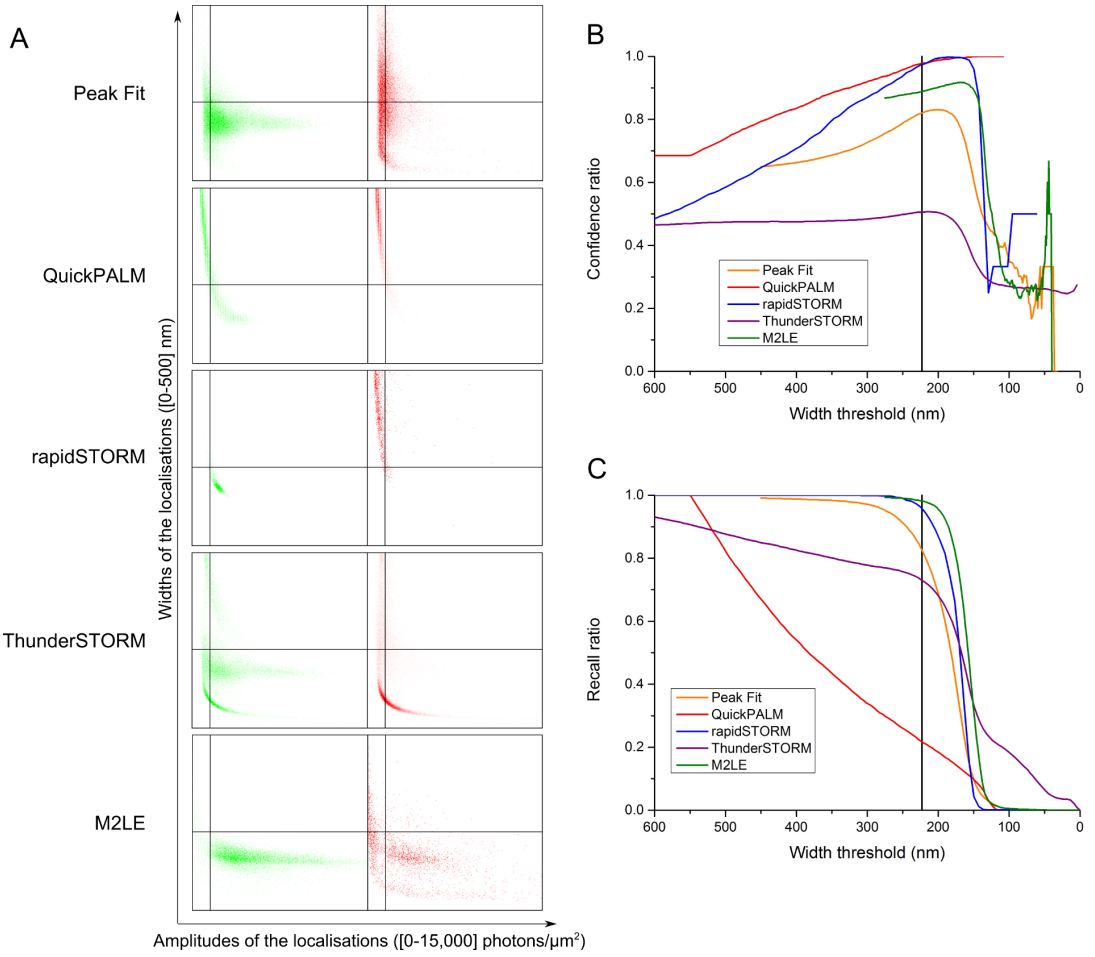


Figure 4.7 *Effect of various fitting algorithms on vlsSMLM calibration.* Five 2D-Gaussian fitting plugins were used to analyse a single calibration $z$-scan. The list of localisations obtained were fed to the vlsSMLM plugin and the outputs compared: in-vls (green) and out-of-vls (red) parameter plots are drawn (**A**). The vlsSMLM thresholds of the structural imaging mode (223 nm, 1,502 photons/µm$^2$) are shown as black horizontal and vertical lines. The confidence (**B**) and recall (**C**) curves for width thresholding are also plotted and compared.

as few parameters as possible, inferring *a fortiori* many characteristics of the PSFs from these few fitted values thanks to a constrained model of the PSF [156]. This is visible in Figure 4.7, where localisations fitted with rapidSTORM, but not with Peak Fit or ThunderSTORM, are observed on a thin 1D-curve in the width *vs.* amplitude parameter plots. Although rapidSTORM performs remarkably well in the calibration of the vlsSMLM, it may be less robust to variations of the PSF shape *in vivo* due to deformations of the wavefront in deep samples or sub-frame diffusion of the single fluorophores.

Moreover, Figure 4.7 also underlines the pertinence of vlsSMLM: the limit of vlsSMLM would be observed if no localisation appeared in the out-of-vls parameter plot (A, right panels). Conversely, vlsSMLM could be used as a way to determine optimal thresholds used as fitting checks in fitting algorithms. And even so, vlsSMLM would still give the possibility to slightly adjust the thickness of the vls for different applications and quantitatively select thresholds for specific needs (Section 4.2.5).

### 4.2.5 Improvement in contrast and quantification using vlsSMLM

Two different sets of thresholds −or vlsSMLM imaging modes− for two different potential applications in vlsSMLM are described in this section. The first −'structural imaging mode'− (Figure 4.4, B) allows controlled enhancement of contrast, while retaining as many of the fitted localisations as possible, in order to maintain the sampling resolution in structures of interest. The width threshold for this mode was defined as the intersection of the confidence and recall curves (223 nm). An amplitude threshold that gave a confidence ratio of 90% for the structural imaging mode was then selected (1,502 photons/$\mu m^2$). The second imaging mode −'confidence mode'− (Figure 4.4, C), favours the confidence ratio over the recall, to ensure that the retained localisations are inside the vls volume. The width threshold was thus defined as the width for which the confidence ratio is maximal (206 nm). The amplitude threshold was then fixed to obtain a confidence ratio of 95% (2,164 photons/$\mu m^2$).

To illustrate the two imaging modes, two different biological structures were imaged. vlsPALM analysis was subsequently performed both to increase contrast and to look at the distribution of 3D clusters. These examples were chosen to exemplify the types of problem addressable by the different imaging modes. In both examples (the yeast vacuoles, or the nucleus of a mammalian stem cell), the cellular structures of interest were located more than 100 nm above the coverslip, *i.e.* outside of the field that can be measured using TIRF illumination. To image such structures, in the absence of light-sheet capability, HILO illumination [105] has to be used. Such broad illumination excites a large proportion of out-

of-focus fluorophores which contributes to an increased fluorescent background. vlsPALM thresholds were applied to reject these out-of-focus fluorophores.

### Structural imaging mode

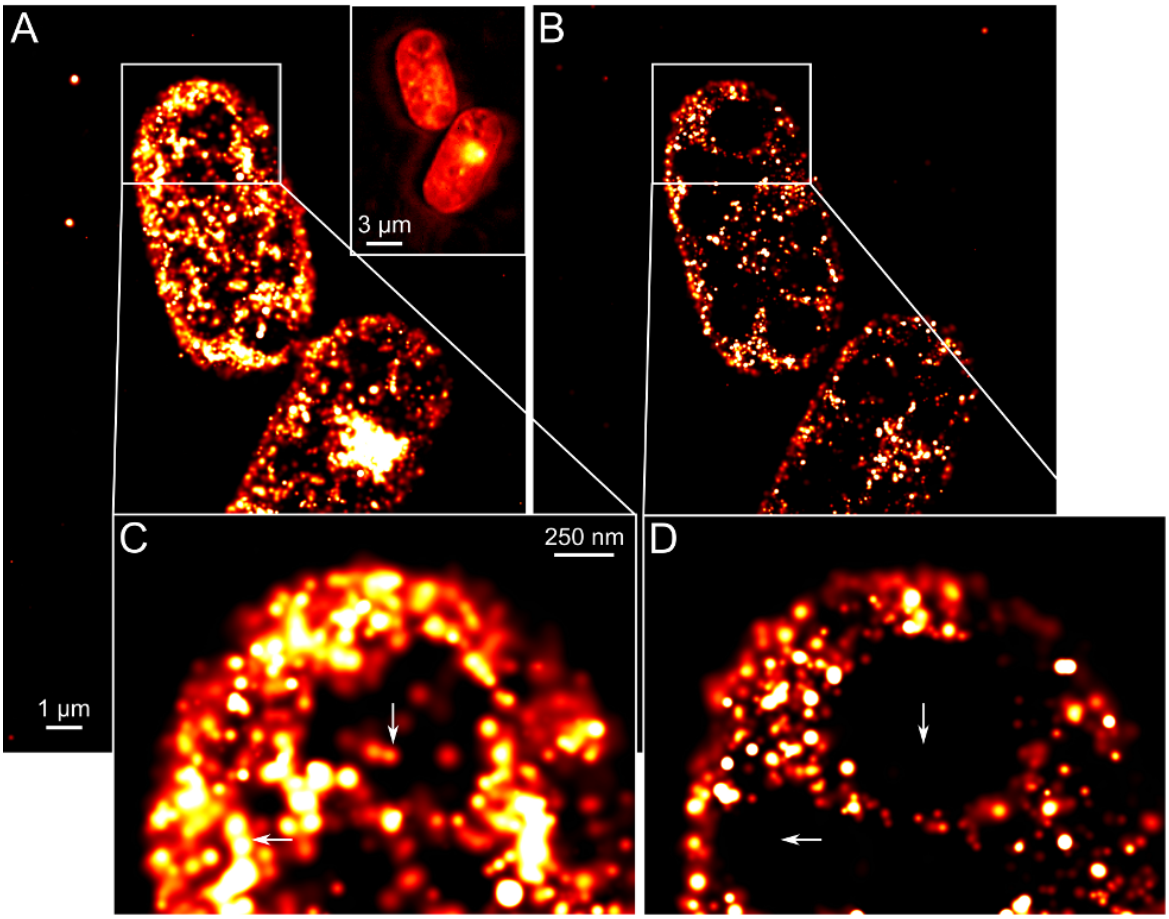


Figure 4.8 *Structural imaging mode.* Fixed *S. pombe* cells expressing cytoplasmic Cdc22-mEos proteins were imaged using PALM. 5,000 frames were analysed with Peak Fit and the resulting list of localisations was used to produce a super-resolved picture directly after fitting (**A**), or after applying the vlsPALM thresholds defined in Figure 4.4, B (**B**). The corresponding diffraction-limited image of the two cells is shown as an **inset in A**. Close-ups of the white rectangles in A-B are shown in **C-D**. The contrast of the large intracellular vesicles of the yeast is increased after vlsPALM filtering (white arrows in C-D).

Fixed fission yeast cells expressing the cytosolic protein Cdc22 fused to mEos2 at its C-terminus were imaged to demonstrate the increase in contrast that the structural imaging mode allows and reveal a cellular organelle. The fission yeast *Schizosaccharomyces pombe* (*S. pombe*) is a powerful and highly tractable eukaryotic model organism, often used to study the cellular responses to DNA damage and the process of DNA replication. In response to nitrogen starvation or to osmotic stress, large vacuoles appear in *S. pombe* cells in order to

restore the concentration of the cytosol [186]. Imaging Cdc22, a protein which is highly expressed and evenly distributed in the cytoplasm of the yeast, allowed visualisation of, in contrast, this organelle.

Applying the vlsPALM thresholds in structural imaging mode, an increase in contrast is observed in the super-resolved image (Figure 4.8, B and D): some vacuoles only appear after thresholding because out-of-focus localisations from below or above the vacuoles are detected and plotted in the non-thresholded picture (Figure 4.8, A and C).

### Confidence mode

Fixed mouse embryonic stem cells stably expressing mEos3.2-tagged centromere protein A (Cenp-A) that form distinctive clusters were imaged to show how quantification of super-resolved clusters benefits from the confidence mode of the vlsPALM analysis. Cenp-A is a histone H3-like protein that is present in nucleosomes at the centromeres in eukaryotic cells. Cenp-A forms foci at a number of defined points in a nucleus and determining the structure of such foci or their stoichiometry is of interest in the yeast genetics field [130].

However, out-of-focus fluorophores have larger and dimmer PSFs (Figure 4.1), making them more difficult to detect and fit over the background. Thus, only clusters which are

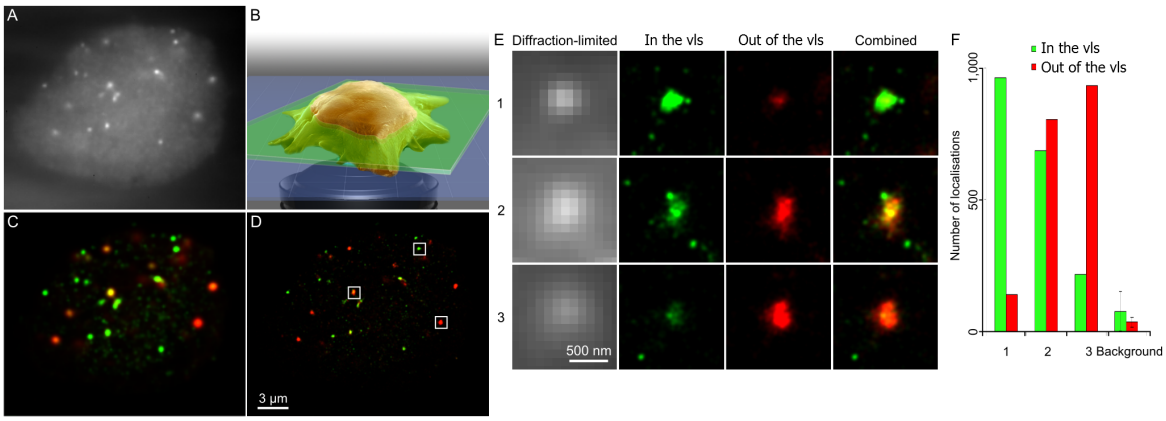


Figure 4.9 *Confidence mode.* Embryonic stem cells expressing Cenp-A-mEos proteins were fixed and imaged. The corresponding movie (summed in **A**) was analysed with Peak Fit and the resulting list of localisations was separated between in-vls (green) and out-of-vls (red) localisations using the vlsPALM thresholds defined in Figure 4.4, C. vlsPALM allows the identification of the in-focus localisations (**B**). All localisations were plotted either as fitted (**C**) or in a super-resolved picture (**D**), but coloured according to the vlsPALM filtering. Three categories of Cenp-A clusters were observed: some were almost entirely within the vls (**D-F, 1**); others were spanning one extremity of the vls, partly in the vls (**D-F, 2**); the last ones were entirely out of the vls (**D-F, 3**). **E**: Diffraction-limited and super-resolved close-ups of the Cenp-A clusters defined in D. **F**: Number of localisations inside (green) and outside (red) of the vls for each cluster. Such classification allows selecting in-focus clusters for further quantification and preventing under-counting due to undetectable out-of-focus emitters.

within the focal plane have all their fluorophores correctly detected, while those outside the focal plane have some of their fluorophores undetected. Using vlsPALM (Figure 4.9, A-D) selects only in-focus clusters (Figure 4.9, E) in order to analyse them for further quantification (Figure 4.9, F), preventing initial under-counting.

## 4.3 Discussion

This chapter presents a simple, cost-effective, powerful method for selecting in-focus fluorophores to increase the contrast in super-resolved images that can be used in conjunction with any 2D super-resolution microscope and any super-resolution PSF-fitting algorithm. This method however is incompatible with basic centroid-finder algorithms that do not give precise information about width and amplitude of the localisations. By virtue of the fact that each PSF is imaged, one by one, a thin, in-focus slice from a super-resolved image can be tuned and selected, and in doing so a virtual-'light-sheet' can be created.

In the experiments described here, using fluorescent proteins (mEos2 and mEos3.2) which emit at $\sim$580 nm, and thresholds of 220 nm for width (standard deviation of the Gaussian fit) and 1,500 photons/$\mu m^2$ for amplitude (Figure 4.4), the contrast of super-resolved images was significantly increased, allowing the observation of cellular organelles (Figure 4.8) and the detection of in-focus protein clusters (Figure 4.9).

### 4.3.1 A quantitative optical sectioning method for existing 2D SMLM nanoscopes

In SMLM, most analysis softwares fit the detected PSFs with a 2D-Gaussian (rapidSTORM, Peak Fit, QuickPALM, M2LE, ThunderSTORM, *etc.*). For most applications, from all the fitted parameters (up to seven parameters) only two −the $(x, y)$ position of the localisation− are used. The width and amplitude of localisations are also often used to estimate the localisation precision. Although the other fitted parameters (*i.e.* the 3D shape of the PSF) contain specific information about the axial position of the fluorophore, they are usually disregarded or only heuristically used as fitting checks in algorithms. The post-analysis method described in this chapter consists of quantitatively applying a threshold on the fitted width and amplitude of all localisations. The width threshold can be thought of as a virtual wide-field pinhole, rejecting any fluorophore located outside the focal plane. Globally, such thresholding amounts to limiting imaging to a sheet of light −the vls− around the focal plane of the microscope.

Similarly to most 3D SMLM techniques (*e.g.* astigmatism [87], DH-PSF [88]) that optically modify the 3D-PSF of the microscope to extract additional information about the axial position of the emitters, one can extract additional −though less precise− axial information from the original 3D-PSF of the instrument. vlsSMLM does not compete with 3D-SMLM techniques, as they have much better axial resolution and are non symmetric across the focal plane, but allows more information to be extracted from existing data. Such analysis enhances the contrast of super-resolved pictures and provides additional quantified optical sectioning around the focal plane.

Interestingly, Figure 4.7 shows why and how vlsSMLM is pertinent: existing fitting softwares would be optimal and vlsSMLM would be useless if no localisation appeared in the out-of-vls parameter plot (A, right panels). Conversely, vlsSMLM could be used as a way to determine optimal width or amplitude thresholds used as fitting checks in fitting algorithms. Even so, vlsSMLM enables fine adjustement of the thickness of the vls for different applications and quantitative selection of thresholds for specific needs (Section 4.2.5).

As in light-sheet illumination, vlsSMLM imaging allows an increase in contrast in the final super-resolved image, although any illumination geometry can be used (TIRF, HILO or epifluorescence). Moreover, the width of the focal volume, or vls, can be tuned by changing the thresholds applied. However, although a main advantage of light-sheet illumination is the minimisation of photo-bleaching of the fluorophores and photo-damage of the sample as only the imaged plane is illuminated, vlsSMLM imaging does not reduce photo-bleaching or photo-damage as it is a post-process analysis. It is therefore not suitable for experiments requiring multiple successive axial slicing to observe multiple planes in a sample.

### 4.3.2 vlsSMLM only requires a simple calibration step

This method only requires a simple $z$-scan calibration of fluorescent beads, normally achieved via a controlled $z$ piezo-driven stage. The calibration is used to build up a 'parameter-plot' (Figure 4.4) that is specific for each individual imaging system or microscope, and then to define thresholds with known confidence and recall rates that can then be applied to the SMLM data. The calibration does not require extensive sampling: as few as 31 fiducial markers and steps of up to 40 nm do not quantitatively affect the results (Figure 4.5).

Also virtually any fixed and separated sub-diffraction fluorescent point source (*e.g.* beads, gold particles or quantum dots) can be used for the calibration. Interestingly, Mutch *et al.* [187] found that "a log-normal distribution [of intensities] such as is observed for the single fluorophores [Alexa Fluor 488] is also observed even when larger numbers of fluo-

rophores are present in a [region of interest]. Indeed, [they] found the measured intensity distributions of 100 nm fluorescent beads (which contain hundreds of fluorophores per bead) to also follow a log-normal distribution." In other words, the authors find that the intensity distribution of single dyes has the same shape as the intensity distribution of beads. Therefore, if the illumination is such that the average intensities collected for both single dyes and beads are equal, the intensity distributions will be identical. This is further confirmed by comparing the parameter plots of diffraction-limited fluorescent beads imaged under low illumination and immobilised single fluorophores (Figure 4.2).

The calibration proved to be robust to very different imaging protocols on the various different instruments tested so far (Figure 4.6). However, the actual values of the vlsSMLM thresholds depend on both the wavelength of the fluorophores and on the specific optics used. Thus, a calibration should be measured on the instrument that is used for the SMLM experiment with beads whose spectrum is matched to the wavelength of the fluorophore used in the SMLM experiment.

### 4.3.3 On thresholding

To even better threshold in-focus from out-of-focus localisations in the parameter plot and maximise the confidence ratio, complex polygons can be drawn in the parameter plot, as is commonly used in flow cytometry analysis. Other parameters could also be added to an $n$-dimensional parameter plot, increasing the precision, robustness and sophistication of the vlsSMLM analysis. However, in the interest of simplicity and universality of the implemented ImageJ plugin, a successive single-parameter thresholding approach is described in this chapter.

Localisations were thresholded first according to their width, then according to their amplitude. Indeed, the amplitude of a PSF does not depend only on whether the fluorophore is in the vls, but also on many different parameters such as its $(x,y)$ position in the inhomogeneous illumination field, which fluorescent state it occupies, or the orientation of its dipole [98]. The width of a localisation, on the contrary, depends only on its axial position, and its diffusion during the exposure time of the frame [163, 188]. Therefore, the width parameter is less convolved with phenomena other than the axial position of the emitter and consequently allows better discrimination between emitters that are inside and outside the vls. Furthermore, the distribution of intensities from single fluorophores follows a log-normal distribution [187]. The long tail of such a distribution means that the intensity of a fluorophore, whether or not it originates from the focal plane, varies a lot. Thus, in a given

$z$ plane, the amplitude of a population of fluorophores will follow the same distribution (as the amplitude of a Gaussian is directly proportional to its intensity, at constant width). A bright fluorophore out of the vls has a similar amplitude as a dimmer fluorophore in the vls. Thus it is not optimal to use intensity (or amplitude) as the only or primary threshold.

### 4.3.4 vlsSMLM, a user-friendly ImageJ plugin

vlsSMLM was implemented as a freely available ImageJ [150] plug-in, which acts as a post-processing layer that can use any 2D-Gaussian fitting results (Figure 4.7) and is thus independent of fitting algorithms. The actual values of the vlsSMLM thresholds are nevertheless dependent on the fitting algorithm used for fitting both calibration and SMLM data. The calibration step should thus be analysed with the specific fitting routine used to fit the SMLM data.

The vlsSMLM plug-in is attached as a supplementary software to this thesis (Software B.4). It offers two functions: the first uses a calibration $z$-scan to calculate (and display) parameter plots with the corresponding confidence and recall rates specific to the instrument used, as shown in Figure 4.4, B-C. The second function takes the list of fits from a SMLM experiment and interactively displays a super-resolved image with user-defined thresholds. It also outputs the list of thresholded fits for further analysis or reconstruction (see the documentation attached to the Software B.4 for more details). The vlsSMLM plug-in has been designed to be an easy-to-use tool and is available both as a stand-alone ImageJ plug-in or directly integrated into the Peak Fit plug-in [149], a quick efficient SMLM fitting algorithm, making the vlsSMLM plug-in able to analyse any SMLM stack without any other pre-processing PSF-fitting step.

# PART B

# Chapter 5

# Introduction to the molecular basis of T cell activation

This chapter provides the biological context for the work presented in the next two chapters (Chapters 6 and 7) by outlining the organisation of the vertebrate immune system, the key role of T cells in adaptive immunity, and the molecular processes underpinning T cell activation.

## 5.1 A brief introduction to the vertebrate immune system

Since the development of life, a multitude of living species have evolved and share common ecological niches which are characterised by competition for resources and inter-dependent interactions between species. At the ends of the inter-species interaction spectrum, strategies of symbiosis[1] and immune defence are found.

The term immune system encompasses of all active and passive processes that a species has developed to protect itself from invasion of parasites and infection with pathogens. These mechanisms include the passive skin barrier in mammals or selected apoptosis in plants. Since the immune system is inherently destructive, the main challenge it faces consists in distinguishing self from non-self. Although immune systems take various creative approaches in the living kingdom, a complex and powerful immune system, composed of two highly intertwined and complementary branches, evolved in jawed vertebrates to protect themselves against and quickly adapt their defence to ever-mutating pathogens.

[1] For example, the endo-symbiotic theory postulates that organelles such as chloroplast or mitochondria originate from the uptake and integration of former free-living bacteria inside another cell.

The vertebrate immune system is formally divided in two components or legs, characterised by distinct specificity, delay and strength of their response to an infection and the memory of the infection:

**Innate immunity.** The first leg of the vertebrate immune system is the innate immune system, responsible for the detection and routine elimination of pathogens. If a pathogen overcomes the passive barriers such as the skin or mucosa, its intrusion is first detected in a non-specific way by the innate immune system: some cells, such as macrophages or dendritic cells, express pattern recognition receptors that recognise regular patterns of molecular structures common to a whole class of micro-organisms but absent from the body's own cells, the so-called pathogen-associated molecular patterns. Examples of such receptors are the mannose and glucan receptors and the scavenger receptor that bind cell-wall carbohydrates of bacteria, yeast and fungi, respectively. The family of Toll-like receptors provides recognition of cell-wall components of both Gram-positive and Gram-negative bacteria. When these receptors are triggered, macrophages release cytokines and chemokines that trigger a local inflammatory response, signalling a zone of infection to the whole immune system.

The inflammatory response induces a great number of processes (*e.g.* vasodilatation of the nearby blood vessels, migration, differentiation and activation of effector immuno-competent cells, blood clotting and wound healing) aiming at both containing the invasion of the pathogen, preventing its spreading to the whole body through the blood and lymph circulation systems, and clearing the infection. This initial innate response is characterised by its un-specificity to the pathogen, its immediacy, and its binary activation irrespectively of the history of previous infections.

**Adaptive immunity.** The inflammatory response also triggers another type of processes forming the adaptive immune system. Contrarily to the innate immune response, the adaptive response is characterised by its specificity to the pathogen, its delayed effects ($\sim$ 4-day post infection), its strength compared to the initial response of the innate immune system and its memory upon re-infection of a pathogen.

Because pathogens reproduce and evolve at a higher rate than the human species, invasion strategies overcoming the innate immune response have appeared over time. The innate immune system can thus be overwhelmed and evaded. This is where adaptive immunity plays its essential role of strong and targeted clearing of the pathogen. After detection and phagocytosis of the pathogen, professional antigen-presenting cells (APC) of the innate immune system present short peptides from the lysis of

the pathogen in the groove of the major histocompatibility complex (MHC) class II, a membrane protein which expression at their plasma membrane is increased during an inflammatory response. This then triggers the clonal expansion and differentiation of a specific subset of cells from a theoretically infinite repertoire. This specific activation is explained in detail in the case of the T cell in Section 5.2. These mature T and B lymphocytes orchestrate the delayed but strong immune answer leading to the successful clearing of the specific pathogen.

Once the pathogen has been cleared from the organism, a long-term memory of the infection enables a fast and effective answer of the adaptive immune system upon re-infection by the same pathogen. The 4 day delay is reduced as the specific lymphocytes only require limited maturation and their greater initial population exponentially increases the speed of their new clonal expansion.

Adaptive and innate immunities, although traditionally distinguished and opposed, are the two complementary and inter-dependent legs of the same system; they have co-evolved and their differences are sometimes debated (*e.g.* recently, the possibility of memory associated to natural killer cells, cytotoxic lymphoid-like cells of the innate immune system, was postulated [189]). Innate immunity plays an essential role in detecting the initial infection and presenting the pathogen for specific selection and maturation of the lymphocytes initiating the adaptive immune response. It is also responsible for routine clearance of pathogens that do not require an energy-expensive and complex adaptive response, and for containing the infection until an effective adaptive response is orchestrated.

In addition to being energy-expensive, a major drawback of the adaptive immune system resides in its accidental dramatic dysfunction: by mis-distinguishing self from non-self, a false-negative detection may miss a life-threatening infection, while a false-positive detection may lead to the development of an allergy or an auto-immune disease. Stringent safe-guards and negative feedback loops have evolved to decrease the error rate and stabilise the fine balance of sensitivity of adaptive immunity.

## 5.2 The T cell, a key player of the adaptive immune system

The adaptive immune system is organised around two types of lymphoid cells, the B and the T cells, named after the organ they grow in (the bone marrow and the thymus, resp.) [190]. Both types of lymphocytes express a large repertoire of immunoglobin-like antigen-recognition receptors: although the repertoire, based on stochastic gene rearrangement,

junctional recombination and somatic hypermutations, is theoretically infinite, each cell only expresses a single and unique receptor, which specifically recognises a unique epitope. The antigen-recognition receptor of the B cell is the Y-shaped B cell receptor, and, upon B cell activation and differentiation into plasma cell, large amounts are secreted in its soluble form referred to as monoclonal antibody (mAb).

The antigen-recognition receptor of the T cell is the T cell receptor (TCR, *cf.* following section). After careful selection to avoid any recognition of self peptides, each naive T cell expresses a single and unique type of TCR that recognises a specific combination of non-self peptide presented in the groove of a specific MHC protein. The type of the MHC protein recognised by a T cell determines its sub-type, characterised by the specific expression of a co-receptor: $CD4^+$ T cells recognise non-self peptides bound to MHC class II molecules (which are only expressed on professional APC); $CD8^+$ T cells, those bound to MHC class I molecules (which are expressed on the membrane of virtually all cells in the body, constitutively presenting peptides which represent the diversity of the proteins degraded by their proteasomes).

Like B cells, $CD8^+$ T cells are the effector cells of the adaptive immune system: while plasma cells (activated B cells) are the mAb factories, enabling neutralisation and opsonisation of, and complement activation against, the extracellular pathogen or toxin they target, activated $CD8^+$ T cells (also called cytotoxic T cells) specifically recognise and kill cells (by inducing programmed cell death, *i.e.* apoptosis) that have been infected with the targeted pathogen (*e.g.* intracellular bacteria or virus).

$CD4^+$ T cells, however, have little direct effector function but orchestrate the whole adaptive immune response. Several specialised subsets, defined by the cytokines they release and induced by different cytokine signals, have been described: $T_H1$ activate macrophages; $T_H1$ and $T_H2$, also called helper T cells, activate the maturation of B cells targeted against the same pathogen into plasma cells; $T_H17$ recruit neutrophils to sites of infection early in the adaptive immune response; lastly, $T_{reg}$ suppresses the activation and development of naive T cells. Finally, $CD4^+$ T cells stimulate the activation of $CD8^+$ T cell targeting the same pathogen.

Because of their essential role, both as cytotoxic effector cells and as coordinator integrating and organising the communication between the various cells of both innate and adaptive immune systems, T cell development, selection and activation have been studied since the 1960s. Understanding the fine mechanisms of T cell specific but sensitive activation and regulation is a major interest to design immuno-therapeutic strategies against auto-immune diseases or cancers.

## 5.3 The complex T cell receptor

### Stoichiometry

Although the stoichiometry of the TCR complex is still an object of controversy (*cf.* Chapter 6), it is known to be composed of several subunits: ligand recognition is achieved by the highly variable ectodomain of the hetero-dimer TCR$\alpha\beta$ (or, in less understood and rarer cases, TCR$\gamma\delta$) whose intracellular domain is almost inexistent; signalling is conducted by invariant transmembrane proteins collectively called CD3 and organised in two hetero-dimers CD3$\varepsilon\delta$ and CD3$\gamma\varepsilon$ and one homo-dimer CD3$\zeta\zeta$. Without CD3, TCR$\alpha\beta$ does not form a complete cell-surface receptor and is degraded before reaching the cell membrane. The cytoplasmic tail of each CD3 chain displays one (CD3$\delta$, $\varepsilon$ and $\gamma$) or three (CD3$\zeta$) immuno-receptor tyrosine-based activation motif (ITAM) domains that can be phosphorylated and which initiates downstream signalling of the receptor.

### Positive and negative selections

Each T cell expresses many copies of a unique combination of recombined genes coding for the TCR$\alpha\beta$ subunit. This genetic recombination mechanism enables the recognition of theoretically any epitope by a T cell, given an infinite number of T cell clones. This is why the adaptive immune system has the potential to adapt and initiate a specific immune answer to any newly mutated pathogen. Nevertheless, because the adaptive immune system should not turn against cells of its own body, a mechanism must exist that enables T cells to identify self from non-self.

Sequentially, genes coding for TCR$\alpha$ and TCR$\beta$ chains, are recombined until a pre-TCR (validating an in-frame recombination of the gene coding for TCR$\alpha$), then a full TCR (*idem* for TCR$\beta$) is expressed on the plasma membrane of the $CD4^-CD8^-$ T cell precursor. A successful TCR expression at the membrane induces the expression of both CD4 and CD8 co-receptors. At this stage, double-positive $CD4^+CD8^+$ T cells undergo two selections based on the affinity of their TCRs to self-peptides presented on MHC molecules by APCs present in the thymus:

1. A positive selection induces apoptosis of T cells expressing TCRs that fail to bind to any peptide-MHC (pMHC) molecule. This selection is also responsible for the differentiation of the T cells into the $CD4^+$ and the $CD8^+$ subsets (*cf.* previous section): basically, a T cell expressing TCRs recognising peptides presented by MHC class I

molecule will decrease its CD4 expression and become a cytotoxic $CD8^+$ T cell; conversely, if it recognises peptides presented by MHC class II, its CD8 expression will decrease and the T cell will become a $CD4^+$ T cell.

2. Independently, a negative selection insures that T cells whose TCRs bind to self-peptide:MHC ligands with high affinity are killed in the thymus.

Together, these positive and negative selection mechanisms enable the generation of a mature T cell repertoire that is both restricted to the recognition of peptides presented by self MHC molecules and tolerant to self peptides. Interestingly, this double selection allows for TCR degeneracy that nuances the specificity of the TCR for a unique non-self pMHC: each TCR can interact with, and is thus specific to, a set of different ligands [191]. TCR degeneracy enlarges the total repertoire of pMHC antigens that can be targeted by a limited number of T cells, although it may enable cross-reactivity of the T cell.

## Sensitivity and specificity

The unmatched sensitivity and specificity of the TCR remains a puzzling challenge to the research community [192]. The TCR discriminates a very weak signal in the presence of considerable noise: (1) each TCR recognises and distinguishes both low-affinity (>500μM) self-pMHC ligand for naive T cell survival and homeostasis, and high-affinity (though still only in the 1-10 μM range) non-self pMHC ligands for T cell activation. (2) Even more strikingly, the degree of activation of a T cell depends on the affinity of its TCR to the non-self pMHC ligands that it is activated with. Different results suggest that (3) T cells can recognise and respond to very few (if not a single) non-self pMHC complexes [193–196] and that a single TCR micro-cluster can activate a T cell [196]. (5) Finally, these 1-10 non-self pMHC molecules are recognised in presence of considerable noise: each APC presents $10^5$-$10^6$ self pMHC complexes on its plasma membrane, most of them being irrelevant to any T cell.

Altogether, these characteristics underline the extraordinary sensitivity and specificity of the TCR for its ligand. It explains the major attention given to the TCR since the 1960s as both a key signal receptor in adaptive immunity and a remarkable object of study in the field of ligand-receptor interaction. Indeed, in most systems, a trade-off exists between sensitivity and specificity, which the TCR somehow resolves, suggesting that TCR triggering is the fruit of the evolution of a complex mechanism that integrates signals at various levels, from the molecular level of the receptor, to the level of the T cell, and to the level of the whole population of responding cells [197].

## 5.4 T cell activation at the immunological synapse

The activation of the TCR is thus a key determining step in immune responses, deciding on a single-cell scale whether to initiate a response that has strong repercussion on the scale of organs or even the whole individual. This decision begins at the contact between two cells: either between a professional APC and a naive T cell in the lymph node deciding on clonal selection and initiation of the adaptive immune response, or between an infected cell and an activated cytotoxic $CD8^+$ T cell deciding on inducing selective apoptosis of the former cell.

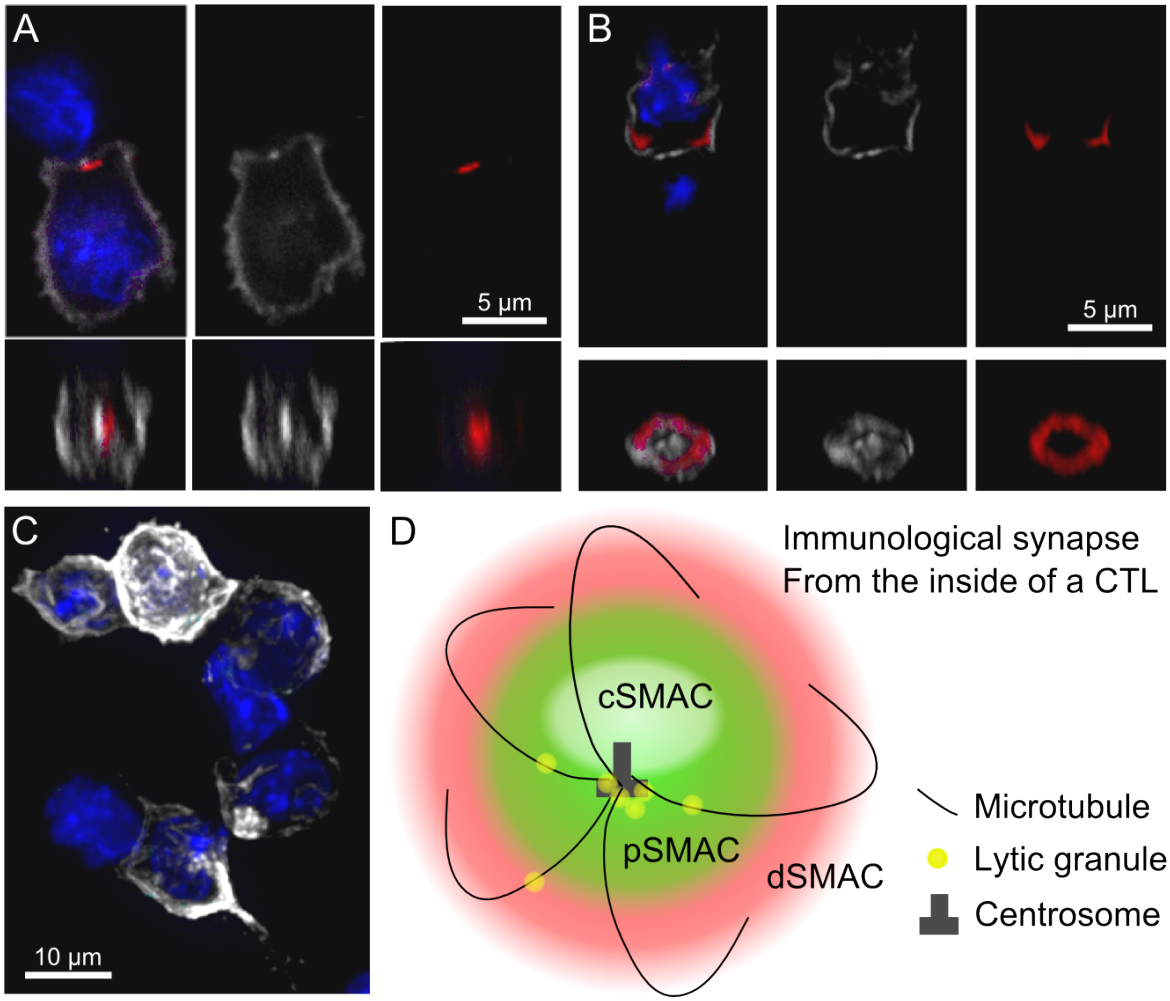


Figure 5.1 *The immunological synapse.* Conjugates of primary $CD8^+$ T cells from a transgenic OT-1 mouse were loaded with their pMHC ligands (ovalbumin peptides) to act as APCs for each others. Conjugates were fixed in solution and immuno-stained with markers of the pSMAC (Lck in red, **A**) or of the dSMAC (actin in red, **B**). **C**: Examples of T cells forming large oriented contacts characteristics of the formation of immunological synapses. **D**: Scheme of the 'bull-eyed' organisation of the immunological synapse at the plasma membrane of a cytotoxic T cell (*cf.* Section 5.4).
Legend: Nuclei in blue; CD8 in white to label the plasma membrane. Upper panels show $(xy)$ sections and lower panels show $(xz)$ (en face) reconstruction. Scale bars: 5 µm in A-B, 10 µm in C.

The importance of cell-cell contact reveals the essential role played by membrane receptors, and especially the TCR, in this process. Several consecutive steps are involved that finely tune and modulate T cell activation, starting with the formation of an adhesive contact between the APC and the T cell and ending with changes in the transcription patterns of the naive T cell inducing its differentiation in an effector T cell, or with the secretion of cytotoxic granules to the infected cell by the activated cytotoxic T cell.

**Initial integrin-mediated cell-cell adhesion.** Cell-cell contact is initiated by binding of integrins and adhesion proteins such as the intracellular adhesion molecule 1 (ICAM-1, or CD54) and CD58 (or lymphocyte function-associated antigen 3 − LFA-3) on the APC, to LFA-1 and CD2 (or LFA-2) on the T cell. Interestingly, LFA-1 expression is increased during T cell activation, leading to stronger and more frequent cell-cell contacts with APCs. Similarly, maturation of the professional APC promotes T cell adhesion by constraining ICAM-1 mobility [198]. It is suggested that initial adhesion contact primarily involves long integrins (*i.e.* ICAM-1:LFA-1), allowing stochastic engagement of the smaller CD58:CD2 interaction in a tighter contact [199]. These closer contacts, of the size of the TCR:pMHC interaction, would enable the nucleation of a zone where the TCRs could probe the membrane of the APC and which could further develop into the formation of a stable cluster [200].

**Extracellular ligand recognition.** Once a tight contact is formed between the APC and the T cell, various receptors can start interacting with their ligands. The integration of two signals is required for a T cell to trigger: (1) signal 1, responsible for the specificity of the activation to the antigen, is achieved when a pMHC is simultaneously recognised by both a TCR and a CD4 or CD8 co-receptor. Signal 1 induces activation of the T cell and guarantees the recognition of a non-self peptide presented by a self-MHC molecule. (2) However, to avoid entry into an anergic state, the T cell needs a second signal, signal 2, that promotes cell survival. Signal 2 is mostly achieved by interaction of the CD28 co-receptor with its CD80 or CD86 ligands, expressed on the membrane of professional APCs during an inflammatory response (*cf.* Chapter 7). This second signal guarantees that T cells only activate during an infection, and prevents the killing of professional APCs by activated cytotoxic T cells.

**TCR triggering: transduction of the signal across the plasma membrane.** Both signal 1 and 2 are detected by transmembrane receptors on the extracellular side of the plasma membrane. How the signal is transduced inside the T cell is still unclear [190, 201, 202]. Several models for this very step, referred to as TCR triggering, have been

proposed and are discussed in the following section. TCR triggering leads the phosphorylation of the ten CD3 ITAMs of the TCR by Lck and Fyn, two protein tyrosine kinases of the Src family.

**Formation of the immunological synapse.** Topologically, after TCR triggering, microclusters of TCRs form [203] and concentrate towards the contact region between the two cells, in a centripotent motion conducted by filamentous actin (F-actin) dragging [204, 205]. A dramatic reorganisation and polarisation of the T cell then follows, resulting in the formation of a dynamic but stable bull-eyed structure in the "small space between the two interacting cells": the so-called immunological synapse [206]. Monks *et al.* described three co-axial structures (or supramolecular activation complexes − SMAC) forming the immunological synapse in 1998 [207]: in the centre resides the central SMAC (cSMAC), where the TCR micro-clusters merge. It is also enriched in short adhesion molecules such as CD2, co-receptors CD4, CD8 and CD28 and signalling kinases such as Lck, protein kinase C-$\theta$ (PKC-$\theta$) and ZAP-70 ($\zeta$-chain-associated protein 70).

The cSMAC is surrounded by a ring of integrins, larger cell-adhesion molecules (*e.g.* LFA-1 and ICAM-1), proteins with a large ectodomain such as the non-specific phosphatase CD45, and the cytoskeletal protein talin. This region is called the peripheral SMAC (pSMAC). Finally, as actin clears from the cSMAC, a larger ring of actin forms the distal SMAC (dSMAC), which is thought to bring the necessary force for the final docking of the centrosome (or microtubule organising centre) to the plasmic membrane. Indeed, a mature immunological synapse is also characterised by the migration of the centrosome of the cell towards the cSMAC in a process reminiscent of cilia and flagella formation [206, 208]. In the case of cytotoxic T cells, the secretory lysosomes are brought towards the minus end of microtubules located at the centrosome, and secrete their contents at the immunological synapse next to the cSMAC. At the cSMAC, cortical actin is actually not entirely cleared but rather remodelled so that lytic granules might migrate through actin pores [209, 210]. This polarisation of the T cell is essential for the focal secretion of toxic granzymes and perforin and thus for the specific killing of the recognised target cell.

The immunological synapse may provide several functions such as stabilising the contact, orientating granule secretion in the case of cytotoxic T cells, ending the T-cell activation and recycling of receptors.

**Activation of intracellular signalling cascades.** The first signalling steps induced by TCR

triggering are the phosphorylation of the ten ITAMs of the CD3 chains of the TCR by Lck and Fyn kinases. Lck exists under various activated forms and its pre-activation and the mechanism by which it phosphorylates the TCR have recently been challenged [211, 212]. However, phosphorylation of the ITAMs trigger the recruitment of ZAP-70 kinase to the plasma membrane, which is a common marker for TCR triggering. In turn, ZAP-70 phosphorylates the scaffold proteins LAT (linker of activated T cells), which indirectly leads to the clivage of $PIP_2$ (phosphatidylinositol biphosphate).

Then, three signalling cascades are triggered [190, 192]: (1) $Ca^{2+}$ ions from the endoplasmic reticulum are released, increasing the intracellular concentration of $Ca^{2+}$ which finally activates the transcription factor NFAT (nuclear factor of activated T cells). (2) The activation of PKC-$\theta$ induces the activation of the transcription factor NF$\kappa$B. (3) The activation of the small G-protein Ras triggers the MAP (mitogen-associated protein) cascade, which is involved in the regulation of the transcription factor AP-1. Integration of these three transcription factors stimulate the expression of interleukin 2 (IL-2) which promotes survival and division of the lymphocyte and regulate the global immune response.

Other signals are integrated and modulate the signalling cascades. Activation of the co-receptor CD28 promotes cell survival, stimulates the metabolism of the cell but also directly enhances TCR signalling by recruiting Lck to the TCR or by activating the MAP cascade. On the top of signal 1 and 2, a third signal, signal 3, is provided by cytokines secreted by other immuno-competent cells. Signal 3 modulates the activity of the T cell and orientates the differentiation of naive $CD4^+$ T cell in specific $T_H$ or $T_{reg}$ subsets enabling an efficient and specific targeting of the immune response to the pathogen (*e.g.* humoral or cell-mediated immunity).

## 5.5 Three molecular models for TCR triggering

In signalling pathways, membrane receptors play an important role as signal initiators, transducing the signal (*i.e.* the information about ligand binding) across the plasma membrane. In the specific case of TCR triggering, three types of mechanism have been proposed to explain signal transduction, namely, the aggregation, conformational change and kinetic-segregation models. Evidence exists for all three mechanisms during TCR triggering (reviewed in ref. [202]) and each mechanism might play a role in TCR triggering. It is unclear,

however, whether any on its own is sufficient to induce triggering [190, 201, 202]. These models attempt to fill the gap between TCR binding to its pMHC ligand, and T cell activation (as revealed by the formation of TCR micro-clusters or the triggering of the downstream signalling cascades). All three models are introduced and discussed in the following paragraphs.

## Aggregation

Like the B cell receptor, the TCR is a tyrosine kinase-associated receptor. Most receptors of this type are activated by passive cross-linking: upon binding of a multivalent ligand (or clustered ligands), two or more receptors cluster. This aggregation locally increases the concentration of their cytoplasmic tails in the cytoplasm. Close-by tails can cross-phosphorylate their tyrosines, either directly, if they have an intrinsic kinase activity (*e.g.* the stem cell factor receptor Kit [213]), or indirectly, by recruiting a tyrosine kinase (*e.g.* the B cell receptor [190, 214]), and become activated.

Artificial aggregation of TCRs using either soluble antibodies or soluble multimeric forms of pMHC is also sufficient to initiate TCR triggering [215, 216]. However, pMHC are usually very rare on the target cell surface and TCR triggering can be observed in the presence of very few pMHC ligands. It is therefore thought that extra CD4 or CD8 co-receptors can bind either to (1) the same non-self pMHC (co-receptor hetero-dimerisation model [217]) or to (2) another self-pMHC ligand (pseudo-dimer model [218]). Either way, aggregation of TCRs would be induced via binding to CD4 or CD8. Nevertheless, TCR triggering can occur in cells completely devoid of co-receptors indicating that this mechanism is not sufficient to explain TCR triggering [219]. Furthermore, Jiang *et al.* recently provided evidence that the CD8 co-receptor is only recruited to the TCR after initial TCR triggering [220, 221].

It is clear, however, that TCR triggering leads to aggregation of TCRs into microclusters of 10 to 100 TCRs [222, 223]. But whether it is a direct consequence of TCR binding to pMHC or a further process downstream of TCR triggering is still unknown [203, 224].

## Conformational change

The conformational change model is a powerful model to describe some ligand-receptor interactions. It can be compared to a key-lock system: when a receptor (the lock) binds to its ligand (the key), the interaction stabilises a different conformation of the receptor (the key ‘opens’ the lock) that presents a catalytic locus, hidden in the close conformation of the

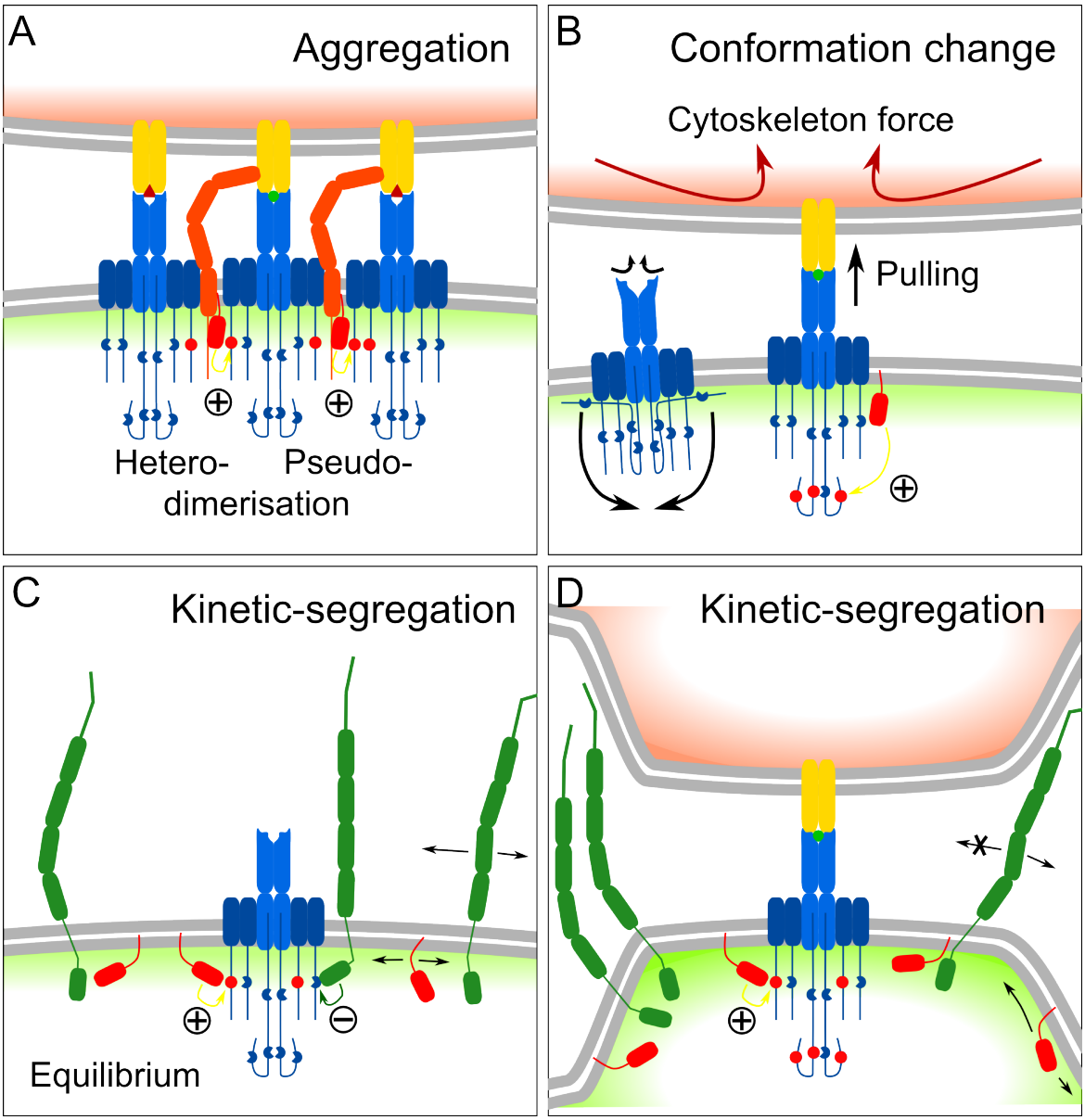


Figure 5.2 *Four molecular models for TCR triggering have been proposed.* **A**: The aggregation model postulates that TCR complexes aggregate upon the engagement of a TCR with its ligand (through the co-receptor-dependent formation of hetero- or pseudo-dimers). **B**: The conformation change model postulates a deep conformational change of the whole TCR complex upon binding, releasing CD3 ITAMs that were buried in the plasma membrane. It is proposed that binding under force may dramatically enhance and stabilise a activated conformation of the complex. **C-D**: The kinetic-segregation model postulates that at equilibrium, the TCR is constantly phosphorylated and dephosphorylated by freely diffusing Lck and CD45 proteins in the plasma membrane. When a contact forms with an APC, phosphatases with large ecto-domains such as CD45, but not the small Lck, are segregated from the contact-zone. If a TCR is held in the contact-zone long enough (upon binding with its ligand), its net phosphorylation increases and the TCR is triggered.
**Legend:** T cell in green; APC in red; MCH complex in yellow, bound to either an antigen peptide (green circle) or a self peptide (dark red triangle); TCR in blue (TCR$\alpha\beta$ in light blue, CD3 in dark blue); ITAMs as dark blue open circles, orange full circles when phosphorylated; CD4/CD8 co-receptor in orange; Lck in red in the membrane of the T cell (phosphorylation of the ITAMs is shown by a yellow arrow and a '+' symbol); CD45 in dark green (dephosphorylation of the ITAMs is shown by a green arrow and a '$-$' symbol).

unbound receptor. This is the principle behind the molecular mechanism of protein motors (*e.g.* the kinesins or the ATP synthase) and the triggering mechanism of the family of the G protein-coupled receptors [225].

Concerning TCR triggering, little evidence for a conformational change has been found so far: although the crystallographic structure of the intact TCR-CD3 complex has not yet been solved, the structure of the TCR in its bound and unbound state suggests a possible subtle conformational change in the membrane-proximal loop of the TCR$\alpha$ constant domain [226]. Adding to this argument, mutation of residues in this loop abrogates TCR triggering, which is suggested to hinder TCR dimerisation [227]. However, the classical static conformational change model seems to poorly describe the mechanism behind TCR triggering: the failure of several crystallographic studies in revealing global large-scale conformational changes between a bound and unbound structure speaks against it [228].

With this unsuccessful model as an argument, Ma *et al.* introduced a dynamic conformational model, the receptor deformation model, where binding under forces, instead of a gain in stability, provides the energy for a deep conformational change of the receptor [229]. Since CD3$\gamma\varepsilon$ hetero-dimer is relatively rigid [230], a conformational change in the TCR ectodomain could be transduced to the CD3$\gamma\varepsilon$ ectodomain and induce mechanical piston-like forces. Those forces could free the CD3$\varepsilon$ cytoplasmic ITAMs which might otherwise be buried in the lipid bilayer of the plasma membrane. Thus, new ITAMs would be exposed to phosphorylation and the TCR would become activated [231].

Such a dynamic model is all the more attractive as it takes into account the mechanical forces at play between two contacting cells *in vivo* where adhesion molecules and dynamic cytoskeleton proteins induce fast filapodia and lamellipodia movements [200, 204, 205]. Furthermore, massive cytoskeleton re-arrangement is observed during the immunological synapse formation that could provide the force required [206, 209]. Finally, this model would give a convincing explanation for the observed fine specificity of the TCR for its non-self ligand as binding under force (or catch bonds) can dramatically increase the stability of an interaction [232, 233]. Variations of this dynamic model involving pulling, shearing or pushing forces are reviewed in length in ref. [202]. Nevertheless, although attractive, this model is entirely putative and is supported by no experimental data so far [229].

## Kinetic-segregation

A recent model, first described seventeen years ago and based on the passive spatial re-organisation of the receptor, was introduced to challenge the aggregation model of TCR

triggering: "Provocatively, we have argued that receptor cross-linking is not sufficient by itself to activate the TCR, but rather that it is phosphatase exclusion mediated by cell–cell contact that is critical." [199]

Because of its two main requirements, this model was called the kinetic-segregation (KS) model [199, 234]. It postulates that, when two cells contact each other, adhesion molecules form a close-contact zone from which membrane proteins with large extracellular domains are physically excluded. This leads to the formation of a local micro-environment depleted of such proteins (*e.g.* unspecific phosphatases). Nevertheless, this micro-environment should be small enough to prevent the activation of an unbound freely diffusing receptor. But when bound to an external ligand on the contacting cell, the receptor will stay, in average, longer in this micro-environment, leading to its activation (*e.g.* through phosphorylation). Hence, it is the kinetics of these contact zones and the chemistry which occurs within them that transfers the signal across the membrane through the receptors.

Different lines of evidence reviewed in [234] suggest that segregation of the TCR is likely to have an important role in TCR triggering: (1) molecules with large ectodomains, such as the inhibitory tyrosine phosphatases CD45 and CD148, are excluded from areas of TCR triggering [235]. (2) Modifications of the intercellular distance at the putative close-contact zone strikingly inhibits TCR triggering: the truncation of CD45 or CD148 ectodomains [235, 236]; the elongation of the pMHC complex [237, 238]; the use of soluble *vs.* surface-associated pMHC ligand [239]; or the use of engineered TCRs with ectodomain differing in nature and size [240, 241] obstruct T cell activation.

Moreover, recent data indicate that in resting T cells, Lck is mainly present in an active form [211]. This is consistent (although debated in [212]) with the concept of a constant equilibrium between unspecific inhibitory phosphatases and kinases such as Lck. The close-contact zones would then locally shift the equilibrium towards phosphorylation and eventually activation if a TCR stayed long enough in this micro-environment deprived of the large CD45 and CD148 phosphatases.

Furthermore, Contento *et al.* reveal a new TCR-independent LFA-1-dependent pathway that polarises T cells and shape them for later antigen recognition [242]. They propose that the first adhesive contacts between T cells and APCs prepare and arrange the TCR signalling micro-environment. This would complete the KS model in which the first step involves adhesion contacts, that could also signal on their own, to prepare for further steps such as TCR triggering or the later immunological synapse formation.

Finally, the KS model has recently regained interest and some of its key prediction have been successfully tested: ligand-specific T cell-like activation was reconstituted in a non-

immune cell and requirement for segregation of CD45 and Lck was demonstrated in this artificial system [243]; ligand-independent TCR triggering was observed in T cell forming artificially large contacts with various adhesive surfaces from which CD45 was segregated (Chang, Fernandes, Ganzinger, Lee *et al.*, submitted).

# Chapter 6

# Counting T cell receptors

> "In conclusion, three decades after the finding that $\alpha\beta$ and CD3 subunits form a single complex, we have to admit that the stoichiometry of the TCR still remains to be resolved." [224]

The original idea developed in this chapter was a collaboration between Prof. S.J. Davis, Prof. D. Klenerman, Prof. A. Carr and Dr S.F. Lee. All T cell lines were transfected, and antibodies were labelled and provided by E. Huang and Dr R.A. Fernandes. All yeast cell lines were designed, transfected, grown and provided by H. Armes and Dr A.T. Watson. All imaging experiments were done by M. Palayret, with the help of H. Armes when yeasts were imaged. All data analysis, and code writing was undertaken by M. Palayret. Dr A. Herbert brought important insights and critical discussion about carefully analysing the data. Dr S.F. Lee and M. Palayret designed and built the super-resolution instrument used in this chapter.

## Aim of the experiments described in this chapter

The organisation of the TCR on the membrane of the resting T cell still needs to be determined. In this chapter, it was therefore tested whether a robust and quantitative single-molecule counting tool could be developed to this aim if carefully designed controls were used to calibrate the measurements. As SMLM techniques appeared in 2006, single-molecule counting was an important topic of discussion and development in the SMLM field when this project started in 2010. Several research groups published counting methods during the course of the project and these are discussed at the relevant points in the chapter.

## 6.1 Introduction

### 6.1.1 Organisation of the TCR on a resting T cell

The TCR is composed of several subunits: a heterodimer composed of TCR$\alpha$ and TCR$\beta$ chains (or TCR$\gamma$ and TCR$\delta$, depending on the specific gene recombination that led to the mature T cell), responsible for the recognition of a specific peptide antigen presented in the groove of the MHC complex; and the dimers CD3$\gamma\varepsilon$, CD3$\delta\varepsilon$ and CD3$\zeta\zeta$, containing the intracellular ITAM motifs which, upon phosphorylation, trigger the downstream signalling cascade which results in T cell activation. However, the stoichiometry of the peptide-recognition TCR$\alpha\beta$ subunit in the complex is still unresolved and subject of controversy [224, 244]. The stoichiometry of the TCR$\alpha\beta$ subunit will be referred to as the stoichiometry of the TCR in this chapter.

More than a theoretical academic dispute, the stoichiometry of the TCR on the resting T cell has important implications on the models of TCR triggering: the understanding of the structure of the TCR is likely to impose important constraints on theories of antigen recognition and TCR triggering [224, 244]. Although so far very little is known about T cell triggering after ligand binding, micro-clusters of TCRs are observed on the plasma membrane upon early T cell activation [203]. TCR micro-clusters are even thought to be the actual *in vivo* cSMAC where T cell activation occurs[1]. Understanding the precise structure of the TCR right before and after ligand binding will provide more insights into how these micro-clusters form and how the antigen-induced signal crosses the plasma membrane to induce downstream signalling. The theoretical implications of the stoichiometry of the TCR before T cell activation and the lack of robust evidence explain why it is an object of controversy in the field.

Adding to the confusion, recent and conflicting evidence were reported:

1. TCRs organised in 'protein islands' (*i.e.* nano-domains of the plasma membrane enriched in specific membrane proteins) were observed on the bottom membrane of live T cells in contact with a non-activating supported-lipid bilayer by high-speed PALM (hsPALM) [248]. This clustered behaviour was confirmed by further transmission electron microscopy (TEM). These data were also consistent with previous Blue-Native-polyacrylamide gel electrophoresis and electron microscopy observations of

[1] Stable and late immunological synapses have been proposed to be the place for secondary signals and effector functions of the T cell after activation [245, 246]. The initial TCR micro-clusters would then be the place of initial TCR triggering. The function of the immunological synapse is, however, subject of discussion [247].

multivalent linear TCR complexes, referred to as TCR nano-clusters [249].

2. An opposite conclusion was drawn by the group of D. Klenerman: using two single-molecule fluorescence microscopy techniques (two-colour coincidence detection − TCCD − and dynamic single-molecule co-localisation − DySCo) and monomeric and dimeric controls, TCRs were observed as monomeric species [250–252].

Technical bias or biological artefacts were proposed to reconcile these results [244]. First, technically, TCCD is biased towards diffusing species and only observes a small confocal volume at the membrane of the cell. Thus, less mobile clusters, which are less uniformly distributed on the membrane, might have been missed. DySCo, by comparing the co-localisation of trajectories of single molecules over time, is similarly biased towards diffusing species. Interestingly, Dunne *et al.* use cells expressing ten-fold fewer TCRs than in the parental cell line. Although the cells still activate normally, lower densities at the cell surface could favour monomeric species over multivalent ones.

Conversely, hsPALM in live cells, because of sub-frame diffusion blurring [163], is biased towards immobile species, as Lillemeier *et al.* acknowledge. Moreover, the photo-blinking behaviour of the fluorescent protein PSCFP2 is not discussed [71], although most fluorescent proteins were shown to reversibly enter dark states [62, 144]. Photo-blinking of the fluorophore induces clustering artefacts in SMLM analyses and should consequently be considered and discussed [82, 144]. Moreover, Lillemeier *et al.* are the first and only ones to use PSCFP2 in a single-molecule experiment, so its single-molecule photo-physical behaviour has not been described and should not be simply assumed. Also, the regions of the cell membrane enriched with TCRs may reflect the observation of the regions of tighter contact of the live cells with the supported lipid bilayer, which are the only regions that are imaged under TIRF illumination [253–255]. Finally, TEM and gel electrophoresis are prone to aggregation artefacts because both require fixing and labelling of the sample. Thus, it is technically not entirely surprising that TCCD and DySCo experiments tend to observe mobile monomeric TCRs when hsPALM and TEM experiments are in favour of protein islands or nano-clusters of TCRs.

A biological artefact was also proposed to reconcile the contradictory observations: the clustered structures observed by Lillemeier *et al.* could be an intermediate in micro-cluster formation due to partial activation of the T cells when forming a contact, even on non-activating surfaces [244, 256]. Indeed, a major difference in the TCCD and the hsPALM experiments resides in the region of the membrane imaged: James *et al.* imaged a small region of the apical membrane, on the top of the cell, while Lillemeier *et al.* imaged the

region forming a contact on different surfaces, at the bottom of the cell. In light of the recent observation of ligand-independent TCR triggering (Chang, Fernandes, Ganzinger, Lee *et al.*, submitted, and supplementary information of ref. [257]), T cells forming a contact on poly-lysine coated glass for 45' at 37°C are expected to activate, even in the absence of TCR ligand. This suggests that the protein islands may reflect some early and partial activation of the T cells but not the actual distribution of the TCR on a resting T cell.

Last, the controversy about the stoichiometry of the TCR can be solved by the simple idea that both monomeric and protein island structures are not exclusive: TCRs could exist as monomers inside protein islands [224, 248, 249]. The important conclusion of the dual-colour fluorescence cross-correlation spectroscopy experiments performed by Lillemeier *et al.* is often forgotten in reviews summarising the controversy: a high fraction of mobile TCR complexes was detected, which "indicate[d] that protein islands [we]re indeed membrane domains and not protein complexes" [248]. As underlined and developed by Schamel *et al.*, protein islands do not explain the mechanism behind TCR triggering, but rather how TCR avidity to its ligand is increased by proximity effects (through concentration of the TCRs in protein islands, or segregation zones [234]) and enables high sensitivity and wide range of response of the receptor [249]. Reciprocally, Dunne *et al.* observed some cytoskeleton-dependent confinement of TCR diffusion, that would be consistent with TCR concentration in membrane domains such as protein islands. In that respect, simulations using a statistical-mechanical model of diffusing monomeric TCRs successfully reproduced, for various hypotheses, such TCR-enriched membrane domains [258].

### 6.1.2 Counting single-molecule localisation microscopy

When counting single molecules, errors originating from different phenomena can be divided into two general categories: over-counting and under-counting [52, 132]. Over-counting results from imperfect photo-physical behaviour of the fluorophores: many dyes and photo-activable fluorescent proteins used in SMLM switch reversibly between a fluorescent and a dark state. Such a reversible behaviour implies that a single fluorophore might be re-activated during the time of an experiment and imaged, and thus counted, more than once. Although this is a sampling advantage in localisation microscopy, it is a drawback when counting is at stake as controlling and correcting for the average number of switching events in an experiment is a real challenge. This is why (theoretically)[2] irreversibly photo-

[2]Although the bulk photo-physical properties of fluorophores are well-described in the literature, the complex and stochastic photo-physical states of single fluorophores have rarely been studied. With the advent of single-molecule techniques, the study of fluorophore at the single-molecule level is critical to under-

activable fluorophores, and especially the bright and monomeric mEos protein, are used in most, if not all, single-molecule counting methods described so far.

Photo-blinking is the other phenomenon inducing over-counting. On the single-molecule level, most photo-activable fluorophores do not stay in a fluorescent state once activated until photo-bleaching: mEos2, for example, has been shown to stochastically enter two dark states, one of which could be depleted by 405 nm illumination [144]. A counter-example, however, is PA-mCherry1, which is irreversibly photo-activable and does not blink [130]. However, compared to mEos, the lower brightness of PA-mCherry1 makes it less suitable for single-molecule detection and thus precise counting [46, 72, 130]. Over-counting due to photo-blinking is corrected by methods either grouping localisations together on the basis of a characteristic dark time (Figure 6.1, A-B; Table 6.2) or statistical analysis using the pair-correlation function $g(r)$ (Figure 6.1, C-D; refs. [82, 83]).

Similarly, various phenomena result in under-counting errors. Since fluorophores are stochastically activated, two fluorophores separated by less than the diffraction limit may be activated simultaneously, and hence they are not resolved as two localisations (but one, or none if the shape of the resulting PSF is too deformed to be fitted correctly). To decrease the probability of these events, low 405 nm activation is preferred, limiting the number of PSFs observed in each frame. Conversely, the finite time of the experiment limits the probability of activating all available probes at the end of imaging. Increasing the 405 nm activation power at the end of the experiment to increase the chance of activating most of the remaining non-activated fluorophores partly solves this issue (*i.e.* Fermi activation as proposed by Lee *et al.* [145]; Section 3.3.4). If the proteins of interest are imaged under constant activation at high density (*e.g.* a protein of the envelope of a virus), the cumulative distribution of the time of detection of the localisations can be used to estimate the number of fluorophores that were missed at the end of the experiment [146].

A last and essential factor inducing under-counting is the photo-activation efficiency [126, 260, 261]: even in the case of the perfect labelling efficiency of a fusion protein, not all fluorescent proteins fold and mature correctly. In addition, in the specific case of SMLM, the probability that a correctly folded fluorophore can be photo-converted to its activated form is lower than 1 [259]. The photo-activation efficiency accounts for all these effects and measures the probability of a fluorescent protein to be photo-activated into a fluorescently detectable form [126]. If the stoichiometry $n$ of the protein of interest is uniform, such under-counting can be corrected by fitting a binomial distribution $\mathscr{B}(n, p^{PE})$ to

stand, tackle and optimise behaviours such as photo-bleaching [31], photo-blinking [144] or photo-activation [122, 259].

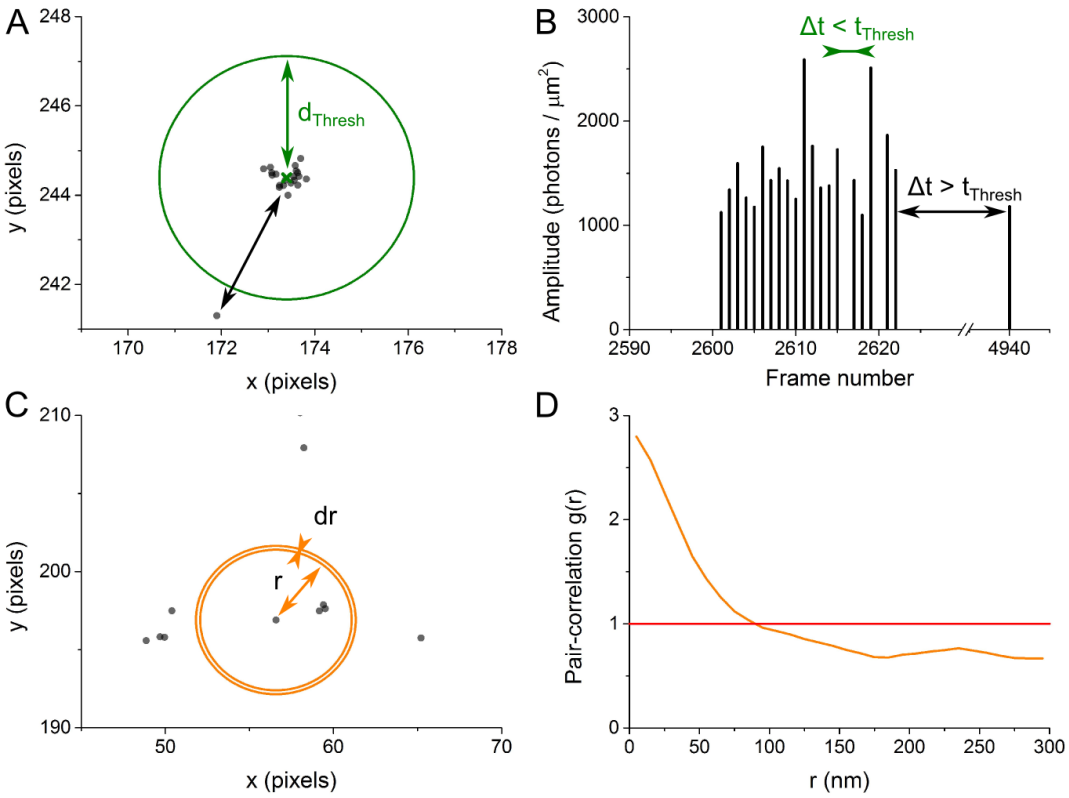


Figure 6.1 *Two types of single-molecule counting methods can be distinguished:* (1) **A-B**: Localisations can be grouped in spatial clusters (**A**) defined by a threshold radius $d_{Thresh}$. Clusters are then temporally divided in groups called 'molecules' thanks to a dark time threshold $t_{Thresh}$: successive localisations of a cluster belong to the same 'molecule' if they are separated by a dark time shorter than $t_{Thresh}$ (**B**). (2) **C-D**: The pair-correlation function $g(r)$ (also referred to as radial distribution function) of the localisations can be calculated. $g(r)$ measures the density of localisations between distances of $r$ and $r+dr$ from each localisation (**C**), divided by the density of a uniform distribution of the same total number of localisations, averaged over all localisations. The pair-correlation reveals radial random distribution is close to 1 (**D**, red line), and radial clustering at distance $r$ if $g(r) \gg 1$ (orange line between 0 and 60 nm).

the distribution of the number of fluorophores detected per cluster, $p^{PE}$ being estimated by a monomeric control [126, 131].

Most of the methods mentioned were developed during the time of the work presented in this chapter. They were implemented and assessed on monomeric, dimeric and trimeric mEos3.1 cytoplasmic constructs in *Schizosaccharomyces pombe*, and monomeric and dimeric mEos2 membrane constructs in T cells. The advantages and drawbacks of each method are discussed in the following results section.

## 6.2 Results

### 6.2.1 Yeast counting controls

To develop and test a single-molecule counting method, control constructs of known stoichiometry were designed: a single, two and three repeats of the photo-activable fluorescent protein mEos3 were expressed at low concentration in *S. pombe* cells by H. Armes. Puchner *et al.* independently developed a very similar strategy, published in 2013, expressing the same constructs in fusion with a membrane protein to target the fluorophores at the membrane of the *S. pombe* cells [131].

The original counting idea consists in grouping, or clustering, localisations in both space and time in so-called 'molecules'[3]: this is based on the observation that activated fluorophores stochastically enters dark (*i.e.* non-fluorescent) states before getting irreversibly photo-bleached (*cf.* Section 3.3 and ref. [144]), which is commonly referred to as blinking[4]. Thus, a single fluorophore may appear in non-consecutive frames during SMLM imaging and induce over-counting. However, although different blinking behaviours and dark times up to minutes were observed, the distribution of the time spent in a dark state is well described by an exponential decay (of constant $\tau_{OFF}$): a single blinking fluorophore is manifested by multiple localisations closely correlated in space (within the localisation precision) and in time (within a few $\tau_{OFF}$). The challenge in single-molecule counting consists in choosing optimal grouping thresholds ($d_{Thresh}$, $t_{Thresh}$) and validating the specificity, pre-

[3] In this thesis, different terms are distinguished for clarity: (1) '*fluorophore*' refers to the physical molecule fluorescing in the sample; (2) '*PSF*' refers to its image detected on the plane of the camera and recorded for further analysis; (3) '*localisation*' refer to the fit of a PSF with a 2D-Gaussian in a specific frame. It is defined by the frame number, and all the fitted parameters ($(xy)$ position, intensity, width, *etc.*). (4) A '*cluster'* refers to the spatial grouping of all localisations of the experiment within a specific distance $d_{Thresh}$. (5) A '*molecule*' finally refers to a sub-division of a cluster in time: a molecule groups all localisations of a cluster separated by dark times smaller than a specific duration $t_{Thresh}$.

[4] A blink is defined as the period a fluorophore spends in its fluorescent state following a first fluorescent emission followed by its entry in a dark state.

cision of the method and its robustness to single-molecule noise and to the stochastic nature of fluorophore photo-physics.

### Mono-, di- and trimeric controls

*S. pombe* cells were stably transfected with constructs of one to three repeats of mEos3. A weak promoter and a sequence destabilising its RNA messenger were used to limit the expression of the constructs to very low levels in the cytoplasm of the cells [262]. Therefore, the observation and characterisation of spatially separated monomers, dimers and trimers of mEos was possible (Table 6.1). Cells were fixed with formaldehyde and immobilised under an agarose gel pad on the coverslip before being imaged under 561 nm TIRF illumination. Each cell was imaged for 4,000 frames (50 ms exposure) under 405 nm Fermi TIRF illumination (*cf.* Section 3.3.4) to optimise the number of spatially-separated fluorescent PSFs observed in each frame.

Table 6.1 *Number of cells and localisations.*

| | **Monomer** | **Dimer** | **Trimer** | **Negative control** |
|---|---|---|---|---|
| Number of cells | 340 | 114 | 339 | 16 |
| Number of thresholded localisations | 1,389 | 666 | 7,280 | 11 |
| Average localisation precision (value at peak) | 11 nm | 11 nm | 11 nm | 8 nm |

After PSF fitting, localisations were first spatially grouped in clusters using a centroid-linkage algorithm: (1) all localisations were initialised in clusters of size one. (2) The closest pair of clusters within the defined distance threshold $d_{Thresh}$ were grouped and the position of the cluster was updated as the intensity-weighted average of all the localisations the new cluster was composed of. (3) This step was then repeated until the two closest clusters were separated by a distance larger than $d_{Thresh}$.

Then, after spatial grouping, each cluster was divided in molecules, or groups of localisations separated by dark times larger than $t_{Thresh}$. In the following sections, different ways of determining the optimal couple of parameters ($d_{Thresh}$, $t_{Thresh}$) for correct counting of the three mEos repeats are described, as published by several groups during the time of this project (Table 6.2).

Table 6.2 *Grouping parameters* ($d_{Thresh}$,$t_{Thresh}$) *used in counting experiments.* †Long-lived dark time in parentheses when two dark times are described.

| **Reference** | **Year of publication** | **Dark time $\tau$ (s)** | **$t_{Thresh}$ (s)** | **$d_{Thresh}$ (nm)** |
|---|---|---|---|---|
| Annibale *et al.* [263] | 2011 | 0.1 | N/A | 133 |
| Coltharp *et al.* [264] | 2012 | 0.1 | 0.4 | 60 |
| Gunzenhäuser *et al.* [146] | 2012 | | 0.3 | 50 |
| Lando *et al.* [130] | 2012 | | N/A | 40 |
| Lee *et al.* [145] | 2012 | 0.06 (2.3†) | N/A | $\sigma_{th}$? |
| Puchner *et al.* [131] | 2013 | 0.58 | 2.66 | 150 |
| Durisic *et al.* [126] | 2014 | 0.66 | 4.1 | $\sigma_{th}$? |

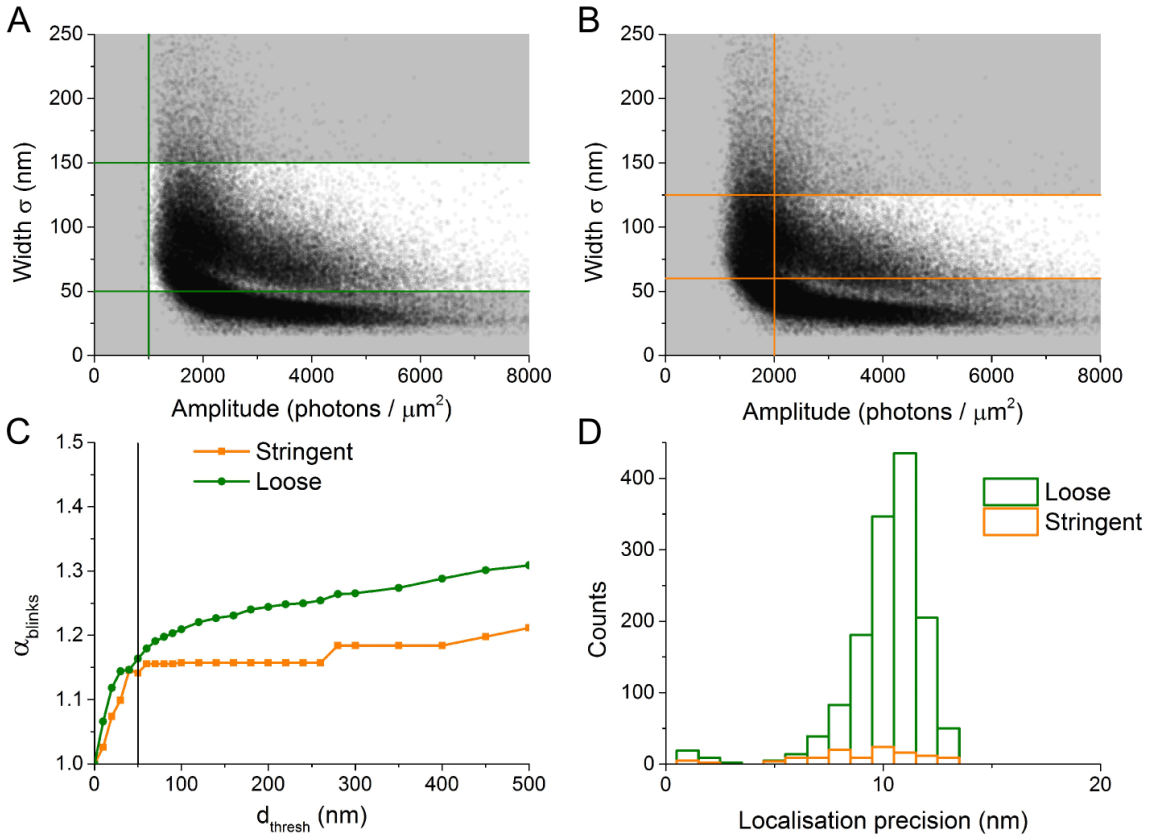


Figure 6.2 *Rejection of localisations upon different localisation thresholdings.* Monomeric mEos3.1 proteins were expressed at low concentration in *S. pombe* cells. After fixation in formaldehyde, cells were imaged under 561 nm TIRF illumination and low continuous Fermi 405 nm activation. SMLM movies were analysed using Peak Fit (*cf.* Section 3.4). **A-B**: width *vs.* amplitude parameter plots of all analysed localisations. The effect of two post-processing thresholdings of the localisations to be rejected are shown (A, loose thresholding; B, stringent). **C**: After either thresholding, localisations were grouped in spatial clusters of varying radius $d_{Thresh}$ and the average number of discrete appearance of molecules per cluster $\alpha_{blinks}$ was calculated. Black vertical line: $d_{Thresh} = 50$ nm. **D**: Distribution of the theoretical precision (*cf.* Equation 3.13) of the localisations after either thresholding. Green: Loose thresholding (peak at 11 nm). Orange: Stringent thresholding (peak at 10 nm).

### Determining the optimal thresholds by estimating the true number of fluorophores

In 2012, Coltharp *et al.* proposed a way to select optimal $d_{Thresh}$ and $t_{Thresh}$ with no other knowledge of the sample than the average number of blinks $\alpha_{blinks}$[5] of the fluorophore [264]. In the work presented in this chapter, $\alpha_{blinks}$ was estimated *in situ* as the average number of blinks (number of molecules for $t_{Thresh} = 1$ frame) per cluster in the monomeric sample. Figure 6.2, C represents this value $\alpha_{blinks}$ calculated for different values of $d_{Thresh}$ and two different localisation thresholding (to select real localisations over noise, *cf.* Table 6.6 and the following section). A plateau is observed at $\alpha_{blinks} = 1.2$, for $d_{Thresh} \sim 40$ nm. The plateau indicates a regime for which the average number of blinks does not depend on spatial grouping in clusters. The regime ($d_{Thresh} \sim 40$ nm) is furthermore consistent with the localisation precision of the experiment ($\sigma_{exp} = 2 \cdot \sigma_{th} = 22$ nm, *cf.* Table 6.1, Figure 6.2, D and Section 3.4.3). As the value of $\alpha_{blinks}$ was unchanged for either localisation thresholding, the more stringent thresholds were kept, in order to limit the number of false localisations, for further analysis.

As described in ref. [264], the total number of fluorophores is thus estimated as $N_{ref} = N_{unprocessed}/\alpha_{blinks}$, where $N_{unprocessed}$ is the number of localisations. For each sample, the matrix $|(N - N_{ref})/N_{ref}|$ was calculated for different values of $d_{Thresh}$ and $t_{Thresh}$, where $N$ is the number of molecules obtained for specific values of ($d_{Thresh}$, $t_{Thresh}$) (Figure 6.3). From such plots, the intersections of the two optimal valleys (dark regions, indicating of good estimates of $N$ to $N_{ref}$) were identified as the optimal values for $d_{Thresh} = 40$ nm and $t_{Thresh} = 150$ ms. In order to validate these thresholds, both values were then used to group the localisations of each sample. The pair-correlation function $g(r)$, representing the degree of clustering of a distribution (a random distribution would give $g(r) = 1$), was compared before ($t_{Thresh} = 50$ ms $= 1$ frame) and after grouping in time ($t_{Thresh} = 150$ ms): in the case of the monomer, after grouping, the molecules were expected to be randomly distributed. The very little variation in the pair-correlation function after grouping in time revealed that the threshold values chosen did not group all localisations originating from the single blinking fluorophore together.

This difficulty underlines the drawback of this method: its robustness highly depends on the prior knowledge or the good estimation of the true number of fluorophores, which is precisely what needs to be assessed in single-molecule counting (the total number of fluorophores gives the average number of blinking events, thus the average stoichiometry of each cluster). Here, it is approximated to the total number of localisations divided by the

[5] Actually, $\alpha_{blinks}$ refers to the average number of 'On' times of the fluorophore, so $\alpha_{blinks} = n_{blinks} + 1$.

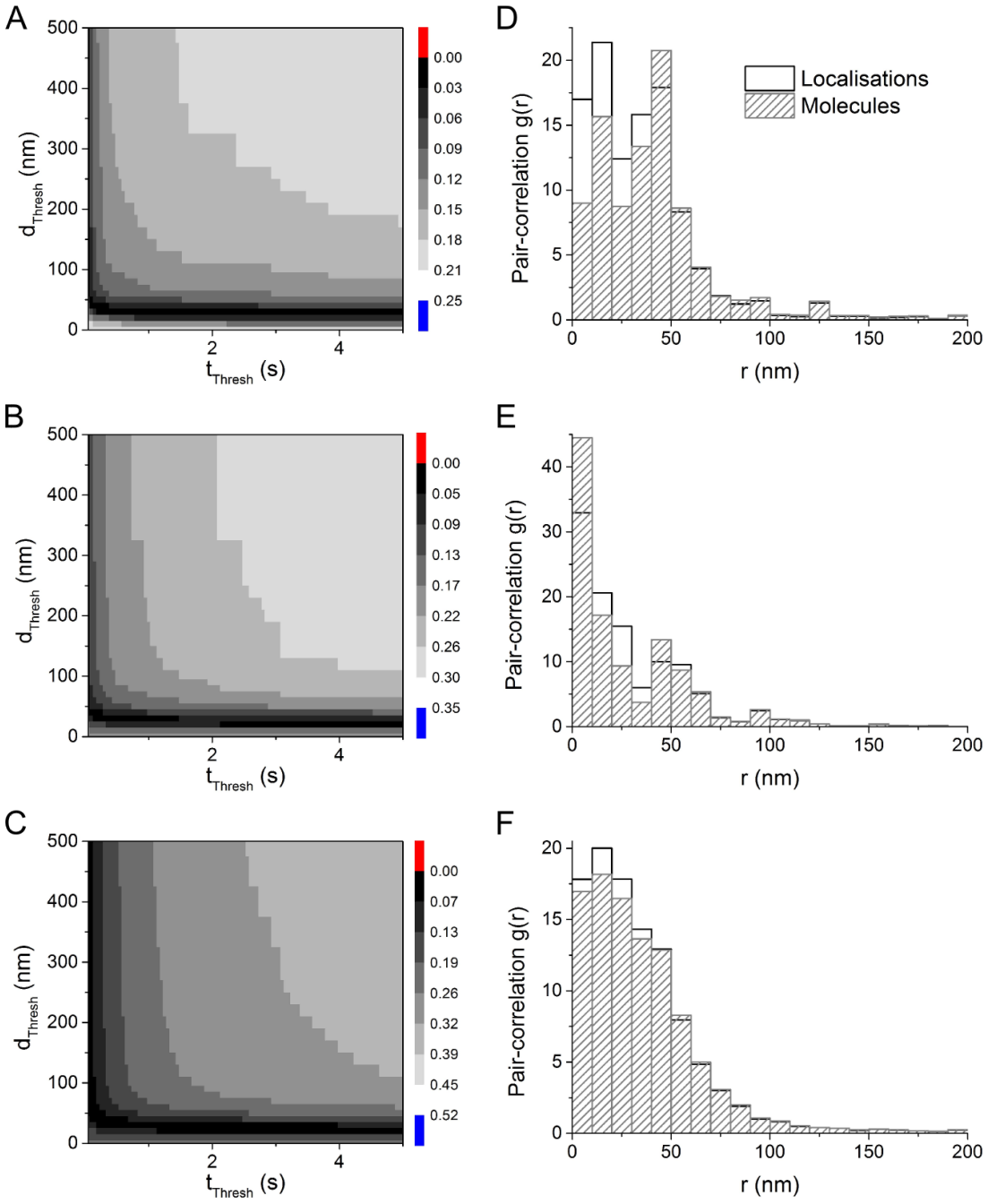


Figure 6.3 *Determination of optimal thresholds.* Following the method of Coltharp *et al.* for single-molecule counting, a single, two, or three mEos3.1 repeats were expressed at low concentration in yeast cells and imaged after fixation under 561 nm TIRF illumination and low continuous Fermi 405 nm activation. After SMLM analysis, localisation were spatially (if closer from the mean centre position than $d_{Thresh}$) and timely (if separated from another localisation by less than $t_{Thresh}$) grouped in 'molecules'. **A-C**: matrix of the total number of molecules $N$ calculated for pairs of thresholds ($d_{Thresh}$, $t_{Thresh}$) relative to an estimation of the expected true number of fluorophore $N_{red}$: $|(N - N_{ref})/N_{ref}|$. **D-F**: Pair-correlation function $g(r)$ of the localisations before grouping (white bars) and after grouping in molecules (pair of thresholds (40 nm, 150 ms), striped grey bars). **A,D**: Monomeric mEos3.1 construct. **B,E**: Dimeric mEos3.1 construct. **C,F**: Trimeric mEos3.1 construct.

average number of blinking events. Since fluorophores sometimes appear in consecutive frames before entering a dark state or photo-bleaching, the number of localisations is an over-estimation of the total number of 'On' times of all fluorophores.

To get a better estimation of the total number of fluorophores $N_{ref}$, localisations of the same fluorophores appearing in consecutive frames need to be grouped. This requires the definition of a spatial threshold $d_{Thresh}$: localisations closer from each other than $d_{Thresh}$ and appearing in consecutive frames originate from the same fluorophore. Unfortunately, $d_{Thresh}$ is exactly what the method tries to estimate. To describe it differently, to find the optimal $d_{Thresh}$, a good estimate of $N_{ref}$ is needed, which itself requires a prior estimation of $d_{Thresh}$. One could study the dependence of this prior $d_{Thresh}$ threshold on the estimation of the optimal threshold, or start with an estimate of $d_{Thresh}$ and apply the method iteratively until it converges to an optimal $d_{Thresh}$. It both implies making an initial empirical assumption. Therefore, the next section describes a semi-empirical method.

### Semi-empirical estimation of the blinking rate

In 2011, Annibale *et al.* proposed to fit a semi-empirical function to the first values of the curve $N(t_{Thresh})$, the total number of molecules obtained after grouping spatial clusters in time with $t_{Thresh}$ [263]. This fit allows to estimate the total number of fluorophores in the sample $N_{true}$, the average number of blinking events $n_{Blinks}$, and the dark time constant $\tau_{OFF}$ of the fluorophore (the exposure of the camera was set to $exposure$ = 50 ms):

$$N(t_{Thresh}) = N_{true} \cdot \left(1 + n_{Blinks} \cdot e^{\left(\frac{exposure - t_{Thresh}}{\tau_{OFF}}\right)}\right) \tag{6.1}$$

This method requires to first group localisations spatially. Although the authors empirically choose a value of $d_{Thresh}$ = 133 nm, a rational estimate is defined as a multiple of the localisation precision of the experiment [145]. Indeed, if the localisation error is Gaussian, 99.7% of successive localisations of an immobile fluorophore will be localised within $3 \cdot \sigma_{exp}$ of the average position of the localisations. Thus, considering that for the microscopes used in this thesis, $\sigma_{exp} \sim 2 \cdot \sigma_{th}$ (*cf.* Section 3.4.3), $d_{Thresh}$ was defined as $3 \cdot \sigma_{exp} \sim 60$ nm (*cf.* Figure 6.2, D).

After grouping localisations in spatial clusters, clusters were divided in molecules for different values of $t_{Thresh}$. The total number of molecules $N(t_{Thresh})$ was calculated and Equation 6.1 was fitted for each sample. The fitted parameters for the three samples are summarised in Table 6.3. Noticeably, the average number of blinking events per fluorophore $n_{Blinks}$ is much lower than previously measured [263]. This imaging protocol would thus

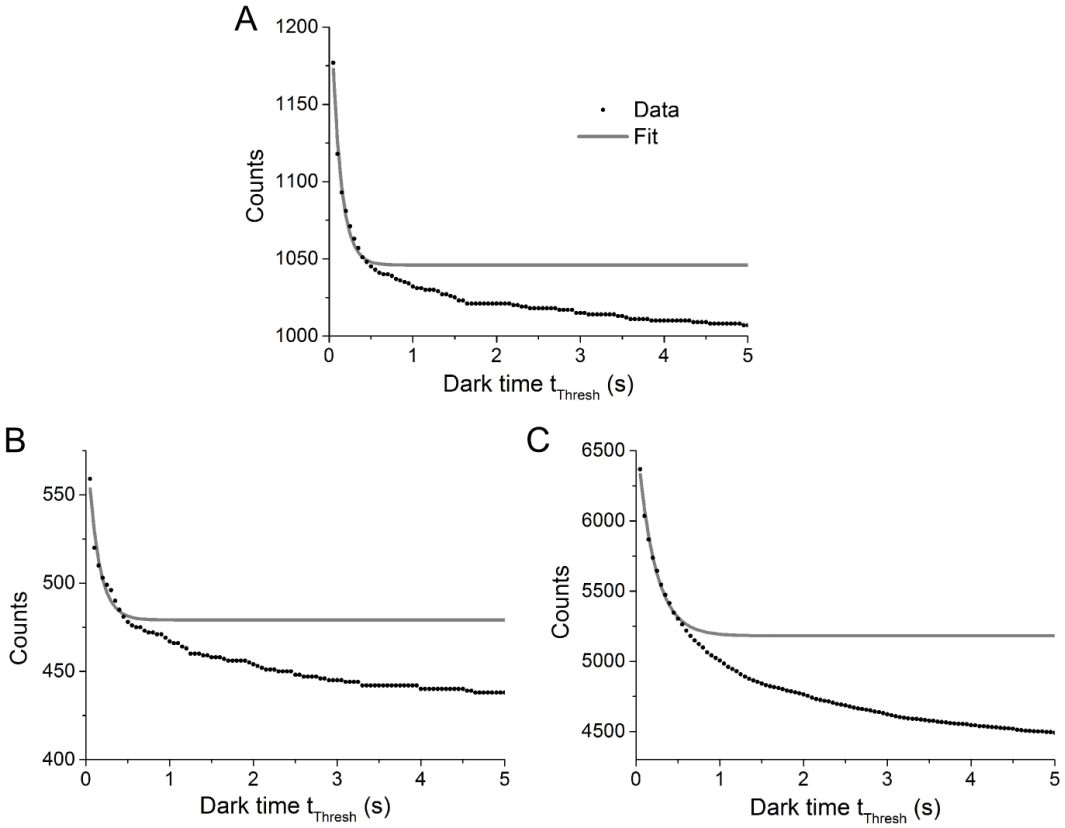


Figure 6.4 *Semi-empirical determination of the optimal dark time threshold.* Localisations from the samples described in Figure 6.3 were grouped spatially in clusters of radius $d_{Thresh} = 60$ nm. Such clusters were divided in 'molecules' separated by dark times higher than different $t_{Thresh}$ threshold values. The number of total molecules obtained were plotted against the threshold value $t_{Thresh}$ (**A-C**, •). The semi-empirical Equation 6.1 was fitted to the first ten points ($t_{Thresh} \leq 0.5$ s) (grey curve). Fitted parameters are summarised in Table 6.3. **A**: Monomeric mEos3.1 construct. **B**: Dimeric mEos3.1 construct. **C**: Trimeric mEos3.1 construct.

Table 6.3 *Semi-empirical fit of Equation 6.1 to the number of molecules obtained after grouping localisations both spatially ($d_{Thresh} = 60$ nm) and for different dark time thresholds $t_{Thresh}$.*

| | **Monomer** | **Dimer** | **Trimer** |
|---|---|---|---|
| $n_{blinks}$ | 0.118 | 0.156 | 0.222 |
| $\tau_{OFF}$ (s) | 0.109 | 0.128 | 0.209 |
| $N_{true}$ | 1,046 | 479 | 5,181 |

be theoretically optimal to count single fluorophores as little correction would need to be applied. However, this would imply that a very low $t_{Thresh}$ dark time threshold, if any, would correctly group all localisations from a single fluorophore together. Such a pair of thresholds ($d_{Thresh}$, $t_{Thresh}$) is very similar to the previous one (40 nm, 150 ms) which, when applied to the monomeric sample, proved to describe poorly spatially separated single fluorophores. Similarly, after grouping localisations with the pair of thresholds (60 nm, 50 ms) for the monomeric sample, the pair-correlation function $g(r)$ of the grouped molecules was not flat but showed some short-range clustering very similarly to Figure 6.3, D.

The poor estimation of $n_{Blinks}$ could be explained by some random single-molecule-like noise that would be detected as a correct PSF and localisation (*i.e.* of correct width and intensity) but that would not blink. Thus, $n_{Blinks}$ represents the average number of blinking events for the whole populations of localisations. Non-blinking single-molecule-like noise would proportionally lower $n_{Blinks}$, therefore inducing false clustering of localisations in molecules.

Although this method poorly accounts for noise, it allows to gain access to *in situ* estimation of the exponential decay $\tau_{OFF}$ of the time spent by the fluorophore in its dark state. Indeed, the presence of non-blinking single-molecule noise does not affect this fitted value that only describes behaviour of blinking species, thus the fluorophore. Values of $\tau_{OFF}$ obtained here are consistent with values described in the literature for the short-lived dark time of mEos ($\tau_{OFF} = 0.06 - 0.66$ s, *cf.* Table 6.2). There are however quite different from the *in vitro* experiments described in Section 3.3 with purified mEos2 and mEos3.2 proteins under similar imaging protocol ($\tau_{OFF} \sim 1$ s).

### Empirical estimate of the thresholds

Knowing the value of the time constant $\tau_{OFF}$ of the exponential decay of the dark times of *in situ* mEos allows to estimate a sensible $t_{Thresh}$ [126, 131, 146]. As proposed in 2013 by Puchner *et al.*, the dark time threshold was defined as the time $t_{Thresh}$, which takes into account 99.8% of the measured dark times, *i.e.* 870 ms[6].

As the pair of thresholds (60 nm, 870 ms) did not affect the clustering observed in the pair-correlation function of the grouped molecules for the monomeric sample, $t_{Thresh}$ was empirically increased until the pair-correlation function flattened, correctly describing the random distribution of the monomeric fluorophores in the sample. This was the case for $t_{Thresh} = 3$ s (Figure 6.5, A), which is remarkably consistent with values used by Durisic *et al.* and Puchner *et al.* (Table 6.2).

[6] $t_{Thresh} = -\tau_{OFF} \ln(1 - 0.998)$

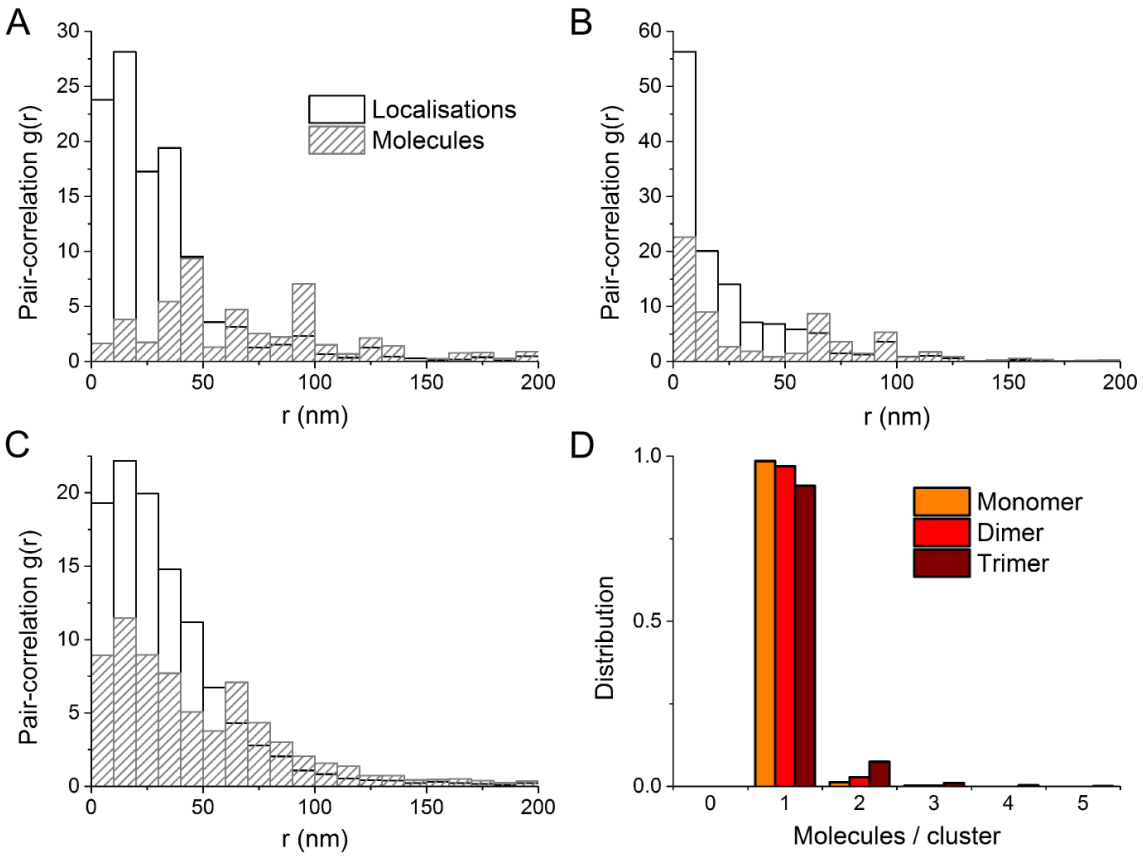


Figure 6.5 *Empirical determination of the optimal dark time threshold.* Localisations from the samples described in Figure 6.3 were grouped spatially in clusters of radius $d_{Thresh} = 60$ nm. Such clusters were divided in 'molecules' separated by dark times higher than increasing $t_{Thresh}$ threshold values. The threshold value $t_{Thresh}$ was increased until clustering effect disappeared from the pair-correlation function of the corresponding grouped molecules in the case of the monomeric construct (**A**). **A-C**: Pair-correlation function $g(r)$ before cluster division in molecules (white bars) or after dividing clusters in molecules (for $t_{Thresh} = 3$ s, striped grey bars). **A**: Monomeric mEos3.1 construct. **B**: Dimeric mEos3.1 construct. **C**: Trimeric mEos3.1 construct. **D**: Distribution of $n$-mers (*i.e.* numbers of molecules in each cluster) for the three mEos3.1 constructs.

Table 6.4 *Fit of binomial distributions* $\mathscr{B}(n, p^{PE})$ *to the number of molecules per cluster.*

| | $p^{PE}$ | | |
|---|---|---|---|
| ***n*** | **Monomer** | **Dimer** | **Trimer** |
| 2 | 2.6% | *5.4%* | 14.2% |
| 3 | 1.3% | 2.8% | *7.6%* |
| 4 | 0.9% | 1.9% | 5.2% |
| 5 | 0.7% | 1.4% | 4.0% |

For each sample, the distribution of molecules per cluster after grouping with (60 nm, 3 s) thresholds was calculated (Figure 6.5). In order to account for under-counting due to imperfect photo-activation efficiency $p^{PE}$, binomial distributions $\mathscr{B}(n, p^{PE})$ for $n$-mers were fitted to these histograms [126, 131] (Table 6.4). The small fraction of counts higher than 1 for the monomeric sample, 2 for the dimeric control, and 3 for the trimeric control, are caused by randomly overlapping fluorophores. Noticeably, the number of miss-folded undetectable fluorophores (column 0 of the histogram) cannot be observed. Thus, only binomial distributions representing populations of $n$-mers for $n \geq 2$ can be fitted (with the help of an additional normalising parameter).

Interestingly, the binomial fits for 2-mers for the dimer sample, and for 3-mers for the trimer sample, output comparable values for the photo-activation efficiency parameter $p^{PE}$. This percentage is however more than ten-fold smaller than what has been previously characterised for a similar mEos2 protein [126, 131]. This difference could be explained by the slightly different fluorophore mEos3.1 used in this work, difference in the imaging protocol (and a possibly more stringent localisation thresholding) or additional single-molecule noise proportionally increasing the proportion of 1-mers in the histograms.

A possible idea to determine the stoichiometry of a single population of proteins is to calculate the histogram of the numbers of molecules per cluster and try to fit several binomial distributions $\mathscr{B}(n, p^{PE})$ for different values of $n$. Then, the comparison of the value of the fitted parameter $p^{PE}$ with the experimental value obtained in the case of the dimer and trimer controls unravels the best description of the histogram. To say it differently, fitting the histogram with $\mathscr{B}(n, p^{PE})$, where $p^{PE}$ is fixed to its value experimentally determined by the dimer and trimer controls, allows to determine the best value $n$ describing the data.

Although theoretically attractive, this counting method assumes a single stoichiometry in the population observed, and is thus not robust to single-molecule-like noise which would be considered as a second monomeric population. This explains why, in the light of this method, the trimer control would be best described as a 4-mer population ($p^{PE} = 5.2\%$) rather than a 3-mer (7.6%). Nevertheless, this counting method, although quantitatively limited in presence of single-molecule noise, allows to qualitatively separate a monomeric population from a multimeric one.

### Pair-correlation study

Because single-molecule-like noise was limiting all previous counting approaches, a method robust to such a noise was proposed. In 2011, a statistical clustering method, so-called pair-correlation-PALM (PC-PALM), first proposed and developed by Veatch *et al.*, and applied

by Sengupta *et al.* to PALM used the pair-correlation function $g(r)$ to detect and correct over-counting due to photo-blinking of the fluorophores (*cf.* Section 6.1.2). Although $g(r)$ was used in the previous counting methods as a tool to assess the quality of the pair of thresholds ($d_{Thresh}$, $t_{Thresh}$), PC-PALM directly corrects the pair-correlation function for blinking of the fluorophore in order to access to the real clustering, or stoichiometry, of the protein of interest.

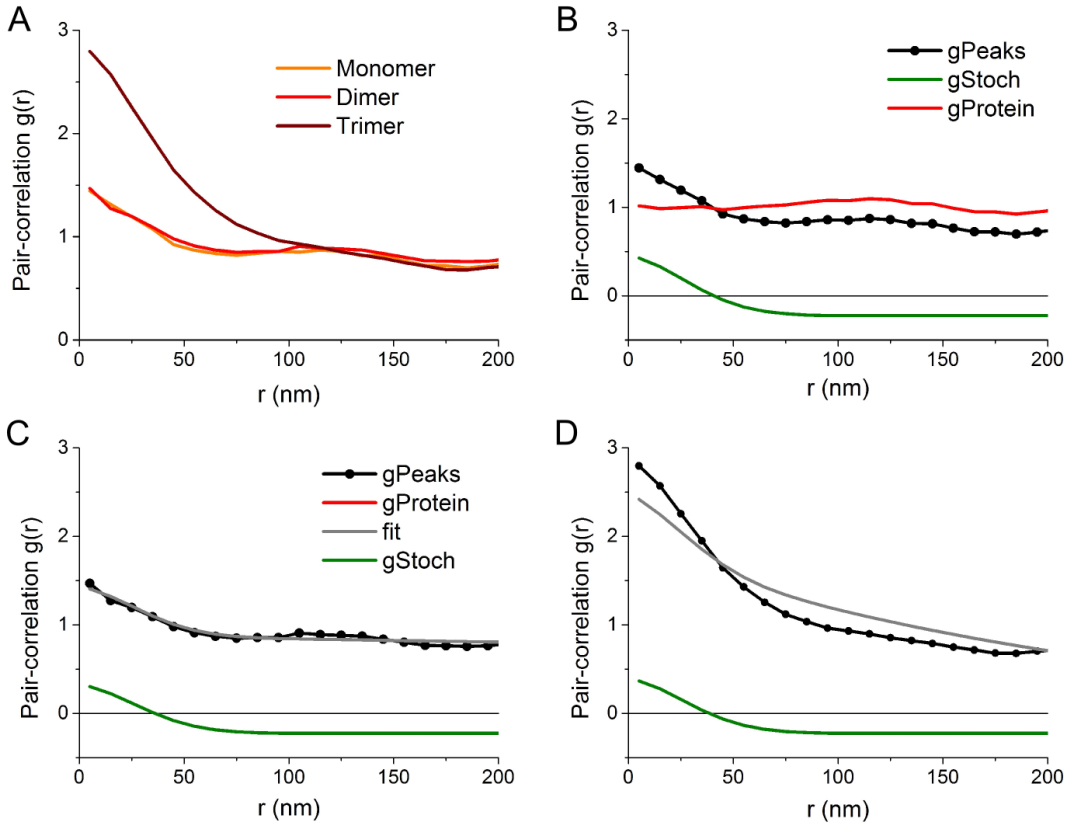


Figure 6.6 *Pair-correlation PALM approach.* Localisations from the samples described in Figure 6.3 were analysed with PC-PALM. **A**: comparison of the pair-correlation function $g(r)$ for the three samples (monomer in orange, dimer in red, trimer in dark red). **B**: $g^{\text{stoch}}(r)$ (Equation 6.2, green curve) was fitted to the pair-correlation $g(r)$ (black curve) of the monomeric mEos3.1 sample. The residual is also plotted (red curve). **C-D**: $g^{\text{stoch}}(r)$ (green curve) was subtracted from the pair-correlation function $g(r)$ (black curve) of the dimeric (**C**) or trimeric (**D**) mEos3.1 samples. The resulting curve was fitted by $g^{\text{protein}}(r) * g^{\text{PSF}}(r)$ (Equation 6.2). The sum of the fit and $g^{\text{stoch}}(r)$ is plotted in grey; $g^{\text{protein}}(r)$ is plotted in red, but takes values higher than 3. Fitted parameters are summarised in Table 6.5.

This method proposes to separate, in the pair-correlation function $g(r)$, the contribution of the stochastic blinking of each fluorophore ($g(r)^{\text{stoch}}$) that induces artificial clustering of localisations, from the real clustering of the fluorophores ($g(r)^{\text{protein}}$), which is itself blurred

(*i.e.* convolved) with the localisation precision $\sigma_{exp}$:

$$
\begin{aligned}
& g(r) = g(r)^{\text{stoch}} + g(r)^{\text{protein}} * g(r)^{\text{PSF}} \\
& \text{with,} \qquad g(r)^{\text{stoch}} = \frac{1}{4\pi\sigma_{exp}^2\ \rho_{\text{average}}} \cdot \exp\left(\frac{-r^2}{4\sigma_{exp}^2}\right) \\
& \qquad\qquad g(r)^{\text{protein}} = A \cdot \exp\left(\frac{-r}{\xi}\right) + 1 \\
& \text{and,} \qquad g(r)^{\text{PSF}} = \frac{1}{4\pi\sigma_{exp}^2} \cdot \exp\left(\frac{-r^2}{4\sigma_{exp}^2}\right)
\end{aligned}
\tag{6.2}
$$

The method is composed of two consecutive steps: first, monomeric fluorophores are imaged to characterise the stochastic blinking of the fluorophore. The pair-correlation function of the localisations is fitted with the theoretical function $g(r)^{\text{stoch}}$, and both the average blinking rate $\alpha_{blinks}$ of the fluorophore and the average experimental localisation precision $\sigma_{exp}$ are extracted. The pair-correlation function of the monomeric mEos3 construct in yeast cells was well fitted with the equation of $g(r)^{\text{stoch}}$ ($R^2 = 0.90$, Figure 6.6). Furthermore, the experimental localisation precision of $\sim 22$ nm (Table 6.5) is consistent with the theoretical precision of the experiment (11 nm, Table 6.1). The average number of discrete appearances of a fluorophore $\alpha_{blinks}$ is, however, much below one (0.064). This counter-intuitive value could reflect the incertitude in the estimation of the average localisation density over the whole field of view as $\alpha_{blinks}$ is calculated in reference to it (*cf.* Section 6.2.2).

Table 6.5 *Fitted parameters of pair-correlation PALM analysis as described in Equation 6.2.*

| | $g(r)^{\text{stoch}}$ fit | | | $g(r)^{\text{protein}}$ fit | | |
|---|---|---|---|---|---|---|
| **Sample** | $\sigma_{exp}$ | $\rho_{\text{average}}$ | $\alpha_{blinks}$ | $A$ | $\xi$ | $N_{clusters}$ |
| **Monomer** | *21.6 nm* | *249 µm$^{-2}$* | 0.064 | – | – | – |
| **Dimer** | 21.6 nm | 267 µm$^{-2}$ | 0.074 | 83.3 | 2.9 µm | $1.3 \cdot 10^6$ |
| **Trimer** | 29.9 nm | 44.4 µm$^{-2}$ | 0.399 | 160.5 | 245 nm | 16,700 |

In the case of a population in a uniform multimeric state (*i.e.* only *n*-meric species), this first step can be used and the resulting average number of blinks $\alpha_{blinks}$ value compared to the monomer control: a dimer should be observed with a similar localisation precision $\sigma_{exp}$ but in average the double number of blinking events. Nevertheless, as previously discussed, the incertitude in the determination of $\alpha_{blinks}$ makes this method not very quantitatively precise nor qualitatively robust: very little difference is observed between the mEos3 monomer and dimer controls (0.064 *vs.* 0.074), and $\alpha_{blinks}$ is more than six-fold higher for the trimer than for the monomer construct (0.399 *vs.* 0.064, Table 6.5).

In PC-PALM, a second step consists in subtracting the contribution from the pair-correlation function due to the stochastic blinking of single fluorophores as revealed by the first

step, then in fitting the resulting function $g(r) - g(r)^{\text{stock}}$ as developed in Equation 6.2. The fitted parameters $A$ and $\xi$ respectively are a measure of the protein density in the average protein cluster observed, and an estimate of the radius of such a cluster [82]. From these parameters, the average number of proteins per clusters is approximated by $N_{clusters} \sim 2\,A\pi\,\xi^2\,\rho_{\text{average}}$ (Table 6.5).

Although PC-PALM is powerful to statistically and quantitatively describe complex protein clusters on the plasma membrane of cells [82] and does not depend on the presence of non-blinking random noise, it requires a high number of localisations to be robust: in the experiments presented in this chapter, very low densities of fluorophores were expressed in cells to easily spatially separate them. Therefore, even when combining the pair-correlation from a large number of imaged cells, the total number of localisations stays much lower than what is advised for significant PC-PALM results ($n_{loc} \sim 1,000 \ll 100,000$, *cf.* Table 6.1 and ref. [155]), explaining the poorly relevant results obtained for the experiments presented here. Another drawback of PC-PALM analysis is that it sums up the complex multi-dimensional localisation data ($(xy)$ position, frame of first appearance, intensity, *etc.*) as an average 1D measurement: it thus better characterises clusters of circular-symmetry shapes and populations of uniform stoichiometry.

### Single-molecule-like noise

Even more than for classic SMLM experiments, counting single-molecule requires a very low background noise. Two types of noise have to be distinguished: (1) out-of-focus diffuse background noise due to an average of lowly fluorescent sources in the cell. This noise can be photo-bleached and impact mostly both the ability to detect single fluorophores and the localisation precision achievable (*cf.* Equation 3.13). (2) Less described in the literature is single-molecule-like noise (or 'single-molecule noise'): some endogenously-expressed fluorescent proteins (*e.g.* riboflavin[7], and proteins of the flavin group of molecules) emits around 550 nm, in the same domain as the red activated form of mEos [265, 266].

In order to avoid the first category of noise, general SMLM precautions were taken (*e.g.* TIRF illumination, use of filtered buffers, plasma-cleaning of coverslips). Additionally, the effect of two different localisations thresholdings were observed in the width-amplitude parameter plot (*cf.* Chapter 4) and further analyses were performed with the more stringent set of parameters (Figure 6.2, A-B and Table 6.6). Localisations that were kept are bright and have an expected symmetric Gaussian shape of well-characterised width. Thus, false

[7] Commonly known as vitamin B2.

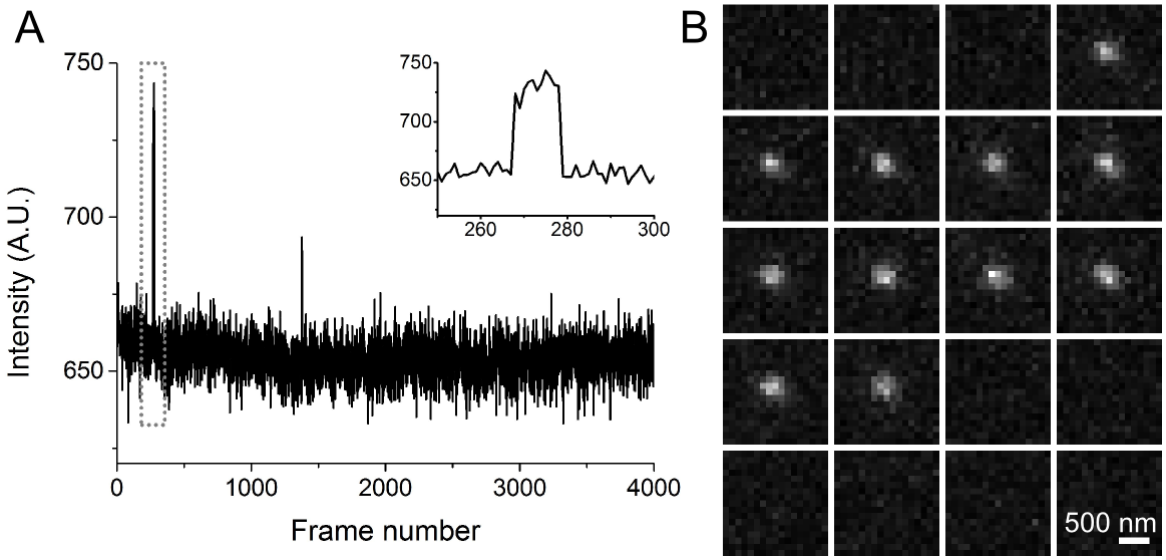


Figure 6.7 *Single-molecule-like noise.* Untransfected yeast cells were fixed and imaged under 561 nm TIRF illumination and low continuous Fermi 405 nm activation. **A**: Intensity trace of a single-molecule PSF observed in the untransfected sample (A.U.: arbitrary units; inset: close-up of the region indicated by the grey dotted rectangle). **B**: Time-lapse of the region of the camera where the PSF is observed (from top to bottom, left to right, frames 265 to 284; exposure: 50 ms). The PSF appeared and disappeared in a single frame, which is the characteristics of a single-molecule. Scale bar: 500 nm.

PSF-fits of background events are rejected. The stringent thresholding allows for better rejection of false localisations but also decreases the number of localisations observed.

Table 6.6 *Two localisation sets of thresholds were compared to reject out-of-focus noise.*

| | **Stringent parameters** | **Loose parameters** |
|---|---|---|
| Maximal width ($\sigma_{max}$) | 125 nm | 150 nm |
| Minimal width ($\sigma_{min}$) | 60 nm | 50 nm |
| Maximal width ratio ($\sigma_{max}/\sigma_{min}$) | 1.6 | 2.3 |
| Minimal amplitude | 2,000 photons/$\mu m^2$ | 1,000 photons/$\mu m^2$ |

The effect of single-molecule noise is even more critical in single-molecule counting. Indeed, single-molecule noise is almost indistinguishable from the signal of a fluorescent probe: such noise also originates from a single fluorescent molecule emitting at a similar wavelength [251]. Figure 6.7 gives the example of such noise: a bright, PSF-shaped, non blinking PSF is observed. Thus, the presence of single-molecule noise implies that the counting analyse needs to deal with two different populations: the mEos-tagged protein of interest and some randomly-distributed (in first approximation) non-blinking single-molecule.

This heavily limits most of the counting techniques studied in this chapter. Puchner

*et al.* propose to correct their molecule numbers by subtracting the mean number of *n*-mers that they counted per cell in an un-transfected negative control sample [131]. For the work presented here, a similar approach gave an average number of 0.69 localisations attributed to noise per cell, corresponding to 0.31 1-mers, and no larger *n*-mers, detected per cell (*cf.* Table 6.1). Such low values do not significantly change any previous analysis. Nevertheless, the difficulty to focus on and image non-blinking single-molecule noise that tends to bleach during the exposure of a single frame has not been discussed by Puchner *et al.*, although it proved to be a real limitation to image single-molecule noise (particularly in negative control cells expressing no fluorophore, as fluorophores tend to appear for a few consecutive frames). This implies that the corrections reported here are a low estimate of the noise to subtract. It is however difficult to meliorate the estimation or get an idea of how far it may stand from its true value.

Finally, fixing the cells may also increase single-molecule noise while decreasing the diffuse background noise. It indeed fixes all cellular proteins: although the fluorescent endogenous proteins responsible for single-molecule noise may diffuse quickly during the exposure time of the camera and be consequently imaged as blurred in the diffuse background noise, when fixed, they would appear as non-blurred single emitters. However, non fixing the yeast cells would also induce diffusion of the mEos3 repeats, decrease the localisation precision (due to blurring), and raise non-trivial questions about tracking blinking fluorophores over time, especially during long dark times between two discrete activations of two mEos3 of the same fusion construct.

### 6.2.2 Studying the dependence of counting analyses on localisation densities using simulations

Both types of analyses described here are dependent on the density of imaged fluorophores: (1) in order to avoid false grouping of separate fluorophores which happen to be within $d_{Thresh}$ of each other, low densities of labelled proteins are required for correct grouping; (2) conversely, PC-PALM requires high sampling to obtain statistically relevant information about the clustering state of the protein of interest, which consequently needs to be expressed at higher densities. To study the density thresholds below and above which each type of analysis is preferred, single fluorophores were simulated, fitted and analysed.

Fluorescent point-emitters were simulated as 2D-Gaussian PSFs whose parameters were randomly drawn from statistical distributions obtained from an experimental list of localisations (horizontal and vertical widths $\sigma_x$ and $\sigma_y$ were drawn from a Gaussian distribution

of mean 129.7 nm and standard deviation 21.5 nm, with the conditions of their maximal ratio being lower than 1.7; total integrated intensities $I$ were drawn from a Gaussian distribution of mean 698 photons and standard deviation 590 photons; Figure 6.8, A-B). For each new frames, a list of $m$ (drawn from a Poisson distribution of mean 5) PSFs was simulated, whom $(x,\ y)$ positions were drawn from a uniform distribution in a 121 μm$^2$ square. Finally, a Poissonian noise of mean 19 photons was added on each pixel of the frame. The number of simulated frames was defined such as to get a specific density of localisation $C$:

$$\text{Frame number} = \frac{C \cdot (\text{Total area})}{\text{Mean number of PSFs per frame}} \tag{6.3}$$

Localisation densities of 0.01, 0.1, 0.5, 1, and 5 localisations/pixel$^2$ (*i.e.* 0.83, 8.3, 41, 83, and 413 localisations/μm$^2$, resp.) were simulated, and further fitted. Because of the optimised but imperfect fitting algorithm (detecting some noise and rejecting some simulated PSFs), the variation of the simulated PSFs (some of which simulated with an intensity below the average noise), the nearest-neighbour-based measure of density of the fitted localisation, and the estimation of the number of frames to simulate the given density $C$, localisation densities of 4.6, 8.4, 29, 52, and 241 localisations/μm$^2$ were observed after fitting (Figure 6.8, C-G, resp.).

For each simulation, both pair-correlation function (Figure 6.8, H) and the distribution of number of molecules found per cluster, for the previous thresholds ($d_{Thresh} = 60$ nm, $t_{Thresh} =$ 3 s $= 60$ frames) (Figure 6.8, I) were computed. As expected, the grouping analysis is very sensitive to the density of localisations and 2-mers are observed for densities as low as 8.4 localisations/μm$^2$. However, the simulation magnifies this dependence since, if an average of five PSFs are observed in an SMLM experiment, most fluorophores appear in consecutive frames and will be considered as single localisations. Thus, in SMLM experiments, PSFs are usually more separated in time, decreasing the number of incorrectly grouped localisations. This is why only experiments with localisation densities lower than a 25-30 localisations/μm$^2$ threshold are here considered for counting analysis by (60 nm, 3 s) grouping. This localisation density is only valid for monomeric samples, and the threshold should be doubled for the dimeric control.

Conversely, the pair-correlation function is poorly defined for low densities (Figure 6.8, H, red and orange) and closely approaches its true value ($g(r) = 1$ for a uniform distribution) for higher densities (H, blue and purple). Thus, PC-PALM (or more qualitatively comparing pair-correlation functions) will be here only considered for localisation densities higher than a 30 localisations/μm$^2$ threshold.

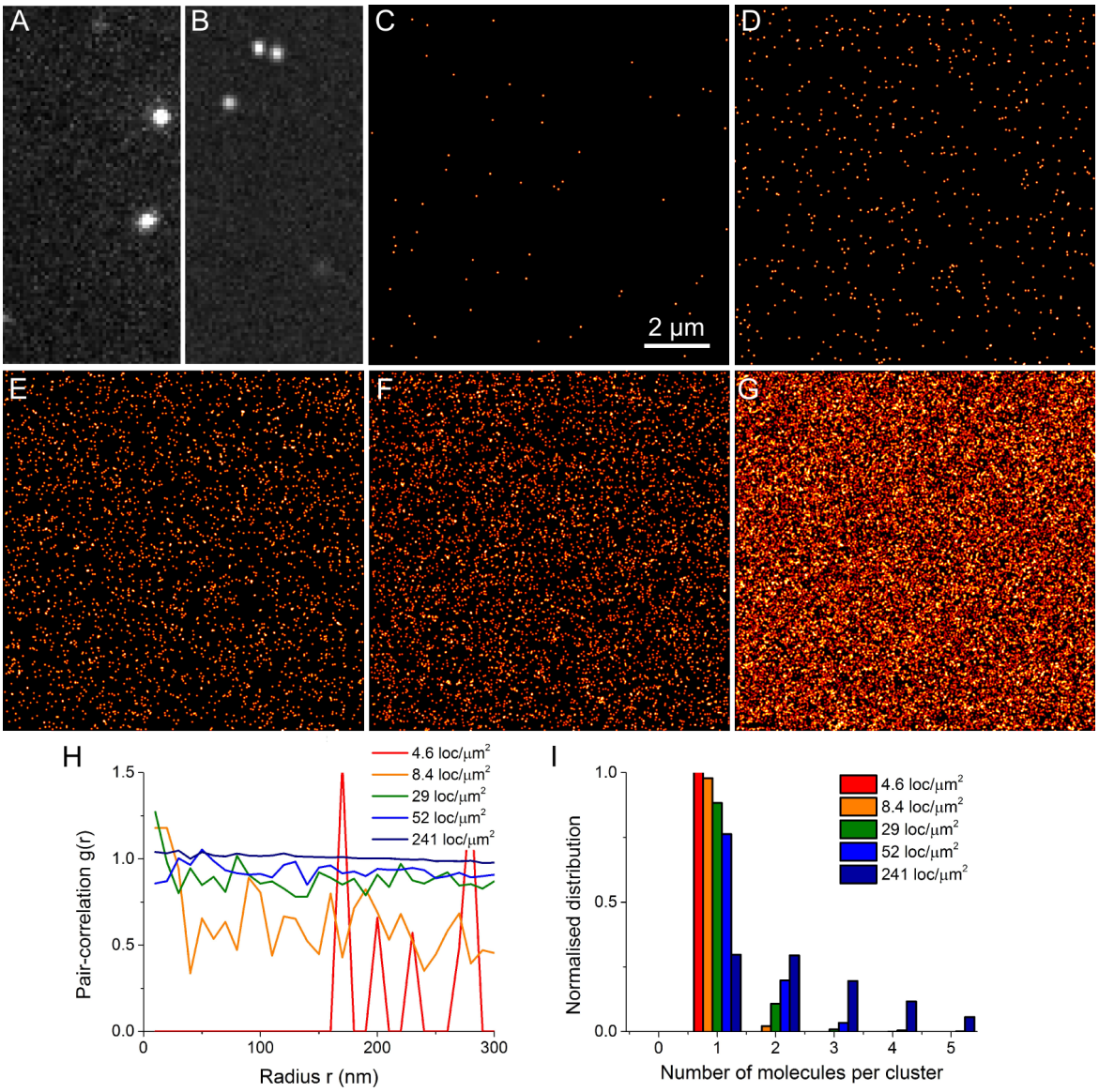


Figure 6.8 *Simulations provide insights on the dependence of counting analyses to localisation densities.* Simulated PSFs were drawn from experimental distributions of fitted localisations (distributions of intensity, width, ellipticity, and noise) for various number of frames in order to simulate different localisation densities. **A**: Region of a presentative frame of the experimental data which provided the distributions of localisations. **B**: Region of a representative simulated frame. **C-G**: Super-resolved figures of the localisations obtained after fitting the simulated data for increasing localisation densities of 0.83, 8.3, 41, 83, and 413 localisations/µm$^2$, resp. Because of various pitfalls in simulation, PSF fitting and estimation of the localisation densities, densities of 4.6, 8.4, 29, 52, and 241 localisations/µm$^2$ were recovered after PSF fitting, resp. **H**: Pair-correlation functions of the recovered list of fitted localisations for the different localisation densities. **I**: Normalised distributions of number of molecules per cluster after spatio-temporally grouping the recovered localisations using the pair of thresholds ($d_{Thresh} = 60$ mm, $t_{Thresh} = 3$ s) for each simulated density of localisations. Scale bar: 2 µm (same scale in panels A-G).

### 6.2.3 State of the TCR

Although none of the counting methods tested here proved to be very robust, their drawbacks have two origins: the stochasticity of photo-blinking of the fluorophore and single-molecule noise detected in the sample. For practical reasons, yeast cells were used as a control model to express multiple repeats of mEos3.1 and test a few counting methods. But the single-molecule noise originating from the fixed yeast cells might not be representative of the noise observed in fixed T cells. This is why a monomeric (CD86), and a dimeric (CD28) membrane protein, or the $\beta$ chain of the TCR were fused to mEos2 and stably expressed in a TCR-deficient hybridoma T cell line at low densities.

Designing a monomeric and a dimeric controls enables the direct comparison of the state of the TCR to them. Since robust methods for counting absolute stoichiometry of complexes are not available yet, the relative stoichiometry of the TCR to known multimers is studied here.

#### Pre-activation and fixation

Observing the state of the TCR on a resting T cell presents challenges that must be carefully addressed: (1) TCRs form micro-clusters at the membrane of the T cell shortly after being triggered [203]; (2) recent work from Chang, Fernandes, Ganzinger, Lee *et al.* (submitted) reveals that T cells trigger on many surfaces that used to be considered as non-activating (*e.g.* IgG-coated glass, and as discussed in the introduction). This implies that imaging the membrane of a live resting T cell might be more challenging than previously thought. This could also account for the difference in the state of the TCR observed on the apical [250] *vs.* the contact-forming [248] side of the cell.

Live T cells stably expressing a TCR$\beta$-mEos2 fusion construct were dropped on a poly-lysine coated coverslip and imaged under 561 nm and low 405 nm TIRF illumination. In such conditions, bright clusters of TCRs were observed (Figure 6.9, C, arrows). The intensity traces over time of these structures did not exhibit the photo-blinking or photo-bleaching single-step behaviour characteristic of single fluorophores (Figure 6.9, A). In comparison, single-molecule behaviour was detected outside of these clusters (Figure 6.9, B and D, arrow heads). These observations indicate that micro-clusters are formed on IgG-coated surfaces which thus activate the T cells. These data are consistent with observations of Williamson *et al.* (ref. [257], supplementary information) that "adherence, even onto non-activating antibodies results in a partial T cell activation". They consequently conclude that to study resting T cells, cells have to be fixed in suspension.

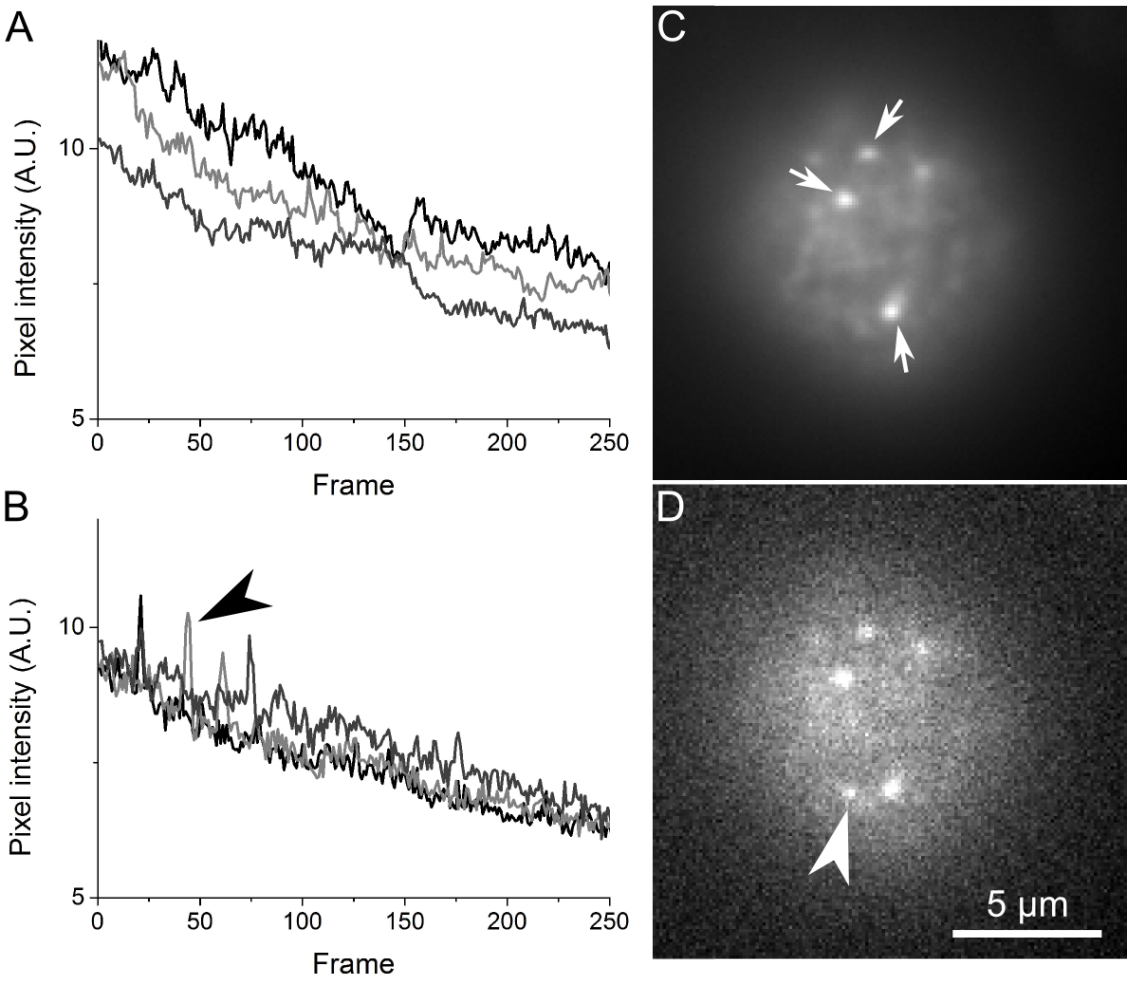


Figure 6.9 *Live T cells form TCR micro-clusters on a non-activating antibody-coated surface.* Live T cells stably expressing a TCR$\beta$-mEos2 fusion protein were dropped on a glass coverslip coated with non-specific antibodies and imaged under both 561 nm TIRF illumination and low and continuous 405 nm activation. **A-B**: The pixel intensity traces of three bright and immobile PSFs (arrows in C), and three single-molecule PSFs stochastically appearing during the experiment (the black arrow head designs the curve corresponding to the PSF shown by the white arrow head in D) were plotted (exposure: 50 ms). **C**: Average intensity of the 250 frames of the experiment for one representative T cell. **D**: One frame of the movie averaged in C, during which a single-fluorophore (arrow head) appeared. Scale bar: 5 µm (same scale in panels C-D). A.U.: arbitrary unit.

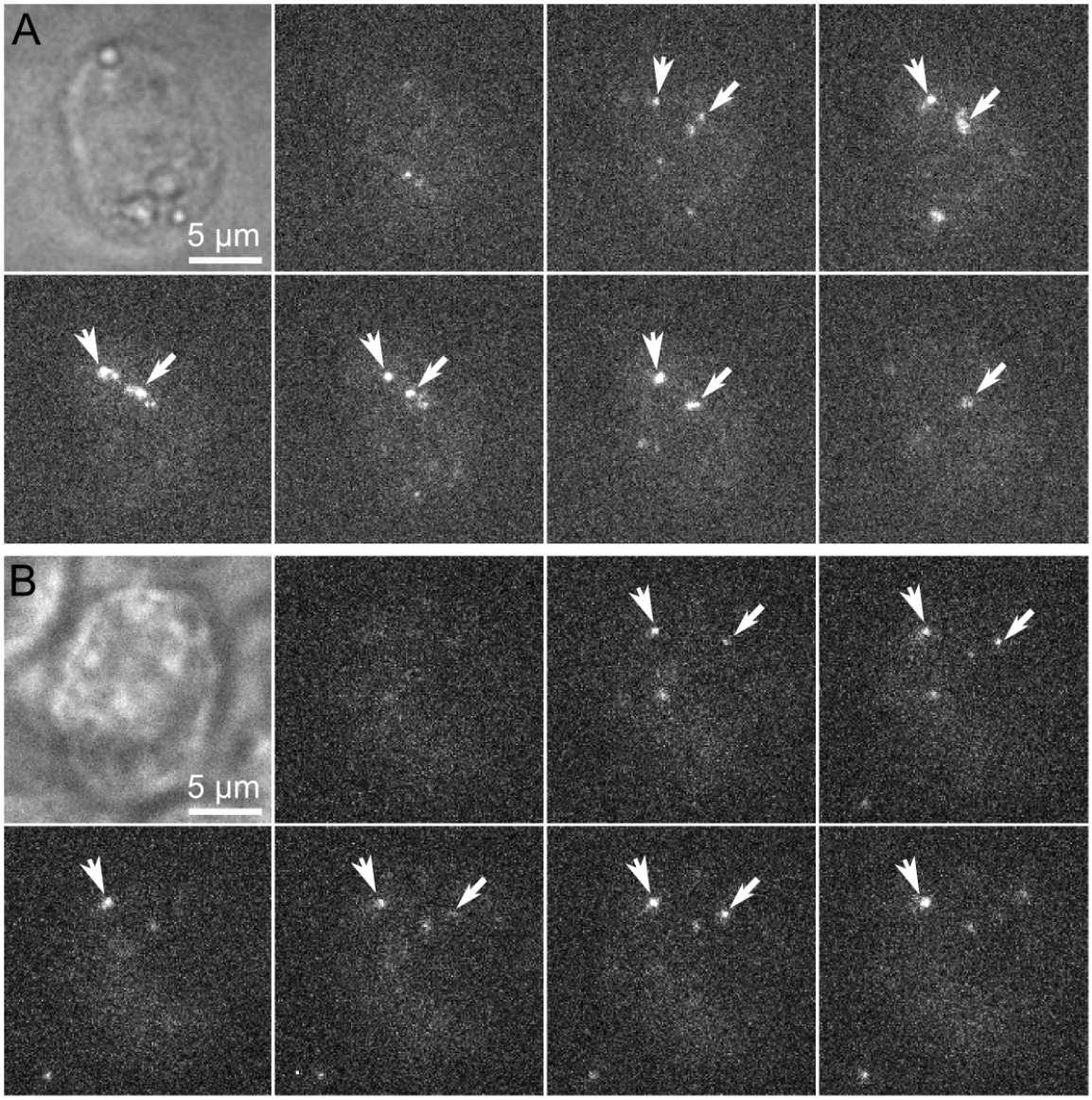


Figure 6.10 *Assessing the fixation of T cells.* Live T cells stably expressing a TCR$\beta$-mEos2 fusion construct were fixed in suspension in 4% formaldehyde and no (**A**) or 0.2% (**B**) glutaraldehyde in T cell medium for 30' at 37°C. After fixation, T cells were washed three times in PBS and immobilised under a 2% agarose gel pad on a glass coverslip. Finally, cells were imaged under 561 nm TIRF illumination and 405 nm continuous Fermi TIRF activation. For each fixation condition, a white light transmission snapshot of a representative cell is shown, followed by seven consecutive frames of the SMLM experiment. Along the seven frame, arrows track two activated fluorescent emitters. Scale bars: 5 µm (same scale for all panels).

In order to image resting T cells, T cells were fixed in solution in 4% formaldehyde and immobilised on the coverslip under a 2% agarose gel pad. This also had the effect of slightly squeezing the cell on the coverslip, enabling to image a larger surface of the membrane of the cells compared to imaging fixed cells sitting (by gravity) on a poly-lysine coated coverslip [251]. However, activated TCR$\beta$-mEos2 proteins that could be followed during more than a single frame were still mobile in the membrane (Figure 6.10, A, arrows). Consistent with this observation, the shapes of the PSFs were also deformed, which is characteristic of sub-exposure diffusion [188]. All movement and asymmetry of the PSFs disappeared when adding 0.2% glutaraldehyde to the fixation buffer (Figure 6.10, B, arrows). Other fixation protocols (methanol, different incubation time and temperature) as proposed by Tanaka *et al.* for fixing membrane proteins were also tried [267]. Optimal activation efficiency, brightness of the activated form of mEos2 and limited movement of the imaged proteins were obtained when incubating the cells in 4% formaldehyde and 0.2% glutaraldehyde in T cell medium for 30' at 37°C. This fixation protocol was therefore used in the experiments presented here.

Although fixed in solution, some cells showed some large-scale clustering, reminiscent of a 'protein island' or 'lipid raft' structure (*e.g.* comparing Figures 6.11 and 6.13). This effect might reflect on pre-activation state of the T cell, in which TCR micro-clusters start to form. As this phenomenon was rarely observed, it is speculated that such cells might have been activated while in contact with surfaces in the flask they were growing in, or in the plastic tube they were fixed in. This underlines how sensitive T cells may be to most surfaces for activation. Further research in the interaction of cells with surfaces of different stiffness and its implication in cell growth and differentiation is required to provide better understanding in the mechanism at stake [268]. Stiffness of surfaces is known to specifically impact T cell growth and activation (*cf.* ref. [269] and personal communication from M. Aßman, who observed different T cell activation behaviour on plastic and glass).

### Population variability of TCR$\beta$-mEos2 expression levels

As discussed in Section 6.2.2, the level of expression of the mEos2-tagged protein of interest is important for all counting analyses studied here. Thus, some control over the level of expressed fusion proteins was required. Moreover, because of the stochastic photo-physics of single fluorophores and the stringent thresholds used to reject false localisation (*cf.* Table 6.6), data from many cells have to be combined to draw any conclusion. Therefore, a uniform population of cells with similar expression levels was seeked.

Examples of the spread of expression levels observed in cells stably expressing the TCR$\beta$-mEos2 construct are given in Figure 6.12. Similar spread was observed for the con-

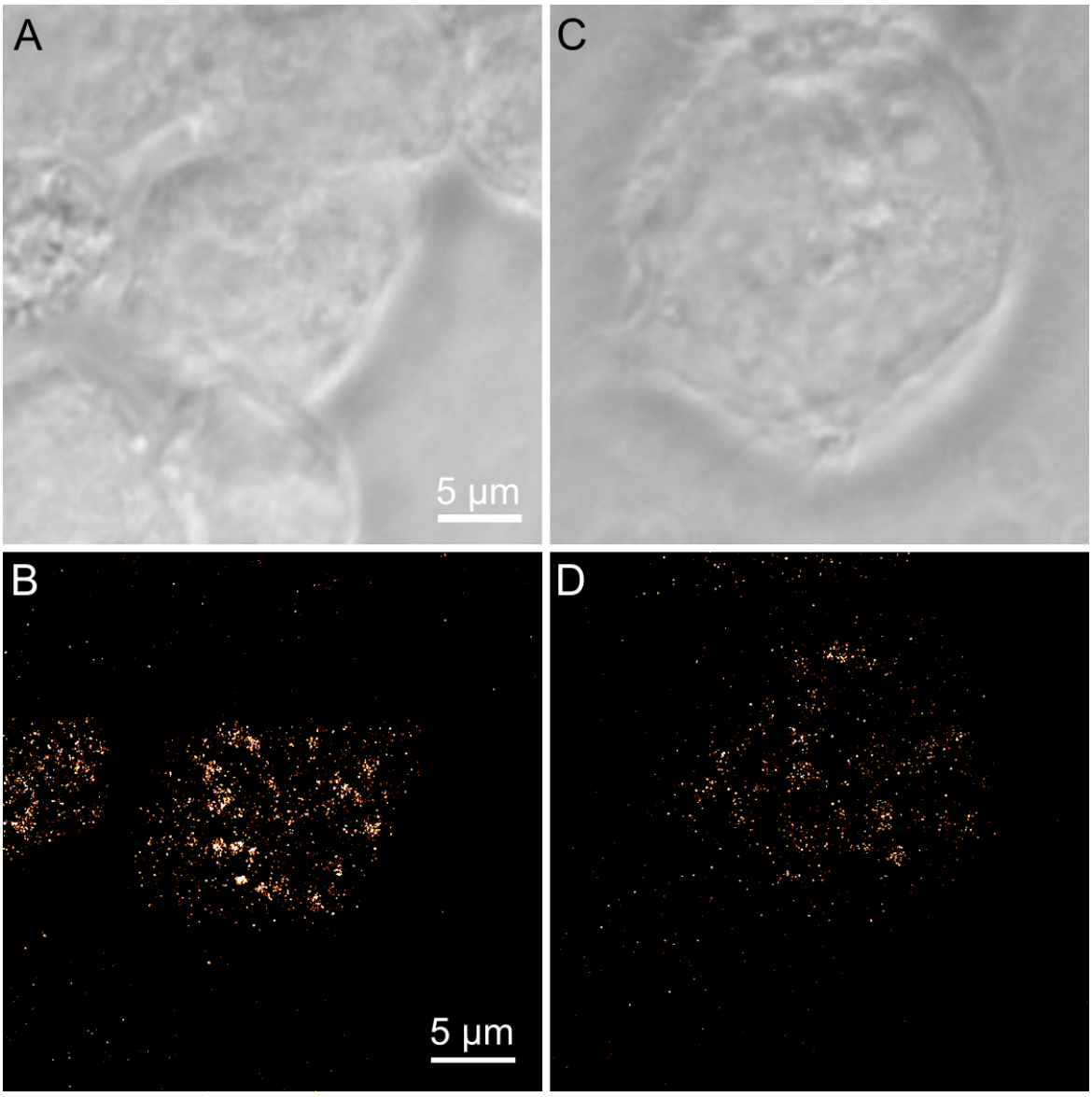


Figure 6.11 *Large-scale clustering suggest pre-activation of T cells.* As in Figure 6.10, B, T cells expressing a TCR$\beta$-mEos2 fusion construct were fixed in suspension in 4% formaldehyde and 0.2% glutaraldehyde in T cell medium for 30' at 37°C. After fixation, T cells were washed three times in PBS and immobilised under a 2% agarose gel pad on a glass coverslip. Finally, cells were imaged under 561 nm TIRF illumination and 405 nm continuous Fermi TIRF activation. From the population of cells imaged, about 1-2% cells showed some large-scale clustering in their super-resolved picture. Two representative examples are shown. **A,C**: White light transmission snapshots of the cells. **B,D**: Corresponding super-resolved figures. Scale bar: 5 µm (same scale for all panels).

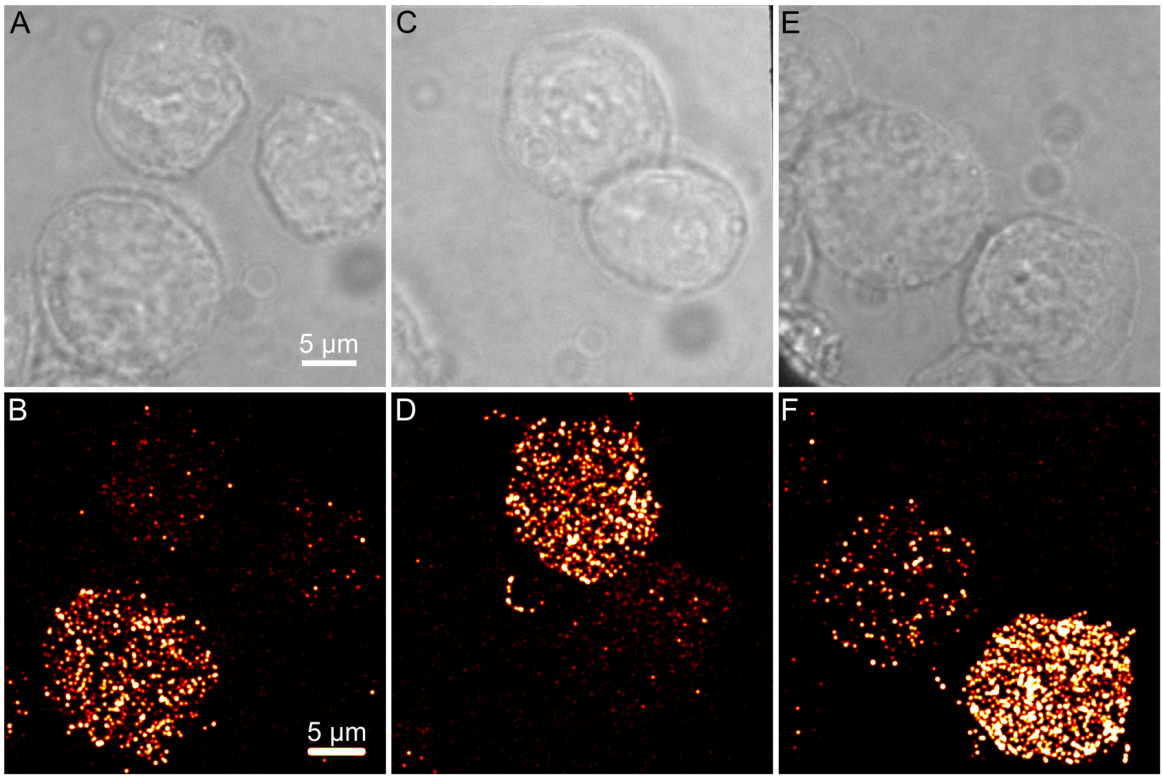


Figure 6.12 *Variation of the expression levels of mEos2-fused proteins.* T cells expressing a TCR$\beta$-mEos2 fusion construct were fixed and imaged as described in Figure 6.11. Various expression levels of the protein on the membrane of the T cells were observed. About 5% of the cells highly expressed the fluorescent construct. Three examples of two to three nearby cells underline the range of expression levels observed in a single population. **A,C,E**: White light transmission snapshots of the cells. **B,D,F**: Corresponding super-resolved figures. Scale bar: 5 µm (same scale for all panels). Super-resolved images are convolved with an additional Gaussian blur ($\sigma$ = 110 nm) to increase the contrast of the figure.

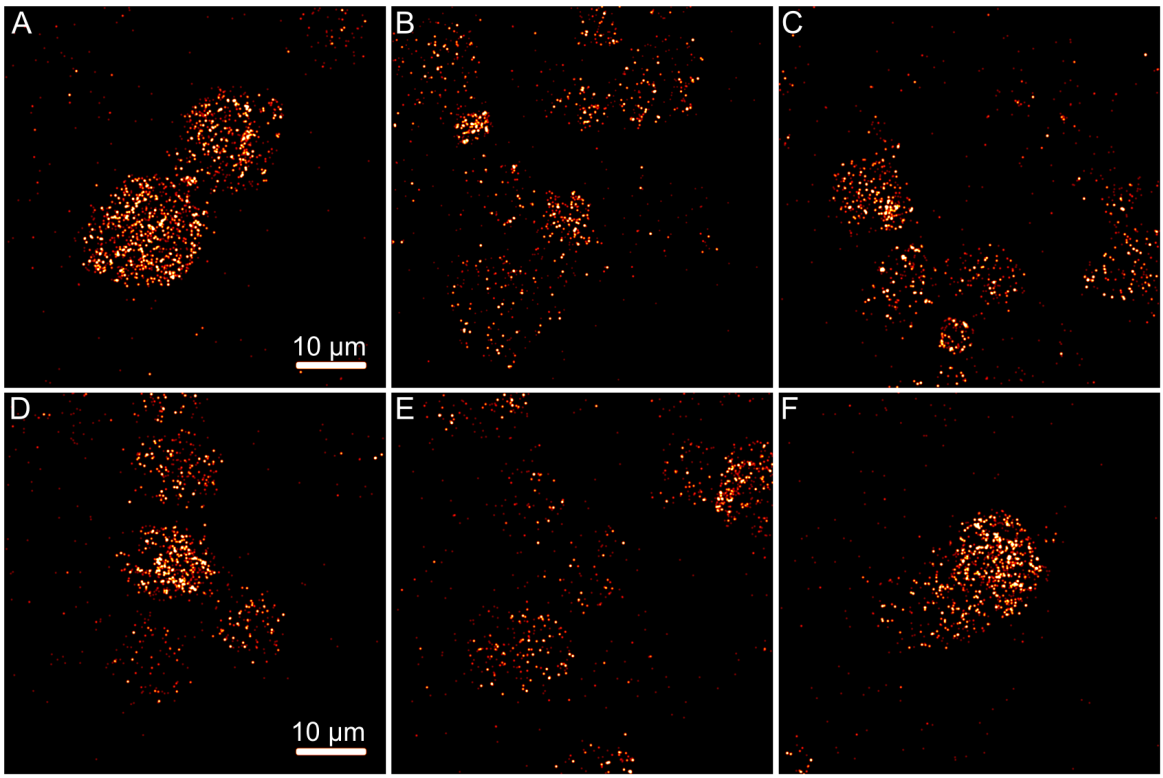


Figure 6.13 *Cells sorted for a specific expression level reverted to the diversity of expression levels of their parental population.* T cells expressing a TCR$\beta$-mEos2 fusion construct were sorted in four populations by flow cytometry depending on their fluorescence levels (as a measure for the expression level of the fusion construct). After recovery, cells from the lowest- (**A-C**) and the highest-expressing (**D-F**) populations were fixed and imaged as described in Figure 6.11. Very similar expression levels of the protein on the membrane of the T cells were observed. For each population, the super-resolved figures of two representative examples of nearby cells that were imaged by PALM are shown. Scale bar: 10 µm (same scale for all panels). Super-resolved images are convolved with an additional Gaussian blur ($\sigma$ = 110 nm) to increase the contrast of the figure.

trol cell lines expressing either CD86 or CD28 constructs. The fraction of high-expression cells represented about 5% of the cells. In order to homogenise the population of cells, each cell line was sorted in four populations, based on their green fluorescence (as a measure of mEos2 expression) by flow cytometry. However, within a week (which was the time required for recovering a population large enough to perform the experiment), the expression levels in each population had spread and usually did not differ from the parental population (*cf.* the highest and lowest expressing populations in Figure 6.13, A-C and D-F, resp.). A similar homogenisation and relaxation phenomenon has been described as a transcriptome noise in stem cell populations [270]. Here, since the population variability could not be easily controlled, sorted populations were screened and, if their expression levels differed, the populations with most comparable densities were further imaged. Finally, cells expressing noticeably high densities of fusion proteins were avoided.

### A rather monomeric TCR?

Despite the difficulties and limitations of the experiment, the three constructs (monomeric CD86-, dimeric CD28-, and TCR$\beta$-mEos2) were imaged under 561 nm illumination and continuous Fermi 405 nm activation. Because the TIRF angle was optimised on each day of experiment, only results from samples imaged on the same day were compared. For each SMLM movie, both the pair-correlation function $g(r)$ and, after grouping the localisations with the parameters (60 nm, 3 s), the distribution of molecules per cluster were computed. Results from different fields of view from the same biological sample were combined (as a weighted mean for the pair-correlation function −Figure 6.14, left−, and as a sum for the distribution of molecules per cluster −Figure 6.14, right). Finally, the average density of localisations was estimated for the whole sample (Figure 6.14, numbers in parenthesis in the legends in the left panels). Results of five independent days of experiments are plotted in Figures 6.14 and 6.15.

In the three experiments presented in Figure 6.14, the localisation densities vary around the threshold value of 30 localisations/μm$^2$ (*cf.* Section 6.2.2). Thus, both pair-correlation and grouping analyses have to be considered and sometimes compared. Interestingly, the TCR$\beta$-mEos2 construct is, in almost all experiments, the construct the least expressed. Although sharing the same promoter than both other constructs, the requirement of TCR$\beta$ to pair with a TCR$\alpha$ to be expressed at the membrane of the cell might explain its globally lower expression. However, in the first two experiments, localisation densities for the three constructs are similar (especially when correcting the number of localisations for the dimeric control CD28-mEos2), validating the qualitative comparison of the results. Since the

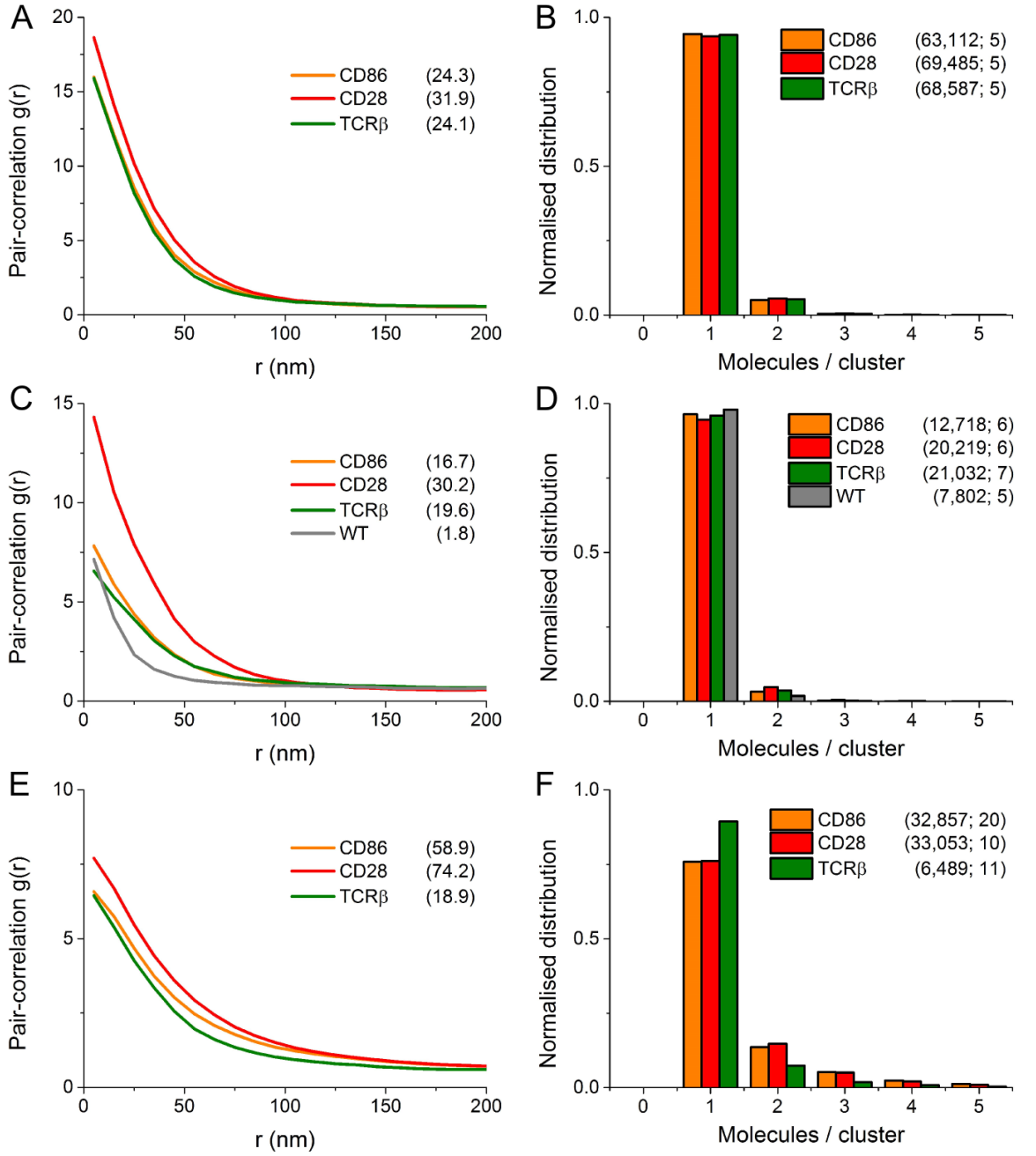


Figure 6.14 *Comparing TCR stoichiometry to a monomer and a dimer controls.* Three repeats of the same experiments were done in three different days and with independent batches of cells. Results from each experiment are presented in each of the three rows. Each day, T cells expressing a monomeric CD86- (orange), a dimeric CD28- (red), a TCR$\beta$-mEos2 (green), or no ('WT', grey, in the second experiment) constructs were fixed and imaged as described in Figure 6.11. Results from more than five cells were combined for each sample (as a weighted mean for the pair-correlation function; as a sum for the distribution of molecules per cluster). **A,C,E**: Plot of the pair-correlation functions of the constructs. Numbers in parentheses in the legend: Density of localisations for each construct. **B,D,F**: Normalised distributions of the number of molecules per cluster for all constructs after spatio-temporal grouping of the localisations with the pair of thresholds (60 nm, 3 s). Numbers in parentheses in the legend: Total number of molecules detected for each construct and number of fields of view combined.

densities are lower than the threshold value of 30 localisations/$\mu m^2$, although close to it, the distribution of molecules per cluster is discussed first.

In the three first experiments, the distribution of molecules per cluster for TCR$\beta$-mEos2 is closer to CD86-mEos2 than to CD28-mEos2 (Figure 6.14, B, D and F). Interestingly, the same conclusion can be drawn from the comparison of the pair-correlation functions (Figure 6.14, A, C and E). In the second experiment, untransfected cells ('WT'), with no mEos2 expression, were fixed and imaged. The localisation density of this negative control is very low compared to any other sample ($1.8 \ll 16.7$ localisations/$\mu m^2$); its distribution of molecules per cluster is even more shifted to lower numbers of molecules than it is in the case of the monomeric CD86-mEos2. Finally, the pair-correlation of the negative control stands below all other pair-correlation functions. This indicates that both CD86- and TCR$\beta$- (and therefore CD28-)mEos2 constructs are well expressed and imaged: for these constructs, results successfully detect some signal above the single-molecule noise.

During the third experiment, a large variation of localisation densities was observed between the three samples (more than a three-fold difference between TCR$\beta$- and CD86-mEos2). As the distribution of molecules per cluster is sensitive to differences in localisation densities (*cf.* Section 6.2.2), and since the densities of both CD86- and CD28-mEos2 are high above the threshold value for which the grouping analysis is valid, the distribution of molecules per cluster should be disregarded (Figure 6.14, F). However, the pair-correlation graph (Figure 6.14, E), consistent with both previous experiments, confirms that the pair-correlation analysis is less sensitive to differences of localisation densities.

Altogether, these three first experiments are in favour of a monomeric TCR$\beta$, consistent with previous work [250, 251]. This conclusion however needs to be balanced by contrasting results obtained in two other experiments (Figure 6.15). The fourth experiment (first row in Figure 6.15) shows very little difference between the pair-correlation functions of both monomeric and dimeric controls (Figure 6.15, A). However, the low localisation densities, much lower than the threshold of 30 localisations/$\mu m^2$, mean that the pair-correlation analysis should be disregarded. The grouping analysis, though, does not reveal much difference between any of the samples, not even the negative control ('WT', Figure 6.15, B). Noticeably, the densities of localisations for TCR$\beta$-mEos2 and the negative controls are almost identical, which indicate that the expression levels are too low for any signal to be statistically detected over the single-molecule noise.

The fifth experiment (Figure 6.15, C-D) is contradictory. The grouping analysis is in favour of a monomeric state of TCR$\beta$-mEos2, for any of the three sorted populations imaged. But the localisation densities are almost all higher than the threshold of 30 locali-

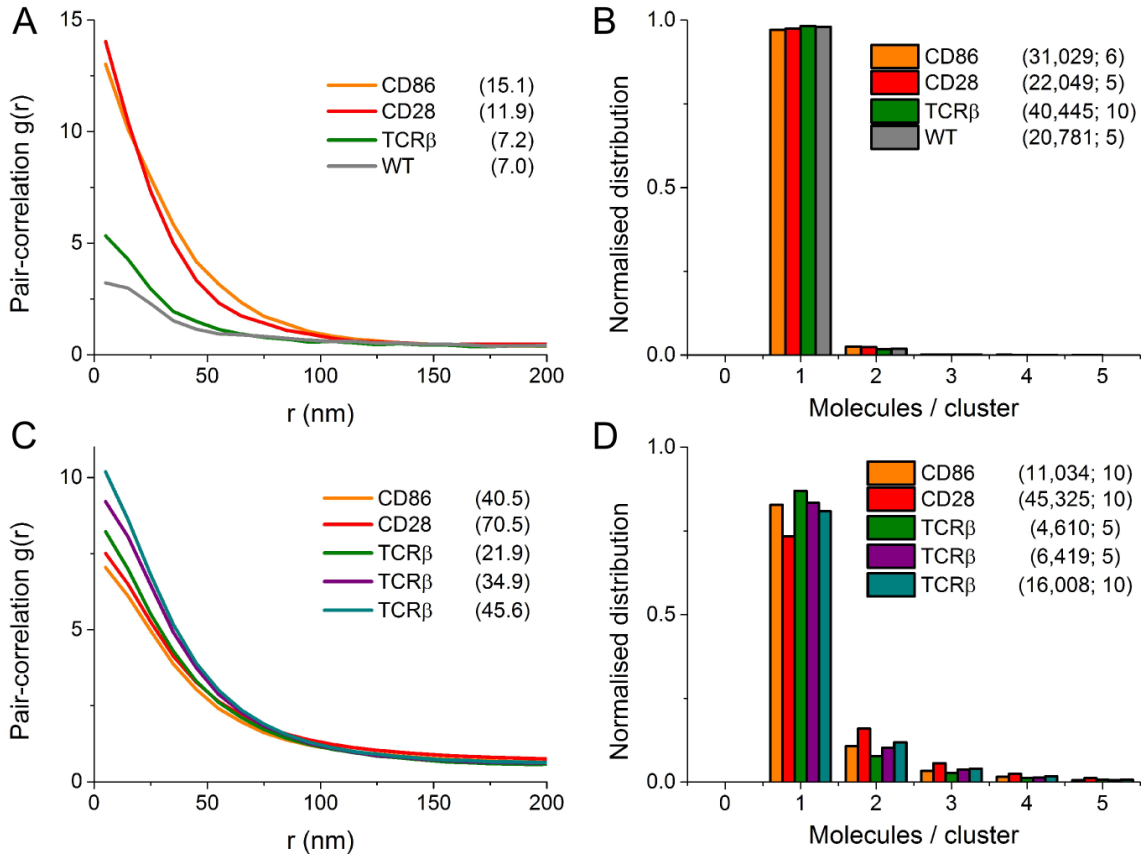


Figure 6.15 *Robustness and repeatability of relative counting of the TCR.* Two additional repeats of the experiments described in Figure 6.14 were performed in two different days and with independent batches of cells. Results from each experiment are presented in each of the three rows. Each day, T cells expressing a monomeric CD86- (orange), a dimeric CD28- (red), a TCR$\beta$-mEos2 (green, purple and cyan, for different expression levels), or no ('WT', grey, in the first experiment) constructs were fixed and imaged as described in Figure 6.11. Results from more than five cells were combined for each sample (as a weighted mean for the pair-correlation function; as a sum for the distribution of molecules per cluster). **A,C**: Plot of the pair-correlation functions of the constructs. Numbers in parentheses in the legend: Density of localisations for each construct. **B,D**: Normalised distributions of the number of molecules per cluster for all constructs after spatio-temporal grouping of the localisations with the pair of thresholds (60 nm, 3 s). Numbers in parentheses in the legend: Total number of molecules detected for each construct and number of fields of view combined together.

sations/$\mu m^2$ above which the grouping analysis looses its validity. Conversely, the pair-correlation analysis shows very little difference between the monomeric and dimeric controls and indicates higher blinking rates (interpreted as clustering state) than the dimeric control for the three sorted populations of cells expressing TCR$\beta$-mEos2.

This last experiment could reveal some pre-activated cells, forming micro-clusters of TCRs. However, the probability to observe such an artefact in three different samples is very low. It nevertheless underlines the poor robustness of the experiment and its difficult reproducibility due to the convolution of many stochastic and uncontrolled parameters: (1) the stochastic photo-blinking of mEos2, (2) stochastic single-molecule noise, (3) the low transcription of a gene, and the resulting expression of low densities of proteins [271, 272], and (4) the possible pre-activation of the T cells before or during the fixation protocol.

### 6.2.4 Two-colour strategy

In an attempt to only select TCR$\beta$-mEos2 PSFs and reject all single-molecule noise, a two-colour strategy was designed [126]: an antigen-binding fragment (Fab) of a monoclonal antibody directed against the ectodomain of TCR$\beta$ was labelled with Atto655 (*cf.* Section 3.3). After fixation, cells were labelled with such Atto655-Fabs, washed, and immobilised under an agarose pad. Samples were then sequentially imaged under 640 nm TIRF illumination, and under both 561 nm TIRF illumination and continuous Fermi 405 nm activation.

For each field of view, localisations of each channel were extracted and their positions channel-corrected (*cf.* Section 3.2.3). The super-resolved image of a representative cell expressing CD3$\delta$-mEos2[8] on its plasma membrane and of a representative TCR-deficient negative control cell are shown in Figure 6.16, B and E, resp. Strikingly, a lot of single-molecule noise is observe in both channels, and the CD3$\delta$-mEos2 expressing cell is indistinguishable from the negative control. Also, CD3$\delta$-mEos2 and $\alpha$-TCR Fabs do not co-localise significantly. This is confirmed by coordinate-based co-localisation analysis (*cf.* Section 3.4.2, Figure 6.16, C and F-H).

These results underline that the two-colour experiment requires some optimisation of the labelling strategy in relation with the fixation of the cells, of the CD3$\delta$-mEos expression level, and of the imaging protocol. However, before investing time on complex optimisation

[8] After a few unsuccessful attempts at labelling anti-human TCR antibodies with Atto655, the experiment was transferred from the human model – J.RT3 cell line – to the mouse model – BW5147 cell line. Both cell line do not express a full TCR complex at their surface: although J.RT3 is deficient in TCR$\beta$ subunit, BW5147 cells lack both CD3$\delta$ and CD3$\zeta$ subunits. Consequently, the transfected subunit of the TCR, labelled with mEos2, changed from human TCR$\beta$ to mouse CD3$\delta$. And BW5147 cells were co-transfected with an unlabelled mouse CD3$\zeta$ chain.

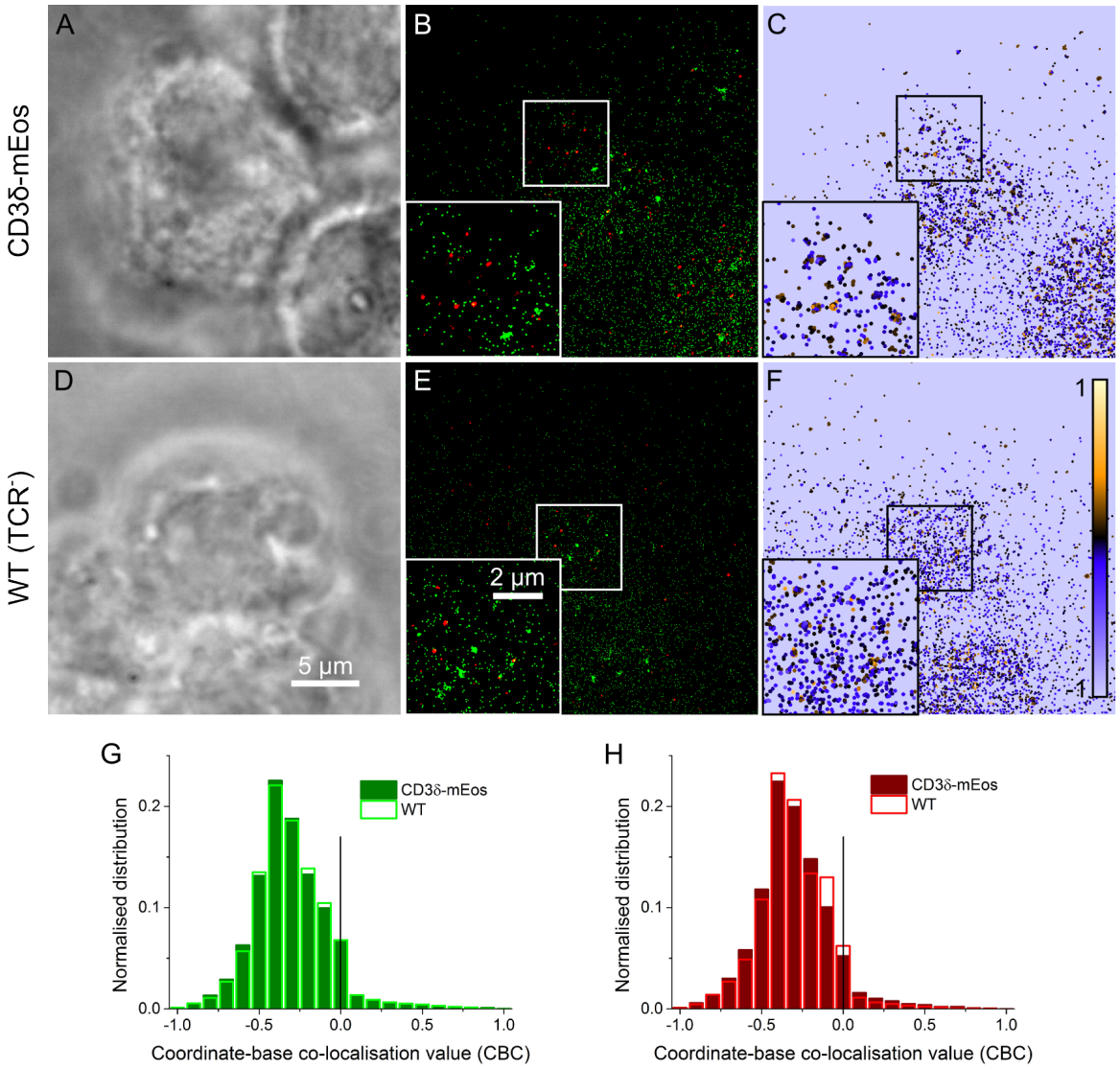


Figure 6.16 *Two-colour labelling to reject single-molecule noise.* CD3$\delta$-deficient T cells expressing either a CD3$\delta$-mEos2 (**top row**) or no ('WT', **middle row**) fusion construct were fixed as described in Figure 6.11. After three washes in PBS, cells were incubated for 30' on ice with anti-TCR$\beta$ Fabs labelled with Atto655. Cells were then washed three times in PBS and immobilised between an agarose gel pad and a glass coverslip. Samples were sequentially imaged under 640 nm TIRF illumination, and under both 561 nm TIRF illumination and continuous Fermi TIRF activation. For each sample, a representative cell is shown. **A,D**: White light transmission snapshot of the cell. **B,E**: Super-resolved figure of the localisations detected in both green (mEos2) and red (Atto655) channels. Localisations were corrected for channel miss-alignment (*cf.* Section 3.2.3). **C,F**: Coordinate-based co-localisation (CBC) analysis of the SMLM localisations of the red channel (*cf.* Section 3.4.2), with respect to the green channel. For each localisation of the red channel, a co-localisation value between -1 (anti-correlation; blue) and 1 (positive correlation; orange) is computed. **G-F**: Normalised distribution of the CBC values for all localisations of each sample (CD3$\delta$-mEos2: plain bars; TCR$^-$: empty bars) with respect to either channel (G: green; H: red). Scale bar: 5 µm (same scale for all panels).

experiments, one might consider and evaluate the benefits and drawbacks of this approach: by removing one stochastic unknown (single-molecule noise), the two-colour SMLM actually adds a few new unknowns that will each decrease the accuracy of the co-localisation such as the labelling efficiency of the Fab, the sampling ratios of both labels, the switching efficiency of Atto655, the compatibility of the imaging conditions for mEos and Atto655, the registration error between both channels, or the accuracy of the labelling of two different subunits on each side of the plasma membrane [52, 132]. In this respect, since TCRs are expressed at the surface of the fixed cells at low density, Fabs could be labelled with conventional non-switching dyes such as AlexaFluor647: most TCRs could be resolved and part of the complexity of the two-colour SMLM experiment would be avoided.

## 6.3 Conclusion and future experiments

Counting absolute number of proteins by single-molecule fluorescence microscopy is still at its beginning and important challenges are still to be overcome. Although it may confirm other results or point towards possible stoichiometries, the robustness and reproducibility of single-molecule counting remains unconvincing. This is due to the convolution of many stochastic parameters that are still not well controlled and corrected for. Spatio-temporal grouping-based counting methods require low densities of complexes which reduce the signal-to-noise ratio and decrease the amount of data recorded per field of view (and because of the stochasticity of photo-blinking, many fields of view are needed). Pair-correlation based methods require higher sampling and densities of complexes. Although less sensitive to single-molecule noise because they involve extensive fitting and estimation of parameters, these methods are more optimised for clustering description than determination of absolute stoichiometry.

Concerning the state of the TCR on a resting T cell, the stochasticity of the photo-blinking of the fluorophore [141] is additionally obscured by issues raised by the specific role of the TCR in T cell activation, since the state of the TCR changes during its triggering which induces clustering. Moreover, recent work showed that T cells actually activate in the absence of ligand when contacting a stiff surface, such as a poly-lysine coated glass surface (considered until recently as a non-activating surface) (Chang, Fernandes, Ganzinger, Lee *et al.*, submitted).

Strategies to tackle the challenges of single-molecule counting need to carefully consider the advantages and drawbacks of increasing the complexity of an already leading-edge experiment, with all the technological complexity and subtle balances that such ex-

periments imply. In this chapter, exploring a two-colour co-localisation strategy to limit single-molecule noise was a convincing idea to investigate but it added suboptimal and unsatisfactory conditions to the experiment instead of increasing its accuracy. In a nutshell, while rejecting noise, many new limitations were faced, introduced by the second label (*e.g.* labelling efficiency, sampling, co-localisation).

Keeping the idea of using two colours to limit single-molecule noise, and because the TCR is expressed at low densities on the plasma membrane, a repeat of the DySCo experiment could compare the state of the TCR in a live cell at both the bottom of the cell contacting the coverslip [251] and the apical membrane with a 3D single-molecule microscope. This would investigate the hypothesis suggesting that the TCR would be monomeric on a resting T cell and form micro-clusters as soon as it would contact a stiff activating surface.

In a longer term, to avoid the intrinsic stochasticity of single-fluorophore photo-blinking [273], recent methods based on bright fluorophores and high localisation precision are emerging that may allow a subunit precision enabling the determination of the stoichiometry of complexes [7, 44]. Szymborska *et al.* confirmed the precise stoichiometry of the very homogeneous nucleopore complex and partially resolved its structure by class averaging.

Another interesting method is quantitative DNA-PAINT, a version of uPAINT microscopy where proteins are tagged with DNA probes that are stochastically binding complementary DNA probes labelled with a dye in solution [96, 274]. Since 'On' times are controlled by the affinity of the complementary probes and 'Off' dark times are controlled by the concentration of DNA probes in solution and the number of tagged proteins at the same position, the acquisition of many binding and dissociation events and the observation of the resulting distribution of dark times at each observed position, for fixed samples, would theoretically enable absolute counting. However, once again, careful study of the impact of the wide distributions (*e.g.* intensity, dark times) characterising most properties of single-fluorophore behaviour on single-molecule counting has to be undertaken [273].

# Chapter 7

# CD28 super-agonism

The original idea developed in this chapter was from Prof. S.J. Davis. All cell lines were transfected, and most antibodies were labelled and provided by M. Aßmann. IL-2 assays were also performed by M. Aßmann. All other experiments were done by M. Palayret. Experimental design was the fruit of the collaboration of Prof. S.J. Davis, Prof. D. Klenerman, Dr S.F. Lee, Dr K.A. Ganzinger, M. Aßmann and M. Palayret. All data analysis, and code writing was undertaken by M. Palayret. Dr S.F. Lee and M. Palayret designed and built the super-resolution instrument used in this chapter.

## Aim of the experiments described in this chapter

This chapter aims at studying the mechanism of T cell super-agonism activation (*cf.* Section 7.1.2) at the single-molecule level for the first time, in parallel with functional IL-2 assays, in order to rule out, validate or refine the different models that have been proposed for super-agonism (*cf.* Section 7.1.3). In the light of previous works by Chang, Fernandes, Ganzinger, Lee *et al.* (submitted) unravelling ligand-independent TCR triggering in accordance with the KS model, predictions from this model are especially targeted by the design of the experiments.

Studying the mechanism of super-agonism is of key importance for theoretical and practical reasons. Any credible model of T cell activation has to explain related phenomena such as antibody-induced receptor triggering. As such, understanding the mechanism of CD28 super-agonism helps the more general comprehension of T cell triggering. The mechanism of CD28 triggering might also apply to other receptors of the immune system [275] and beyond. More practically, in light of the dramatic effect of the TGN1412 SA *in vivo*, a more complete understanding of CD28 triggering and super-agonism will allow to target

new signalling proteins to develop innovative drugs for immunotherapy.

# 7.1 Introduction

## 7.1.1 CD28, a co-stimulatory membrane protein

When recognising an antigen-presenting cell (APC), $CD4^+$ T cells become activated and start proliferating, allowing for a strong and specific immune response against the pathogen. Activation of a T cell requires two different signals delivered by an APC: signal 1, or triggering of the TCR (see Chapter 6), and signal 2, induced by the triggering of a co-stimulatory receptor.

Signal 1 is delivered by the TCR recognising its specific antigen (a non-self peptide presented on a MHC receptor on the APC membrane). This signal alone is not sufficient to activate a T cell. Indeed, without a co-stimulatory signal, the cell becomes anergic, *i.e.* it becomes harder to activate in the future.

Signal 2, *i.e.* the co-stimulatory signal, is not antigen-specific and induced by membrane proteins of the B7 family expressed on the APC upon stimuli specific to an infection, such as products of pathogens or of dead or necrotic cells, through the engagement of Toll-like receptors on the APC. This signal does not activate the T cell on its own, but modifies the interpretation of signal 1. This mechanism prevents inappropriate activation of a T cell that recognises self-antigens, which would lead to the development of an auto-immune reaction. The CD28 (cluster of differentiation 28) receptor is the only co-stimulatory receptor constitutively expressed on T cells. Engagement of both CD28 on naive T cells by either CD80 (B7-1, $K_D = 4$ μM) or CD86 (B7-2, $K_D = 20$ μM) ligands on APCs and the TCR induces IL-2 transcription, expression of high-affinity IL-2 receptor and T cell proliferation [276, 277]. While CD80 is a homo-dimer, CD86 is monovalent and, *in vivo*, binds favourably to CD28 [277]. Each CD28 homo-dimer engages only one CD86 monomer. Upon activation, T cells express other receptors such as CTLA-4 (cytotoxic T-lymphocyte-associated protein 4), ICOS (inducible T-cell co-stimulator) or PD-1 (programmed cell-death protein 1) on the T cell membrane to further modulate this signal, either through interaction with the same B7 ligands (CTLA-4, inhibitory) or B7-like ligands (ICOS, co-stimulatory in a subset of cells) [276].

CD28 is expressed on the plasma membrane as a homo-dimer thanks to a disulfide bond on the ectoplasmic side of the protein, close to the plasma membrane [277]. Its cytoplasmic tail contains different signalling motifs: a YMNM PI-3 kinase binding site whose activation

leads to the BCL-$X_L$ pro-survival pathway, and a separate PYAP SH3-kinase binding site critical for proliferation and IL-2 production [276]. These motifs are phosphorylated by external Src tyrosine kinases, but the mechanism by which triggering happens through ligand recognition is unknown. Also, during TCR triggering, the TCR recruits kinases such as Lck and ZAP-70 that become activated and, if recruited to the vicinity of CD28, can phosphorylate the tyrosines on CD28, introducing a cross-talk between the signalling pathways of both signal 1 and signal 2. This idea gets very interesting in the light of ligand-independent triggering of the TCR seeming to play a role in the anti-CD28 SA mechanism. However, the precise mechanism by which TCR and CD28 cooperate, whether at the cell surface or further downstream, is still unknown [278].

### 7.1.2 Super-agonism

Similar to the TCR, the natural ligand of CD28 can be replaced by a monoclonal antibody (mAb) which binds to and cross-links CD28 in experimental systems [279]. Most antibodies against CD28, referred to as 'conventional antibodies' (CA), similarly to the natural ligand CD86, are co-stimulatory as they amplify an anti-TCR signal, but do not induce T cell activation on their own. Surprisingly, some specific antibodies, subsequently called 'super-agonist' (SA), can fully activate T cells without TCR engagement both *in vitro* and *in vivo* (Figure 7.1) [278, 280]. A similar class of mAbs was discovered targeting the TCR that activate T cells without requirement for signal 2 [281]. Interestingly, as for SA targeting the TCR, soluble SAs targeting CD28 do not activate T cells. Immobilisation of the SA antibody is necessary for activation of cells independently of TCR triggering. Immobilisation of the SA via Fc receptors is also required *in vivo* [282].

In the rat animal model, two antibodies (one SA and one CA) have been thoroughly studied [278]. A couple of differences between them were observed: (1) the CA blocks SA-binding to CD28, suggesting that both antibodies bind related epitopes on CD28 or that they sterically exclude each other's binding, and that the CA binds CD28 in a more efficient way than the SA; (2) although interaction of either antibody with CD28 is very stable, the CA binds much faster to CD28 than the SA, confirming the previous conclusion. This is, however, specifically observed in primary T cells, but not in CD28-transfected fibroblast cells. This indicates that the binding rate of the SA depends on its local environment. Tacke *et al.* propose a model where CD28 is expressed on the plasma membrane with two hypothetical conformations in equilibrium. The SA would only bind to and stabilise a signalling-competent conformation; the CA would indifferently bind to either conformation. Binding

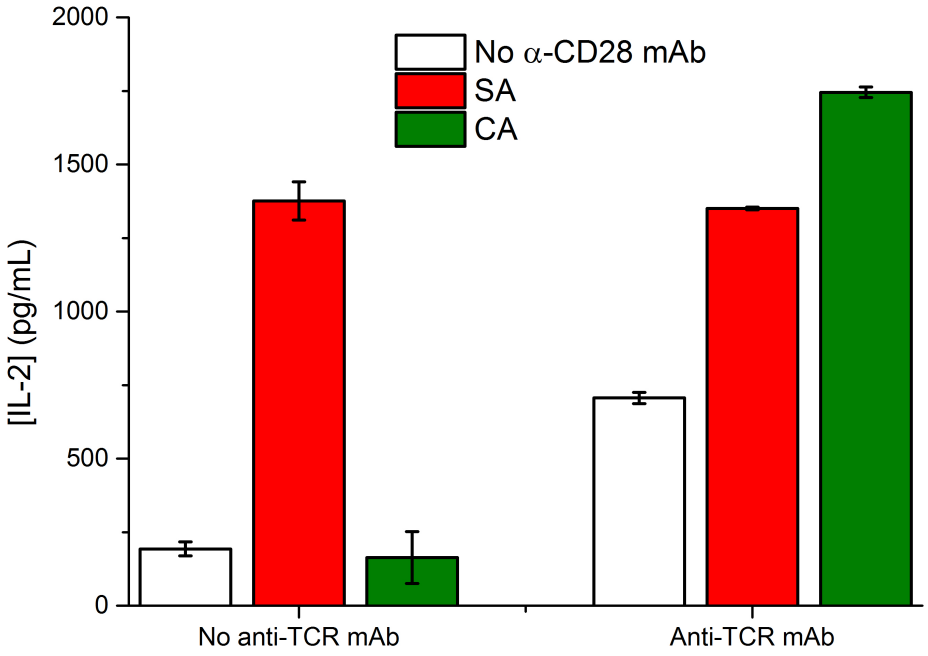


Figure 7.1 *Super-agonistic antibodies do not require TCR engagement (signal 1) for activating T cells.* The IL-2 secretion from cells incubated both with (**right panel**) or without (**left panel**) an anti-TCR SA (to trigger the TCR without need of signal 2), and with either no anti-CD28 antibody or one of two anti-CD28 antibodies (a so-called super-agonist −SA− and a conventional −CA− antibody) is recorded. IL-2 production is used as a marker for T cell activation.

of the SA would indeed be slower than binding of the CA. It would also induce a shift in the conformational equilibrium of CD28, explaining the ability of the SA to activate T cells without TCR co-engagement. This model, however, does not explain the necessity of SA immobilisation.

Super-agonists are not known natural ligands of CD28 *in vivo*. Super-agonism could therefore be regarded as an *in vitro* artefact. In preclinical murine model, the stimulation of CD28 with a SA activated and expanded $CD4^+$ T cells, and preferentially regulatory T cells, without detectable toxic or proinflammatory effect. Anti-CD28 SAs were hoped to be useful as anti-inflammatory immune modulators. In 2006, however, the unfortunate Phase I clinical trial of the anti-CD28 SA TGN1412 drew attention to the unexpected potency of this class of antibodies *in vivo*, which resulted in cytokine release syndrome, severe lymphopenia and life-threatening multi-organ failure in six trial volunteers [283]. Therefore, the medical interest for understanding the mechanism of super-agonism is evident.

### 7.1.3 A structural difference

A systematic study unravelled a convincing correlation between the functional class of SA and topology of epitope binding [284]: in rat and human cell lines, all studied mitogenic antibodies bind to the C"D loop of CD28, whereas all CAs bind close to the CD86 binding motif. The resolution of the crystal structure of the ectoplasmic domain of CD28 bound to an SA Fab, together with cryo-EM data, confirmed the predicted topology of both epitopes [285]: SAs bind on the 'side' of the extra-cellular domain of CD28, close to the plasma membrane, orthogonally to the epitope of CAs, localised on the 'top' of the homo-dimer. Topologically, an SA Fab is consequently $\sim 75$ Å closer to the plasma membrane than a CA Fab [234]. Importantly, the correlation between mitogenic potential and epitope position is not only verified for anti-CD28 antibodies, but also for anti-TCR and anti-PD1 antibodies (personal communication from Prof SJ Davis).

In summary, different models were proposed to investigate the functional difference of the two classes of mAbs [284, 285]:

**Preferential engagement of signalling-competent CD28:** this model is based on the hypothesis of an oligomerisation heterogeneity of the CD28 population. The SA would favourably bind and cross-link a signalling-competent mobile fraction, the 'side' epitope of CD28 being more difficult to access than the 'top' one in signalling-incompetent immobile micro-clusters [284]. It is, however, hypothetical whether these two subpopulations exist and this model does not explain the requirement for antibody immo-

bilisation in super-agonism activation.

**Differential cross-linking:** whereas the physiological ligand CD86 is monomeric, and each CD28 dimer engages only one CD86 monomer (probably due to steric constraints), both SA and CA bind CD28 divalently and are thus able to cross-link CD28 in possibly large-scale linear lattices through periodic CD28-mAb interactions [285]. Such lattice structures were described for the interaction of CTLA-4 with CD80. Through avidity, they are thought to dramatically increase the stability of the CD80-CTLA-4 interaction and the downstream inhibitory signalling responsible for ending the signalling cascade. Antibody-induced cross-linking of CD28 could similarly amplify CD28 signalling. The position of the SA epitope, on the 'side' of the CD28 homo-dimer, could hypothetically favour the binding of two different CD28 homo-dimers over the binding of both epitopes of the same homo-dimer, favouring cross-linking and explaining the increased triggering effect of the SA over the CA. However, no difference in cross-linking ability has been described so far. Nevertheless, a systematic difference of binding kinetics or dissociation constants between both classes of antibodies could also induce differential cross-linking. However, although this has not been investigated yet, the binary 'all-or-nothing' activation and the number of antibodies tested for each class makes this possibility unlikely. Furthermore, this model does not account for the requirement for antibody immobilisation in super-agonism activation, since cross-linking is favoured in solution.

**Antibody-induced conformational change:** binding of SAs could favour an 'active' conformation of CD28. Indeed, since all SAs bind to the same epitope, as in the key-lock model of ligand interaction, binding of the SA, but not the CA, could stabilise an otherwise less stable but signalling-competent conformation of CD28. This model is nevertheless unlikely as it requires long range conformational changes spanning across the plasma membrane, which is rare in interactions between antibodies and protein antigens [286]. Crystallographic evidence suggests that a rigid-body interaction with very little conformational change characterises the binding of CTLA-4 with its ligand [287]. Also, antibodies binding to shared epitopes rarely bind in exactly the same way [288]. However, a novel physical model involving a piston-like movement induced by the binding of the SA close to the plasma membrane, inspired by the mechanism of the aspartate receptor [289], could explain the activation of CD28 but still needs to be investigated [290]. Against this model, Evans *et al.* argue that the recent crystal structure is in favour of a single stable state of the CD28 homo-dimer

[285]. Lastly, as proposed, the piston model also fails to account for the requirement for antibody immobilisation.

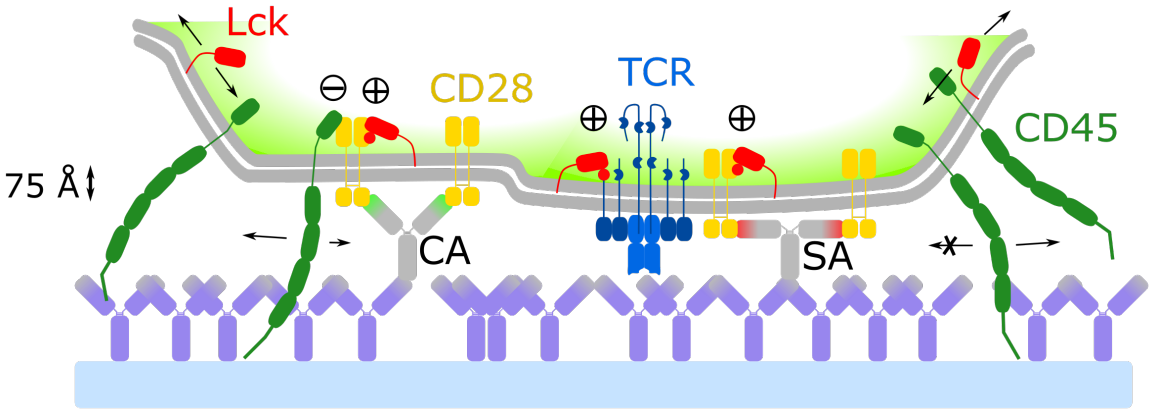


Figure 7.2 *Kinetic-segregation model for CD28 super-agonism.* The 75 Åof height difference between the SA and the CA could be responsible for differential segregation of phosphatases with large ecto-domains such as CD45. When a T cell (top, light green), decorated with CA forms a contact on a glass surface coated with secondary antibodies, the size of the contact does not prevent CD45 to diffuse in the contact. Thus, a null net phosphorylation of the CD28 and TCR receptors would be observed, leading to no activation of the cell. However, when the cell is decorated with the SA, the 75 Åshorter contact may hinder the entry and diffusion of membrane proteins with large ecto-domains, such as CD45. Thus, CD45 is excluded from the contact zone where the small Lck kinase is free of diffusing. This local segregation shifts the balance of kinase/phosphatase and the net phosphorylation of CD28 and the TCR get positive. If the receptors do not diffuse out of this local segregation zone, downstream signalling induces activation of the cell.

**Proximity effect:** the SA could also alter the arrangement of signalling proteins, either by physically interfering with signalling components and influencing the proximity of intracellular effector proteins, or by segregating surface receptors in a size-dependent manner analogous to the kinetic-segregation (KS) model proposed for TCR triggering [234] (Figure 7.2). Indeed, by binding to an epitope closer to the plasma membrane, SAs could either (1) sterically and very locally seclude all transmembrane protein with an ectodomain from getting near CD28 in a more efficient way than CAs, or (2) induce a closer contact zone inducing better size-dependent segregation of large-ectodomain transmembrane proteins. The requirement of antibody immobilisation also suggests the importance of the formation of a contact between the T cell and a surface (either the coverslip coated with anti-Fc secondary antibodies or a cell membrane presenting Fc receptors). This requirement is a typical prediction of the KS model.

## 7.2 Results

A dramatic increase in T cell activation, as measured by IL-2 production, was reproduced in mouse T cells (Figure 7.1) when stimulating with an indirectly immobilised SA antibody against CD28, compared to a CA. The super-agonistic signal, *i.e.* the binding of SA antibodies to CD28, consequently needs to pass from the extracellular surface through the plasma membrane to activate the downstream signalling pathways. Similarly to TCR triggering, this information can travel by different means: a change of conformation, a binding-induced aggregation, or a change of localisation.

In order to understand the effect of anti-rat-CD28 SA antibodies on CD28 at the mechanistic scale, a chimera CD28 (ectodomain of rat-CD28 fused to the transmembrane and signalling domain of the mouse-CD28) was fused to the photo-activable fluorescent protein mEos and stably expressed in the mouse BW5147 cell line. Therefore, the precise sub-diffraction distribution and diffusion of CD28 could be studied and compared under SA or CA activation.

### 7.2.1 Super-agonistic antibodies slow CD28 down

Stably transfected T cells were incubating for 15' at 37°C with 50 µg/mL of either SA or CA, dropped onto a coverslip coated with polyclonal secondary antibodies, and imaged under 561 nm TIRF illumination (Figure 7.3). A very small amount of additional 405 nm illumination was necessary for mEos activation.

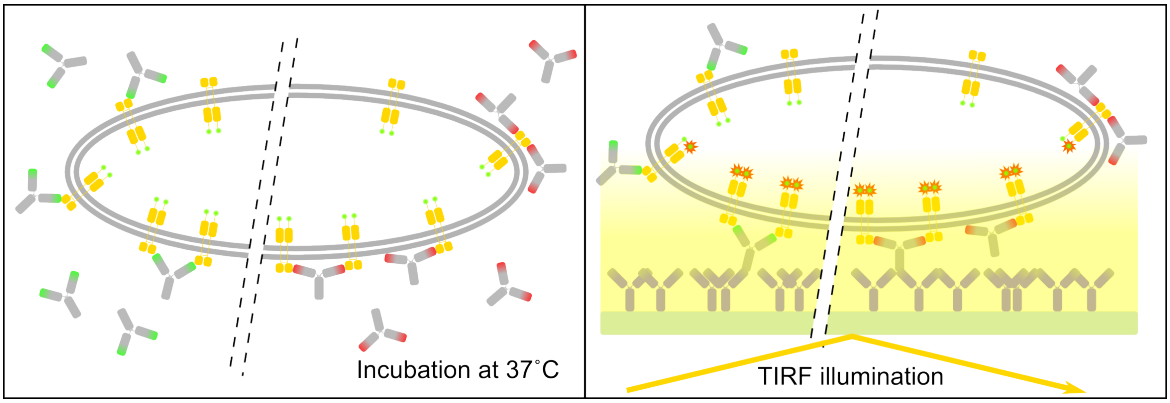


Figure 7.3 *Scheme of the diffusion experiments.* TCR-deficient cells were stably transfected with a construct of a mouse CD28 protein with the ectoplasmic domain of rat CD28, fused to a 30 amino acid linker and the mEos3.2 fluorescent protein at its intracellular end. Cells were incubated at 37°C for 15' with either SA, CA or no antibody (**left**), dropped on a coverslip coated with secondary antibodies and imaged under TIRF illumination (**right**).

At 37°C, activation by SAs induced the formation of clusters of localisations in the super-resolution image (Figure 7.4, top left panel) compared to activation by CAs (middle left panel), or cells left incubating in medium without antibody (bottom left). Since all localisations from all frames were plotted, such clusters can originate from two non exclusive effects: (1) real aggregation of separate CD28 fluorescently-tagged proteins, or (2) slowly diffusing CD28 proteins observed during multiple successive frames.

To study both effects, and because single fluorophores could be visually followed during several frames, localisations within 300 nm from each other were grouped into trajectories, allowing blinking events of up to four frames (as described in ref. [154] and Section 3.4.2). The trajectory radius of 300 nm (less than the dimension of three pixels of the camera), together with a frame exposure of 50 ms (frame rate of 20 Hz) allowed detection of diffusion coefficients up to 0.1 $\mu m^2/s$ [79]. A characteristic example of CD28-mEos tracks is given in Movie B.1.

Mean square displacement (MSD) analysis [291, 292] of the long trajectories (longer than ten frames, the five first time-points being used for the linear regression) showed a qualitative slowing down of CD28 induced by the SA (Figure 7.4, top middle panel) compared to activation by the CA or absence of activation (resp. middle and bottom middle panels). However, in order to quantify this behaviour, and because many trajectories were short [293], an approach using the probability distribution of square displacements was performed [294]: the probability $P(r^2,\tau)$ that a particle is found within a circle of radius $r$ from its initial position after a time-lag $\tau$ was calculated from the trajectories of at least five cells for ten multiples of the exposure time ($\tau \in \{50k \text{ ms}; k \in [\![1,\ 10]\!]\}$). $P(r^2, 50 \text{ ms})$ corresponds to the cumulative jump-distance distribution described by Grünwald *et al.* [293, 295, 296].

For each time-lag $\tau$, models of $p$ diffusing populations with diffusion constants $D_i$ can be fitted to the distributions [294, 297]:

$$P(r^2,\tau) = 1 - \sum_{i=1}^{p} \left[ f_i \exp - \frac{r^2(\tau)}{SD_i} \right] \tag{7.1}$$

This is exemplified for $p \in [\![2,\ 4]\!]$ populations for the distributions at $\tau = 100$ ms in Figure 7.4 (right column). All conditions (top to bottom: SA, CA or no antibody activation) are well-approximated by the models of three or four diffusing populations (resp. orange and yellow) as revealed by the residuals that show very little systematic deviation. Conversely, a model of two populations (red) does not efficiently describe the data. The best parsimonious description is thus a model of three diffusing populations.

For each population, the mean square displacement $SD_i(\tau)$ is proportional to the time-

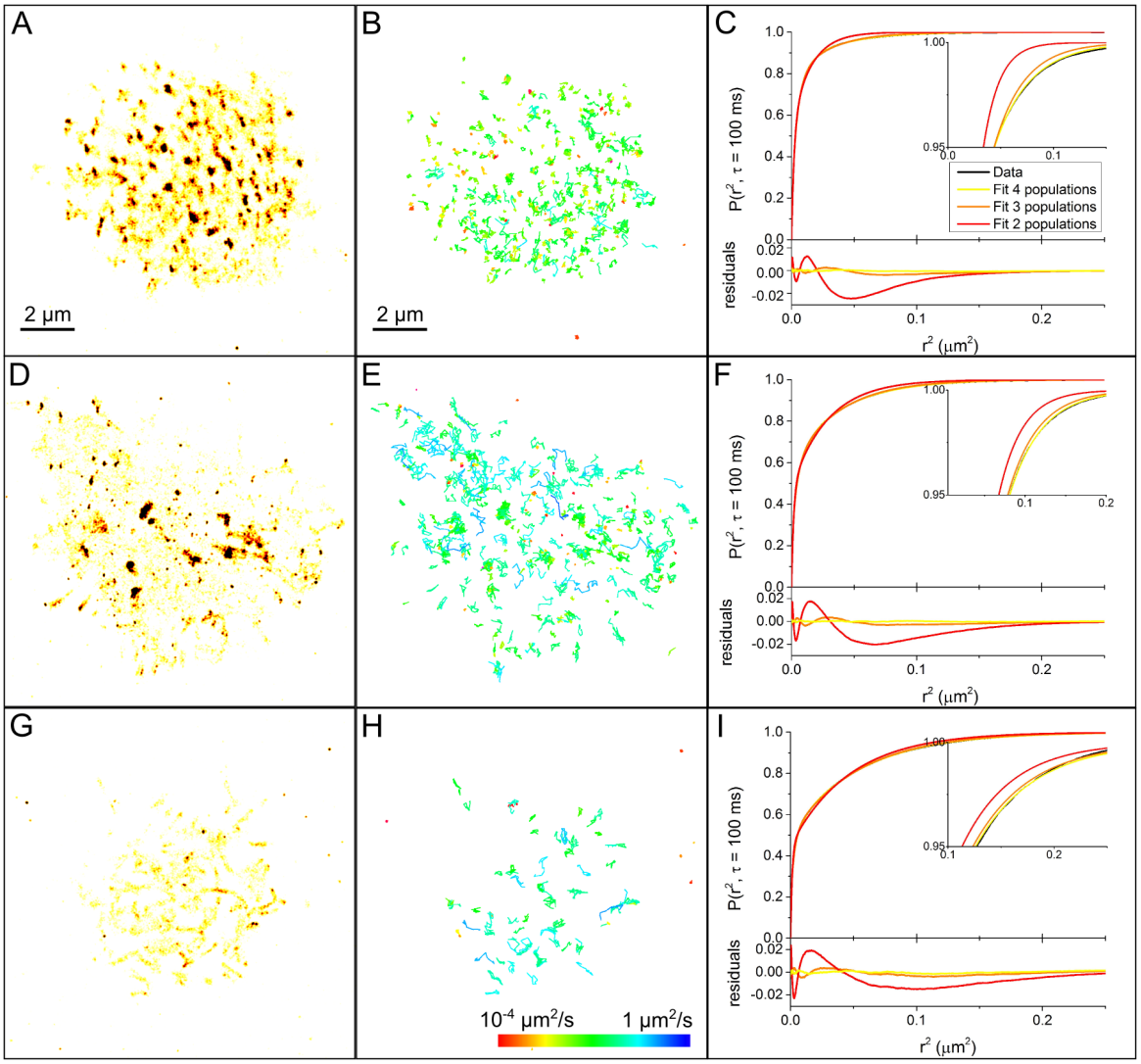


Figure 7.4 *Analysis of CD28 sptPALM trajectories.* Live TCR$^-$ T cells transfected with a [full-length CD28]-mEos construct were decorated with either a SA (**A-C**), a CA (**D-F**) or no antibody (**G-I**) and then dropped onto and imaged on a coverslip coated with secondary antibodies. All PSFs were fitted with 2D-Gaussians. All localisations were plotted as 2D-Gaussians of similar intensity and of width equal to the average precision of the localisations (**A,D,G**, intensity increasing from yellow to red to black). Localisations were also grouped in trajectories (localisations within 300 nm from each other, allowing blinking events of up to four frames) and trajectories grouping more than ten localisations were plotted (**B,E,H**). Colours of the trajectories code for the MSD diffusion coefficient of the trajectory (calculated with the five first time-lags) as indicated in the log-scale. **C,F,I**: the cumulative jump-distance distribution for the time-lag $\tau = 100$ ms (black) and the fit of models of two (red), three (orange) and four (yellow) diffusing populations. **Inset**: zoom-in on the inflexion of the distribution with different scales for the x-axis. Residuals from the fits are also plotted.

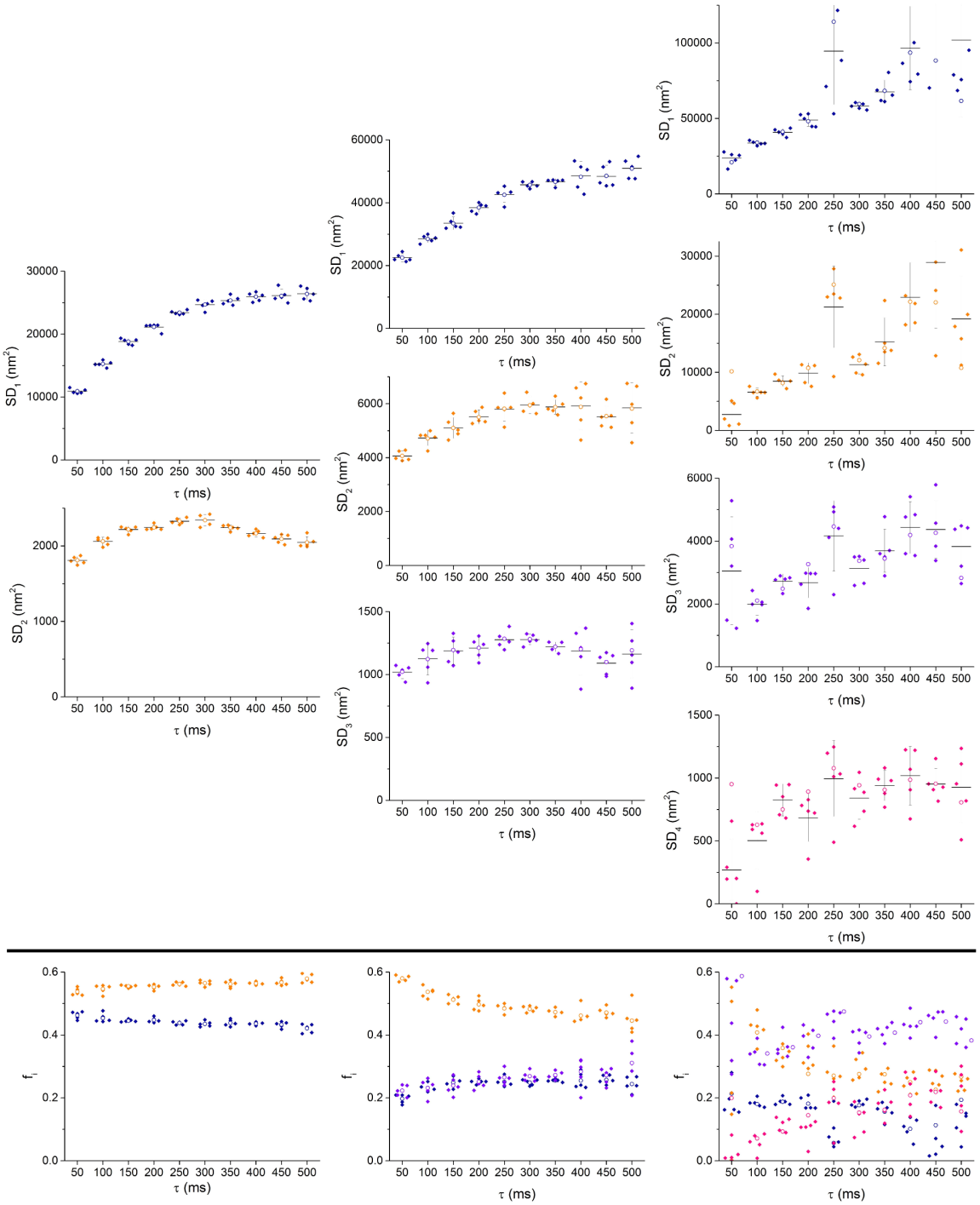


Figure 7.5 *Choice of the number of diffusing populations.* A model of two (**left column**), three (**middle**) and four (**right**) diffusing populations were fitted to the data shown in Figure 7.4, top row. For each time-lag $\tau$, the full distribution $P(r^2, \tau)$ (○) and five separate parts randomly drawn from it (♦, horizontal bar: mean, whiskers: one standard deviation of the mean) were fitted with Equation 7.1. For each model, both $SD_i(\tau)$ (**top rows**) and $f_i(\tau)$ (**bottom row**) are drawn for each population $i$ (colours for each population $i \in [\![1,\ 4]\!]$: dark blue, orange, purple, pink).

lag $\tau$ if the motion of the population is purely Brownian. However, if the localisation error $\sigma$ is assumed to be normally distributed, the relation between $SD_i$ and $\tau$ is linear because of the localisation precision [298, 299]:

$$SD_i(\tau) = 4\,D_i\,\tau + 4\,\sigma^2 \tag{7.2}$$

The curves $SD_i(\tau)$ are shown for the case of the SA activation in Figure 7.5. Curves for each of the populations of three models (two, three and four diffusing populations − left, middle, right columns, resp.) are given, together with the variation of the relative proportions $f_i(\tau)$ of the populations (bottom row). In order to test the robustness of the jump-distance distribution fit − from which the parameters $SD_i(\tau)$ and $f_i(\tau)$ are extracted −, all trajectories ($n_{cells} \geq 5$) are used to calculate the cumulative jump-distance distribution (distribution of distances separating two positions in trajectories separated by $\tau$ in time). This new distribution, for each time-lag $\tau$ is randomly divided into five distributions. The same analysis is then performed for the initial jump-distance distribution (○) and for its five separate parts randomly drawn (♦).

Whereas the values of the parameters ($SD_i$ and $f_i$) are reproducibly well fitted in the case of two or three populations, the poor robustness of the fit of four populations reveals that the latter has excessive degrees of freedom for the available quantity of data. This confirms the choice of a model of three diffusing populations (Figure 7.5, middle column) as the best parsimonious model for the data described here.

Since the mean precision of the experiments is $\sigma \sim 40$ nm, squared displacements below $\sigma^2 = 1{,}600$ nm$^2$ are to be considered null, and the corresponding tracked particles, immobile. Interestingly, a linear regression of $SD_1(\tau)$ following Equation 7.2 confirms the range of the precision: $\sigma = 66$ nm. Consequently, the movement of the third and slowest population falls under the precision of the experiment (Figure 7.5, middle column, $SD_3$). Furthermore, this fixed population is always observed, even for mEos-tagged proteins other than CD28, such as CD86-mEos (Section 7.2.2), and is therefore not specific to the super-agonism experiment. This population might reflect a non-CD28-specific immobile fraction of transmembrane proteins, the presence of dust on the coverslip, protein aggregates from dead cells, or antibody aggregates sticking on the glass. It is henceforth ignored and the relative fraction of the first population to the second is defined as:

$$f_1' = \frac{f_1}{f_1 + f_2} \tag{7.3}$$

The $SD_i(\tau)$ plots are characterised by a linear slope for $\tau \leq 200$ *ms*, plateauing for

larger values of $\tau$, typical of a spatially-restricted diffusing population of molecules [292, 297, 300]. A linear regression of the first four points determines the diffusion coefficients $D_i$ (Equation 7.2). The time-lag-mean value $F_1'$ of the relative fraction $f_1'(\tau)$ is also calculated. Final values $D_1$, $D_2$ and $F_1'$ are given in Figure 7.6, both for the total jump-distance distribution ($\circ$) and for its five random sub-divisions (plotted as lower-upper-quartile bars $\pm 1$ standard deviation).

At $37°C$, as expected, the diffusion of the fast population of CD28 is slowed down when applying either SA or CA (Figure 7.6, 'Full-length at $37°C$'). The effect of SA activation on the diffusion coefficient, however, is significantly larger than CA activation ($D_1^{\mathrm{SA}} = 0.026\ \mu\mathrm{m}^2/\mathrm{s} < D_1^{\mathrm{CA}} = 0.053\ \mu\mathrm{m}^2/\mathrm{s}$; $p = 5 \cdot 10^{-7}$). The diffusion of the slower population is, however, not significantly affected by the type of activation ($p = 0.07$). In the absence of activation, diffusion of the slow population is indistinguishable from being null, indicating that a model of two diffusing populations would best describe this experimental condition. Finally, the relative fraction of the fast population $F_1'$ specifically increases in the case of CA activation: the CA slows down the fast population of CD28 qualitatively less, but quantitatively more, than the SA.

It is expected that passive diffusion is correlated with temperature. Indeed, at 20°C, globally lower diffusion behaviour is observed ('Full-length at 20°C'); this is in particular visible for the fast diffusing population. Interestingly, at this temperature the slow population mimics the behaviour of the fast population at 37°C: since all diffusion is slowed down, part of the slowing effect observed in the fast population at 37°C has consequently moved to the slow population at 20°C in the analysis. The increase of the relative fraction of the fast population in the case of no activation indicates that more of the fast diffusing population is detected by the analysis. Indeed, this is a thresholding effect due to the radius parameter of 300 nm chosen for single molecule tracking: molecules diffusing faster than 0.1 $\mu\mathrm{m}^2/\mathrm{s}$ cannot be tracked [79]. Therefore, a decrease in temperature slows these non tracked molecules such that they can now be detected, consequently increasing the proportion of the fast population.

### Deconvolving diffusion from the downstream effects of early T cell activation

T cell activation happens within five minutes of contact with an activating surface, even in the absence of a TCR ligand (Chang, Fernandes, Ganzinger, Lee *et al.*, submitted). To separate the dramatic downstream effects of T cell activation (which induces immunological synapse formation, involving deep reorganisation of the cell architecture [301]) from the direct early mechanical effect of the SA, BW5147 cells which do not express TCR and

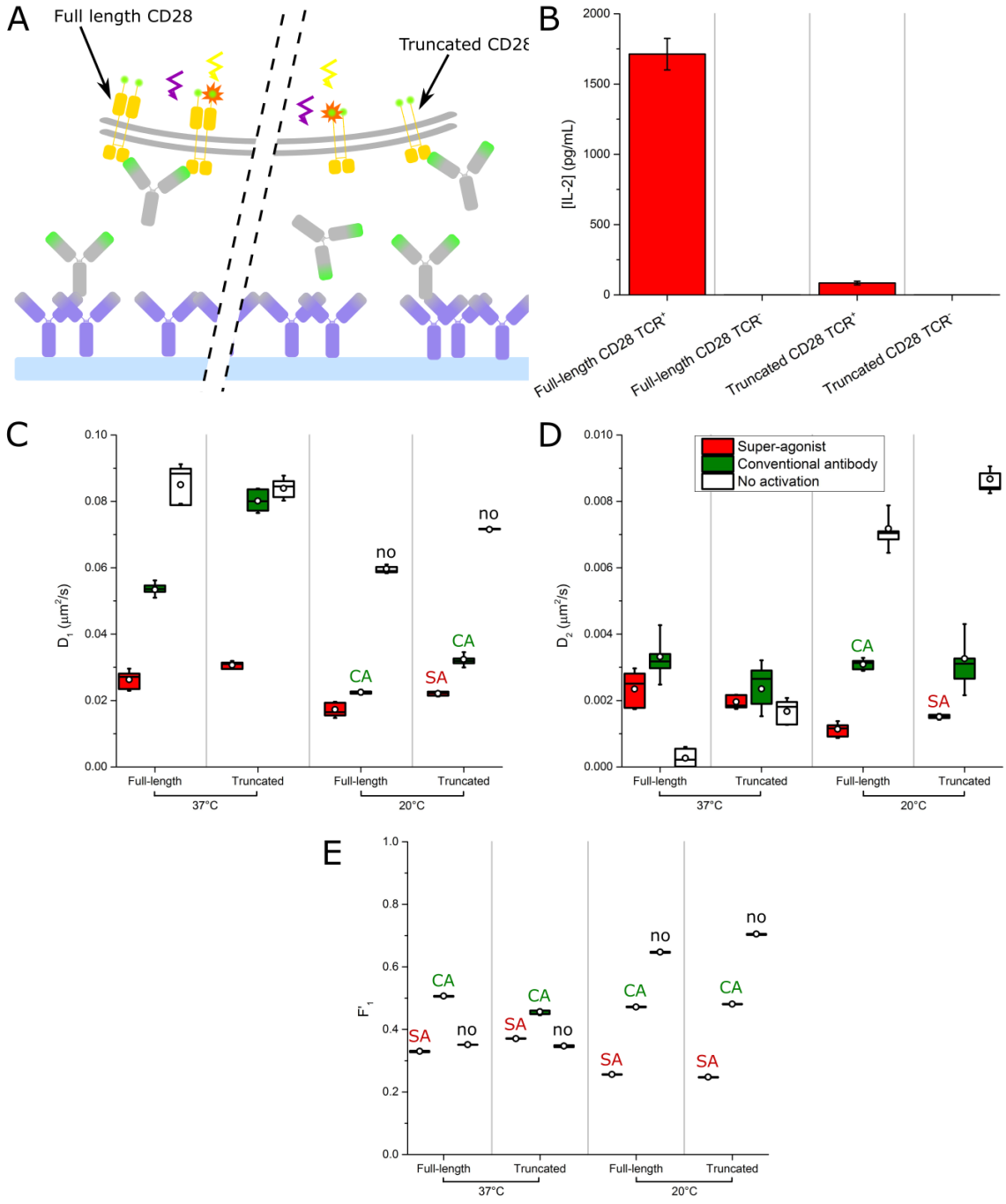


Figure 7.6 *Robust decrease of diffusion of CD28.* The effect of SA (red), CA (green) or no antibody (white) activation on a full-length and a signalling-incompetent ('truncated') CD28-mEos constructs were compared. **A**: Scheme of the diffusion experiments shown for CA incubation. Purple arrows symbolise 405 nm illumination stochastically switching mEos to its red form; yellow arrows, 561 nm illumination. **B**: IL-2 production of the cells expressing either construct at 37°C in $TCR^+$ and $TCR^-$ cells, measured by M. Aßmann (three repeats, $\pm$ one standard deviation of the mean). **C-D**: Diffusion coefficients of the fast ($D_1$) and slower ($D_2$) diffusing populations, calculated for both CD28 constructs at both 20°C and 37°C. **E**: Fraction $F_1'$ of the first population relative to the first and second populations (Equation 7.3). Values for the total jump-distance distribution (○) and for its five random sub-divisions (lower-upper-quartile bars $\pm 1$ standard deviation of the mean) are shown.

therefore cannot be activated were used. As the diffusion experiments are on this time-scale, the effects of ligand-independent TCR triggering and super-agonistic activation would be convolved and difficult to separate were the TCR expressed.

To focus on the initial passive reorganisation of receptors in isolation from downstream signalling-induced reorganisation processes, a truncated version of CD28 without its intra-cellular signalling domain was engineered by M. Aßmann. The absence of TCR and CD28 signalling were checked by IL-2 assay (Figure 7.6, B). In both cases, IL-2 production was depleted.

Slightly faster, but very similar diffusion behaviours to the full CD28 protein were observed both at 37° and 20°C (Figure 7.6, 'Truncated' at '37°C' and at '20°C'). Indeed, because part of the intra-cellular domain is truncated, the apparent size of CD28 is reduced which consequently increases its diffusion motion [302].

An important increase in the diffusion coefficient of the fast moving population for the CA activation is noticeable, compared to the full-length CD28, especially at 37°C. This indicates that the truncated version of CD28, while preventing convolution of the SA effect with any downstream signalling effect, increases the dynamic range of the diffusion analysis. Truncated signalling-incompetent CD28 is therefore used as the standard CD28 construct for all following diffusion experiments in this thesis.

Finally, in order to directly and formally validate the comparison between the IL-2 assay and the diffusion experiments, a single cell line was grown to be studied with both protocols: TCR-sufficient BW cells were transfected with a [full-length CD28]-mEos construct. Both IL-2 assay (M. Aßmann, personal communication) and the diffusion experiments (Figure 7.7) were in accordance with previous IL-2 results for $TCR^+$ cells transfected with a full-length CD28 construct (Figure 7.6, B), and diffusion results for $TCR^-$ cells transfected with a full-length CD28-mEos construct (Figure 7.6, C-E), respectively.

### Specificity of the decrease of CD28 diffusion

Since CD28 is dimeric [276], both antibodies (SA or CA) and CD28 present each two corresponding binding sites [285, 303]. Large scale linear structures can therefore form if the ratio of antibody bound to CD28 and CD28 itself is close to one. Such a structure, similar to polymers, could form a large meshwork increasing the viscosity of CD28 in the fluid plasma membrane and sterically decreasing the diffusivity of its components. To test whether the SA-specific decrease in diffusivity of CD28 affects all transmembrane proteins, both truncated but unlabelled CD28, and another transmembrane protein, CD86, fused to mEos, were stably transfected in T cells and imaged as previously described.

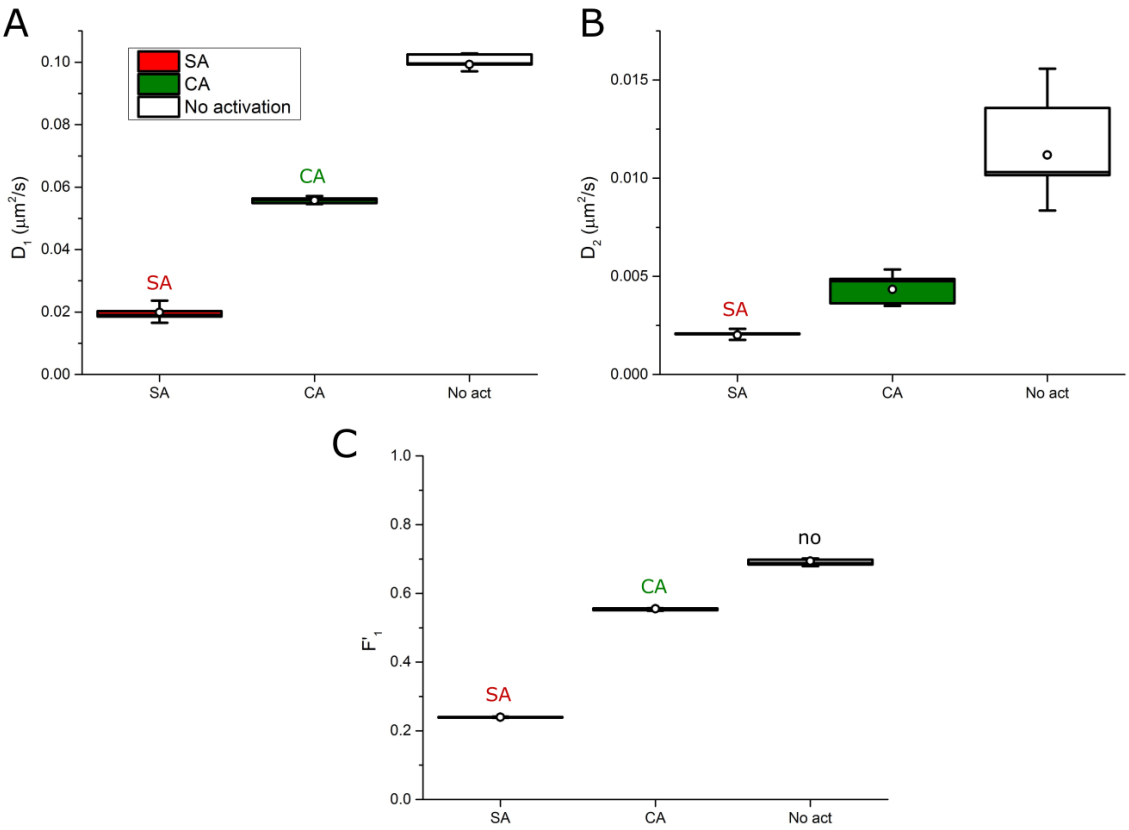


Figure 7.7 *Compatibility of IL-2 and diffusion experiments.* A single cell line was used in both IL-2 and diffusion experiments in order to formal validate their compatibility. The diffusion of the full-length CD28-mEos construct expressed in TCR-sufficient T cells is observed, after either SA (red), CA (green) or no antibody (white) incubation at 37°C. **A-C**: Diffusion coefficients of the fast and slower diffusing populations and their relative fractions for the three incubation conditions. Same data representation as for Figure 7.6.

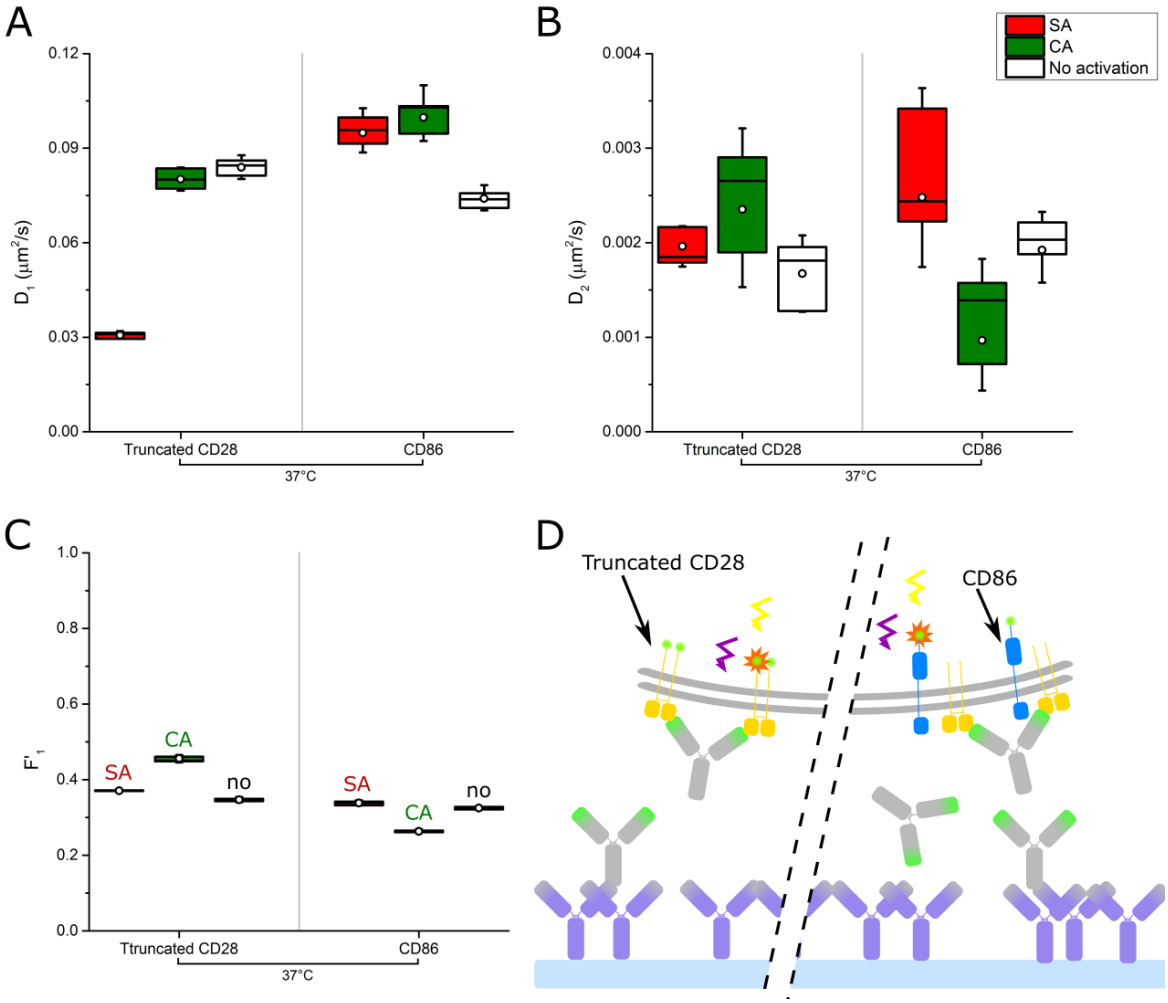


Figure 7.8 *Specificity of the decrease of CD28 diffusion.* The diffusion of the truncated signalling-incompetent CD28-mEos construct is compared to the diffusion of a CD86-mEos construct co-transfected with the unlabelled truncated CD28 protein, after either SA (red), CA (green) or no antibody (white) incubation at 37°C. **A-C**: Diffusion coefficients of the fast and slower diffusing populations and their relative fractions for the three incubation conditions. Same data representation as for Figure 7.6. **D**: Scheme of the diffusion experiments shown for CA activation.

The diffusion of CD86 was affected by neither of the activation antibodies (Figure 7.8). The SA, therefore, − at least to some extent − specifically slows down CD28 diffusion.

### 7.2.2 Super-agonist activation requires divalent engagement of CD28

#### CD28 monomers do not trigger

To test the hypothesis whether a meshwork of SA and CD28 is responsible for the effect of the SA on CD28 diffusion, a monomeric version of CD28 was engineered: the ectodomain of a monomeric transmembrane protein, human PD-1, was fused to replace the ectodomain of CD28 in the truncated CD28-mEos construct. Two monoclonal antibodies against distal epitopes of PD-1, were used either separately or in combination during the 15' incubation in place of the previous mAbs.

Each of the antibody separately induced a decrease in diffusion of PD-1-CD28 proteins, very similar to the CA antibody (Figure 7.9, 'CA 1' and 'CA 2'). Strikingly, applying both antibodies simultaneously caused a drop in diffusivity reminiscent of the effect of SA on CD28 diffusion ('CA 1 + CA 2'). Simplistically, this result can be interpreted as two different roles played by the two sets of antibodies: one forms CD28 dimers from two PD-1-CD28 monomers; the other one induces cross-linking.

However, since a different system is used (different set of antibodies and antigen), the values obtained are not directly comparable in a quantitative way. For better comparison, three populations were used although parameters are noticeably correlated, indicating that a model of two populations would have been a better parsimonious model to describe the data. Nevertheless, this results, together with its IL-2 equivalent (Figure 7.9, B), emphasises the importance of the divalence of CD28 for super-agonism activation.

#### Effect of the antibody concentration

In order to further compare the behaviour of both SA and CA, the effect of their concentrations on CD28 diffusivity was investigated. The diffusivity of both populations of CD28 importantly decreased with higher concentration of SAs through the whole range from 0.1 to 50 µg/mL (Figure 7.10, B-D). This is consistent with previous dilution experiments measuring the effect of SA on proliferation of T cells [278] or IL-2 assays (Figure 7.10, A).

Strikingly, the concentration of the CA has quite a different effect on the diffusion of CD28: the diffusion of the fast population of CD28 reaches a minimum at an intermediary concentration of 1 µg/mL (bottom row).

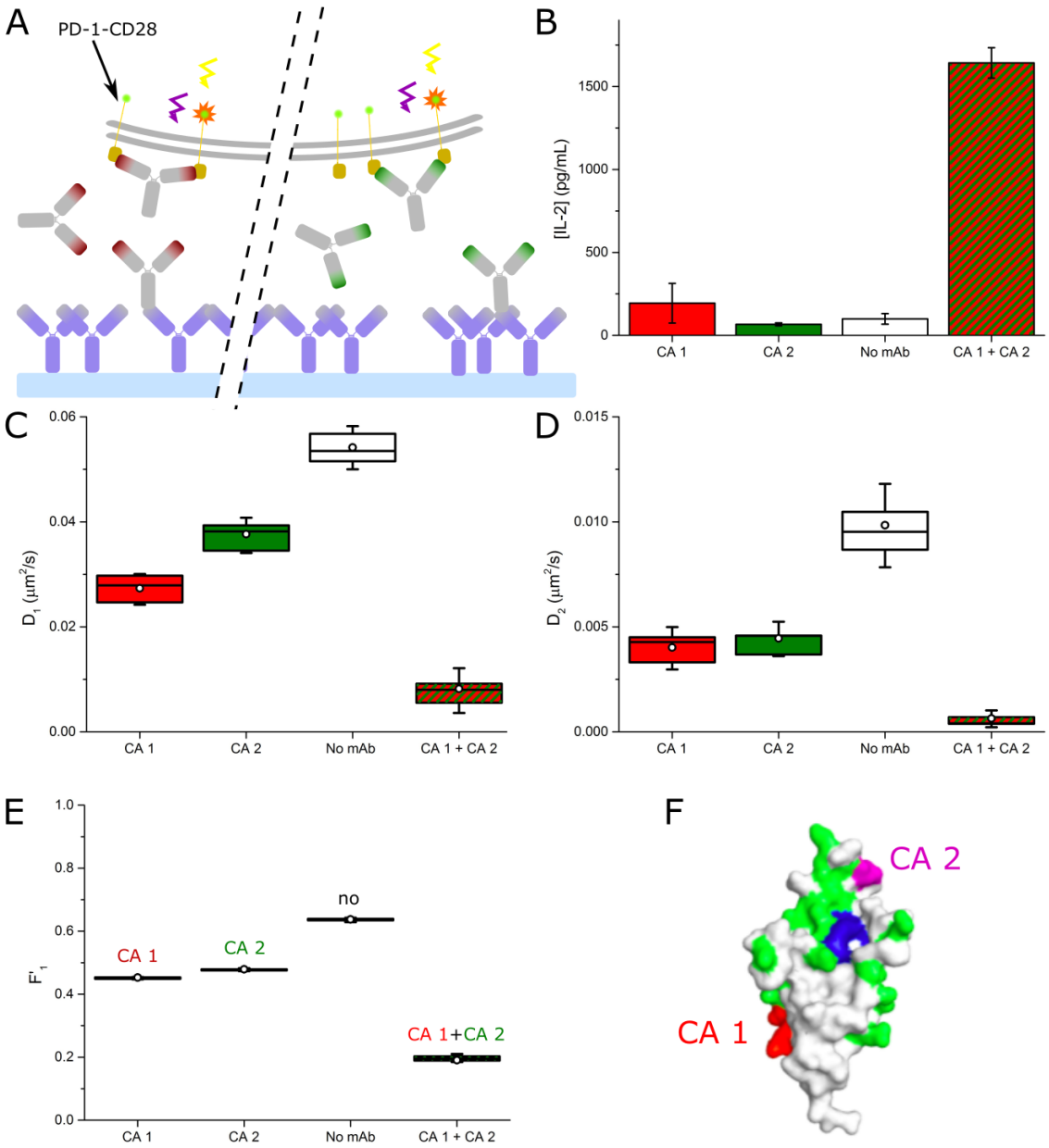


Figure 7.9 *Effect of cross-linking.* The effect of the incubation of two mAbs ('CA 1' and 'CA 2'), separately (red, green) or in combination (green and red stripes), or no antibody (white) on the diffusion of a monomeric CD28-mEos-like construct, PD-1-CD28-mEos, is used to study the effect of cross-linking. **A**: Scheme of the diffusion experiments shown for activation with either antibody. **B**: IL-2 production measured in all four conditions by M. Aßmann. **C-E**: Diffusion coefficients of the fast and slower diffusing populations and their relative fractions for the three incubation conditions. Same data representation as for Figure 7.6. **F**: Crystal structure of PD-1 ectoplasmic domain (the plasma membrane would be at the bottom) showing the epitopes of both mAbs (figure courtesy of S.J. Davis).

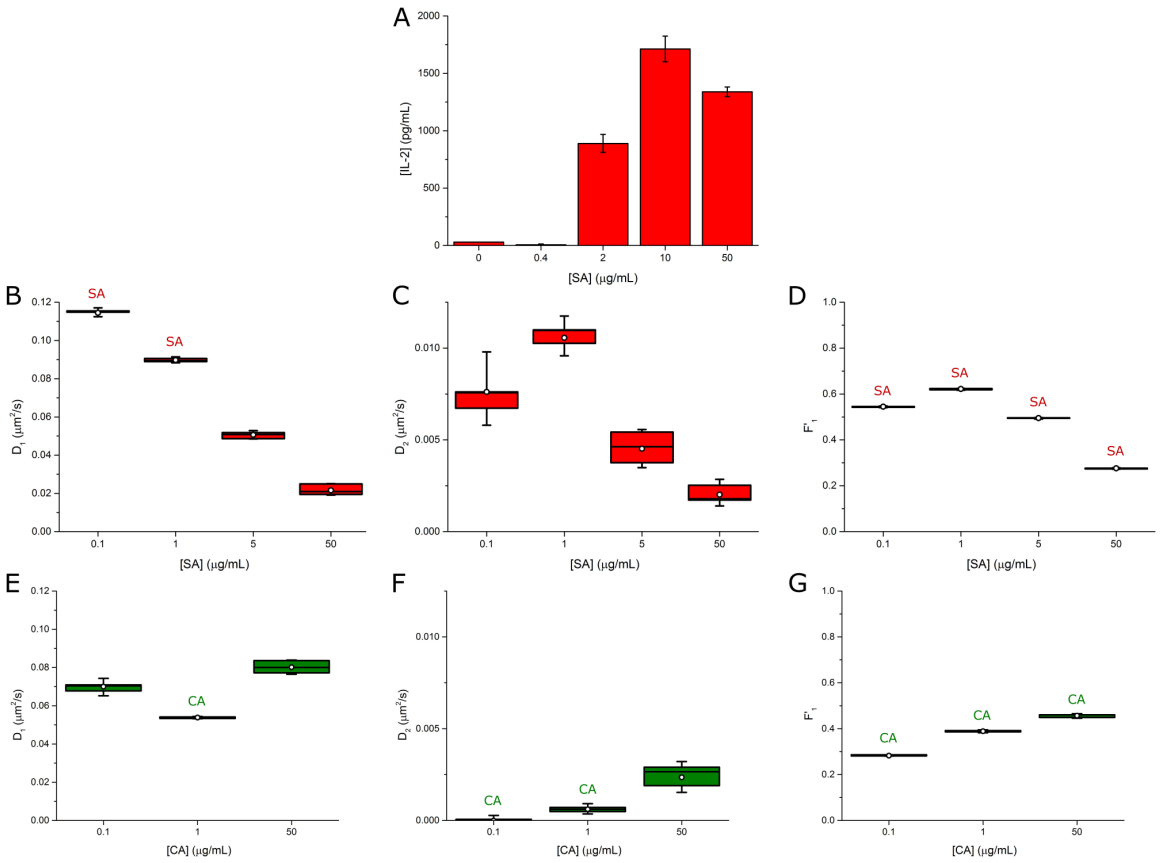


Figure 7.10 *Effect of the antibody concentration.* The effect of the incubation of different concentrations of SA (red, **A-D**) and CA (green, **E-G**) mAbs on the diffusion of the transfected signalling-incompetent CD28-mEos construct was studied. **A**: IL-2 production, measured by M. Aßmann for a series of SA concentrations. **B-D** and **E-G**: Diffusion coefficients of the fast and slower diffusing populations and their relative fractions for the three incubation conditions. Same data representation as for Figure 7.6.

By comparing levels of surface expression of CD28 between the stably transfected cell lines and primary cells by flow cytometry, R. Knox roughly estimated that between 0.5 and 1 million of CD28 homo-dimers were expressed per cell (personal communication). From this value, a quick estimation of the ratio of antibody over CD28 homo-dimer can be calculated (Table 7.1). This indicates that the range of concentrations chosen probably spans conditions of excess of CD28 and of excess of antibody.

Table 7.1 *Approximative ratio of mAb to CD28 expressed on the surface of the T cells in the experiments for different concentrations of antibodies.*

| [mAb] (µg/mL) | 0.1 | 1 | 5 | 50 |
|---|---|---|---|---|
| [mAb] (mol/L) | $7 \cdot 10^{-10}$ | $7 \cdot 10^{-9}$ | $3.5 \cdot 10^{-8}$ | $3.5 \cdot 10^{-7}$ |
| **# mAb/CD28** | $\sim 0.8$ | $\sim 8$ | $\sim 40$ | $\sim 400$ |

### 7.2.3 Effect of different coverslip antibody-coatings

Together with its concentration during incubation, the interaction of the activation antibody with CD28, which differs when the antibodies are decorating the cells in solution or coated on the coverslip, is critical to observe super-agonism. As for TCR triggering [235], M. Aßmann has shown that immobilisation on a surface is required for SA activation by measuring IL-2 after incubating cells with $F(ab')_2$ fragments of SA that do not bind to anti-Fc secondary antibodies (personal communication, also ref. [278]). However, IL-2 production was recovered when cells were dropped on coverslips coated with secondary antibodies directed against the $\kappa$ chain of $F(ab')_2$.

Here, the effect of different activation protocols is tested: first, instead of decorating the cells in solution (Figure 7.11, 'mAb in solution'), activation antibodies (either SA or CA) were used to coat the coverslip ('mAb coated'), in place of secondary antibodies. For non-decorated cells placed on mAb coated coverslips, the SA-specific decrease of diffusion of CD28 is not observed any more; conversely, the diffusion of the slower CD28 population speeds up and the fraction of the faster population increases. Indeed, when the cells are not decorated, the formation of a meshwork of CD28 is not favoured because of combined geometric and mobility effects due to the immobility of the antibodies.

However, when cells are decorated in solution with the activation antibodies and dropped on coverslips also coated with the same activation antibodies ('mAb coated & in solution'), the SA-specific effect is recovered. This suggests that the secondary antibodies play the role of immobilising the activation antibodies on the coverslip. Both immobilisation and cell-decoration are therefore required to observe SA-specific CD28 slowing down.

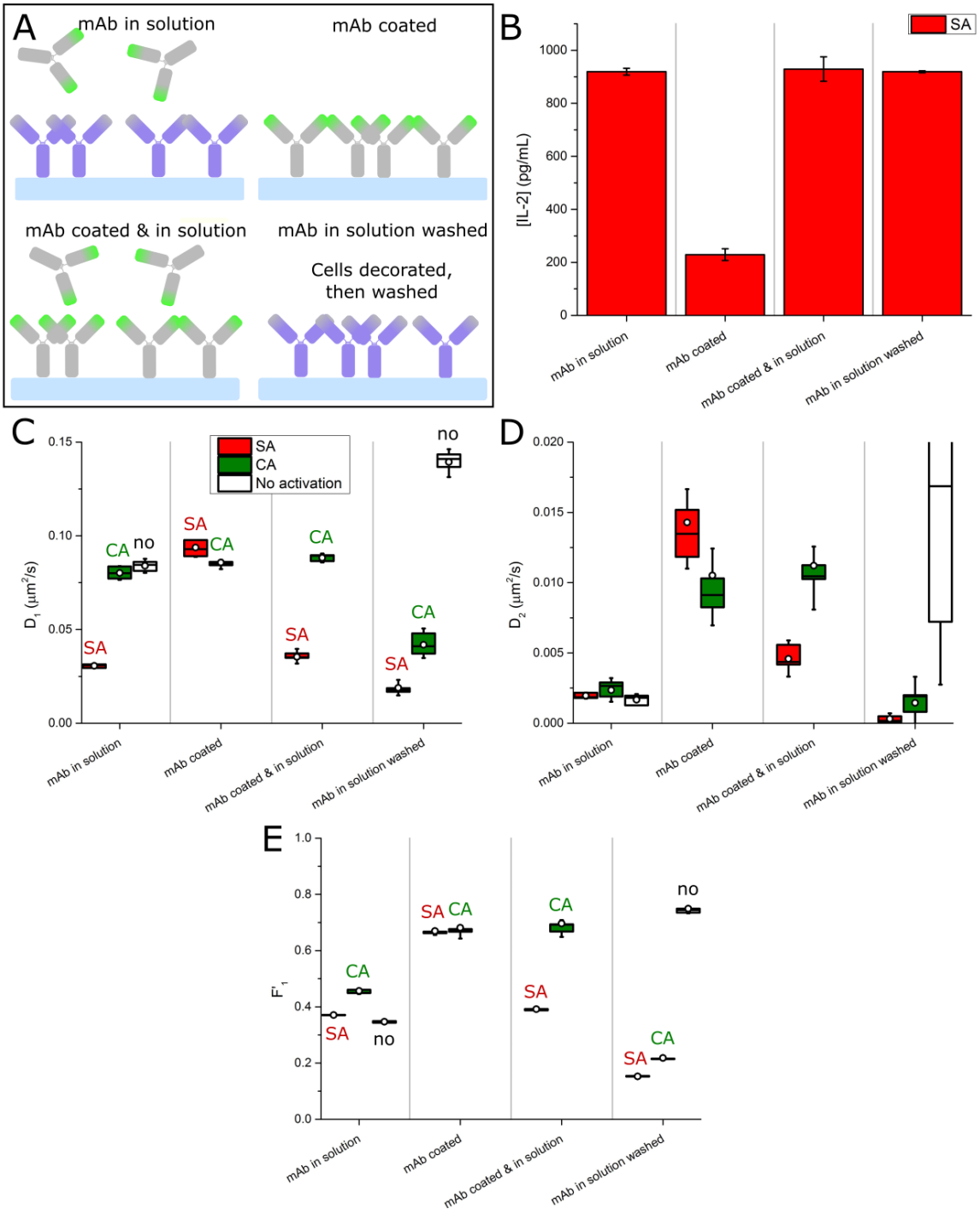


Figure 7.11 *Effect of different coverslip antibody-coatings.* The effects of different antibody-coatings on the signalling-incompetent CD28-mEos protein were compared. **A**: Scheme of the different coating protocols represented for the CA. Different combinations of steps were experimented: cells were either decorated with the mAb in solution (SA, red; CA, green; or no antibody, white) or left in warm medium; in one case ('mAb in solution, then washed'), unbound mAbs were then washed off; finally, they were dropped on coverslips coated with either the mAb or a secondary polyclonal antibody against the mAb. **B**: IL-2 production, measured by M. Aßmann for the four immobilisation conditions described in A. Since the CA do not induce IL-2 secretion, experiments only involved the SA. **C-E**: Diffusion coefficients of the fast and slower diffusing populations and their relative fractions for the four immobilisation conditions. Same data representation as for Figure 7.6.

A more complex case consists in repeating the initial experiment, but washing out the excess of activation antibodies after their incubation with the cells (‘mAb in solution, washed’). Strikingly, the slowing down effect is even more increased, and affects both CA and SA activation. A possible interpretation for this observation is that the activation antibodies are either better immobilised on the coverslip or better decorating the T cells. Indeed, by washing out the unbound activated antibody, there are no antibodies left in solution that compete with CD28-bound antibodies and that effectively partially block the secondary antibodies. The immobilisation of activation antibodies is thus increased.

### 7.2.4 CD28-bound antibodies

Because the SA and the CA used in this study have different binding kinetics, the thermodynamic equilibrium is probably not reached when imaging begins in the case of SA activation. To investigate whether this would affect the distribution of the antibodies bound to CD28, both antibodies were labelled with Atto655, a far-red photo-switching fluorescent dye. After incubation with either mAb (20% labelled), cells were thoroughly washed from any excess of antibody, and imaged in a simultaneous two-colour PALM-dSTORM experiment.

The labelling and imaging protocols were optimised to obtain sufficient, but not too high, density of both labels (mEos and Atto655) for thousands of frames. Atto655 was chosen as a probe absorbing and emitting in separate wavelength domains than mEos, and whose photo-blinking is not controlled by near-UV light. Thus, the densities of both labels can be controlled independently: mEos through 405 nm illumination [121], Atto655 by the percentage of labelled over unlabelled antibodies used. A reducing agent was not used for live-cell imaging because of cytotoxic effects [134, 304]. Both labelling strategies are thus orthogonal.

For both antibody activations, the average projection of each channel (Figure 7.12) reveals a cluster distribution similar to the one previously observed in the PALM-only experiments (Figure 7.4, ‘SA’ and ‘CA’). This distribution is induced by the antibodies as a uniform distribution of CD28 proteins is observed in their absence (‘No mAb’). Almost no cross-talk of mEos in the far-red channel was recorded (except for high-intensity intracellular vesicles). The untransfected original cell line was also imaged (‘WT’): very little if any background was recorded in both channels. These observations validate the two-colour labelling and imaging protocol.

At this diffraction-limited scale, a good overall co-localisation is observed between both

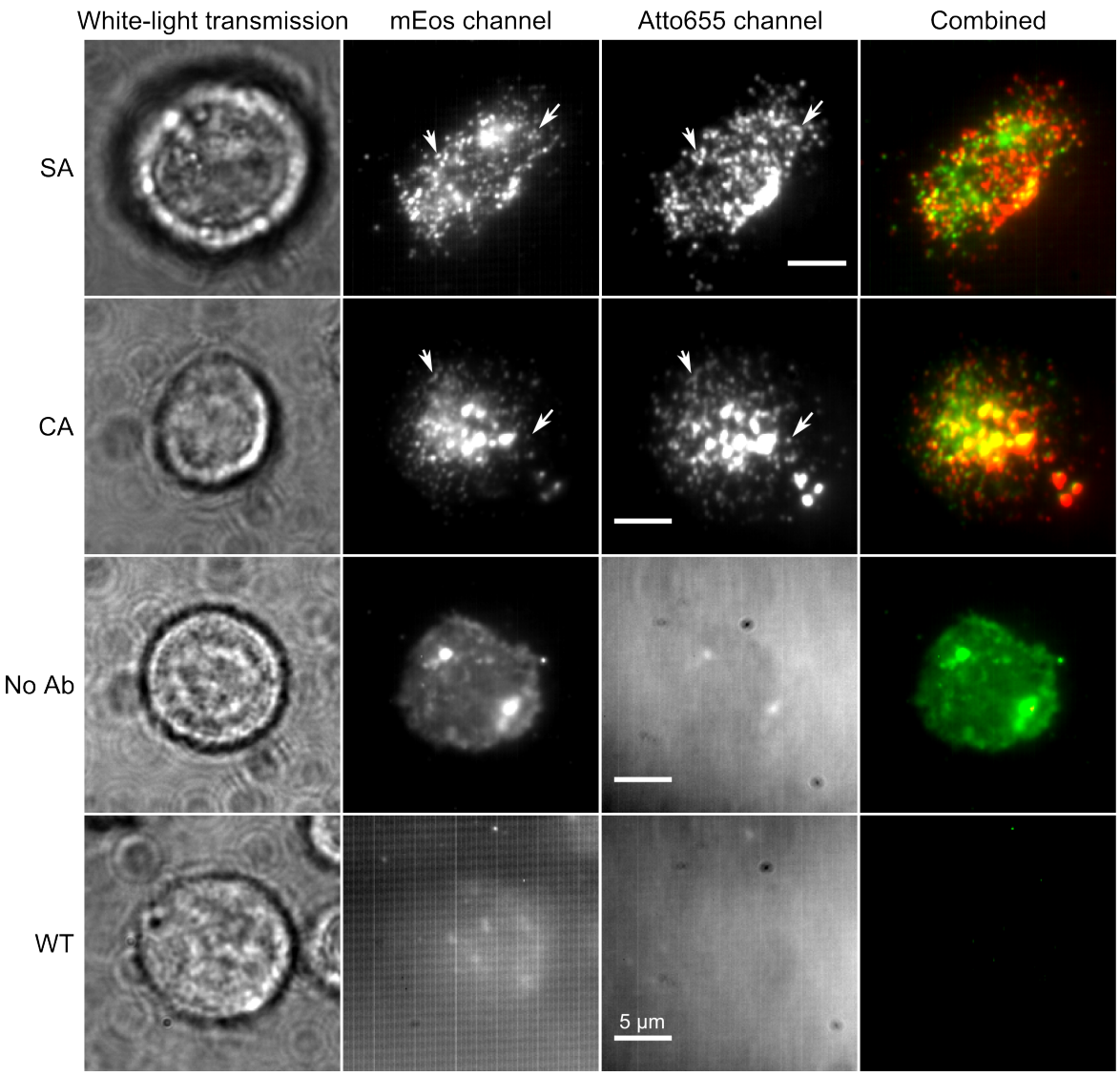


Figure 7.12 *Bulk co-localisation of CD28 and anti-CD28 mAbs.* The signalling-incompetent CD28-mEos construct was stably expressed in TCR-deficient T cells, incubated for 15' at 37°C with either a SA, a CA or no antibody. 20% of the activation mAbs were labelled with Atto655. Cells were washed to remove any labelled but unbound mAb and resuspended in the same incubation buffer containing only unlabelled mAbs. Both fluorophores were simultaneously imaged in two spectrally separated channels. A white-light transmission of a representative cell at the end of the imaging (**first column**), the average projection of each channel (**second and third columns**) and their superposition (**last column**) are given for all three incubation conditions and for an untransfected cell incubated with no mAb as a negative control (**'WT'**). Arrows: examples of co-localised clusters.

channels (arrows for specific characteristics, and 'Combined' column). The non-trivial registration of the channels, the movement of the live cells and the slight difference of illuminations makes the projection of both channels not identical. But many features and clusters are definitely co-localised.

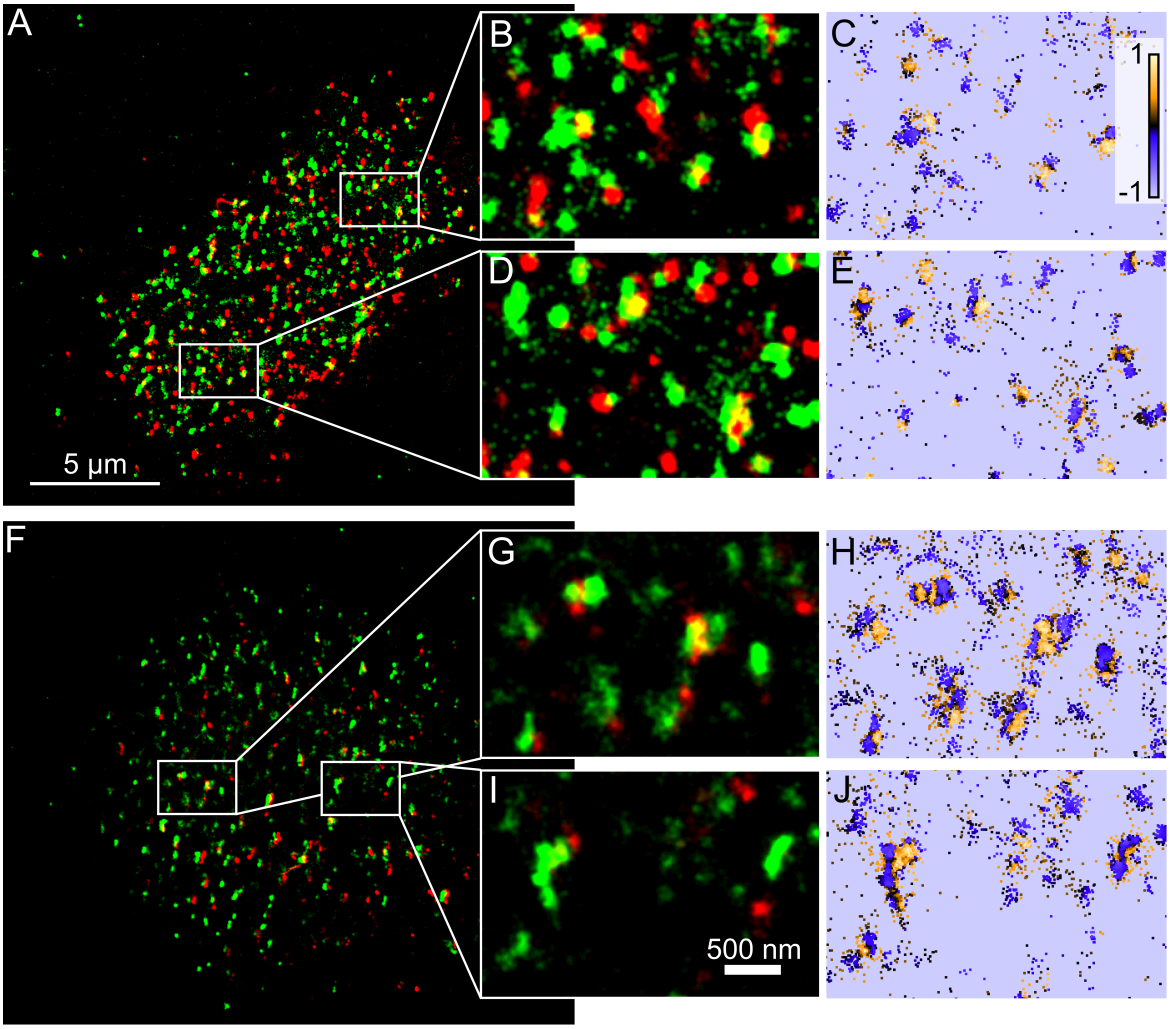


Figure 7.13 *Super-resolved co-localisation of CD28 and anti-CD28 mAbs.* The data from the experiments described in Figure 7.12 were analysed for super-resolution: for each cell, the PSFs of each channel were fitted. Localisation positions were corrected for channel registration and superposed in a combined super-resolved figure where each localisation is represented as a 2D-Gaussian of similar intensity and of width equal to the average localisation precision (green for CD28-mEos, red for mAb-Atto655). **Top row** corresponds to the representative T cell activated by the SA in Figure 7.12; **bottom row**, to the one activated by the CA. **A,F**: Super-resolved figures. **B,D,G,I**: Zoom of the indicated region of the super-resolved figure. **C,E,H,J**: Coordinate-based co-localisation representation of the green channel of the corresponding super-resolved zoomed region with respect to the red channel. Each localisation is plotted as a pixel which colour codes its CBC value (calculated with $R_{max} = 200$ nm, ranging from -1 −blue−, to 0 −black−, to 1 −yellow−).

Each channel was processed for SMLM, the list of localisations was corrected with

channel registration, and a corresponding super-resolved picture was rebuilt (Figure 7.13). Consistent with faster diffusion, clusters in the case of CA activation (bottom) are on average larger and less circular than for SA activation (top). For both activations, however, clusters of CD28 are co-localised with clusters of mAbs. To quantify the co-localisation and avoid biases introduced by image processing steps and intensity thresholding, a coordinate-based co-localisation analysis was performed [116] (right column, CD28 with respect to CD45): for each localisation detected, a score is calculated, ranging from -1 (blue) to 0 (black), to 1 (yellow), meaning that the localisation is respectively anti-correlated, not correlated, or correlated with the localisations from the other channel.

Most CD28 clusters show some co-localisation with either mAb. However, partial labelling (20% of the antibodies only are labelled, and not all CD28 molecules are imaged as only a proportion of all mEos proteins are correctly folded and can be activated [126]), and the limited number of frames recorded restrict the sampling required for detection of total co-localisation. Furthermore, cells are imaged live. Imaging is only started when cells have settled on the coverslip to limit their movement. However, some membrane- and intracellular reorganisation happen during the course of the experiment, and prevent perfect co-localisation. It can also explain small cluster displacements, that are observed even after non-linear achromatism correction between channels, within and between channels, depending on when the localisations of the cluster were imaged during the experiment.

### 7.2.5 Variation of the height separating the plasma membrane from the coated surface

To test the KS model, and specifically its size-dependency hypothesis, a taller CD28 protein was engineered: a $\sim 75$ Å-high Fc fragment of a human IgG1 was genetically fused between the mouse transmembrane domain of CD28 and its rat ectodomain. In functional assays, this addition blocks the SA-induced IL-2 production and T cell activation (Figure 7.14, B). Remarkably, incubating the cells with a putative SA antibody which targets the 'side' of the inserted Fc domain (S.J. Davis, personal communication), close to the plasma membrane, allows the recovery of IL-2 production, confirming the importance of the relative proximity of the targeted epitope of CD28 and the plasma membrane.

A similar experiment was performed in $TCR^-$ cells with a signalling-incompetent truncated version of the Fc-CD28 construct in order to observe the effect of the different activations on CD28 diffusivity (Figure 7.14). Incubation with anti-CD28 SA or CA induced very similar diffusion effects to the previous truncated CD28 construct. Compared to the

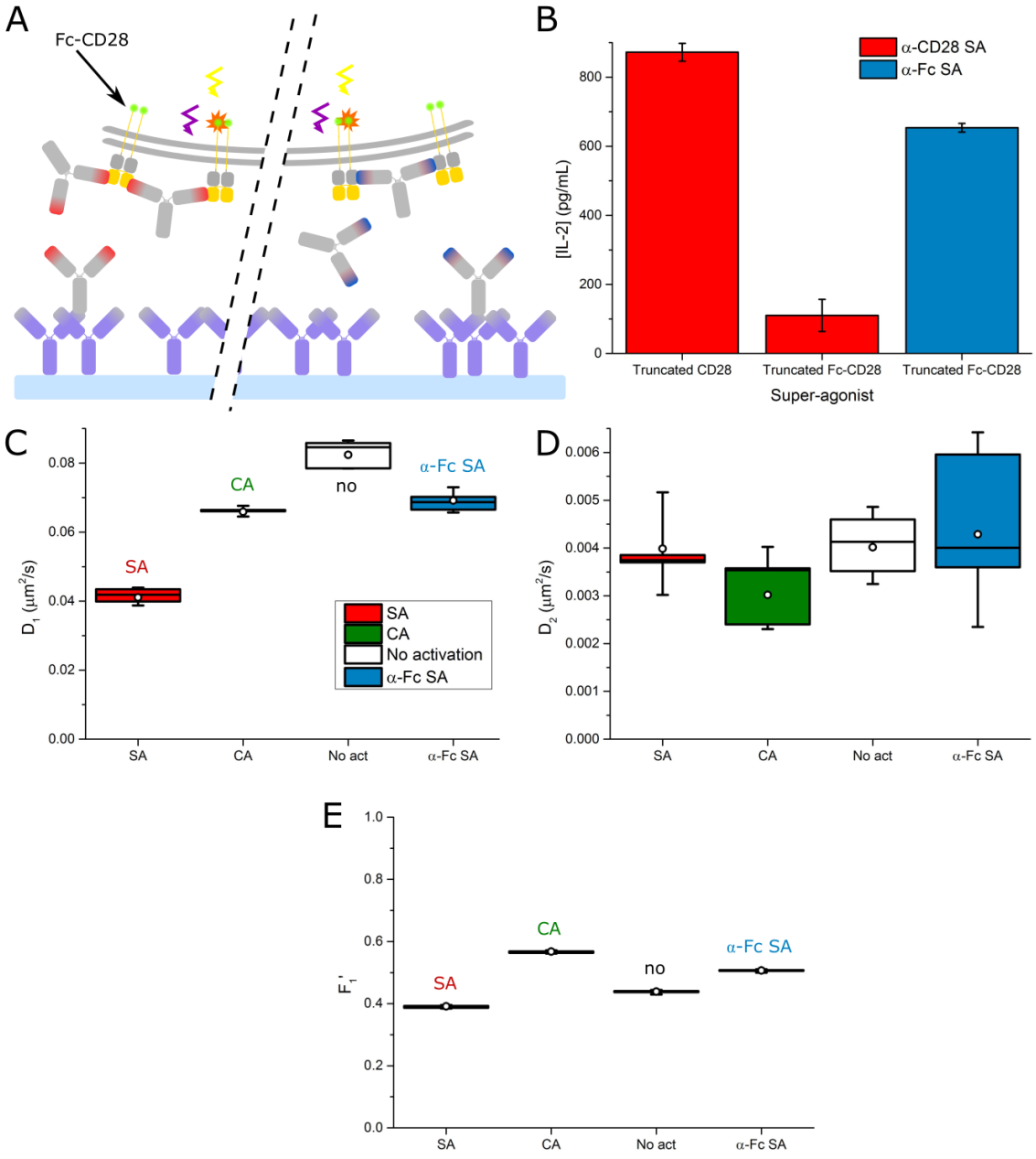


Figure 7.14 *Variation of the height separating the plasma membrane from the coated surface.* A $\sim 75$ Å-tall human Fc domain was added between the transmembrane and the ectodomain of the signalling-incompetent CD28-mEos construct to increase the distance of the epitopes of the SA and the CA to the plasma membrane. The effect of a putative SA targeting the 'side' of the added Fc domain on the diffusion of the new construct was compared to effect of the original anti-CD28 mAbs. **A**: Scheme of the experiment with the new construct Fc-CD28, drawn for the original anti-CD28 SA and the anti-Fc putative SA. **B**: IL-2 production, measured by M. Aßmann for the original anti-CD28 SA for both original and new constructs, and for the anti-Fc putative SA for the new construct. **C-E**: Diffusion coefficients of the fast and slower diffusing population and their relative fraction for the four incubation conditions. Same data representation as for Figure 7.6.

original signalling-incompetent CD28-mEos construct, the fast population of the taller Fc-CD28-mEos is diffusing slightly faster when CA-activated, and slightly slower when SA-activated, but those variations of $\sim$0.01µm/s$^2$ are not significant. Even more strikingly, the application of the putative anti-Fc SA reduced the diffusion of Fc-CD28-mEos to a similar level as the anti-CD28 CA. These results suggest that slowing down of CD28 diffusion, on its own, is not sufficient to induce IL-2 release.

### 7.2.6 Evidence for a size-dependent segregation?

In view of the KS model, the specific effect of SA incubation on CD28 diffusion could play a role in T cell triggering (through the kinetic arm of the model, by locally increasing the time CD28 stays in a contact zone). To test the other requirement of the KS model, the distribution of CD28 was observed simultaneously with the distribution of CD45, a large transmembrane phosphatase which segregation from the contact zones in T cells is necessary for T cell triggering (Chang, Fernandes, Ganzinger, Lee *et al.*, submitted). Small anti-CD45 Fabs were labelled with Atto655 dyes and added to the incubation antibodies. Cells were washed from any unbound Fab before being resuspended in their activation buffer and imaged using a sptPALM-dSTORM approach.

The combined average of both channels (Figure 7.15, left column) reveal some co-localisation of CD45 and CD28 when neither SA nor CA is added in solution, and an increased segregation of both proteins when SA or CA are used. The super-resolved figures underline a more complex situation (middle and right columns): in the case of incubation in the absence of any mAb, a uniform distribution of both CD28 and CD45 is observed, consistent with the previous results of random diffusion of CD28. Also consistent with results described above, the membrane of the cell in contact with the coated coverslip presents CD28 clusters when the cells are incubated with SA or CA. Two observations are noticeable about the distribution of CD45: (1) in comparison with the uniform distribution of CD45 in the absence of antibody (bottom row), some clusters of CD45 appear on the membrane of the T cells in the presence of SA or CA. (2) the distribution of CD45 is less uniform in the presence of SA (top row) than in presence of CA (middle row).

In order to compare the different conditions in a quantitative manner, the coordinate-based co-localisation (CBC − see Section 3.4.2) analysis of more than five cells with respect to either channel was performed (Figure 7.15, right column, bottom close-ups, CBC image with respect to the more homogeneous CD45 channel). For each cell, the median CBC value was analysed (Figure 7.16). Although no significant difference can be observed in

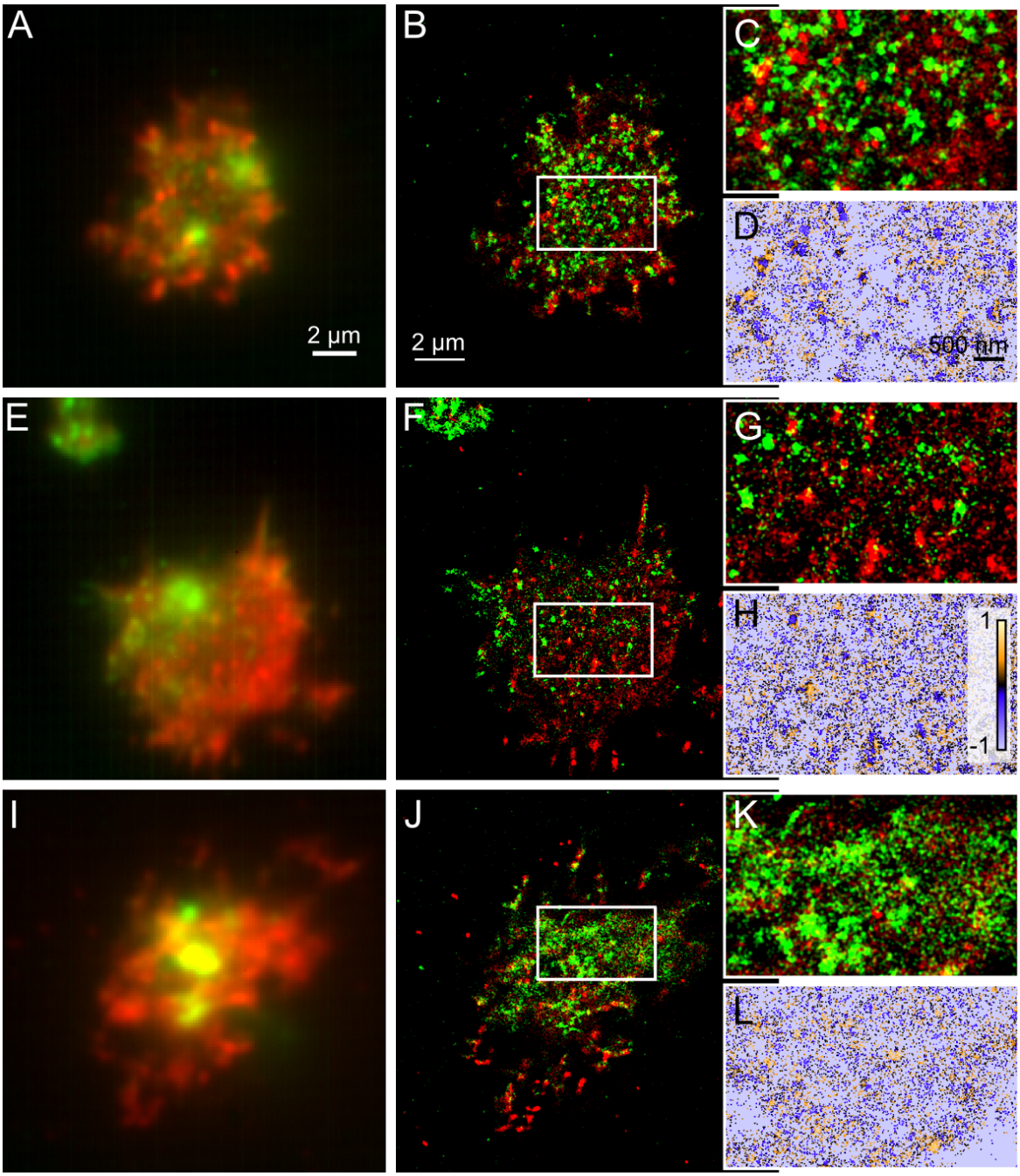


Figure 7.15 *Simultaneous imaging of CD28 and CD45.* Live TCR-deficient T cells expressing the signalling-incompetent CD28-mEos construct were incubated with anti-CD45 Fab fragments labelled with Atto655 and either the SA (**A-D**), the CA (**E-H**) or no antibody (**I-L**). Unbound Fab fragments were washed off and cells were resuspended in their incubation buffer and dropped on a coverslip coated with secondary polyclonal antibodies. For each incubation condition, a representative cell is shown. **A,E,I**: Combined average projection of each channel (CD28-mEos in green, anti-CD45 Fab-Atto655 in red). **B,F,J**: Combined channel-corrected super-resolved figure (each localisation is shown as a 2D-Gaussian of unit intensity and of width equal to the average localisation precision). **C,G,K**: Zoom of the region marked as a white rectangle. **D,H,L**: Coordinate-based co-localisation (CBC) representation of the red channel of the corresponding super-resolved zoomed region with respect to the green channel. Each localisation is plotted as a pixel whose colour codes its CBC value (calculated with $R_{max} = 200$ nm, ranging from -1 −blue−, to 0 −black−, to 1 −yellow−).

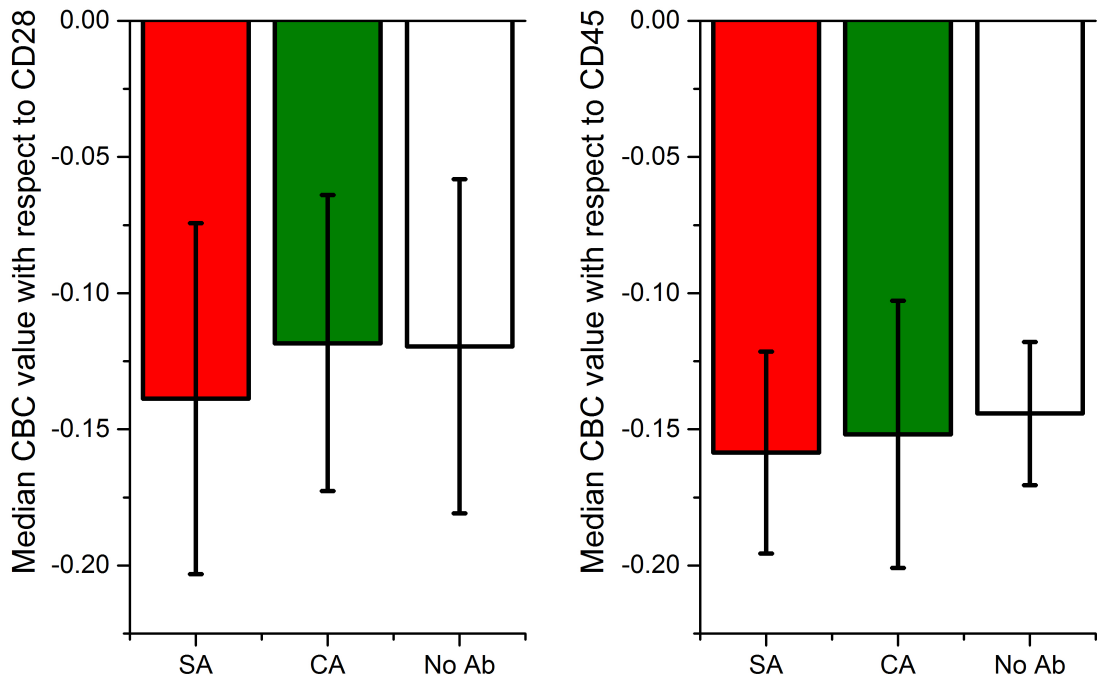


Figure 7.16 *Quantitative coordinate-based co-localisation analysis.* For each incubation condition (SA, CA or no antibody), five live cells were imaged. For each live cell, the CBC values of the localisations of each channel were calculated with respect to the other channel. The median CBC values of the five cells are plotted (mean of the distribution $\pm$ one standard deviation of the mean) with respect to CD28 (**left panel**) and with respect to CD45 (**right panel**).

co-localisation with respect to either channel between the conditions, a slight trend can be hypothesised: CD28 and CD45 are less co-localised when cells are incubated with SA than in the presence of CA.

These results suggest that there might be some SA-induced segregation of CD45. The difference is, however, not significant and more evidence is required to confirm this conclusion.

## 7.3 Discussion

The results presented in this chapter reveal that the SA specifically slows down the diffusion of CD28 on the membrane of a live T cell immobilised on a surface. A critical description of the hypotheses of the diffusion model is essential to understand the limits of the conclusions that can be drawn from these data, and the additional questions they raise. Can this phenomenon be explained on the mechanistic scale by a difference of avidity, affinity or kinetics of the mAbs? Is this correlation between a decrease in diffusion and activation of T cells causal? What does it reveal about CD28 activation?

### 7.3.1 Clusters of localisations: protein clusters or trajectories?

Clusters of localisations were observed when incubating the T cells with different anti-CD28 antibodies: the clustering was more pronounced in the case of an SA compared to a CA activation (Figure 7.4). This observation can originate from two, non-exclusive, types of protein behaviour: (1) clusters of localisations can reflect a clustered distribution of proteins; (2) it can also reflect the transient trace of a single fluorophore over a few frames, which, if fixed or diffusing slowly, will be observed as multiple localisations clustered together in time and space.

To distinguish between both scenarii, and because single CD28 molecules were observed in consecutive frames, the localisations were grouped into trajectories (if closer than 300 nm from each other within up to four frames). If the clustering of localisations was only due to diffusion (hypothesis 2), the distribution of trajectories (represented by their mean position in time) should not differ between SA and CA activation. Interestingly, although the distribution of localisations is more uniform when the mean positions of the trajectories are plotted, clusters do not disappear (Figure 7.17, A-F), indicating that clusters of localisations are induced by both protein clustering and diffusion effects.

To further check that the grouping algorithm does not artificially group trajectories of

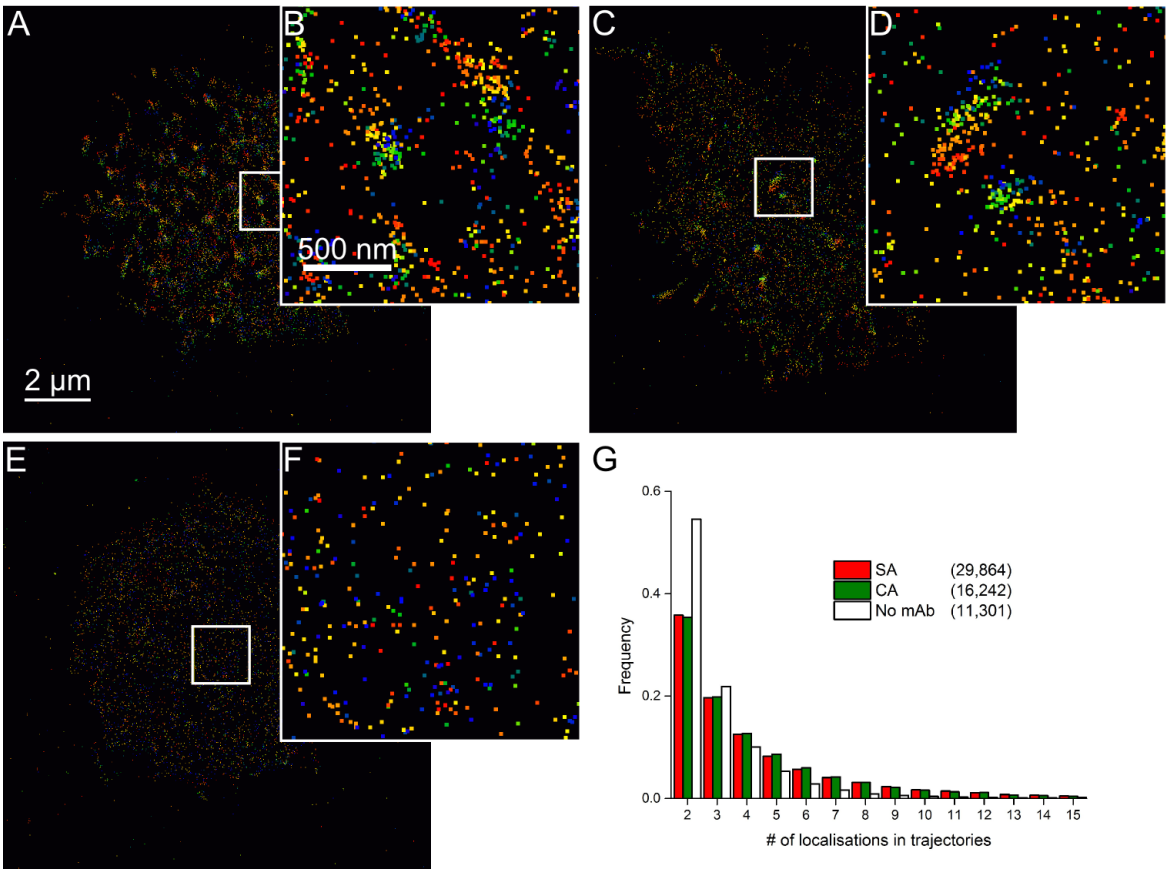


Figure 7.17 *Differentiating protein clusters from single particle trajectories.* Trajectories of representative cells (corresponding to Figure 7.4) transfected with a full length CD28-mEos construct and incubated with either SA (**A-B**), CA (**C-D**) or no mAb (**E-F**), were further analysed. **A,C,E**: Each trajectory grouping more than two localisations is plotted as a single pixel at its time-average position. The colour of the pixel code for the time of first appearance of the trajectory during the experiment (from 0 −blue−, to 3'20" −red−). **B,D,F**: Zoom of the region of the cell indicated by a white rectangle. G: Distribution of the number of localisations per trajectory (also referred as their 'length'). The total number of trajectories detected for each cell is given in parentheses in the legend.

physically different molecules, the distributions of the trajectory lengths were also compared. For both antibody activations, the distributions were almost identical (Figure 7.17, G). In the absence of mAb activation, lengths of the trajectories were much smaller, due to the quicker diffusion of the proteins which cannot be followed if they diffuse more than 300 nm between consecutive frames. Finally, for each cell, the distribution of displacements were plotted and a good fit with a log-normal function was obtained ($R^2 = 0.98$, 0.99 and 0.92 for SA, CA and no mAb activation, resp.), further confirming the correct grouping of localisations in trajectories [154].

### 7.3.2 Choice of the diffusion analysis

Different methods have been proposed to study the diffusivity of single proteins, all based on relating the squared displacement of the trajectories with the diffusion constant of a molecule undergoing Brownian motion (Equation 7.2). The mean-square displacement (MSD) method calculates a diffusion constant for each single trajectory [291, 292]. This linear regression method proves to be very accurate and efficient when long trajectories are available, especially for multi-tagged or long-lived fluorescent particles (*e.g.* intracellular trafficking vesicles or quantum dots). However, for small trajectories with few localisations, such as single-molecule trajectories, the regression is done on much fewer data points and is consequently less accurate and consistent [293].

For such trajectories, a jump-distance (JD) analysis was proposed: all square displacements from consecutive frames (or 'jump distances') from all trajectories are binned together and the overall probability of square displacements is fitted with a model of multiple populations or Brownian-diffusing proteins (Equation 7.1) [295, 296]. This analysis does not directly allow to calculate a diffusion coefficient for each trajectory, but it can unravel transitory changes of diffusion behaviours within all trajectories, since all square displacements are binned regardless of their belonging to a specific trajectory. Also, no data is lost, since even for the smallest trajectory a square displacement can be calculated [293]. Nevertheless, this method only takes into account displacements between consecutive frames, thus accumulating errors due to the time resolution of the acquisition: the localisation in each frame basically represents the average position of the diffusing molecule during the exposure time of the camera.

A more complete method, based on the analysis of the distribution of square displacements for different times, generalises the JD analysis [294]. In this method, a JD analysis is performed for square displacements from multiple time windows between frames. Instead

of calculating the mean square displacement for each trajectory, this method proposes to calculate the mean square displacement $SD_i$ for each population $i$ detected in the JD analyses. This analysis thus cumulates the efficiency of JD analysis for small trajectories and the robustness and precision of the MSD analysis, and was therefore chosen for the diffusion analysis in this chapter.

For each analysis, five fields of view containing at least one cell were recorded for 4,000 frames (200 s). In order to measure the quality of the analysis (involving two fitting steps), which depends on the number and length of the trajectories, the analysis could have been repeated on each field of view or each cell. This would rather reveal the cell-to-cell variability, due to differences in CD28 expression, cell landing, *etc*. Conversely, all cells were analysed together and a bootstrap approach was preferred. Because in the JD analysis all displacements are considered independently from each other and from the trajectories they belong to, the distribution of all squared displacements was randomly divided in five distributions that were separately analysed. The distribution of the extracted results is plotted as a box plot (25 and 75 percentiles, and mean $\pm$ one standard deviation of the mean) as in Figure 7.6 and similar.

This 'bootstrap' analysis can be seen as a means to computationally homogenise the five cells. It allows to test the robustness of the fit (which depends on the size of the dataset) and possibly extract statistical tests. Finally, the whole distribution was also fitted ($\circ$) as it contains the whole dataset and is thus more precise than the mean of the bootstrap distribution.

### 7.3.3 Physical origin of the multiple diffusing populations

The diffusion analysis separates populations with different diffusion behaviour. The meaning of these populations needs to be carefully discussed. First, the assumptions of the two fitting models used in the analysis should be recalled:

1. All proteins are freely diffusing, following a 2D Brownian motion (Equation 7.2). Biologically, this might not be the case, as CD28 could be secluded into micro-clusters, lipid rafts or membrane regions related to the close cell cortex structure. It is, however, a good model in general for short displacements compared to the diameter of the seclusion area. Indeed, for short time scales ($\tau \leq 200$ ms), the square displacements and the time-lapse $\tau$ are well described by a linear correlation (Figure 7.5).

2. Only a discrete number of homogeneous populations of diffusing CD28 were fitted (Equation 7.1). Biologically a large continuum of diffusing CD28 populations

is rather expected since the antibody-CD28 complexes may form long linear structures, referred as to membrane-bound immune complexes (MBICs). These structures are expected to present a large variation of sizes.

The most parsimonious model fitting the data was a model of three populations. For some experiments, though, the populations were highly correlated (*e.g.* Figure 7.9 or Figure 7.14) and a model of two populations would be more parsimonious to describe the data. For the sake of comparison, the model of three populations was consistently used for all experiments in this chapter.

The third 'fixed' population ($SD_3(\tau) \leq \sigma$) is always observed in each cell line and for all tested constructs (CD28 as well as CD86 fused to mEos). This is interpreted as an artefact of the imaging protocol, probably due to cell debris or fluorescent dust. This population is therefore fitted but disregarded in all results. The two other populations can be interpreted in two complementary ways:

1. The diffusion analysis, indifferently on the validity of its hypotheses, is a theoretical mathematical means to compare different activation conditions in a quantitative, statistical and parsimonious manner. The populations are in this sense a way to describe the data, statistically compare results, and draw conclusions about trends.

2. A second interpretation gives more biological insights on the putative mechanism at play, but is highly speculative and subject to criticism, It would confer some biological meaning to the division into two diffusing populations. For example, the two populations could refer to antibody-bound ($D_2$) and antibody-unbound ($D_1$) CD28 subpopulations. A more plausible interpretation would consider CD28 proteins bound to an MBIC that is itself bound to a secondary antibody coating the coverslip ($D_2$) or not ($D_1$). Since the SA and the CA bind similarly to the secondary antibodies, the number of MBICs bound to the coverslip ($D_2$) is similar for both, but the sizes or interactions of the MBICs could be different between both mAbs and this would only significantly affect the diffusion of the unbound MBICs ($D_1$).

   A CD28-protein that belongs to an MBIC bound to an immobilised secondary antibody can still move around the antibody fixed on the coverslip: the linear MBIC chain can be seen as an ideal polymer chain with one fix point. On scales smaller than $\sqrt{n} \cdot l$ ($n$ being the number of antibodies linking the CD28 to the fix point, and $l$ the size of a CD28-antibody element) [305], the CD28 protein, although part of a bound MBIC complex, still diffuses. This shows that the CD28 population bound to bound MBICs are not fixed and thus do not belong to the third population ($D_3$).

Although appealing, there is not enough biological information available to support this latter interpretation. Also, not all of the above results are consistent with it: *e.g.* in the cross-linking experiments (Figure 7.9), MBICs only form when both antibodies are added to the cells. No second population should then be observed (only diffusive CD28 proteins or CD28-antibody complexes $-D_1-$ and fixed CD28-antibodies complexes $-D_3$). The absence of the third population ($D_2$) is probably why results are highly correlated and a model of two population would have described the data better. However, in the case of the dual-antibody activation, large MBICs are restored and three independent populations should then be observed, instead of the observed correlated diffusion coefficients.

This is why, although interesting, no final biological interpretation of the CD28 populations is given in this chapter. The diffusion results are rather used as a quantitative way to compare and analyse trends. More biological knowledge is required to draw any solid conclusion about the nature of the diffusive populations.

However, although little can be said about CD28 populations, and since CD28 expression is not trivial to vary, the concentration or immobilisation of the mAbs was varied to gain more knowledge and evidence about the molecular mechanism of T cell SA-mediated activation.

### 7.3.4 Differences of affinity and kinetic rates

Although unlikely between two classes of antibodies defined by a binary behaviour, it is not impossible that together with the difference of epitope positions, a difference of thermodynamic or kinetic constants characterises SAs compared to CAs. Therefore, M. Aßmann is purifying the Fab fragments of both SA and CA antibodies used in this study and is determining their precise $K_D$ by Biacore surface plasma resonance.

Since the $K_D$ is equal to the ratio of the dissociating $k_{off}$ to the association $k_{on}$ kinetic rates, an approximative comparison of the thermodynamic constants can be estimated from flow cytometry experiments. And because dissociating rates are relatively similar for both mAbs studied here (flow cytometry experiments by M. Aßmann and ref. [278]), the comparison can be restricted to the association rates $k_{on}$. Furthermore, although the thermodynamic binding equilibrium is reached in the IL-2 experiments − after 48 h of mAb incubation − an estimation of the association rate of the SA indicates that only $\sim 2/3$ of the final bound fraction of SAs are bound after the 15' incubation before imaging occurs in the sptPALM experiments described in this chapter [278]. The CA, however, has reached its thermodynamics binding equilibrium after 15'.

The dilution experiments (Figure 7.10) can be studied as precipitin reaction curves [306]: as the concentration of mAb increases, larger MBICs are formed, slowing down their diffusion, until mAbs are introduced in excess and favourably bind monovalently CD28 proteins, decreasing the size of the MBICs and increasing their diffusivity. At equivalence (when the fraction of antibodies that is cross-linked is maximal) and at equilibrium, Dembo *et* Goldstein demonstrate that the mAb concentration is equal to half of the monovalent $K_D$ [307].

Since the thermodynamic equilibrium is reached for CA binding in the diffusion experiment, from Figure 7.10.E the equivalence was extracted ($\sim$ 1 µg/mL) and the estimation of the monovalent equilibrium constant was calculated: $K_D^{CA} \sim 3.5 \cdot 10^{-9}$ mol/L. The thermodynamic equilibrium is not reached in the case of SA incubation for the diffusion experiments, but it was for the IL-2 experiments, which had a 48 h incubation period. Thus, similarly, the equivalence was extracted from Figure 7.10, A ($\sim$10 µg/mL) and the dissociation constant was calculated: $K_D^{SA} \sim 3.5 \cdot 10^{-8}$ mol/L $= 0.1\, K_D^{CA}$.

These values are noticeably consistent with the observation of Tacke *et al.* that the SA "had to be used at a 10-fold higher concentration [than the CA] to achieve a comparable binding over time" [278]. This also confirms that after 15' of incubation, the SA has not reached its binding equilibrium: indeed, the equivalence is not observed at 10 µg/mL in Figure 7.10, B.

In summary, the thermodynamic monovalent dissociation constants of the CA to CD28 is approximately an order of magnitude smaller than the dissociation constant of the SA to CD28. This is driven by a 10-fold difference of their respective binding rates. The precise values measured by surface plasma resonance should validate these results. Since $TCR^-$ cell lines and signalling-incompetent CD28 proteins are used, cells are locked in a pre-activation state. This, repeating the dilution experiments at later time-points when SA-binding equilibrium is reached (*e.g.* after 2 h incubation) is possible and would also cross-validate these conclusions.

Similar experiments with different pairs of SAs and CAs would be necessary to determine whether this difference in affinity is specific to the mAbs studied in this chapter or a new characteristic defining both classes of antibodies. In this sense, Tacke *et al.* postulated that the shared epitopes of SAs, closer to the plasma membrane, are less accessible, explaining the lower association rate of the SA, and thus its higher $K_D$. But if the monovalent affinity is different, does it affect cross-linking of CD28 by the mAbs? Does it affect the avidity of the antibodies?

### 7.3.5 Requirements for cross-linking of CD28

Since both CD28 and mAbs are divalent, the mAbs can cross-link CD28 homo-dimeric receptors and form long linear structures, also called membrane-bound immune complexes (MBICs). Consistent with previous studies showing that only monovalent anti-CD28 mAbs can blockade CD28 signalling [308], soluble SA Fabs were unable to induce IL-2 production [309]. Using the opposite approach, bivalent SA were also unable to induce IL-2 production by monomeric CD28-like receptors (Figure 7.9, B). Strikingly, T cell activation was strongly recovered by cross-linking the monomeric CD28-like receptors with two different bivalent antibodies and allowing the formation of MBICs.

As expected, similar results were observed in diffusion experiments (Figure 7.9): little slowing down in the monomeric CD28-like receptors is induced by incubation with either mAb alone, but a strong decrease in diffusivity appears when both antibodies are used in combination. Interestingly though, even in the absence of any second-order cross-linking, one antibody ('CA 1') significantly slows down CD28-like monomers more than the other one ('CA 2').

Incidentally, the epitopes of both anti-PD-1 antibodies have been mapped (Figure 7.9, F, courtesy of S.J. Davis). The epitope of 'CA 1' antibody is located near the plasma membrane, on the 'side' of PD-1, whereas the epitope of 'CA 2' is on 'top' of PD-1. Therefore, 'CA 1' falls into the antibody class of putative SA. This classification is furthermore fully consistent with the previous observation of a significant decrease of PD-1-CD28 diffusivity compared to 'CA 2' putative CA. It also underlines that although cross-linking has the major effect on slowing down CD28 diffusion, another independent phenomenon plays also some part in it.

This observation confirms that although it may decrease the affinity of SAs, the specific epitope location of SAs may also increase their avidity, playing a complex role in slowing the diffusion of their ligands. Such a phenomenon was theoretically described by Å. Larsson when studying divalent binding of mAb to a monomeric cell surface antigen [310]. Binding of a divalent mAb is described as a two-step reaction between (1) soluble diffusing antibodies and monomeric receptors, and (2) monovalently bound antibodies anchored on the membrane and monomeric receptors, thus separating the effects of monovalent affinity and avidity.

Moreover, although not entirely convincing as the two Fab arms of an antibody are considered to be independent because of the flexible hinge linking them to the Fc domain [311, 312], Larsson suggests that if the monomeric receptor has a rigid structure, "the best fit for the divalent binding is obviously obtained when the angle between the epitope and the

membrane surface, together with the predominant Fab-Fab angle, amounts to 180°." Practically, IgG1 antibodies such as those used in this chapter have a Fab-Fab angle estimated to $30-180°$ [313]. For such antibodies, cross-linking would then be critically favoured for antigens oriented with an angle to the plasma membrane of $0-75°$, *i.e.* not on 'top' of the receptor (see Figure 3 in ref. [310]).

A stronger argument preserving the large distribution of Fab-Fab angles is that once bound to one receptor, the plasma membrane sterically restricts the overall accessible Fab-Fab angles. The restriction is more stringent when the epitope is located close to the plasma membrane. Interestingly, the plasma membrane blocks Fab-Fab angles that do not allow binding of another receptor. Thus, thermodynamically, the closer the epitope is to the plasma membrane, the more cross-linking is favoured because the proportion of accessible states that allow binding is increased. This would directly and mechanistically link epitope location (and thus the SA class of antibody) to its effect on CD28 diffusion.

Finally, as not all transmembrane proteins (*e.g.* CD86-mEos in Figure 7.8, co-expressed with CD28 proteins in cells activated with anti-CD28 mAbs) having an extracellular domain see their diffusivity reduced in presence of the SA, cross-linking of CD28 receptors is not forming a large mesh-work sterically limiting the diffusion of all transmembrane proteins as in a fence and picket model of the plasma membrane [314], but rather separated ball-like clusters as indeed visible in Figures 7.4 and 7.13.

### 7.3.6 Importance of the formation of a close-contact zone

As for antibody-induced TCR triggering, antibody-induced CD28 co-stimulation requires immobilisation of the cross-linking antibody on a surface both *in vitro* and *in vivo* (M. Aßmann, personal communication and ref. [278, 282]). The Fc part of the activating antibody also seems to play a role in T cell activation [308, 315]. Together, these conclusions suggest a critical role for a zone of contact between the membrane of the T cell and the surface on which anti-CD28 antibodies are immobilised.

Because SAs bind to epitopes on CD28 $\sim 75$ Å closer to the plasma membrane than CAs, it has been proposed that the distance separating the T cell from the activating surface was critical for SA-mediated T cell activation [234]. To test this hypothesis, a new construct, inserting a $\sim 75$ Å-tall human Fc domain between the transmembrane domain and the ectoplasmic domain of the previous CD28 construct, was engineered. Thus, the previously used anti-CD28 SA and CA target the same epitopes which are located a little further from the T cell membrane. An anti-Fc mAb that binds an epitope on the 'side' of the added Fc

domain (S.J. Davis, personal communication) was also used as a putative SA that can bind at a similar distance from the membrane than the anti-CD28 SA in the case of the original CD28 construct (Figure 7.14, A).

Strikingly, as predicted in the proposed hypothesis, the addition of the 75 Å domain depleted IL-2 production. Furthermore, targeting the base of the new construct with the anti-Fc putative SA allowed the recovery of T cell activation (Figure 7.14, B). Interestingly, although the additional domain increases CD28 diffusion from 0.025 to 0.04 $\mu m^2/s$ for anti-CD28 SA incubation, the effect of incubation with the anti-Fc putative SA was comparable to the effect of the CA and did not recover the slow diffusivity of the original CD28 construct activated by the anti-CD28 SA ($0.07 \gg 0.025$ $\mu m^2/s$) (Figure 7.14, C-E). The original anti-CD28 SA is no longer an SA for Fc-CD28 in terms of IL-2, but still looks like a SA for Fc-CD28 in terms of diffusion.

This is the only experiment for which IL-2 and diffusion experiments do not strongly correlate in this chapter. A first explanation is that the cell line used for the diffusion experiments did not correctly express the new construct[1]. Repeating the experiment with newly transfected cells should allow for testing this hypothesis. Otherwise, a critical difference in kinetic rates between the anti-Fc putative SA and the anti-CD28 SA could also explain the difference observed: the thermodynamic equilibrium may be reached much more slowly for the putative SA, and the diffusion experiment might only describe an early out-of-equilibrium situation at the difference of the IL-2 experiments. Repeating the experiment at a later time-point (*e.g.* after 2 h of incubation) will test this possibility.

### 7.3.7 From correlation to causality?

A very strong correlation between SA-induced IL-2 production and the slowing down of CD28 receptors is revealed by almost all experiments in this chapter. An outlier is the experiment for which the extracellular domain of CD28 is separated from the plasma membrane by an extra $\sim 75$ Å, as discussed in the previous section. Can any information be inferred from such a correlation? What does it mean in terms of the mechanism of SA-mediated leucocyte receptor triggering?

The previous discussions suggest a mechanism of a two-step binding reaction model

[1]Different cell lines are used: for the IL-2 experiment, BW5147 cells are simultaneously transfected with CD3$\delta$ and CD3$\zeta$ chains to recover TCR expression and with the following construct: [rat ectodomain of CD28]-[human Fc domain]-[mouse transmembrane and signalling domains of CD28]; for the diffusion experiment, BW5147 cells are only transfected with the mEos-tagged and signalling-incompetent version of the previous construct: [rat ectodomain of CD28]-[human Fc domain]-[mouse transmembrane domain of CD28]-[30 amino acid linker]-[mEos3.2].

linking epitope binding site to avidity and thus to cross-linking and CD28 diffusivity (Section 7.3.5).

Nevertheless, such conclusions are mostly based on experiments done with a unique pair of SA and CA. An important exception, however, concerns the cross-linking experiment (Figure 7.9) where two putative SA and CA (respectively 'CA 1' and 'CA 2') are used. Noticeably, this independent pair of SA and CA shows all similar characteristics compared to the original pair: (1) the putative SA is so-called because of the location of its epitope on its ligand close to the plasma membrane, in opposition to the putative CA (Figure 7.9, F); (2) the binding rate $k_{on}$ of the putative SA is 10-fold lower than that of the putative CA, but have relatively similar $k_{off}$ (S.J. Davis, personal communication); (3) the putative SA decreases the diffusivity of its receptor more than the putative CA (Figure 7.9, C-D); (4) finally, it might also induce a slightly higher IL-2 production, although large cross-linking is prevented, than the putative CA (Figure 7.9, B). Importantly, this suggests that the previous binding model and conclusions could apply to the whole classes of SA and CA rather than being specific for a pair of mAbs. Repeating similar experiments with other pairs of SA and CA will challenge the possibility of such a generalisation.

This model mechanistically links epitope binding location with diffusion behaviour but how CD28-mediated signalling occurs remains elusive. Although a correlation does not automatically implies a link of causality, it suggests a possibility of a shared common cause if not a direct causal effect. Cross-linking of receptors is known to locally accumulate intracellular domains of receptors that may directly or indirectly induce their cross-phosphorylation and cross-activation (*e.g.* receptor tyrosine kinases, reviewed in ref. [316]). CD28, however, cannot directly cross-activate (*i.e.* trans-autophosphorylate) as it lacks intrinsic kinase activity. CD28 depends on extrinsic kinases such as Lck or ZAP-70. If a CD28 receptor recruits kinases, a local accumulation of CD28 would, however, favour the likelihood of neighbouring receptors to become phosphorylated by these kinases. Lastly, cross-linking alone does not account for the requirement of antibody immobilisation.

The KS model presents the advantage of offering an explanation for both a causal link between a decrease in diffusivity and signalling (the receptor needs to stay long enough in the close-contact zone to get activated), and the requirement for antibody immobilisation (to form a close-contact zone that segregates activating and deactivating proteins). Indeed, an accumulation of cross-linked CD28 could potentially create a large zone of close-contact between the T cell and the APC (or the secondary antibody-coated surface). Transmembrane molecules with large extodomains would be excluded from such close-contact zones. Such a segregation would locally change the equilibrium between cytoplasmic (*e.g.* ZAP-70) or

small transmembrane (*e.g.* Lck) kinases and abundant transmembrane phosphatases with large ectodomains (*e.g.* CD45 or CD148) [317], locally increasing the net phosphorylation of the CD28 receptors immobilised in the close-contact zone, which would induce their triggering.

The importance of the proximity of the epitope to the plasma membrane for cell activation (Figure 7.14, A-B) also suggests a mechanism sensitive to the height of the contact between the T cell and the coated coverslip. Therefore, to test the mechanism proposed by the KS model and specifically the existence of height-dependent segregation zones (*cf.* Section 7.2.6), the localisations of both CD28 and CD45, a transmembrane non-specific phosphatase with a large ectodomain and which plays a critical role in TCR triggering, were studied and compared.

### 7.3.8 Possible evidence for segregation

A dual-colour PALM-dSTORM protocol was optimised to simultaneously observe both CD28 and CD45, a transmembrane protein with a large rigid extracellular domain that is segregated from close-contact zones in TCR triggering (Chang, Fernandes, Ganzinger, Lee *et al.*, submitted). The dual tagging of CD28 intra-cellularly by the photo-activable fluorescent protein mEos and extra-cellularly by anti-CD28 mAbs labelled with a far red dye served as a positive control to test the possibilities and limits of the method. Partial co-localisation of mEos and anti-CD28 mAbs was observed in both diffraction-limited and super-resolved modes (Figure 7.12 and 7.13). Total co-localisation was prevented by multiple factors typical of single-molecule experiments: partial labelling, limited sampling, and movements due to live-cell imaging (as revealed by the displacement of clusters of trajectories over the acquisition time in Figure 7.17, B and D). However, although finding a protocol to image two spectrally-separated independently-photo-switchable fluorophores simultaneously at correct densities with buffer conditions compatible with live cell imaging was non-trivial [107], the signal-to-noise ratio of single emitters and the quality of the recorded data positively validated the method.

Such drawbacks could account for the non-significantly different average co-localisation of CD28 and CD45 observed after SA and CA incubation (Figure 7.15 and 7.16) [52, 107]. Nonetheless, the trend might suggest a decrease in co-localisation in the case of SA activation, which would be an evidence for SA-induced increase of segregation of CD45 from CD28, as postulated by the KS model. Further optimisation of the protocol (*e.g.* modification of the imaging buffer, longer imaging time), as well as investigating the possibility

to fix T cells without disrupting the contact formed with the coverslip will allow to tackle some of the drawbacks.

In parallel, functionally testing predictions of the KS model in a top-down approach (*e.g.* testing the effect of CD45 proteins with a truncated ectodomain on both IL-2 production and CD28 diffusion) and imaging of other components of the signalling cascade (*e.g.* Src tyrosine kinases such as Lck, or the TCR) will allow a better understanding of mechanism behind SA-mediated CD28 signalling. Indeed, the segregation of phosphatases with large ectodomains, such as CD45, and small kinases, such as Lck, is a direct prediction of the KS model. Furthermore, since the SA induces T cell activation in absence of signal 1, in a ligand-independent but TCR-dependent manner (Figure 7.6, IL-2 production is only observed in TCR-sufficient cells), the SA might induce ligand-independent TCR triggering. Observation of the distribution, the diffusion and the possible segregation of the TCR on the membrane of SA-decorated cells is therefore of great interest.

### 7.3.9 Temporal segregation in light of the kinetic-segregation model

In case of CD28 super-agonism T cell activation, the segregation of CD45 may turn out to be on much smaller length scales than previously observed on supported-lipid bilayers and on glass coated with a single layer of activating mAb (ref. [243] and Chang, Fernandes, Ganzinger, Lee *et al.*, submitted). In the experiments presented in this chapter, effectively two randomly-oriented layers of antibodies separate the cell from the glass surface (the activating mAb decorating the cell, and the secondary antibodies coating the glass). This configuration may not favour the observation of clear segregation at length scales larger than the precision of the SMLM imaging. Segregation of CD45 phosphatases from contact-zones may only be very transient and may never be observable in the co-localisation experiments.

However, even transient CD45 segregation would result in an overall decrease of CD45 and CD28 diffusion rates, since the segregation would impose an additional barrier to diffusion. Another way to look at it, is to consider the chance of encounter between CD28 and CD45: it can be decreased by reducing the number of CD45 proteins (*segregation side* of the KS model) or (independently and non-exclusively) by reducing their relative speed (*kinetic side*) (Figure 7.18). Measuring the variation of CD45 diffusion rates between CA and SA activations would enable the estimation of such an effect.

Thus, if CD45-CD28 encounter rate was indeed decreased in the case of the SA, the dephosphorylation rate of CD28 would decrease whereas the phosphorylation rate would be expected to remain constant (since intracellular Lck should be unaffected, since Lck has

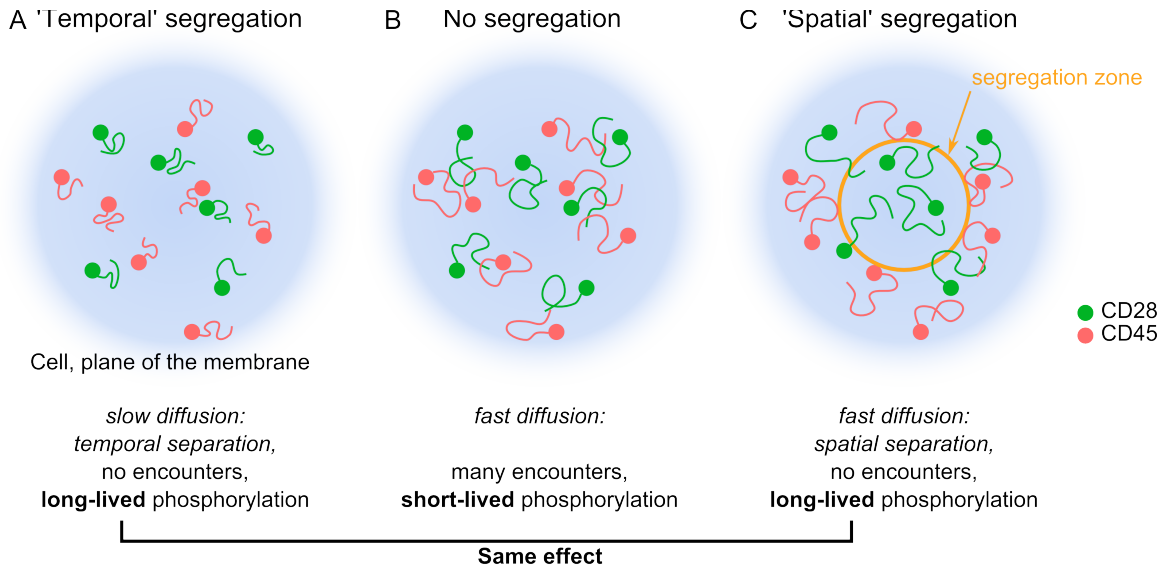


Figure 7.18 *Temporal segregation of membrane receptors.* Illustration of the effect of diffusion decrease of two receptors on their encounter rates. **A**: Slow diffusion of CD45 (red) and CD28 (green) decreases the rates of encounter of both species which need much more time (varying with the square of the distance) to explore the same region. Thus this temporal segregation, in light of the KS model, would induce long-lived phosphorylation of CD28. **B**: Conversely, fast diffusion observed on non antibody-activated cells induces frequent encounters between both CD45 and CD28 proteins. Thus, only short-lived phosphorylation could be observed. **C**: Temporal segregation induces the same effect as conventional spatial segregation. If CD45 are prevented to diffuse in a close-contact zone (orange circle), encounters between both CD45 and CD28 will be prevented in this zone, for any diffusion rate. Thus, long-lived phosphorylation, as postulated by the KS model, will be observed.

no ectoplasmic domain). Thus, in line with the KS model, the kinase-phosphatase balance would shift; therefore the number of CD28 molecules that remain phosphorylated for a time sufficient to activate the cell would increase.

Seen in this light, the significantly and reproducibly increased confinement, or decreased diffusion rates, of CD28 for the SA compared to the CA are very interesting, since a slowing-down of both 'partners' (CD28, CD45) may effectively amplify their segregation. Repeating the final co-localisation experiment (Figure 7.15) at labelling densities and laser powers that allow simultaneous single-particle tracking of both CD28 and CD45 would enable to test this hypothesis. Also, as this last experiment may be technically challenging, observing CD45 diffusion alone, after CA or SA activation, on a single-molecule level or by fluorescence recovery after photo-bleaching will be sufficient to initially validate a specific decrease of CD45 diffusion by the SA.

### 7.3.10 Conclusions and future experiments

Results of this chapter indicate a strong correlation between SA-mediated T-cell activation and lower diffusivity of CD28 proteins. They also suggest a two-step binding reaction of anti-CD28 mAbs to CD28 homo-dimers: (1) soluble mAbs first bind monovalently to a CD28 receptor, the rate of the reaction depending on the proximity of the epitope on CD28 to the plasma membrane (lower rates for membrane-proximal epitopes); (2) once bound to one receptor, mAbs bind to a second receptor, the binding constant of the reaction decreasing with the proximity of the epitope to the plasma membrane for geometric and thermodynamic reasons. Experiments need to be repeated at later time-points and with other pairs of SA and CA mAbs to validate the generalisation of this working model to both classes of antibodies.

Although this model suggests the importance of differential cross-linking for super-agonism, it neither accounts for the SA-specific slowing down of CD28 in the absence of cross-linking (Section 7.2.2) nor for the requirement for antibody immobilisation and the possible importance of the size of the gap separating the plasma membrane from the contacted surface. From the four originally proposed models, only the KS model accounts for these observations. Some initial but non-significant evidence for size-dependent segregation of transmembrane proteins is in line with the predictions of the KS model. Repeating the Fc-CD28 diffusion experiment is critical to understand the possible link between both differential cross-linking and KS models.

Additional imaging of other components of the signalling cascade of CD28 and functional experiments further challenging the KS model are necessary to confirm these re-

sults and elaborate the missing steps bridging CD28 cross-linking and CD28 signalling. Finally, in a long-term perspective, similar experiments would need to be repeated in a more biologically-relevant system of cell-cell interaction such as a supported lipid bilayer functionalised with Fc receptors [318].

# PART C

# Chapter 8

# Materials and methods

## 8.1 Materials and methods common to all projects

### 8.1.1 Microscope set-up

Two microscope set-ups of similar design were used in the experiments presented here (*cf.* Figure 3.1). The set-up used in Chapters 3, 4 and 6 is described here. Where both set-ups differ, specificities of the microscope used in Chapter 7 are specified in brackets.

Collimated 640 nm, 561 nm , 488 nm, and 405 nm laser beams were spectrally filtered, aligned and focussed at the back aperture of an Olympus UPlanApo 1.49 $n_a$ 60x oil TIRF objective mounted on an IX71 [IX73] Olympus inverted microscope frame (*cf.* Table 8.1 for the specific lasers and filters). The power of the collimated beams at the back aperture of the microscope were typically of 20, 50, 5, <0.01 mW, resp., corresponding to power densities of 40-400 W/cm$^2$ (<60 mW/cm$^2$ for the 405 nm activation line) at the sample (*cf.* Table 8.1). The lens objective was regularly cleaned off oil left-overs thanks to three organic solvents: methanol (Sigma Aldrich, 154903), m-xylene (Sigma Aldrich, 95672), and methanol (Sigma Aldrich, 154598).

The fluorescent signal was separated from the illumination beams by a four-band dichroic (Semrock, Di01-R405/488/561/635) and filtered with either a 488 nm long-pass filter (Semrock, BLP01-488R, 'green channel'), a combination of a 561 nm long-pass (Semrock, BLP01-561R [BLP02-561R]) and a band-pass filters (Semrock, FF01-593/40 for yeast imaging; Semrock, FF01-587/35 for mammalian cell imaging) ('red channel'), or a 640 nm long-pass filter (Semrock, FF01-642/LP, 'far red channel'). The filtered signal was then expanded through a 2.5x achromatic beam expander (Olympus, PE 2.5x 125) and finally projected on an EMCCD camera (Photometrics, Evolve 512 [Evolve Delta]).

Table 8.1 *Optical characteristics of the microscope set-ups.* Characteristics of the set-up used in Chapters 3, 4 and 6 are given. Where characteristics differ, specificities of the microscope used in Chapter 7 are specified in brackets. All filters are from Semrock.

| | **640 nm line** | **561 nm line** | **488 nm line** | **405 nm line** |
|---|---|---|---|---|
| **Laser** | Coherent, Cube 640-100C [Toptica, iBeam Smart CD_11005] | Cobolt, Jive 200 [Cobolt, Jive 500] | Toptica, iBeam Smart 488 100 mW | Oxxius, LaserBoxx 405 [Cobolt, MLD 405] |
| **Clean-up filter** | FF01-640/14 [LD01-640/8] | FF01-561/14 [LL02-561] | LL01-488 [LL01-488] | FF01-417/60 [FF01-405/10] |
| **Beam combiner** | N/A [FF705-Di01] | FF605-Di02 [Di02-R561] | FF552-Di02 [Di02-R488] | FF458-Di02 [Di02-R405] |
| **Typical power at the back aperture** | 20 mW | 50 mW | 5 mW | <10 μW |
| **Beam diameter after collimation** | ∼10 mm | ∼7 mm | ∼6.5 mm | ∼8 mm |
| **Power density at the sample** | ∼100 W/cm$^2$ | ∼400 W/cm$^2$ | ∼40 W/cm$^2$ | <60 mW/cm$^2$ |

For simultaneous two-colour imaging, the signal was only filtered with the 561 nm long-pass filter. A dualview was inserted in the optical path between the beam expander and the camera to split the collected signal in two channels projected on two halves of the camera (Photometrics, DV2 mounted with a Semrock, FF635-Di01 dichroic). The short-pass channel was further filtered with a 580 nm band-pass filter (Semrock, FF01-587/35), and the long-pass channel with both the 640 nm long-pass filter and an additional 700 nm band-pass filter (Semrock, FF01-692/40). Before imaging, the dualview was aligned thanks and multi-colour beads were simultaneously imaged in both channels for their registration (*cf.* Section 3.2.3).

### 8.1.2 General imaging protocol

Samples were directly imaged on square glass coverslips (VWR International, borosilicate glass thickness #1, 631-0122). Before any use, auto-fluorescence from the coverslips were eliminated by their washing in an argon plasma for >30' (Harrick Plasma, PDC-002). Samples were resuspended and washed in buffers filtered twice with 200-nm filters (Millex GP, PR04064) to limit any fluorescence background in the buffer.

Samples were typically imaged for 2,000-4,000 frames of 30-50 ms exposure under TIRF illumination. Automated sequences written as plug-ins or macros for μManager [173] were programmed to ensure unbiased and consistent imaging protocols. The quality and reproducibility of the TIRF illumination was qualitatively monitored by the angle of the reflected total-internal reflection beam at the back aperture of the microscope.

Two modes of 405 nm activation were used for switching mEos fluorescent proteins on:

**Continuous constant activation** , used by default. The intensity of the 405 nm illumination was chosen on a first adjustment sample such as PSFs were separated in each frame, before preparing another sample to take the measurements.

**Continuous Fermi activation** , in order to optimise the number of PSFs appearing in each frame along the whole imaging time (*cf.* Section 3.3.4). This type of activation was used in all the experiments of Chapter 6 and when indicated as such in the other chapters. The maximum intensity of the 405 nm illumination was chosen as for the constant activation, although a denser PSF coverage per frame were aimed at.

Recorded SMLM movies were analysed with Peak Fit [149] using the parameters according to Table A.3. Further post-processing algorithms are described in Section 3.4 and 7.2.1.

### 8.1.3 SMLM data representation

From the final list of localisations was rebuilt a super-resolved image. Four different representations are used in this work:

**Same amplitude and width.** Each localisation is rebuilt as a 2D-Gaussian of same intensity (arbitrary) and same width (the theoretical precision of the experiment, *i.e.* the value at the peak of the distribution of theoretical precisions of all localisations as defined in Section 3.4.3). This representation is the default one and was used in Figure 4.9, all figures from Chapter 6 except Figure 6.16, and Figure 7.4.

**Individual amplitude and width.** Again, each localisation is rebuilt as a 2D-Gaussian, but both intensity and width are specific to each localisation: the intensity of the 2D-Gaussian is equal to the fitted intensity of the localisation, and the width to the theoretical precision of the estimation of its position (*cf.* Section 3.4.3). Figures 3.13 (G-H) and 4.8 were rebuilt following this protocol.

**Time of first appearance.** Localisations appear at a given frame during the SMLM acquisition. To distinguish between clustering due to transient photo-blinking of the fluorophore and real clustering of multiple aggregated fluorophores, each localisation can be plotted as a small circle which colour codes for its frame of appearance: thus, uni-colour clusters indicate photo-blinking, and multi-colour ones suggest aggregation. If localisations are grouped, the time of first appearance, *i.e.* the earlier frame of the localisations belonging to the group, is used instead of the frame. This was the representation chosen for Figure 7.17.

**Trajectories.** When fluorophores are tracked and localisations grouped in trajectories, a mean-square displacement (MSD) analysis allows to estimate diffusion coefficients for each trajectory [291, 292]. The MSD of the long trajectories (>10 frames) are computed and the five first time-points are used for linear regression and to estimate the diffusion coefficient. Trajectories are then plotted as lines joining the consecutive positions of the localisations belonging to the specific trajectory. The colour of the trajectory codes for the estimated diffusion coefficient (on a log-scale value). This representation is used in Figure 7.4. However, in Figure 3.4, the colour of each section of the rebuilt trajectories codes for the frame of appearance of the localisations during the acquisition (orientating the trajectory time-wise). Also, in Figure 3.12 and Movie S1, each trajectory is defined by a different colour independently on its mobility.

For two-colour co-localisation observations, two complementary representations were implemented and used in Figures 6.16, 7.13 and 7.15:

**Superposition of the super-resolved images.** As in two-colour conventional fluorescence microscopy, the data from each channel of the dualview can be independently analysed. After registration of the lists of localisations to correct for channel mis-alignment (*cf.* Section 3.2.3), both super-resolved images can be rebuilt by one of the methods previously described and superposed using two different colours (*e.g.* green for the short-pass channel, and red for the long-pass one).

**Coordinate-based co-localisation images.** Similarly, after registration of the lists of localisations, a coordinate-based co-localisation (CBC) can be computed (*cf.* Section 3.4.2): for each localisation of each channel, a CBC value between -1 (anti-correlation) and +1 (perfect co-localisation) is calculated and defines the degree of co-localisation of the localisation with the other channel. These values are then used to rebuild two images (one for each channel) where each localisation of one channel is plotted as a small circle which colour codes for its CBC value.

### 8.1.4 Imaging fluorescent beads and isolated fluorophores

The stock of beads or fluorophore of interest (*cf.* Table 8.2) were sonicated for 30 s and diluted 1/100 in MilliQ water. The diluted particles were then sonicated for 2-10' and diluted again 1/1,000 in MilliQ water. An imaging hydrophobic gasket (Bio-rad, SLF0201) was applied on each coverslip. The coverslip was then coated with 100 µL of fresh sterile poly-L-lysine (Sigma, P4832) for 15' at room temperature, before being washed three times with 100 µL of MilliQ water. 50 µL of the diluted particles were dropped on the coverslip for 10' at room temperature, washed three times with 100 µL of MilliQ water and imaged under TIRF illumination.

## 8.2 Materials and methods for Chapter 3

### 8.2.1 Double-helix microscope

Collimated 640 nm (Toptica, iBeam Smart 405-S_10924) and 405 nm (Toptica, iBeam Smart 640-S_10925) laser beams were spectrally filtered (Semrock, FF01-640/14 and FF01-405/10, resp.), combined (Semrock, dichroic mirror Di02-R405), aligned and focussed at the back aperture of a Nikon Plan Apo 1.20 $n_a$ 60x water objective mounted on a Nikon

Table 8.2 *Separated beads and fluorophores used in this thesis.* †: high concentration (1/10 dilution of the stock of purified proteins) were used to record bulk measurements.

| **Figure** | **Separated fluorophores** |
|---|---|
| Figure 3.3, 3.4, 3.6 and 3.15 | Invitrogen, 0.1 µm TetraSpeck Microspheres (T-7279) |
| Figure 3.7 | *id.* |
| Figure 3.8†, 3.9, 3.10 and 3.11 | Purified mEos2 and mEos3.1 |
| Figure 4.1, 4.2 (A), 4.3, 4.4, 4.5, 4.6 (A, $1^{st}$ row), and 4.7 | Molecular Probes, 0.04 µm FluoSpheres NeutrAvidin-Labeled Microspheres (F-8771) |
| Figure 4.2 (B) | Alexa647-labelled Tau monomer |
| Figure 4.6 (A, $2^{nd}$, $3^{rd}$, $5^{th}$ rows) | Invitrogen, 0.1 µm TetraSpeck Microspheres (T-7279) |
| Figure 4.6 (A, $4^{th}$ row) | Invitrogen, Qdot 655 ITK (Q21321MP) |

Eclipse Ti inverted microscope frame. The power of the collimated beams at the back aperture of the microscope were typically of 50 mW and <50 µW, resp., corresponding to power densities of 600 W/cm$^2$ and <600 mW/cm$^2$, resp., at the sample. The lens objective was regularly cleaned off oil left-overs as described in Section 8.1.

The beam of a second 640 nm laser (qioptiq, iFlex-2000) was focussed to create a thin sheet of light to illuminate a plan of the sample perpendicular to the optical axis of the imaging objective lens. The collimated laser beam was expanded up to a diameter of $\sim$10 mm. A cylindrical lens (Thorlabs, LJ1567RM-A, $f = 100$ mm) was collimated with the back aperture of the illumination objective (Mitutoyo, M Plan Apo 0.28 $n_a$ 10x air objective) to horizontally focus the laser beam in the focal object plane of the objective. A horizontal light-sheet was consequently formed at the focal image plane of the illumination objective which was aligned with the optical axis of the imaging objective.

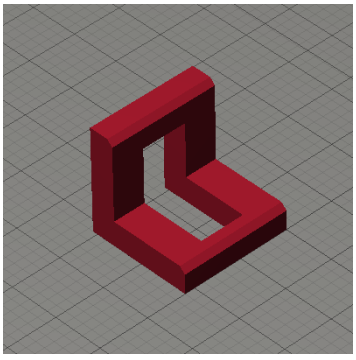

Figure 8.1 *3D-printed L-shaped plastic support to hold the sample and allow side light-sheet illumination.*

To hold the sample, two cleaned glass coverslips (*cf.* Section 8.1) were glued on a 3D-printed L-shaped plastic support (Figure 8.1), perpendicularly to each other. To avoid optical artefacts at the entry of the light-sheet in the solution, slight protrusion of the vertical coverslip over the horizontal one at their joint was preferred to the opposite. Once set, the sealing of the sample holder was checked by filling it with buffer. Finally, the buffer was removed, the sample was added on the bottom coverslip and topped up with some buffer to fill the height of the light-sheet at when entering in the solution. The geometry of this home-made holder enables at the same time entry of the light-sheet in the buffer (through the vertical coverslip) a few micrometers above the bottom horizontal coverslip and absorption of the light-sheet when leaving the solution on the other side.

The fluorescent signal emitted by the sample was separated from the illumination beams by a quad-band dichroic (Semrock, Di01-R405/488/561/635) and a $4f$ Fourier system (Newport, two collimated lenses PACO87AR.14, $f = 200$ mm) was collimated with the image plane of the microscope. At the intermediate Fourier image plane, a DH-PSF phase mask was placed and aligned (DoubleHelix LLC, matched for 580 nm wavelength, and of 7.25 mm diameter; *cf.* Section 3.2.2). Finally, the signal was filtered by the combination of a 640 nm long-pass (Semrock, BLP01-635R) and a band-pass filters (Semrock, FF02-675/67) and projected on the chip of an EMCCD camera (Photometrics, Evolve Delta) placed at the focal image plane of the second Fourier lens (*cf.* Figure 3.2).

Calibration $z$-stacks (thanks to a piezo-stage) and SMLM acquisitions were recorded on µManager [173] and analysed with the easy-dhpsf algorithm (Matlab routine available at https://code.google.com/p/easy-dhpsf/source/checkout [319]).

### 8.2.2 Automation of SMLM imaging

Polydimethylsiloxane (PDMS) micro-fluidic devices were obtained as described in ref. [100] and bonded to a glass coverslip after incubation of the coverslip in an oxygen plasma for 1'. The design and growing conditions of the strain of *S. pombe* imaged in Figure 3.17 are also described in ref. [100], as is the preparation of the sample. In short, live cells were loaded into the device at a rate of 10 µL/h and maintained at 28°C ($\pm$ 2°C) by pumping heated water through the control layer of the PDMS device. Once the cells had reached the trapping region the pump was switched off and the residual pressure in the tubing maintained a slow, smooth flow.

For the data presented in Figure 3.17 and Movie B.2, images were acquired under 561 nm HILO excitation (at power densities of $\sim$4 kW/cm$^2$) and 405 nm pulsed HILO

activation ($\sim$5 W/cm$^2$). A pulse sequence was chosen to ensure the irreversible bleaching of single mEos2 molecules in the cluster prior to the next imaging cycle. Acquisitions of 10 frames (with 33 ms exposure) were performed between two activation pulses. Although in SMLM experiments, acquisition cycles would be repeated until no further fluorescence activation is observed ($\sim$5,000 frames), in this proof-of-concept experiment, acquisition was stopped after the first PALM imaging cycle. Illumination beams and position of sample were controlled using mechanical shutters and a motorised $(xyz)$ stage (Prior, Optiscan III, V31XYZEF) and a bespoke script written as a μmanager [173] plug-in (Software B.3).

## 8.3 Materials and methods for Chapter 4

### 8.3.1 Bead calibration experiments

The main bead calibration experiments were performed as described in Section 8.1 and Table 8.2 by M. Palayret. The acquisition protocol consisted in recording a $z$-stack of 201 steps, each axially separated by 10 nm. For each step, 10 frames were imaged with a 33 ms exposure.

Additionally, in order to test the robustness of the vlsSMLM method, 'quick & dirty' calibration experiments were repeated by T.J. Etheridge and Dr U. Endesfelder on two other TIRF instruments (Figure 4.6, A, $2^{nd}$ and $3^{rd}$-$4^{th}$ rows, resp.). Consequently, additional precisions about these instruments and the imaging protocols follow:

**Figure 4.6, A, $2^{nd}$ row.** 560 nm emitting TetraSpeck beads were fixed on a coverslip and imaged every 20 nm using a $z$ piezo-stage on a replica of the instrument described in Section 8.1 (*cf.* Figure 3.1). The fluorescence signal was spectrally separated from the illumination light by a 561 nm long-pass (Semrock, BLP01-561R) and a band-pass filters (Semrock, FF01-593/40). The exposure of each frame was set to 100 ms.

**Figure 4.6, A, $3^{rd}$ and $4^{th}$ rows.** 660 nm emitting TetraSpeck beads (Invitrogen) or 655 nm emitting quantum dots were fixed on a coverslip. Chamber slides were mounted on a Nikon Ti Eclipse inverted microscope equipped with a 100x oil immersion objective lens (Apo TIRF 100X 1.49 Oil, Nikon). The 647 nm beam of a multi-line argon krypton mixed gas ion laser (Coherent, Innova70C) was projected into the microscope on a quad-band dichroic mirror (F73-888, AHF). Fluorescence light was collected by the objective, spectrally separated from the excitation light by a band-pass filter (F47-700, AHF) and projected on an EMCCD (Andor, iXon DU897). Videos of the traces

of the different fluorescent particles were recorded at different axial position in 20 nm steps using a $z$ piezo-stage.

### 8.3.2 Purification of mEos3.1

The purification of mEos3.1 from *Escherichia coli* was adapted from Fang *et al.* by Dr A.T. Watson [320]. The *E. coli* codon-optimised mEos3.1 gene was cloned into the N-terminal 6xHis-tagging expression vector pTWO-E (a kind gift from the Pearl lab) and the resulting plasmid was transformed into *E. coli* BL21(DE3) cells (Novagen). Three litres of culture were grown to an A600 nm absorbance of 0.6 and cooled to 20°C. IPTG[1] (Fisher Scientific) was then added to a final concentration of 0.5 mM to induce protein expression, and the cultures were further incubated in a shaker for 14–16 h. Collected cell pellets were placed at -20°C overnight (not snap-frozen).

Pellets were resuspended in buffer A (10 mM Tris[2], 100 mM NaCl, 50 mM $Na_2HPO_4$, at pH 8.0) with EDTA[3]-free protease inhibitor mix (Roche) (one tablet per 3 L of culture) and [4-(2-Aminoethyl) benzenesulfonyl fluoride hydrochloride] at 10 µg/mL, to a total volume of 35 mL in a 50 mL centrifuge tube. Cells were lysed by sonication using a Sonics Vibra-Cell for 5 s pulses spaced by 10 s resting time, to a total sonication time of 3'. Lysed cells were centrifuged at 18,500 rpm (32,000g) in an Allegra 64R ultracentrifuge (Beckman Coulter) with a F0650 rotor for 1 h. The supernatant was applied to a 5 mL Ni-NTA agarose resin (Qiagen) (pre-equilibrated using buffer A) and incubated for 1 h at 4°C with gentle agitation. The column was washed with eight column volumes of buffer B (50 mM $KH_2PO_4$, 300 mM NaCl, 20 mM imidazole, 5% glycerol, at pH 7.9), and the protein was eluted with two column volumes of buffer C (50 mM $KH_2PO_4$, 300 mM NaCl, 250 mM imidazole, 5% glycerol, at pH 7.9).

The protein was further purified on an SD200 size exclusion column pre-equilibrated with buffer D (10 mM Tris, 100 mM NaCl, 5% glycerol, at pH 8.0 and degassed) and protein aliquots were snap-frozen in liquid nitrogen and stored at -80°C. The protein purification was performed at 4°C. The exposure to light was minimised by covering tubes and columns in foil, using red light-emitting diodes and growing cultures in the dark.

[1] IPTG: Isopropyl b-D-thiogalactopyranoside.
[2] Tris: tris(hydroxymethyl)aminomethane.
[3] EDTA: ethylenediaminetetraacetic acid

### 8.3.3 Imaging separated fluorophores

For Figure 4.2, purified mEos3.1 fluorescent protein and SNAP-Cell TMR-Star dye (New England BioLabs, S9105S) were diluted $1/10^5$ in twice-200-nm-filtered PBS (Invitrogen, 003002) and fixed for 5' on poly-L-lysine-coated plasma-cleaned coverslips as described in Section 8.1. For each acquisition, 4,000 frames were imaged with a 50 ms exposure. The FF01-587/35 (Semrock) emission band-pass filter was used.

The $\delta$K280 mutant of the neuronal microtubule-associated Tau protein was labelled by Dr Magnus Kjaergaard. The two natural cysteine residues at positions 291 and C322 were mutated to alanine, and a cysteine was introduced at position 260. This enabled fluorescently-labelling of the protein without introducing bulky residues in the repeat domain that is responsible for aggregation. The construct was expressed in E. coli, and labelled with either AlexaFluor647 using maleimide chemistry. Mass spectroscopy, SDS-PAGE (sodium dodecyl sulfate polyacrylamide gel electrophoresis) and analytical size exclusion all showed the protein labelling to have been successful, and the material to be apparently free of pre-formed aggregates (data not shown). Labelled protein was kept in a 50 mM ammonium acetate buffer (pH 7) for 90' at 37°C without shaking. The sample was then prepared as described in Section 8.1, altough the coverslip was coated with negatively charged poly-L-glutamate, to immobilise the positively charged Tau proteins, for 30'. Dr S.F. Lee imaged the samples under constant 640 nm TIRF illumination at various power densities.

### 8.3.4 *S. pombe* experiments

For the experiment described in Figure 4.8, Dr A.T. Watson established the *S. pombe* cell line, H. Armes prepared the sample and imaged it. Below is summed a brief description of both steps.

The gene sequence of mEos2 was sub-cloned into the pFA6a-kanMX6 C-terminal gene tagging plasmid [321] to create pFA6a-mEos2-kanMX6. The mEos2-kanMX6 sequence was then integrated directly downstream of the *S. pombe* cdc22 gene open-reading frame, essentially as described in ref. [321], to create the AW709 strain (h-, cdc22-mEos2-kanMX6, leu1-32, ura4D18). A PCR against the inserted fragment showed that the diploid cells were heterozygote for cdc22-mEos2.

Cells were grown from frozen stocks on YEA (yeast extract 0.5% w/v, glucose 3.0% w/v, adenine, leucine and uracil all at 225 mg/L, and 2% Agar) plates then cultured in Edinburgh Minimal Media (EMM2) (filter sterilised) in a shaking incubator at 30°C. Fresh

plates were prepared for new experiments and the cultures set up 12-24 hours before the experiment. Samples for fixing were taken at an optical density (OD) at 595 nm of 0.1-0.2. Samples were spun down at 8,000 g. Cell pellets were fixed in 1% formaldehyde (made from 16% methanol-free stock, Fisher Scientific) in MilliQ water at room temperature for 15'. The fixed sample was spun down and washed three times in MilliQ water before being re-suspended in 10-20 µL of MilliQ water.

Finally, 5 µL of the resuspended sample were added between an agarose pad (100 µL of 1% agarose −Sigma, A0169− in MilliQ water pipetted between two cleaned coverslips) and a cleaned coverslip (*cf.* Section 8.1). For each acquisition, 5,000 frames were recorded with a 50 ms exposure.

### 8.3.5 Embryonic stem cells

For the experiment described in Figure 4.9, Dr S. Basu established the embryonic stem cell line, prepared the sample and imaged it. Below, a brief summary describes both steps.

mEos3.2 (mEso3.2 plasmid kindly given by Tao Xu [121]) was first cloned at the N-terminus of Cenp-A (cDNA plasmid from Thermo Scientific, clone MMM1013-64851) using a standard cloning vector. PCR of mEos3.2 and Cenp-A were carried out with primers described in Table 8.3. Then, mEos3.2-Cenp-A was cloned into the NcoI/XbaI site of a mammalian expression vector (pEF.myc.ER-E2-Crimson; Addgene plasmid 38770) [322]. Sequencing of the vector was carried out using the pEF forward primer and the BGH reverse primer (Table 8.3).

Table 8.3 *DNA primers used for Cenp-A-mEos3.2 cloning and sequencing.* Restriction sites are written in lower case.

| **Primer name** | **Sequence** |
|---|---|
| NcoI_mEos3_F | TGAACACGTGGCCAccatggGTAGTGCGATTAAGCCAGACATGAAGATCA |
| XhoI_mEos3_R | AGGctcgagTCGTCTGGCATTGTCAGGCAATC |
| XhoI_NheI_Cenp-A_F | AGGctcgaggctagcATGGGCCCGCGTCGCAAA |
| Xba1_Cenp-A_R | AGGtctagaTTAGGGGAGTCCGCCCTCG |
| pEF_F | TCTCAAGCCTCAGACAGTGGTTCAAAGT |
| BGH_R | TAGAAGGCACAGTCGAGG |

Mouse embryonic Mbd3$^{Flox/-}$ [323] stem cells were cultured in standard serum and LIF (leukaemia inhibitory factor) conditions as previously described [324]. These cells were transfected with the mEos3.2-Cenp-A plasmid using lipofectamine 2000 (Life Technologies), and after 24 h, a stable cell line was selected and maintained using 500 µg/mL ge-

neticin selection. These cells were then trypsinised and resuspended in PBS, fixed in 1% methanol-free formaldehyde (ThermoScientific, 28908) for 5' and imaged on clean coverslips (*cf.* Section 8.1). The acquisition consisted of 5,000 frames recorded with a 50 ms exposure.

## 8.4 Materials and methods for Chapter 6

The *S. pombe* strains used in Chapter 6 were designed and cloned by Dr A.T. Watson, and the corresponding samples prepared by H. Armes. The T-cell lines were designed and cloned by E. Huang. Sample preparation for the T cells and all imaging were performed by M. Palayret.

### 8.4.1 *S. pombe* cell lines

Dr A.T. Watson initially designed these constructs using the sequence for mEos3.1 with the codons optimised for expression in *S. pombe*. Three constructs were designed consisting of a single, double or triple repeat of mEos3.1 separated by a TGS linker and under the control of the uracil inducible promoter Urg1. The Urg1 promoter, when induced, gives a very high expression level, thus the sequence of the determinant of selective removal (DSR), which reduces expression level through transcript removal [325], an effect that increases with repeats, was added at the C-terminal end of the gene construct at varying levels (1-6 repeats).

The expression and size of the three constructs were confirmed on a Western blot. Expression levels of both induced and un-induced samples from the varying DSR levels were also examined. Even un-induced, the Urg1 promoter is 'leaky': expression can still be observed indicating that DSR induction is necessary to fully prevent expression, or, in the case of the experiments described in this work, to obtain very low expression. Consequently, constructs containing six DSRs were transformed into leu$^-$ AW459 yeast from the pAW8 plasmid using cassette exchange and further imaged [326].

### 8.4.2 T cell lines

The genes encoding human CD28, human CD86, human TCR$\beta$, murine CD3$\delta$, murine CD3$\zeta$ and mEos2 fluorescent protein were amplified by PCR. PCR fragments were ligated to form CD28-mEos2, CD86-mEos2, TCR$\beta$-mEos2 and CD3$\delta$-mEos2 constructs, which together with CD3$\zeta$ were each cloned into the pHR-SIN lentiviral vector. Human

hybridoma J.RT3-T3.5 cells [327], deficient for TCR$\beta$, were infected with VSV-G pseudotyped viruses produced from transiently transfected HEK-293T cells with either of the three CD28-mEos2, CD86-mEos2 or TCR$\beta$-mEos2 constructs as described in ref. [250]. Similarly, mouse hybridoma BW5147 cells, lacking expression of CD3$\delta$ and CD3$\zeta$, were co-infected with similar viruses carrying the CD3$\delta$-mEos2 and CD3$\zeta$ constructs. Correct surface expression of the appropriate membrane receptor was confirmed by flow cytometry (using the blue emission of the inactivated form of mEos2 and appropriate staining antibodies). Finally cells were sorted by flow cytometry.

The mouse anti-mouse-TCR$\beta$ antibodies (clone F23.1) were purified and fragmented as described in ref. [250]. Fabs were labelled with Atto655 according to the kit labelling protocol (Sigma Aldrich).

### 8.4.3 SMLM imaging

*Circa* $2 \cdot 10^6$ T cells were washed (2x) in warm JMEM and resuspended in 1 mL of fixing buffer (4% formaldehyde (Lancaster, 14190), 0.2% glutaraldehyde (Sigma Aldrich, G6257)). Cells were fixed for 30' at 37°C, then washed (3x) in 200 µL cold filtered PBS and finally resuspended in 50 µL. Agarose pads were formed by dropping 100 µL of 2% agarose (Sigma, A0169) in filtered PBS[4] between two plasma-cleaned coverslips. Agarose pads were left to set at 4°C for >10'. Then, one of the two coverslips sandwiching each agarose pad was carefully removed thanks to a scalpel and 20 µL of the fixed sample were dropped on the pad. A new plasma-cleaned was added on the top of the pad, over the cells, and the whole sample was mounted upside down on the objective (so that the cells were immobilised on the bottom coverslip in contact with the objective thanks to the weight of the agarose pad).

Yeasts were grown in Edinburgh Minimal Medium supplemented with 0.1 g/L adenine and leucine up to an OD of 0.3-0.4 at 595 nm absorption. 8 mL of cells were washed in MilliQ water and resuspended in 1 mL of 1% formaldehyde (Lancaster, 14190) in MilliQ water and fixed for 30' at room temperature. Fixed cells were washed (5x) in MilliQ water and finally resuspended in $\sim$20 µL MilliQ water. Before imaging, 5 µL of the sample were pipetted onto the agarose pad and plasma-cleaned coverslip was placed on the top, as above.

During the whole preparation, for either yeast and T-cell samples, samples were strictly protected from UV or blue light. Only red light-emitting diodes were used whenever the

[4]To prevent any contamination, metallic tools were forbidden from the agarose stock. Similarly, a critical step to avoid single-molecule noise in the sample is to thoroughly melt and mix the agarose. Un-melted agarose crystals might explain the high background noise observed in some original experiments.

sample was not completely covered with aluminium foil. A transmission red light was used to search for immobilised cells and adjust the focus before starting the acquisition. To insure repeatability, the acquisition was entirely led by a macro written in µManager controlling the shutters, the camera and the 405 nm laser power. For each cell, 1,000 frames with a 50 ms exposure were imaged under 561 nm illumination only to photo-bleached pre-activated mEos proteins and the background noise. Then, an acquisition of 4,000 frames (50 ms exposure) was taken under both constant TIRF 561 nm illumination and Fermi TIRF 405 nm activation (*cf.* Section 3.3.4). Finally, a transmission red light snapshot of the cell was recorded.

For the two-colour imaging experiment presented in Figure 6.16, the sample preparation varied slightly: after fixation, cells were washed (3x) in cold filtered PBS and incubated in 50 µL of 6.25 µg/mL Atto655-labelled $\alpha$murine-TCR$\beta$ Fabs for 30' on ice. Cells were then washed (3x) in cold filtered PBS and immobilised as previously between an agarose gel pad and a glass coverslip. Samples were sequentially imaged under 640 nm TIRF illumination (2,000 frames; 50 ms exposure), and under both 561 nm TIRF illumination and continuous Fermi TIRF activation (2,000 frames; 50 ms exposure).

## 8.5 Materials and methods for Chapter 7

Molecular cloning of the various constructs used in Chapter 7, transfection of the cell lines with the various constructs, IL-2 experiments, anti-murine-CD45 ($\alpha$mCD45) mAb purification and Fab generation and labelling were the work of M. Aßmann. M. Palayret cultured the cell lines and prepared the samples for SMLM imaging and performed the imaging experiments presented in this work and their analyses.

### 8.5.1 Molecular Cloning

Different genes of interest (*cf.* Table 8.4) were inserted into the pHR-CSGWdNotI/dEcoRI (pHR) vector via the MluI/BamHI/NotI cloning sites [328]: the structure of the constructs were designed as [pHR-MluI-(gene of interest)-BamHI-(10 amino-acid linker)-mEos3.2]. After cloning each gene in the pHR vector, competent Top10 bacteria were transformed with each construct for building working stocks of plasmids (Invitrogen, HiPure plasmid mini-prep kit). Each construct was sequenced to confirm the correct insertion and the absence of undesirable mutations.

Table 8.4 *Gene constructs used in Chapter 7.* Legend: rCD28: ecto-domain of rat CD28; mCD28: transmembrane and intracellular domain of murine CD28; trunc-mCD28: mCD28 which signalling motifs have been truncated; linker: a 30-amino-acid linker; hPD-1: the ecto-domain of human-PD-1.

| Name | Gene construct | Figures |
|---|---|---|
| CD28 | [rCD28]-[mCD28] | Figure 7.8 |
| CD28-mEos | [rCD28]-[mCD28]-[linker]-mEos3.2 | Figures 7.4, 7.6, 7.7 & 7.17 |
| Truncated CD28-mEos | [rCD28]-[trunc-mCD28]-[linker]-mEos3.2 | Figures 7.6, 7.8, 7.10, 7.11, 7.12, 7.13 & 7.15 |
| PD-1-mEos | [hPD-1]-[trunc-mCD28]-[linker]-mEos3.2 | Figure 7.9 |
| CD86-mEos | [murine-CD86]-[linker]-mEos3.2 | Figure 7.8 |
| Fc-CD28-mEos | [human-Fc domain]-[trunc-mCD28]-[linker]-mEos3.2 | Figure 7.14 |

### 8.5.2 Stable transfection with lentivirus

Stable transfection of cell lines was achieved by transducing them with lentivirus, and was confirmed by flow cytometry. HEK-293Tcells [329] were used for virus production. They were transfected (using the GeneJuice transfection reagant) with the p8.91 vector, containing the structural proteins and enzymes needed to generate infectious viral particles, the pMDG vector, containing viral coat proteins for packaging, and the pHR vector, containing the gene of interest (*cf.* previous section), flanked by long terminal repeats, under control of the CMV promoter as proposed in ref. [328].

Viruses were harvested 48 h post-transfection, filtered with a 0.45 µL syringe filter and added to $10^6$ BW5147 cells in 0.5 mL JMEM (*cf.* next section). The following day the medium was replaced with fresh JMEM. After 5-7 days, the expression of the gene of interest was tested by flow cytometry. Expression was matched for different constructs within one experiment, *e.g.* full-length and truncated CD28-mEos3.2, or truncated CD28 and truncated Fc-CD28.

### 8.5.3 Cell Culture

All cell lines imaged in Chapter 7 originate from the BW5147 cell line that is deficient in CD3$\delta$ and CD3$\zeta$ chains. Thus, if not transfected with adequate constructs, they do not express any TCR on their plasma membrane.

Mouse leukaemia BW5147 T-cell lines were cultured in JMEM medium (RPMI-1640 medium without phenol red (Gibco, 11835-063) supplemented with 10% foetal calf serum

(Thermo Scientific, HyClone SV30160.03), 10 mM HEPES[5] (Sigma, H0887), 1 mM sodium pyruvate (Gibco, 11360-039), 2 mM L-glutamine (Gibco, 2503-024) and antibiotics [50 units penicillin and 50 µg streptomycin per mL] (Gibco, 15140-122)). They were split ∼1/10 into fresh medium every 2-3 days to keep them at a density between $10^5$ and $10^6$ cells/mL. Cells were grown at 37°C in a 5% $CO_2$ atmosphere and regularly counted in a haemocytometer. Trypan blue (Sigma, T8154), a dye that penetrates dead but not viable cells, was mixed 1:1 (v/v) with cells before counting to assess the general health of the cultures.

### 8.5.4 Sample preparation

In both IL-2 experiments and sptPALM imaging, cells were decorated with mAbs when incubating in an activation solution for ∼15' and directly dropped (with no washing step) on a glass surface coated with 500 µg/mL donkey anti-mouse secondary antibodies (Jackson ImmunoResearch Laboratories Inc, 715-001-003) (*cf.* Figure 7.3). The activation buffer was made fresh for each experiment and consisted in 50 µg/mL (except where indicated, especially Figure 7.10) mAb in JMEM buffer. The list of mAbs used in this thesis is given in Table 8.5. In the experiment presented in Figure 7.11, the coating and decorating protocols were varied as indicated in the legend and the accompanying text.

Table 8.5 *Monoclonal antibodies used in Chapter 7.* †: putative SA, based on the location of the epitope of the mAb. All mAbs (except from the rat mAb KT3) are recognised by donkey anti-mouse secondary antibodies.

| Clone | Protein target | SA / CA behaviour | Source |
|---|---|---|---|
| JJ316 | rat-CD28 | SA | BD Pharmingen, 554992 |
| JJ319 | rat-CD28 | CA | eBioscience, 16-0280 |
| Clone 2 | human-PD1 | CA | Prof. S.J. Davis |
| Clone 10 | human-PD1 | CA | Prof. S.J. Davis |
| Clone 19 | human-PD1 | SA† | Prof. S.J. Davis |
| IC10 | human-Fc domain | SA† | kind gift from Dr John Young, Institute of Animal Health, Compton, UK |
| KT3 | mouse-CD3 | SA | Bio-Rad AbD Serotec Limited, MCA500XZ |

Once the cells were decorated and dropped on the coated glass surface, their IL-2 secretion was either monitored by M. Aßmann (with TCR-sufficient BW5147 cells, except when indicated in Figure 7.6) or the cells forming a contact with the glass coverslip were imaged with sptPALM by M. Palayret (with TCR-deficient BW5147 cells, except when indicated in Figure 7.7).

[5]HEPES: 4-(2-hydroxyethyl)-1-piperazineethanesulfonic acid

### 8.5.5 IL-2 in vitro stimulation assay

Thermo Scientific Nunc MicroWell 96-well optical-bottom plates with coverglass base were wet-coated in 1x coating buffer (from the Mouse IL-2 ELISA Ready-SET-Go! kit, eBioscience) overnight at 4°C with donkey anti-mouse polyclonal secondary antibody at 500 µg/mL. Wells were washed three times with 250 µL sterile PBS (a blocking step did not affect results, and was thus omitted).

$10^7$ cells/mL resuspended in the activation solution (50 µg/mL mAb in JMEM). Cells were incubated at room temperature for ∼15'. Each condition was preformed in duplicates or triplicates, *i.e.* 2-3 wells per condition. Each well received $5 \cdot 10^5$ cells in 100 µL activation solution. Wells were then incubated at 37°C in a 5% $CO_2$ atmosphere for 48 h.

The cell supernatant was analysed for released IL-2 with the Mouse IL-2 ELISA Ready-SET-Go! kit (eBioscience), following the kit protocol. An experimental calibration curve was used to convert the measured absorption at 450 nm into concentration of released IL-2 in the cell supernatant. IL-2 concentrations were corrected for day-to-day variations (up to 2-4 fold differences observed between replicates performed on different days) by normalisation to a positive control (activation of the cells by 10 µg/mL KT3 mAb directly coated with the secondary antibody on the glass; no decorating mAb). To be able to display IL-2 concentration in pg/mL units, the normalised values were multiplied with a typical (average) experimental IL-2 concentration of the positive control. All error bars display the standard deviation of the mean.

### 8.5.6 Generating Atto655-labelled Anti-murine-CD45 Fabs

The YW62.3.20 [330, 331] monoclonal antibody is a pan-reactive anti-mouse CD45 IgG2b. Hybridoma expressing the antibody in the supernatant was grown. Specific binding of the mAb present in the supernatant to CD45-expressing but not CD45-deficient BW5147 cells was confirmed by flow cytometry. After three weeks, the mAb was purified on protein-G coupled sepharose beads from the supernatant of 2 L of hybridoma culture. Ten fractions were collected, pooled, concentrated on Vivaspin 20 columns (Sartorius Stedium Biotech) and purified by fast protein liquid chromatography (FPLC) with a SuperDex 200 HR column in an ÄKTA FPLC system. Purity of the mAb was confirmed by SDS-PAGE. As no contaminant bands were detected, all antibody-containing fractions were pooled, concentrated to 2 mg/mL as above, and frozen in 1 mL aliquots.

To produce Fabs, 6 mg of the mAb was digested with immobilised papain slurry (ThermoScientific). The supernatant and two washes of the slurry were purified on protein-G

coupled sepharose beads, pooled and further purified by FPLC with a SuperDex 75 HR column. No Fc or whole antibody contamination was observed in the sepharose bead elution. Purity of the Fab fragments was confirmed by SDS-PAGE.

To label the anti-mouse CD45 Fab fragments, the protocol of the Atto655 protein labelling kit (Sigma Aldrich) was optimised. Freshly made 0.2 M sodium bicarbonate at pH 9.0 was added to 100 µL of Fab at 1 mg/mL in HEPES buffered saline (150 mM NaCl, 20 mM HEPES in MilliQ water) to achieve a final pH of 8.3. Then, 6.7 nmol of Atto655-NHS ester in PBS were added to the Fabs and the reaction was incubated for 2 h at room temperature, protected from light. The labelled Fabs were purified from unbound dye with gel filtration columns from the antibody conjugate purification kit (LifeTechnologies). Specific binding of the labelled anti-CD45 Fab was confirmed by flow cytometry.

### 8.5.7 Single-particle tracking PALM imaging

For sptPALM imaging, $1.25 \cdot 10^5$ cells were washed twice in 200 µL JMEM, resuspended in 100 µL of the considered warm activation solution, and incubated for 10' at 37°C (except where indicated in Figure 7.6; the incubation was then done at room temperature). Square hydrophobic imaging gaskets (Bio-rad, SLF0201) were applied on plasma-cleaned coverslips and 100 µL of secondary antibodies were dropped on each coverslip. After 15', one coverslip was washed (3x) with warmed filtered PBS (37°C) and 50 µL of the sample were dropped on the coated coverslip. The sample was then directly mounted on the objective and cells were imaged as soon as they formed a contact with the coverslip (followed until them with white transmission light).

A plexiglass chamber was designed to enclose the sample, the stage of the microscope and the objective, but not the cooled EMCCD camera, and stably heated to 37°C thanks to two vibration-free heaters (DigitalPixel, DP2000 Intelligent Heater). To avoid thermal drift and obtain a stable temperature, heaters were switched on 2 h before imaging. In Figure 7.6, where indicated, the heaters were kept off and the samples were imaged at 20°C.

For each cell, the acquisition consisted in 3,000 frames with a 50 ms exposure under constant TIRF 561 nm illumination ($\sim$130 W/cm$^2$) and 405 nm activation (<0.61 W/cm$^2$). Analysis is thoroughly described and discussed in Section 7.2.1.

For two-colour imaging (Figures 7.12, 7.13 and 7.15), the sample preparation slightly differed:

**Labelling with activation mAb.** Cells were incubated for 15' at 37°C in 200 µL of warm activation buffer made of 40 µg/mL unlabelled mAb and 20 µg/mL Atto655-labelled

mAb in JMEM. After incubation, cells were washed (3x) in 100 µL warm JMEM and finally resuspended in 100 µL warm JMEM (with no mAb), before being dropped on the coated coverslip.

**Labelling CD45.** Cells were incubated for 15' at 37°C in 200 µL of warm activation buffer made of 10 µg/mL activating mAb and 2.5 µg/mL $\alpha$-mCD45 Fab-Atto655. After incubation, cells were washed (3x) in 200 µL warm JMEM and finally resuspended in 100 µL warm incubation buffer as originally described (50 µg/mL of the considered mAb in JMEM), before being dropped on the coated coverslip.

However, the acquisition protocol was similar for both experiments: after alignment and calibration of the dualview (*cf.* Section 8.1), cells were imaged after stabilisation of the formation of a contact with the coated coverslip ($\sim$1-5' after apparition in the TIRF field), under constant TIRF 640 nm ($\sim$150 W/cm$^2$), 561 nm ($\sim$130 W/cm$^2$) illuminations and 405 nm (<0.5 W/cm$^2$) activation. Both colours were simultaneously imaged in the two channels of the dualview. Because of some achromatism, the focal planes for both channels were not identical. The focus was thus carefully adjusted in an intermediary position for which in-focus PSFs were observed in both channels. Acquisitions consisted in movies of 3,000 frames with a 50 ms exposure.

# References


[1] M. H. Horrocks, M. Palayret, D. Klenerman, and S. F. Lee, "The changing point-spread function: single-molecule-based super-resolution imaging.," *Histochemistry and cell biology*, vol. 141, pp. 577–85, June 2014.

[2] M. Palayret, "Single molecule super-resolution microscopy: All for one and one for all," *Physiology News*, no. 95, pp. 24–27, 2014.

[3] G. G. Stokes, "On the Change of Refrangibility of Light," *Philosophical Transactions of the Royal Society of London*, vol. 142, pp. 463–562, Jan. 1852.

[4] E. Abbe, "Beiträge zur Theorie des Mikroskops und der mikroskopischen Wahrnehmung," 1873.

[5] A. Santos and I. T. Young, "Model-based resolution: applying the theory in quantitative microscopy.," *Applied optics*, vol. 39, pp. 2948–58, June 2000.

[6] R. E. Thompson, D. R. Larson, and W. W. Webb, "Precise nanometer localization analysis for individual fluorescent probes.," *Biophysical journal*, vol. 82, pp. 2775–2783, 2002.

[7] A. Szymborska, A. de Marco, N. Daigle, V. C. Cordes, J. A. G. Briggs, and J. Ellenberg, "Nuclear pore scaffold structure analyzed by super-resolution microscopy and particle averaging.," *Science (New York, N.Y.)*, vol. 341, pp. 655–8, Aug. 2013.

[8] F. Chen, P. W. Tillberg, and E. S. Boyden, "Expansion microscopy," *Science*, pp. science.1260088–, Jan. 2015.

[9] M. G. L. Gustafsson, "Surpassing the lateral resolution limit by a factor of two using structured illumination microscopy," *Journal of Microscopy*, vol. 198, pp. 82–87, May 2000.

[10] S. W. Hell and J. Wichmann, "Breaking the diffraction resolution limit by stimulated emission: stimulated-emission-depletion fluorescence microscopy.," *Optics letters*, vol. 19, pp. 780–2, June 1994.

[11] S. W. Hell, "Far-field optical nanoscopy.," *Science (New York, N.Y.)*, vol. 316, pp. 1153–8, May 2007.

[12] M. G. L. Gustafsson, "Nonlinear structured-illumination microscopy: wide-field fluorescence imaging with theoretically unlimited resolution.," *Proceedings of the National Academy of Sciences of the United States of America*, vol. 102, pp. 13081–6, Sept. 2005.

[13] S. W. Hell, "Toward fluorescence nanoscopy.," *Nature biotechnology*, vol. 21, pp. 1347–55, Nov. 2003.

[14] M. Hofmann, C. Eggeling, S. Jakobs, and S. W. Hell, "Breaking the diffraction barrier in fluorescence microscopy at low light intensities by using reversibly photoswitchable proteins.," *Proceedings of the National Academy of Sciences of the United States of America*, vol. 102, pp. 17565–9, Dec. 2005.

[15] V. Westphal, M. A. Lauterbach, A. Di Nicola, and S. W. Hell, "Dynamic far-field fluorescence nanoscopy," *New Journal of Physics*, vol. 9, pp. 435–435, Dec. 2007.

[16] V. Westphal, S. O. Rizzoli, M. A. Lauterbach, D. Kamin, R. Jahn, and S. W. Hell, "Video-rate far-field optical nanoscopy dissects synaptic vesicle movement.," *Science (New York, N.Y.)*, vol. 320, pp. 246–9, Apr. 2008.

[17] A. Chmyrov, J. Keller, T. Grotjohann, M. Ratz, E. D'Este, S. Jakobs, C. Eggeling, and S. W. Hell, "Nanoscopy with more than 100,000 'doughnuts'.," *Nature methods*, vol. 10, pp. 737–40, Aug. 2013.

[18] E. Betzig, G. H. Patterson, R. Sougrat, O. W. Lindwasser, S. Olenych, J. S. Bonifacino, M. W. Davidson, J. Lippincott-Schwartz, and H. F. Hess, "Imaging intracellular fluorescent proteins at nanometer resolution.," *Science (New York, N.Y.)*, vol. 313, pp. 1642–1645, Sept. 2006.

[19] M. J. Rust, M. Bates, and X. Zhuang, "Sub-diffraction-limit imaging by stochastic optical reconstruction microscopy (STORM).," *Nature methods*, vol. 3, pp. 793–795, 2006.

[20] S. T. Hess, T. P. K. Girirajan, and M. D. Mason, "Ultra-high resolution imaging by fluorescence photoactivation localization microscopy.," *Biophysical journal*, vol. 91, pp. 4258–72, Dec. 2006.

[21] T. Müller, C. Schumann, and A. Kraegeloh, "STED microscopy and its applications: new insights into cellular processes on the nanoscale.," *Chemphyschem : a European journal of chemical physics and physical chemistry*, vol. 13, pp. 1986–2000, June 2012.

[22] J. R. Allen, S. T. Ross, and M. W. Davidson, "Structured illumination microscopy for superresolution.," *Chemphyschem : a European journal of chemical physics and physical chemistry*, vol. 15, pp. 566–76, Mar. 2014.

[23] E. Betzig, "Proposed method for molecular optical imaging.," *Optics letters*, vol. 20, pp. 237–9, Feb. 1995.

[24] S. W. Hell and M. Kroug, "Ground-state-depletion fluorscence microscopy: A concept for breaking the diffraction resolution limit," *Applied Physics B Lasers and Optics*, vol. 60, pp. 495–497, May 1995.

[25] J. Fölling, M. Bossi, H. Bock, R. Medda, C. A. Wurm, B. Hein, S. Jakobs, C. Eggeling, and S. W. Hell, "Fluorescence nanoscopy by ground-state depletion and single-molecule return.," *Nature methods*, vol. 5, pp. 943–5, Nov. 2008.

[26] M. Heilemann, S. van de Linde, M. Schüttpelz, R. Kasper, B. Seefeldt, A. Mukherjee, P. Tinnefeld, and M. Sauer, "Subdiffraction-resolution fluorescence imaging with conventional fluorescent probes.," *Angewandte Chemie (International ed. in English)*, vol. 47, pp. 6172–6, Jan. 2008.

[27] J. L. Ptacin, S. F. Lee, E. C. Garner, E. Toro, M. Eckart, L. R. Comolli, W. E. Moerner, and L. Shapiro, "A spindle-like apparatus guides bacterial chromosome segregation.," *Nature cell biology*, vol. 12, pp. 791–8, Aug. 2010.

[28] S. F. Lee, M. A. Thompson, M. A. Schwartz, L. Shapiro, and W. E. Moerner, "Super-resolution imaging of the nucleoid-associated protein HU in Caulobacter crescentus.," *Biophysical journal*, vol. 100, pp. L31–3, Apr. 2011.

[29] K. Lidke, B. Rieger, T. Jovin, and R. Heintzmann, "Superresolution by localization of quantum dots using blinking statistics.," *Optics express*, vol. 13, pp. 7052–62, Sept. 2005.

[30] P. Hoyer, T. Staudt, J. Engelhardt, and S. W. Hell, "Quantum dot blueing and blinking enables fluorescence nanoscopy.," *Nano letters*, vol. 11, pp. 245–50, Jan. 2011.

[31] C. Duan, V. Adam, M. Byrdin, J. Ridard, S. Kieffer-Jaquinod, C. Morlot, D. Arcizet, I. Demachy, and D. Bourgeois, "Structural evidence for a two-regime photobleaching mechanism in a reversibly switchable fluorescent protein.," *Journal of the American Chemical Society*, vol. 135, pp. 15841–50, Oct. 2013.

[32] S. W. Englander, D. B. Calhoun, and J. J. Englander, "Biochemistry without oxygen.," *Analytical biochemistry*, vol. 161, pp. 300–6, Mar. 1987.

[33] C. E. Aitken, R. A. Marshall, and J. D. Puglisi, "An oxygen scavenging system for improvement of dye stability in single-molecule fluorescence experiments.," *Biophysical journal*, vol. 94, pp. 1826–35, Mar. 2008.

[34] M. Swoboda, J. Henig, H.-M. Cheng, D. Brugger, D. Haltrich, N. Plumeré, and M. Schlierf, "Enzymatic oxygen scavenging for photostability without pH drop in single-molecule experiments.," *ACS nano*, vol. 6, pp. 6364–9, July 2012.

[35] I. Rasnik, S. A. McKinney, and T. Ha, "Nonblinking and long-lasting single-molecule fluorescence imaging.," *Nature methods*, vol. 3, pp. 891–3, Nov. 2006.

[36] Y. Harada, K. Sakurada, T. Aoki, D. D. Thomas, and T. Yanagida, "Mechanochemical coupling in actomyosin energy transduction studied by in vitro movement assay.," *Journal of molecular biology*, vol. 216, pp. 49–68, Nov. 1990.

[37] J. Vogelsang, T. Cordes, C. Forthmann, C. Steinhauer, and P. Tinnefeld, "Controlling the fluorescence of ordinary oxazine dyes for single-molecule switching and super-resolution microscopy.," *Proceedings of the National Academy of Sciences of the United States of America*, vol. 106, pp. 8107–12, May 2009.

[38] M. Heilemann, E. Margeat, R. Kasper, M. Sauer, and P. Tinnefeld, "Carbocyanine dyes as efficient reversible single-molecule optical switch.," *Journal of the American Chemical Society*, vol. 127, pp. 3801–6, Mar. 2005.

[39] G. T. Dempsey, M. Bates, W. E. Kowtoniuk, D. R. Liu, R. Y. Tsien, and X. Zhuang, "Photoswitching mechanism of cyanine dyes.," *Journal of the American Chemical Society*, vol. 131, pp. 18192–3, Dec. 2009.

[40] N. Olivier, D. Keller, P. Gönczy, and S. Manley, "Resolution doubling in 3D-STORM imaging through improved buffers.," *PloS one*, vol. 8, p. e69004, Jan. 2013.

[41] K. Kundu, S. F. Knight, N. Willett, S. Lee, W. R. Taylor, and N. Murthy, "Hydrocyanines: a class of fluorescent sensors that can image reactive oxygen species in cell culture, tissue, and in vivo.," *Angewandte Chemie (International ed. in English)*, vol. 48, pp. 299–303, Jan. 2009.

[42] L. Carlini, A. Benke, L. Reymond, G. Lukinavičius, and S. Manley, "Reduced dyes enhance single-molecule localization density for live superresolution imaging.," *Chemphyschem : a European journal of chemical physics and physical chemistry*, vol. 15, pp. 750–5, Mar. 2014.

[43] S. van de Linde, A. Löschberger, T. Klein, M. Heidbreder, S. Wolter, M. Heilemann, and M. Sauer, "Direct stochastic optical reconstruction microscopy with standard fluorescent probes.," *Nature protocols*, vol. 6, pp. 991–1009, July 2011.

[44] E. Lubeck and L. Cai, "Single-cell systems biology by super-resolution imaging and combinatorial labeling.," *Nature methods*, vol. 9, pp. 743–8, July 2012.

[45] G. T. Dempsey, J. C. Vaughan, K. H. Chen, M. Bates, and X. Zhuang, "Evaluation of fluorophores for optimal performance in localization-based super-resolution imaging.," *Nature methods*, vol. 8, pp. 1027–36, Dec. 2011.

[46] J. Lippincott-Schwartz and G. H. Patterson, "Photoactivatable fluorescent proteins for diffraction-limited and super-resolution imaging.," *Trends in cell biology*, vol. 19, pp. 555–65, Nov. 2009.

[47] S.-n. Uno, M. Kamiya, T. Yoshihara, K. Sugawara, K. Okabe, M. C. Tarhan, H. Fujita, T. Funatsu, Y. Okada, S. Tobita, and Y. Urano, "A spontaneously blinking fluorophore based on intramolecular spirocyclization for live-cell super-resolution imaging," *Nature Chemistry*, vol. 6, pp. 681–689, July 2014.

[48] A. Sharonov and R. M. Hochstrasser, "Wide-field subdiffraction imaging by accumulated binding of diffusing probes.," *Proceedings of the National Academy of Sciences of the United States of America*, vol. 103, pp. 18911–18916, 2006.

[49] G. Giannone, E. Hosy, F. Levet, A. Constals, K. Schulze, A. I. Sobolevsky, M. P. Rosconi, E. Gouaux, R. Tampé, D. Choquet, and L. Cognet, "Dynamic superresolution imaging of endogenous proteins on living cells at ultra-high density.," *Biophysical journal*, vol. 99, pp. 1303–10, Aug. 2010.

[50] I. Schoen, J. Ries, E. Klotzsch, H. Ewers, and V. Vogel, "Binding-activated localization microscopy of DNA structures.," *Nano letters*, vol. 11, pp. 4008–11, Sept. 2011.

[51] J. B. Delehanty, H. Mattoussi, and I. L. Medintz, "Delivering quantum dots into cells: strategies, progress and remaining issues.," *Analytical and bioanalytical chemistry*, vol. 393, pp. 1091–105, Feb. 2009.

[52] H. Deschout, F. Cella Zanacchi, M. Mlodzianoski, A. Diaspro, J. Bewersdorf, S. T. Hess, and K. Braeckmans, "Precisely and accurately localizing single emitters in fluorescence microscopy.," *Nature methods*, vol. 11, pp. 253–66, Mar. 2014.

[53] P. Dedecker, F. C. De Schryver, and J. Hofkens, "Fluorescent proteins: shine on, you crazy diamond.," *Journal of the American Chemical Society*, vol. 135, pp. 2387–402, Feb. 2013.

[54] R. Y. Tsien, "The green fluorescent protein.," *Annual review of biochemistry*, vol. 67, pp. 509–44, Jan. 1998.

[55] U. Rothbauer, K. Zolghadr, S. Tillib, D. Nowak, L. Schermelleh, A. Gahl, N. Backmann, K. Conrath, S. Muyldermans, M. C. Cardoso, and H. Leonhardt, "Targeting and tracing antigens in live cells with fluorescent nanobodies.," *Nature methods*, vol. 3, pp. 887–9, Nov. 2006.

[56] M. H. Kubala, O. Kovtun, K. Alexandrov, and B. M. Collins, "Structural and thermodynamic analysis of the GFP:GFP-nanobody complex.," *Protein science : a publication of the Protein Society*, vol. 19, pp. 2389–401, Dec. 2010.

[57] P. J. M. Zessin, K. Finan, and M. Heilemann, "Super-resolution fluorescence imaging of chromosomal DNA.," *Journal of structural biology*, vol. 177, pp. 344–8, Feb. 2012.

[58] I. Nikić, T. Plass, O. Schraidt, J. Szymański, J. A. G. Briggs, C. Schultz, and E. A. Lemke, "Minimal tags for rapid dual-color live-cell labeling and super-resolution microscopy.," *Angewandte Chemie (International ed. in English)*, vol. 53, pp. 2245–9, Feb. 2014.

[59] G. Los and L. Encell, "HaloTag: a novel protein labeling technology for cell imaging and protein analysis," *ACS chemical . . .* , vol. 3, no. 6, pp. 373–382, 2008.

[60] S. A. Jones, S.-H. Shim, J. He, and X. Zhuang, "Fast, three-dimensional super-resolution imaging of live cells.," *Nature methods*, vol. 8, pp. 499–508, June 2011.

[61] N. C. Shaner, M. Z. Lin, M. R. McKeown, P. A. Steinbach, K. L. Hazelwood, M. W. Davidson, and R. Y. Tsien, "Improving the photostability of bright monomeric orange and red fluorescent proteins.," *Nature methods*, vol. 5, pp. 545–51, June 2008.

[62] R. M. Dickson, A. B. Cubitt, R. Y. Tsien, and W. E. Moerner, "On/off blinking and switching behaviour of single molecules of green fluorescent protein.," *Nature*, vol. 388, pp. 355–8, July 1997.

[63] G. Jung, C. Bräuchle, and A. Zumbusch, "Two-color fluorescence correlation spectroscopy of one chromophore: Application to the E222Q mutant of the green fluorescent protein," *The Journal of Chemical Physics*, vol. 114, p. 3149, Feb. 2001.

[64] G. Jung, J. Wiehler, B. Steipe, C. Bräuchle, and A. Zumbusch, "Single-molecule microscopy of the green fluorescent protein using simultaneous two-color excitation.," *Chemphyschem : a European journal of chemical physics and physical chemistry*, vol. 2, pp. 392–6, June 2001.

[65] R. Ando, H. Mizuno, and A. Miyawaki, "Regulated fast nucleocytoplasmic shuttling observed by reversible protein highlighting.," *Science (New York, N.Y.)*, vol. 306, pp. 1370–3, Nov. 2004.

[66] F. V. Subach, L. Zhang, T. W. J. Gadella, N. G. Gurskaya, K. A. Lukyanov, and V. V. Verkhusha, "Red fluorescent protein with reversibly photoswitchable absorbance for photochromic FRET.," *Chemistry & biology*, vol. 17, pp. 745–55, July 2010.

[67] H. Chang, M. Zhang, W. Ji, J. Chen, Y. Zhang, B. Liu, J. Lu, J. Zhang, P. Xu, and T. Xu, "A unique series of reversibly switchable fluorescent proteins with beneficial properties for various applications.," *Proceedings of the National Academy of Sciences of the United States of America*, vol. 109, pp. 4455–60, Mar. 2012.

[68] J. C. Vaughan, S. Jia, and X. Zhuang, "Ultrabright photoactivatable fluorophores created by reductive caging.," *Nature methods*, vol. 9, pp. 1181–4, Dec. 2012.

[69] S. J. Lord, N. R. Conley, H.-l. D. Lee, R. Samuel, N. Liu, R. J. Twieg, and W. E. Moerner, "A photoactivatable push-pull fluorophore for single-molecule imaging in live cells.," *Journal of the American Chemical Society*, vol. 130, pp. 9204–5, July 2008.

[70] G. H. Patterson and J. Lippincott-Schwartz, "A photoactivatable GFP for selective photolabeling of proteins and cells.," *Science (New York, N.Y.)*, vol. 297, pp. 1873–7, Sept. 2002.

[71] D. M. Chudakov, V. V. Verkhusha, D. B. Staroverov, E. A. Souslova, S. Lukyanov, and K. A. Lukyanov, "Photoswitchable cyan fluorescent protein for protein tracking.," *Nature biotechnology*, vol. 22, pp. 1435–9, Nov. 2004.

[72] F. V. Subach, G. H. Patterson, S. Manley, J. M. Gillette, J. Lippincott-Schwartz, and V. V. Verkhusha, "Photoactivatable mCherry for high-resolution two-color fluorescence microscopy.," *Nature methods*, vol. 6, pp. 153–9, Feb. 2009.

[73] R. Ando, H. Hama, M. Yamamoto-Hino, H. Mizuno, and A. Miyawaki, "An optical marker based on the UV-induced green-to-red photoconversion of a fluorescent protein.," *Proceedings of the National Academy of Sciences of the United States of America*, vol. 99, pp. 12651–6, Oct. 2002.

[74] J. Wiedenmann, S. Ivanchenko, F. Oswald, F. Schmitt, C. Röcker, A. Salih, K.-D. Spindler, and G. U. Nienhaus, "EosFP, a fluorescent marker protein with UV-inducible green-to-red fluorescence conversion.," *Proceedings of the National Academy of Sciences of the United States of America*, vol. 101, pp. 15905–10, Nov. 2004.

[75] N. G. Gurskaya, V. V. Verkhusha, A. S. Shcheglov, D. B. Staroverov, T. V. Chepurnykh, A. F. Fradkov, S. Lukyanov, and K. A. Lukyanov, "Engineering of a monomeric green-to-red photoactivatable fluorescent protein induced by blue light.," *Nature biotechnology*, vol. 24, pp. 461–5, Apr. 2006.

[76] H. Mizuno, T. K. Mal, K. I. Tong, R. Ando, T. Furuta, M. Ikura, and A. Miyawaki, "Photo-induced peptide cleavage in the green-to-red conversion of a fluorescent protein.," *Molecular cell*, vol. 12, pp. 1051–8, Oct. 2003.

[77] K. Nienhaus, G. U. Nienhaus, J. Wiedenmann, and H. Nar, "Structural basis for photo-induced protein cleavage and green-to-red conversion of fluorescent protein EosFP.," *Proceedings of the National Academy of Sciences of the United States of America*, vol. 102, pp. 9156–9, June 2005.

[78] N. Chenouard, I. Smal, F. de Chaumont, M. Maška, I. F. Sbalzarini, Y. Gong, J. Cardinale, C. Carthel, S. Coraluppi, M. Winter, A. R. Cohen, W. J. Godinez, K. Rohr, Y. Kalaidzidis, L. Liang, J. Duncan, H. Shen, Y. Xu, K. E. G. Magnusson, J. Jaldén, H. M. Blau, P. Paul-Gilloteaux, P. Roudot, C. Kervrann, F. Waharte, J.-Y. Tinevez, S. L. Shorte, J. Willemse, K. Celler, G. P. van Wezel, H.-W. Dan, Y.-S. Tsai, C. Ortiz de Solórzano, J.-C. Olivo-Marin, and E. Meijering, "Objective comparison of particle tracking methods.," *Nature methods*, vol. 11, pp. 281–9, Mar. 2014.

[79] S. Manley, J. M. Gillette, G. H. Patterson, H. Shroff, H. F. Hess, E. Betzig, and J. Lippincott-Schwartz, "High-density mapping of single-molecule trajectories with photoactivated localization microscopy.," *Nature methods*, vol. 5, pp. 155–7, Feb. 2008.

[80] F. Persson, M. Lindén, C. Unoson, and J. Elf, "Extracting intracellular diffusive states and transition rates from single-molecule tracking data.," *Nature methods*, vol. 10, pp. 265–9, Mar. 2013.

[81] A. Löschberger, C. Franke, G. Krohne, S. van de Linde, and M. Sauer, "Correlative super-resolution fluorescence and electron microscopy of the nuclear pore complex with molecular resolution.," *Journal of cell science*, vol. 127, pp. 4351–5, Oct. 2014.

[82] P. Sengupta, T. Jovanovic-Talisman, D. Skoko, M. Renz, S. L. Veatch, and J. Lippincott-Schwartz, "Probing protein heterogeneity in the plasma membrane using PALM and pair correlation analysis," 2011.

[83] S. L. Veatch, B. B. Machta, S. A. Shelby, E. N. Chiang, D. A. Holowka, and B. A. Baird, "Correlation functions quantify super-resolution images and estimate apparent clustering due to over-counting.," *PloS one*, vol. 7, p. e31457, Jan. 2012.

[84] B. Rieger and S. Stallinga, "The lateral and axial localization uncertainty in super-resolution light microscopy.," *Chemphyschem : a European journal of chemical physics and physical chemistry*, vol. 15, pp. 664–70, Mar. 2014.

[85] M. Badieirostami, M. D. Lew, M. A. Thompson, and W. E. Moerner, "Three-dimensional localization precision of the double-helix point spread function versus astigmatism and biplane.," *Applied physics letters*, vol. 97, p. 161103, Oct. 2010.

[86] M. F. Juette, T. J. Gould, M. D. Lessard, M. J. Mlodzianoski, B. S. Nagpure, B. T. Bennett, S. T. Hess, and J. Bewersdorf, "Three-dimensional sub-100 nm resolution fluorescence microscopy of thick samples.," *Nature methods*, vol. 5, pp. 527–9, June 2008.

[87] B. Huang, W. Wang, M. Bates, and X. Zhuang, "Three-dimensional super-resolution imaging by stochastic optical reconstruction microscopy.," *Science (New York, N.Y.)*, vol. 319, pp. 810–3, Feb. 2008.

[88] S. R. P. Pavani, M. A. Thompson, J. S. Biteen, S. J. Lord, N. Liu, R. J. Twieg, R. Piestun, and W. E. Moerner, "Three-dimensional, single-molecule fluorescence imaging beyond the diffraction limit by using a double-helix point spread function.," *Proceedings of the National Academy of Sciences of the United States of America*, vol. 106, pp. 2995–9, Mar. 2009.

[89] G. Shtengel, J. A. Galbraith, C. G. Galbraith, J. Lippincott-Schwartz, J. M. Gillette, S. Manley, R. Sougrat, C. M. Waterman, P. Kanchanawong, M. W. Davidson, R. D. Fetter, and H. F. Hess, "Interferometric fluorescent super-resolution microscopy resolves 3D cellular ultrastructure.," *Proceedings of the National Academy of Sciences of the United States of America*, vol. 106, pp. 3125–30, Mar. 2009.

[90] F. Huang, T. M. P. Hartwich, F. E. Rivera-Molina, Y. Lin, W. C. Duim, J. J. Long, P. D. Uchil, J. R. Myers, M. A. Baird, W. Mothes, M. W. Davidson, D. Toomre, and J. Bewersdorf, "Video-rate nanoscopy using sCMOS camera-specific single-molecule localization algorithms.," *Nature methods*, vol. 10, pp. 653–8, 2013.

[91] J. Siegel, D. S. Elson, S. E. D. Webb, D. Parsons-Karavassilis, S. Lévêque-Fort, M. J. Cole, M. J. Lever, P. M. W. French, M. A. A. Neil, R. Juskaitis, L. O. Sucharov, and T. Wilson, "Whole-field five-dimensional fluorescence microscopy combining lifetime and spectral resolution with optical sectioning," *Optics Letters*, vol. 26, p. 1338, Sept. 2001.

[92] P. Blandin, S. Lévêque-Fort, S. Lécart, J. C. Cossec, M.-C. Potier, Z. Lenkei, F. Druon, and P. Georges, "Time-gated total internal reflection fluorescence microscopy with a supercontinuum excitation source," *Applied Optics*, vol. 48, p. 553, Jan. 2009.

[93] X. Michalet, R. A. Colyer, G. Scalia, S. Weiss, O. H. W. Siegmund, A. S. Tremsin, J. V. Vallerga, F. Villa, F. Guerrieri, I. Rech, A. Gulinatti, S. Tisa, F. Zappa, M. Ghioni, and S. Cova, "New photon-counting detectors for single-molecule fluorescence spectroscopy and imaging.," *Proceedings of SPIE*, vol. 8033, p. 803316, May 2011.

[94] H. Shroff, C. G. Galbraith, J. A. Galbraith, H. White, J. Gillette, S. Olenych, M. W. Davidson, and E. Betzig, "Dual-color superresolution imaging of genetically expressed probes within individual adhesion complexes.," *Proceedings of the National Academy of Sciences of the United States of America*, vol. 104, pp. 20308–13, Dec. 2007.

[95] F. V. Subach, G. H. Patterson, M. Renz, J. Lippincott-Schwartz, and V. V. Verkhusha, "Bright monomeric photoactivatable red fluorescent protein for two-color super-resolution sptPALM of live cells.," *Journal of the American Chemical Society*, vol. 132, pp. 6481–91, May 2010.

[96] R. Jungmann, M. S. Avendaño, J. B. Woehrstein, M. Dai, W. M. Shih, and P. Yin, "Multiplexed 3D cellular super-resolution imaging with DNA-PAINT and Exchange-PAINT.," *Nature methods*, vol. 11, pp. 313–8, Mar. 2014.

[97] I. Testa, A. Schönle, C. v. Middendorff, C. Geisler, R. Medda, C. A. Wurm, A. C. Stiel, S. Jakobs, M. Bossi, C. Eggeling, S. W. Hell, and A. Egner, "Nanoscale separation of molecular species based on their rotational mobility," *Optics Express*, vol. 16, p. 21093, Dec. 2008.

[98] M. P. Backlund, M. D. Lew, A. S. Backer, S. J. Sahl, and W. E. Moerner, "The role of molecular dipole orientation in single-molecule fluorescence microscopy and implications for super-resolution imaging.," *Chemphyschem : a European journal of chemical physics and physical chemistry*, vol. 15, pp. 587–99, Mar. 2014.

[99] A. S. Backer, M. P. Backlund, A. R. von Diezmann, S. J. Sahl, and W. E. Moerner, "A bisected pupil for studying single-molecule orientational dynamics and its application to three-dimensional super-resolution microscopy.," *Applied physics letters*, vol. 104, p. 193701, May 2014.

[100] L. Bell, A. Seshia, D. Lando, E. Laue, M. Palayret, S. F. Lee, and D. Klenerman, "A microfluidic device for the hydrodynamic immobilisation of living fission yeast cells for super-resolution imaging," *Sensors and Actuators B: Chemical*, vol. 192, pp. 36–41, Mar. 2014.

[101] T. J. Etheridge, R. L. Boulineau, A. Herbert, A. T. Watson, Y. Daigaku, J. Tucker, S. George, P. Jönsson, M. Palayret, D. Lando, E. Laue, M. A. Osborne, D. Klenerman, S. F. Lee, and A. M. Carr, "Quantification of DNA-associated proteins inside eukaryotic cells using single-molecule localization microscopy.," *Nucleic acids research*, pp. gku726–, Aug. 2014.

[102] A. Edelstein, N. Amodaj, K. Hoover, R. Vale, and N. Stuurman, "Computer control of microscopes using μManager.," *Current protocols in molecular biology / edited by Frederick M. Ausubel ... [et al.]*, vol. Chapter 14, p. Unit14.20, Oct. 2010.

[103] Photometrics, "Evolve 512 datasheet," *http://www.photometrics.com/products/datasheets/evolve_512.pdf*, 2015.

[104] M. Hirsch, R. J. Wareham, M. L. Martin-Fernandez, M. P. Hobson, and D. J. Rolfe, "A stochastic model for electron multiplication charge-coupled devices–from theory to practice.," *PloS one*, vol. 8, p. e53671, Jan. 2013.

[105] M. Tokunaga, N. Imamoto, and K. Sakata-Sogawa, "Highly inclined thin illumination enables clear single-molecule imaging in cells.," *Nature methods*, vol. 5, pp. 159–61, Feb. 2008.

[106] J. Huisken, J. Swoger, F. Del Bene, J. Wittbrodt, and E. H. K. Stelzer, "Optical sectioning deep inside live embryos by selective plane illumination microscopy.," *Science (New York, N.Y.)*, vol. 305, pp. 1007–9, Aug. 2004.

[107] P. Annibale, M. Scarselli, M. Greco, and A. Radenovic, "Identification of the factors affecting co-localization precision for quantitative multicolor localization microscopy," *Optical Nanoscopy*, vol. 1, p. 9, Nov. 2012.

[108] C. Geisler, T. Hotz, A. Schönle, S. W. Hell, A. Munk, and A. Egner, "Drift estimation for single marker switching based imaging schemes.," *Optics express*, vol. 20, pp. 7274–89, Mar. 2012.

[109] Mad City Labs Incorporation, "Nano-Cyte, 3D stability for imaging," *http://www.madcitylabs.com/pdfs/NanoCyteBrochure.pdf*, 2015.

[110] D. Baddeley, D. Crossman, S. Rossberger, J. E. Cheyne, J. M. Montgomery, I. D. Jayasinghe, C. Cremer, M. B. Cannell, and C. Soeller, "4D super-resolution microscopy with conventional fluorophores and single wavelength excitation in optically thick cells and tissues.," *PloS one*, vol. 6, p. e20645, Jan. 2011.

[111] M. Bates, G. T. Dempsey, K. H. Chen, and X. Zhuang, "Multicolor super-resolution fluorescence imaging via multi-parameter fluorophore detection.," *Chemphyschem : a European journal of chemical physics and physical chemistry*, vol. 13, pp. 99–107, Jan. 2012.

[112] L. S. Churchman, Z. Okten, R. S. Rock, J. F. Dawson, and J. A. Spudich, "Single molecule high-resolution colocalization of Cy3 and Cy5 attached to macromolecules measures intramolecular distances through time.," *Proceedings of the National Academy of Sciences of the United States of America*, vol. 102, pp. 1419–23, Feb. 2005.

[113] M. Lehmann, S. Rocha, B. Mangeat, F. Blanchet, H. Uji-I, J. Hofkens, and V. Piguet, "Quantitative multicolor super-resolution microscopy reveals tetherin HIV-1 interaction.," *PLoS pathogens*, vol. 7, p. e1002456, Dec. 2011.

[114] A. D. Maude, "Interpolation–mainly for graph plotters," *The Computer Journal*, vol. 16, pp. 64–65, Jan. 1973.

[115] A. Goshtasby, "Image registration by local approximation methods," *Image and Vision Computing*, vol. 6, pp. 255–261, Nov. 1988.

[116] S. Malkusch, U. Endesfelder, J. Mondry, M. Gelléri, P. J. Verveer, and M. Heilemann, "Coordinate-based colocalization analysis of single-molecule localization microscopy data.," *Histochemistry and cell biology*, vol. 137, pp. 1–10, Jan. 2012.

[117] I. Koyama-Honda, K. Ritchie, T. Fujiwara, R. Iino, H. Murakoshi, R. S. Kasai, and A. Kusumi, "Fluorescence imaging for monitoring the colocalization of two single molecules in living cells.," *Biophysical journal*, vol. 88, pp. 2126–36, Mar. 2005.

[118] J. Xu, J. Chang, Q. Yan, T. Dertinger, M. Bruchez, and S. Weiss, "Labeling Cytosolic Targets in Live Cells with Blinking Probes.," *The journal of physical chemistry letters*, vol. 4, pp. 2138–2146, July 2013.

[119] V. Adam, "Phototransformable fluorescent proteins: which one for which application?," *Histochemistry and cell biology*, Feb. 2014.

[120] J. Ries, C. Kaplan, E. Platonova, H. Eghlidi, and H. Ewers, "A simple, versatile method for GFP-based super-resolution microscopy via nanobodies.," *Nature methods*, vol. 9, pp. 582–4, June 2012.

[121] M. Zhang, H. Chang, Y. Zhang, J. Yu, L. Wu, W. Ji, J. Chen, B. Liu, J. Lu, Y. Liu, J. Zhang, P. Xu, and T. Xu, "Rational design of true monomeric and bright photoactivatable fluorescent proteins.," *Nature methods*, vol. 9, pp. 727–9, July 2012.

[122] F. V. Subach, V. N. Malashkevich, W. D. Zencheck, H. Xiao, G. S. Filonov, S. C. Almo, and V. V. Verkhusha, "Photoactivation mechanism of PAmCherry based on crystal structures of the protein in the dark and fluorescent states.," *Proceedings of the National Academy of Sciences of the United States of America*, vol. 106, pp. 21097–102, Dec. 2009.

[123] S. A. McKinney, C. S. Murphy, K. L. Hazelwood, M. W. Davidson, and L. L. Looger, "A bright and photostable photoconvertible fluorescent protein.," *Nature methods*, vol. 6, pp. 131–3, Feb. 2009.

[124] D. R. Whelan and T. D. M. Bell, "Image artifacts in Single Molecule Localization Microscopy: why optimization of sample preparation protocols matters.," *Scientific reports*, vol. 5, p. 7924, Jan. 2015.

[125] B. Huang, M. Bates, and X. Zhuang, "Super-resolution fluorescence microscopy.," *Annual review of biochemistry*, vol. 78, pp. 993–1016, Jan. 2009.

[126] N. Durisic, L. Laparra-Cuervo, A. Sandoval-Álvarez, J. S. Borbely, and M. Lakadamyali, "Single-molecule evaluation of fluorescent protein photoactivation efficiency using an in vivo nanotemplate.," *Nature methods*, vol. 11, pp. 156–62, Mar. 2014.

[127] S. F. Lee, Q. Vérolet, and A. Fürstenberg, "Improved super-resolution microscopy with oxazine fluorophores in heavy water.," *Angewandte Chemie (International ed. in English)*, vol. 52, pp. 8948–51, Aug. 2013.

[128] K. Klehs, C. Spahn, U. Endesfelder, S. F. Lee, A. Fürstenberg, and M. Heilemann, "Increasing the brightness of cyanine fluorophores for single-molecule and super-resolution imaging.," *Chemphyschem : a European journal of chemical physics and physical chemistry*, vol. 15, pp. 637–41, Mar. 2014.

[129] H. Shroff, C. Galbraith, J. Galbraith, and E. Betzig, "Live-cell photoactivated localization microscopy of nanoscale adhesion dynamics," *Nature methods*, vol. 5, no. 5, pp. 417–423, 2008.

[130] D. Lando, U. Endesfelder, H. Berger, L. Subramanian, P. D. Dunne, J. McColl, D. Klenerman, A. M. Carr, M. Sauer, R. C. Allshire, M. Heilemann, and E. D. Laue, "Quantitative single-molecule microscopy reveals that CENP-A(Cnp1) deposition occurs during G2 in fission yeast.," *Open biology*, vol. 2, p. 120078, July 2012.

[131] E. M. Puchner, J. M. Walter, R. Kasper, B. Huang, and W. A. Lim, "Counting molecules in single organelles with superresolution microscopy allows tracking of the endosome maturation trajectory.," *Proceedings of the National Academy of Sciences of the United States of America*, vol. 110, pp. 16015–20, Oct. 2013.

[132] A. Shivanandan, H. Deschout, M. Scarselli, and A. Radenovic, "Challenges in quantitative single molecule localization microscopy.," *FEBS letters*, vol. 588, pp. 3595–602, Oct. 2014.

[133] S. van de Linde, R. Kasper, M. Heilemann, and M. Sauer, "Photoswitching microscopy with standard fluorophores," *Applied Physics B*, vol. 93, pp. 725–731, Oct. 2008.

[134] S. van de Linde, U. Endesfelder, A. Mukherjee, M. Schüttpelz, G. Wiebusch, S. Wolter, M. Heilemann, and M. Sauer, "Multicolor photoswitching microscopy for subdiffraction-resolution fluorescence imaging.," *Photochemical & photobiological sciences : Official journal of the European Photochemistry Association and the European Society for Photobiology*, vol. 8, pp. 465–9, Apr. 2009.

[135] C. M. Hardaway, R. B. Badisa, and K. F. A. Soliman, "Effect of ascorbic acid and hydrogen peroxide on mouse neuroblastoma cells.," *Molecular medicine reports*, vol. 5, pp. 1449–52, June 2012.

[136] J. D. Campbell, M. Cole, B. Bunditrutavorn, and A. T. Vella, "Ascorbic acid is a potent inhibitor of various forms of T cell apoptosis.," *Cellular immunology*, vol. 194, pp. 1–5, May 1999.

[137] H. Sakagami and K. Satoh, "Modulating factors of radical intensity and cytotoxic activity of ascorbate (Review)," Jan. 1997.

[138] R. J. Schmidt, L. Y. Chung, A. M. Andrews, and T. D. Turner, "Toxicity of L-ascorbic acid to L929 fibroblast cultures: relevance to biocompatibility testing of materials for use in wound management.," *Journal of biomedical materials research*, vol. 27, pp. 521–30, Apr. 1993.

[139] W. C. Duim, B. Chen, J. Frydman, and W. E. Moerner, "Sub-diffraction imaging of huntingtin protein aggregates by fluorescence blink-microscopy and atomic force microscopy.," *Chemphyschem : a European journal of chemical physics and physical chemistry*, vol. 12, pp. 2387–90, Sept. 2011.

[140] R. Henriques, C. Griffiths, E. Hesper Rego, and M. M. Mhlanga, "PALM and STORM: unlocking live-cell super-resolution.," *Biopolymers*, vol. 95, pp. 322–31, May 2011.

[141] S. van de Linde and M. Sauer, "How to switch a fluorophore: from undesired blinking to controlled photoswitching.," *Chemical Society reviews*, vol. 43, pp. 1076–87, Feb. 2014.

[142] L. Goldman, "Quantitative analysis of a fully generalized four-state kinetic scheme.," *Biophysical journal*, vol. 91, pp. 173–8, July 2006.

[143] C. Flors, J.-i. Hotta, H. Uji-i, P. Dedecker, R. Ando, H. Mizuno, A. Miyawaki, and J. Hofkens, "A stroboscopic approach for fast photoactivation-localization microscopy with Dronpa mutants.," *Journal of the American Chemical Society*, vol. 129, pp. 13970–7, Nov. 2007.

[144] P. Annibale, M. Scarselli, A. Kodiyan, and A. Radenovic, "Photoactivatable Fluorescent Protein mEos2 Displays Repeated Photoactivation after a Long-Lived Dark State in the Red Photoconverted Form," *The Journal of Physical Chemistry Letters*, vol. 1, pp. 1506–1510, May 2010.

[145] S.-H. S.-H. Lee, J. Y. Shin, A. Lee, and C. Bustamante, "Counting single photoactivatable fluorescent molecules by photoactivated localization microscopy (PALM).," *Proceedings of the National Academy of Sciences of the United States of America*, vol. 109, pp. 17436–17441, Oct. 2012.

[146] J. Gunzenhäuser, N. Olivier, T. Pengo, and S. Manley, "Quantitative super-resolution imaging reveals protein stoichiometry and nanoscale morphology of assembling HIV-Gag virions.," *Nano letters*, vol. 12, pp. 4705–10, Oct. 2012.

[147] A. Small and S. Stahlheber, "Fluorophore localization algorithms for super-resolution microscopy," *Nature Methods*, vol. 11, pp. 267–279, 2014.

[148] EPFL, "Single-Molecule Localization Microscopy Challenge ISBI 2013," *http://bigwww.epfl.ch/smlm/software/*, 2015.

[149] A. Herbert, "Peak Fit, a Single-molecule Plugins," *http://www.sussex.ac.uk/gdsc/ intranet/microscopy/imagej/smlm_plugins*, 2014.

[150] C. A. Schneider, W. S. Rasband, and K. W. Eliceiri, "NIH Image to ImageJ: 25 years of image analysis," 2012.

[151] S. W. Smith, "Linear Image Processing," in *The Scientist and Engineer's Guide to Digital Signal Processing*, ch. 24, pp. 397–422, 1997.

[152] A. V. Abraham, S. Ram, J. Chao, E. S. Ward, and R. J. Ober, "Quantitative study of single molecule location estimation techniques.," *Optics express*, vol. 17, pp. 23352–73, Dec. 2009.

[153] P. Winckler, L. Lartigue, G. Giannone, F. De Giorgi, F. Ichas, J.-B. Sibarita, B. Lounis, and L. Cognet, "Identification and super-resolution imaging of ligand-activated receptor dimers in live cells.," *Scientific reports*, vol. 3, p. 2387, Jan. 2013.

[154] S. A. Shelby, D. Holowka, B. Baird, and S. L. Veatch, "Distinct stages of stimulated fcεri receptor clustering and immobilization are identified through superresolution imaging," *Biophysical Journal*, vol. 105, pp. 2343–2354, 2013.

[155] P. Sengupta, T. Jovanovic-Talisman, and J. Lippincott-Schwartz, "Quantifying spatial organization in point-localization superresolution images using pair correlation analysis.," *Nature protocols*, vol. 8, pp. 345–54, Feb. 2013.

[156] S. Wolter, A. Löschberger, T. Holm, S. Aufmkolk, M.-C. Dabauvalle, S. van de Linde, and M. Sauer, "rapidSTORM: accurate, fast open-source software for localization microscopy.," *Nature methods*, vol. 9, pp. 1040–1, Nov. 2012.

[157] J. Hoshen and R. Kopelman, "Percolation and cluster distribution. I. Cluster multiple labeling technique and critical concentration algorithm," *Physical Review B*, vol. 14, pp. 3438–3445, Oct. 1976.

[158] M. Ester, H. Kriegel, J. Sander, and X. Xu, "A density-based algorithm for discovering clusters in large spatial databases with noise.," *KDD*, 1996.

[159] R. A. Finkel and J. L. Bentley, "Quad trees a data structure for retrieval on composite keys," *Acta Informatica*, vol. 4, no. 1, pp. 1–9, 1974.

[160] D. Baddeley, M. B. Cannell, and C. Soeller, "Visualization of localization microscopy data.," *Microscopy and microanalysis : the official journal of Microscopy Society of America, Microbeam Analysis Society, Microscopical Society of Canada*, vol. 16, pp. 64–72, Feb. 2010.

[161] K. I. Mortensen, L. S. Churchman, J. A. Spudich, and H. Flyvbjerg, "Optimized localization analysis for single-molecule tracking and super-resolution microscopy.," *Nature methods*, vol. 7, pp. 377–381, 2010.

[162] R. J. Ober, S. Ram, and E. S. Ward, "Localization accuracy in single-molecule microscopy.," *Biophysical journal*, vol. 86, pp. 1185–200, Feb. 2004.

[163] D. J. Rowland and J. S. Biteen, "Top-hat and asymmetric Gaussian-based fitting functions for quantifying directional single-molecule motion.," *Chemphyschem : a European journal of chemical physics and physical chemistry*, vol. 15, pp. 712–20, Mar. 2014.

[164] R. B. Murphy, "On the meaning of precision and accuracy," *Precision measurement and calibration: Selected NBS papers on statistical concepts and procedures, NBS Special Publication*, vol. 300, pp. 357–360, 1969.

[165] J. C. Waters, "Accuracy and precision in quantitative fluorescence microscopy.," *The Journal of cell biology*, vol. 185, pp. 1135–48, June 2009.

[166] N. Banterle, K. H. Bui, E. A. Lemke, and M. Beck, "Fourier ring correlation as a resolution criterion for super-resolution microscopy.," *Journal of structural biology*, vol. 183, pp. 363–7, Sept. 2013.

[167] U. Endesfelder, S. Malkusch, F. Fricke, and M. Heilemann, "A simple method to estimate the average localization precision of a single-molecule localization microscopy experiment.," *Histochemistry and cell biology*, vol. 141, pp. 629–38, June 2014.

[168] D. R. Rines, D. Thomann, J. F. Dorn, P. Goodwin, and P. K. Sorger, "Live cell imaging of yeast.," *Cold Spring Harbor protocols*, vol. 2011, pp. pdb.top065482–, Sept. 2011.

[169] J. A. Waddle, T. S. Karpova, R. H. Waterston, and J. A. Cooper, "Movement of cortical actin patches in yeast.," *The Journal of cell biology*, vol. 132, pp. 861–70, Mar. 1996.

[170] P. Nurse, "Genetic control of cell size at cell division in yeast.," *Nature*, vol. 256, pp. 547–51, Aug. 1975.

[171] T. Yeo, S. Ong, and R. Sinniah, "Autofocusing for tissue microscopy," *Image and Vision Computing*, vol. 11, pp. 629–639, Dec. 1993.

[172] M. Held, M. H. A. Schmitz, B. Fischer, T. Walter, B. Neumann, M. H. Olma, M. Peter, J. Ellenberg, and D. W. Gerlich, "CellCognition: time-resolved phenotype annotation in high-throughput live cell imaging.," *Nature methods*, vol. 7, pp. 747–54, Sept. 2010.

[173] A. D. Edelstein, M. A. Tsuchida, N. Amodaj, H. Pinkard, R. D. Vale, and N. Stuurman, "Advanced methods of microscope control using $\mu$Manager software," Nov. 2014.

[174] S. J. Holden, T. Pengo, K. L. Meibom, C. Fernandez Fernandez, J. Collier, and S. Manley, "High throughput 3D super-resolution microscopy reveals Caulobacter crescentus in vivo Z-ring organization.," *Proceedings of the National Academy of Sciences of the United States of America*, vol. 111, pp. 4566–71, Mar. 2014.

[175] L. Zhu, W. Zhang, D. Elnatan, and B. Huang, "Faster STORM using compressed sensing.," *Nature methods*, vol. 9, pp. 721–3, July 2012.

[176] N. Brede and M. Lakadamyali, "GraspJ: an open source, real-time analysis package for super-resolution imaging," *Optical Nanoscopy*, vol. 1, p. 11, Dec. 2012.

[177] A. Kechkar, D. Nair, M. Heilemann, D. Choquet, and J. B. Sibarita, "Real-Time Analysis and Visualization for Single-Molecule Based Super-Resolution Microscopy," *PLoS ONE*, vol. 8, no. 4, 2013.

[178] X. Chen, L. Ren, Y. Qiu, and H. Liu, "New method for determining the depth of field of microscope systems.," *Applied optics*, vol. 50, pp. 5524–33, Oct. 2011.

[179] Y. Hiraoka, J. Sedat, and D. Agard, "The use of a charge-coupled device for quantitative optical microscopy of biological structures," *Science*, vol. 238, pp. 36–41, Oct. 1987.

[180] J. G. McNally, T. Karpova, J. Cooper, and J. A. Conchello, "Three-dimensional imaging by deconvolution microscopy.," *Methods (San Diego, Calif.)*, vol. 19, pp. 373–85, Nov. 1999.

[181] J.-B. Sibarita, "Deconvolution microscopy.," *Advances in biochemical engineering/biotechnology*, vol. 95, pp. 201–43, Jan. 2005.

[182] D. S. C. Biggs, "3D deconvolution microscopy.," *Current protocols in cytometry / editorial board, J. Paul Robinson, managing editor ... [et al.]*, vol. Chapter 12, pp. Unit 12.19.1–20, Apr. 2010.

[183] R. Henriques, M. Lelek, E. F. Fornasiero, F. Valtorta, C. Zimmer, and M. M. Mhlanga, "QuickPALM: 3D real-time photoactivation nanoscopy image processing in ImageJ.," *Nature methods*, vol. 7, pp. 339–40, May 2010.

[184] M. Ovesný, P. Křížek, J. Borkovec, Z. Svindrych, and G. M. Hagen, "ThunderSTORM: a comprehensive ImageJ plug-in for PALM and STORM data analysis and super-resolution imaging.," *Bioinformatics (Oxford, England)*, pp. 1–2, Apr. 2014.

[185] R. Starr, S. Stahlheber, and A. Small, "Fast maximum likelihood algorithm for localization of fluorescent molecules.," *Optics letters*, vol. 37, pp. 413–5, Feb. 2012.

[186] N. Bone, J. B. Millar, T. Toda, and J. Armstrong, "Regulated vacuole fusion and fission in Schizosaccharomyces pombe: an osmotic response dependent on MAP kinases.," *Current biology : CB*, vol. 8, pp. 135–44, Jan. 1998.

[187] S. A. Mutch, B. S. Fujimoto, C. L. Kuyper, J. S. Kuo, S. M. Bajjalieh, and D. T. Chiu, "Deconvolving single-molecule intensity distributions for quantitative microscopy measurements.," *Biophysical journal*, vol. 92, pp. 2926–43, Apr. 2007.

[188] H. Deschout, K. Neyts, and K. Braeckmans, "The influence of movement on the localization precision of sub-resolution particles in fluorescence microscopy," *Journal of Biophotonics*, vol. 5, pp. 97–109, 2012.

[189] J. C. Sun, S. Lopez-Verges, C. C. Kim, J. L. DeRisi, and L. L. Lanier, "NK cells and immune "memory".," *Journal of immunology (Baltimore, Md. : 1950)*, vol. 186, pp. 1891–7, Feb. 2011.

[190] K. Murphy, P. Travers, and M. Walport, *Janeway's Immunobiology*, vol. 7. 2008.

[191] L. B. Nicholson and D. C. Wraith, "T-cell receptor degeneracy: the dog that did not bark. Adaptation of the self-reactive T-cell response to limit autoimmune disease.," *Molecular immunology*, vol. 40, pp. 997–1002, Feb. 2004.

[192] G. P. Morris and P. M. Allen, "How the TCR balances sensitivity and specificity for the recognition of self and pathogens.," *Nature immunology*, vol. 13, pp. 121–8, Feb. 2012.

[193] Y. Sykulev, M. Joo, I. Vturina, T. J. Tsomides, and H. N. Eisen, "Evidence that a single peptide-MHC complex on a target cell can elicit a cytolytic T cell response.," *Immunity*, vol. 4, pp. 565–71, June 1996.

[194] D. J. Irvine, M. A. Purbhoo, M. Krogsgaard, and M. M. Davis, "Direct observation of ligand recognition by T cells.," *Nature*, vol. 419, pp. 845–9, Oct. 2002.

[195] C. V. Harding and E. R. Unanue, "Quantitation of antigen-presenting cell MHC class II/peptide complexes necessary for T-cell stimulation.," *Nature*, vol. 346, pp. 574–6, Aug. 1990.

[196] B. N. Manz, B. L. Jackson, R. S. Petit, M. L. Dustin, and J. Groves, "T-cell triggering thresholds are modulated by the number of antigen within individual T-cell receptor clusters.," *Proceedings of the National Academy of Sciences of the United States of America*, vol. 108, pp. 9089–94, May 2011.

[197] A. J. T. George, J. Stark, and C. Chan, "Understanding specificity and sensitivity of T-cell recognition.," *Trends in immunology*, vol. 26, pp. 653–9, Dec. 2005.

[198] W. A. Comrie, S. Li, S. Boyle, and J. K. Burkhardt, "The dendritic cell cytoskeleton promotes T cell adhesion and activation by constraining ICAM-1 mobility," *The Journal of Cell Biology*, vol. 208, pp. 457–473, Feb. 2015.

[199] A. S. Shaw and M. L. Dustin, "Making the T Cell Receptor Go the Distance: A Topological View of T Cell Activation," *Immunity*, vol. 6, pp. 361–369, Apr. 1997.

[200] B.-C. Chen, W. R. Legant, K. Wang, L. Shao, D. E. Milkie, M. W. Davidson, C. Janetopoulos, X. S. Wu, J. A. Hammer, Z. Liu, B. P. English, Y. Mimori-Kiyosue, D. P. Romero, A. T. Ritter, J. Lippincott-Schwartz, L. Fritz-Laylin, R. D. Mullins, D. M. Mitchell, J. N. Bembenek, A.-C. Reymann, R. Bohme, S. W. Grill, J. T. Wang, G. Seydoux, U. S. Tulu, D. P. Kiehart, and E. Betzig, "Lattice light-sheet microscopy: Imaging molecules to embryos at high spatiotemporal resolution," *Science*, vol. 346, pp. 1257998–1257998, Oct. 2014.

[201] M. M. Davis, "A new trigger for T cells.," *Cell*, vol. 110, pp. 285–7, Aug. 2002.

[202] P. A. van der Merwe and O. Dushek, "Mechanisms for T cell receptor triggering.," *Nature reviews. Immunology*, vol. 11, pp. 47–55, 2011.

[203] M. L. Dustin and J. T. Groves, "Receptor signaling clusters in the immune synapse.," *Annual review of biophysics*, vol. 41, pp. 543–56, Jan. 2012.

[204] M. L. Dustin, "Cell adhesion molecules and actin cytoskeleton at immune synapses and kinapses.," *Current opinion in cell biology*, vol. 19, pp. 529–33, Oct. 2007.

[205] A. T. Ritter, K. L. Angus, and G. M. Griffiths, "The role of the cytoskeleton at the immunological synapse.," *Immunological reviews*, vol. 256, pp. 107–17, Nov. 2013.

[206] G. M. Griffiths, A. Tsun, and J. C. Stinchcombe, "The immunological synapse: a focal point for endocytosis and exocytosis.," *The Journal of cell biology*, vol. 189, pp. 399–406, May 2010.

[207] C. R. Monks, B. A. Freiberg, H. Kupfer, N. Sciaky, and A. Kupfer, "Three-dimensional segregation of supramolecular activation clusters in T cells.," *Nature*, vol. 395, pp. 82–6, Sept. 1998.

[208] J. C. Stinchcombe and G. M. Griffiths, "Communication, the centrosome and the immunological synapse.," *Philosophical transactions of the Royal Society of London. Series B, Biological sciences*, vol. 369, Sept. 2014.

[209] J. C. Brown and W. W. Newcomb, "Herpesvirus capsid assembly: insights from structural analysis.," *Current opinion in virology*, vol. 1, pp. 142–9, Aug. 2011.

[210] G. D. Rak, E. M. Mace, P. P. Banerjee, T. Svitkina, and J. S. Orange, "Natural killer cell lytic granule secretion occurs through a pervasive actin network at the immune synapse.," *PLoS biology*, vol. 9, p. e1001151, Sept. 2011.

[211] S. J. Davis and P. A. van der Merwe, "Lck and the nature of the T cell receptor trigger.," *Trends in immunology*, vol. 32, pp. 1–5, Jan. 2011.

[212] O. Ballek, J. Valečka, J. Manning, and D. Filipp, "The pool of preactivated Lck in the initiation of T-cell signaling: a critical re-evaluation of the Lck standby model.," *Immunology and cell biology*, Nov. 2014.

[213] M. A. Lemmon and J. Schlessinger, "Cell signaling by receptor tyrosine kinases.," *Cell*, vol. 141, pp. 1117–34, June 2010.

[214] J. Yang and M. Reth, "Oligomeric organization of the B-cell antigen receptor on resting cells.," *Nature*, vol. 467, pp. 465–9, Sept. 2010.

[215] R. Schwinzer, R. A. Franklin, J. Domenico, H. Renz, and E. W. Gelfand, "Monoclonal antibodies directed to different epitopes in the CD3-TCR complex induce different states of competence in resting human T cells.," *Journal of immunology (Baltimore, Md. : 1950)*, vol. 148, pp. 1322–8, Mar. 1992.

[216] L. Wooldridge, A. Lissina, D. K. Cole, H. A. van den Berg, D. A. Price, and A. K. Sewell, "Tricks with tetramers: how to get the most from multimeric peptide-MHC.," *Immunology*, vol. 126, pp. 147–64, Feb. 2009.

[217] A. Trautmann and C. Randriamampita, "Initiation of TCR signalling revisited," *Trends in Immunology*, vol. 24, pp. 425–428, Aug. 2003.

[218] M. Krogsgaard, Q.-J. Li, C. Sumen, J. B. Huppa, M. Huse, and M. M. Davis, "Agonist/endogenous peptide-MHC heterodimers drive T cell activation and sensitivity.," *Nature*, vol. 434, pp. 238–43, Mar. 2005.

[219] R. M. Locksley, S. L. Reiner, F. Hatam, D. R. Littman, and N. Killeen, "Helper T cells without CD4: control of leishmaniasis in CD4-deficient mice.," *Science (New York, N.Y.)*, vol. 261, pp. 1448–51, Sept. 1993.

[220] P. A. van der Merwe and S.-P. Cordoba, "Late arrival: recruiting coreceptors to the T cell receptor complex.," *Immunity*, vol. 34, pp. 1–3, Jan. 2011.

[221] N. Jiang, J. Huang, L. J. Edwards, B. Liu, Y. Zhang, C. D. Beal, B. D. Evavold, and C. Zhu, "Two-stage cooperative T cell receptor-peptide major histocompatibility complex-CD8 trimolecular interactions amplify antigen discrimination.," *Immunity*, vol. 34, pp. 13–23, Jan. 2011.

[222] R. Varma, G. Campi, T. Yokosuka, T. Saito, and M. L. Dustin, "T cell receptor-proximal signals are sustained in peripheral microclusters and terminated in the central supramolecular activation cluster.," *Immunity*, vol. 25, pp. 117–27, July 2006.

[223] T. Yokosuka, K. Sakata-Sogawa, W. Kobayashi, M. Hiroshima, A. Hashimoto-Tane, M. Tokunaga, M. L. Dustin, and T. Saito, "Newly generated T cell receptor microclusters initiate and sustain T cell activation by recruitment of Zap70 and SLP-76.," *Nature immunology*, vol. 6, pp. 1253–62, Dec. 2005.

[224] W. W. A. Schamel and B. Alarcón, "Organization of the resting TCR in nanoscale oligomers," *Immunological Reviews*, vol. 251, pp. 13–20, Jan. 2013.

[225] G. Lebon, T. Warne, and C. G. Tate, "Agonist-bound structures of G protein-coupled receptors.," *Current opinion in structural biology*, vol. 22, pp. 482–90, Aug. 2012.

[226] L. Kjer-Nielsen, M. A. Dunstone, L. Kostenko, L. K. Ely, T. Beddoe, N. A. Mifsud, A. W. Purcell, A. G. Brooks, J. McCluskey, and J. Rossjohn, "Crystal structure of the human T cell receptor CD3 epsilon gamma heterodimer complexed to the therapeutic mAb OKT3.," *Proceedings of the National Academy of Sciences of the United States of America*, vol. 101, pp. 7675–80, May 2004.

[227] T. Beddoe, Z. Chen, C. S. Clements, L. K. Ely, S. R. Bushell, J. P. Vivian, L. Kjer-Nielsen, S. S. Pang, M. A. Dunstone, Y. C. Liu, W. A. Macdonald, M. A. Perugini, M. C. J. Wilce, S. R. Burrows, A. W. Purcell, T. Tiganis, S. P. Bottomley, J. McCluskey, and J. Rossjohn, "Antigen ligation triggers a conformational change within the constant domain of the alphabeta T cell receptor.," *Immunity*, vol. 30, pp. 777–88, June 2009.

[228] M. G. Rudolph, R. L. Stanfield, and I. A. Wilson, "How TCRs bind MHCs, peptides, and coreceptors.," *Annual review of immunology*, vol. 24, pp. 419–66, Jan. 2006.

[229] Z. Ma, P. A. Janmey, and T. H. Finkel, "The receptor deformation model of TCR triggering.," *FASEB journal : official publication of the Federation of American Societies for Experimental Biology*, vol. 22, pp. 1002–8, Apr. 2008.

[230] Z. J. Sun, K. S. Kim, G. Wagner, and E. L. Reinherz, "Mechanisms contributing to T cell receptor signaling and assembly revealed by the solution structure of an ectodomain fragment of the CD3 epsilon gamma heterodimer.," *Cell*, vol. 105, pp. 913–23, June 2001.

[231] C. Xu, E. Gagnon, M. E. Call, J. R. Schnell, C. D. Schwieters, C. V. Carman, J. J. Chou, and K. W. Wucherpfennig, "Regulation of T cell receptor activation by dynamic membrane binding of the CD3epsilon cytoplasmic tyrosine-based motif.," *Cell*, vol. 135, pp. 702–13, Nov. 2008.

[232] B. T. Marshall, M. Long, J. W. Piper, T. Yago, R. P. McEver, and C. Zhu, "Direct observation of catch bonds involving cell-adhesion molecules.," *Nature*, vol. 423, pp. 190–3, May 2003.

[233] C. D. Buckley, J. Tan, K. L. Anderson, D. Hanein, N. Volkmann, W. I. Weis, W. J. Nelson, and A. R. Dunn, "The minimal cadherin-catenin complex binds to actin filaments under force," *Science*, vol. 346, pp. 1254211–1254211, Oct. 2014.

[234] S. J. Davis and P. A. van der Merwe, "The kinetic-segregation model: TCR triggering and beyond.," *Nature immunology*, vol. 7, pp. 803–9, Aug. 2006.

[235] J. Lin and A. Weiss, "The tyrosine phosphatase CD148 is excluded from the immunologic synapse and down-regulates prolonged T cell signaling," *Journal of Cell Biology*, vol. 162, pp. 673–682, Aug. 2003.

[236] C. Irles, A. Symons, F. Michel, T. R. Bakker, P. A. van der Merwe, and O. Acuto, "CD45 ectodomain controls interaction with GEMs and Lck activity for optimal TCR signaling.," *Nature immunology*, vol. 4, pp. 189–97, Feb. 2003.

[237] K. Choudhuri, D. Wiseman, M. H. Brown, K. Gould, and P. A. van der Merwe, "T-cell receptor triggering is critically dependent on the dimensions of its peptide-MHC ligand.," *Nature*, vol. 436, pp. 578–82, July 2005.

[238] K. Choudhuri, M. Parker, A. Milicic, D. K. Cole, M. K. Shaw, A. K. Sewell, G. Stewart-Jones, T. Dong, K. G. Gould, and P. A. van der Merwe, "Peptide-major histocompatibility complex dimensions control proximal kinase-phosphatase balance during T cell activation.," *The Journal of biological chemistry*, vol. 284, pp. 26096–105, Sept. 2009.

[239] Z. Ma, K. A. Sharp, P. A. Janmey, and T. H. Finkel, "Surface-anchored monomeric agonist pMHCs alone trigger TCR with high sensitivity.," *PLoS biology*, vol. 6, p. e43, Feb. 2008.

[240] C. Bluemel, S. Hausmann, P. Fluhr, M. Sriskandarajah, W. B. Stallcup, P. A. Baeuerle, and P. Kufer, "Epitope distance to the target cell membrane and antigen size determine the potency of T cell-mediated lysis by BiTE antibodies specific for a large melanoma surface antigen.," *Cancer immunology, immunotherapy : CII*, vol. 59, pp. 1197–209, Aug. 2010.

[241] S. E. James, P. D. Greenberg, M. C. Jensen, Y. Lin, J. Wang, B. G. Till, A. A. Raubitschek, S. J. Forman, and O. W. Press, "Antigen sensitivity of CD22-specific chimeric TCR is modulated by target epitope distance from the cell membrane.," *Journal of immunology (Baltimore, Md. : 1950)*, vol. 180, pp. 7028–38, May 2008.

[242] R. L. Contento, S. Campello, A. E. Trovato, E. Magrini, F. Anselmi, and A. Viola, "Adhesion shapes T cells for prompt and sustained T-cell receptor signalling.," *The EMBO journal*, vol. 29, pp. 4035–47, Dec. 2010.

[243] J. R. James and R. D. Vale, "Biophysical mechanism of T-cell receptor triggering in a reconstituted system.," *Nature*, vol. 487, pp. 64–9, July 2012.

[244] J. J. Illingworth and P. Anton van der Merwe, "Dissecting T-cell activation with high-resolution live-cell microscopy.," *Immunology*, vol. 135, pp. 198–206, Mar. 2012.

[245] S. J. Davis and P. van der Merwe, "The immunological synapse: required for T cell receptor signalling or directing T cell effector function?," *Current Biology*, vol. 11, pp. R289–R290, Apr. 2001.

[246] S. Cemerski, J. Das, E. Giurisato, M. A. Markiewicz, P. M. Allen, A. K. Chakraborty, and A. S. Shaw, "The balance between T cell receptor signaling and degradation at the center of the immunological synapse is determined by antigen quality.," *Immunity*, vol. 29, pp. 414–22, Sept. 2008.

[247] J. L. Rodríguez-Fernández, L. Riol-Blanco, and C. Delgado-Martín, "What is an immunological synapse?," *Microbes and infection / Institut Pasteur*, vol. 12, pp. 438–45, June 2010.

[248] B. F. Lillemeier, M. a. Mörtelmaier, M. B. Forstner, J. B. Huppa, J. T. Groves, and M. M. Davis, "TCR and Lat are expressed on separate protein islands on T cell membranes and concatenate during activation.," *Nature immunology*, vol. 11, pp. 90–6, Jan. 2010.

[249] W. W. A. Schamel, I. Arechaga, R. M. Risueño, H. M. van Santen, P. Cabezas, C. Risco, J. M. Valpuesta, and B. Alarcón, "Coexistence of multivalent and monovalent TCRs explains high sensitivity and wide range of response.," *The Journal of experimental medicine*, vol. 202, pp. 493–503, Aug. 2005.

[250] J. R. James, S. S. White, R. W. Clarke, A. M. Johansen, P. D. Dunne, D. L. Sleep, W. J. Fitzgerald, S. J. Davis, and D. Klenerman, "Single-molecule level analysis of the subunit composition of the T cell receptor on live T cells.," *Proceedings of the National Academy of Sciences of the United States of America*, vol. 104, pp. 17662–7, Nov. 2007.

[251] P. D. Dunne, R. A. Fernandes, J. McColl, J. W. Yoon, J. R. James, S. J. Davis, and D. Klenerman, "DySCo: quantitating associations of membrane proteins using two-color single-molecule tracking.," *Biophysical journal*, vol. 97, pp. L5–7, Aug. 2009.

[252] J. R. James, J. McColl, M. I. Oliveira, P. D. Dunne, E. Huang, A. Jansson, P. Nilsson, D. L. Sleep, C. M. Gonçalves, S. H. Morgan, J. H. Felce, R. Mahen, R. A. Fernandes, A. M. Carmo, D. Klenerman, and S. J. Davis, "The T cell receptor triggering apparatus is composed of monovalent or monomeric proteins.," *The Journal of biological chemistry*, vol. 286, pp. 31993–2001, Sept. 2011.

[253] M. A. Purbhoo, H. Liu, S. Oddos, D. M. Owen, M. A. A. Neil, S. V. Pageon, P. M. W. French, C. E. Rudd, and D. M. Davis, "Dynamics of subsynaptic vesicles and surface microclusters at the immunological synapse.," *Science signaling*, vol. 3, p. ra36, Jan. 2010.

[254] I. Parmryd and B. Onfelt, "Consequences of membrane topography.," *The FEBS journal*, vol. 280, pp. 2775–84, June 2013.

[255] D. M. Owen, C. Rentero, J. Rossy, A. Magenau, D. Williamson, M. Rodriguez, and K. Gaus, "PALM imaging and cluster analysis of protein heterogeneity at the cell surface.," *Journal of biophotonics*, vol. 3, pp. 446–54, July 2010.

[256] P. A. van der Merwe, P. D. Dunne, D. Klenerman, and S. J. Davis, "Taking T cells beyond the diffraction limit.," *Nature immunology*, vol. 11, pp. 51–2, Jan. 2010.

[257] D. J. Williamson, D. M. Owen, J. Rossy, A. Magenau, M. Wehrmann, J. J. Gooding, and K. Gaus, "Pre-existing clusters of the adaptor Lat do not participate in early T cell signaling events.," *Nature immunology*, vol. 12, pp. 655–62, July 2011.

[258] Y. Neve-Oz, Y. Razvag, J. Sajman, and E. Sherman, "Mechanisms of localized activation of the T cell antigen receptor inside clusters.," *Biochimica et biophysica acta*, Oct. 2014.

[259] V. Adam, K. Nienhaus, D. Bourgeois, and G. U. Nienhaus, "Structural basis of enhanced photoconversion yield in green fluorescent protein-like protein Dendra2.," *Biochemistry*, vol. 48, pp. 4905–15, June 2009.

[260] M. F. Garcia-Parajo, M. Koopman, E. M. van Dijk, V. Subramaniam, and N. F. van Hulst, "The nature of fluorescence emission in the red fluorescent protein DsRed, revealed by single-molecule detection.," *Proceedings of the National Academy of Sciences of the United States of America*, vol. 98, pp. 14392–7, Dec. 2001.

[261] M. H. Ulbrich and E. Y. Isacoff, "Subunit counting in membrane-bound proteins.," *Nature methods*, vol. 4, pp. 319–21, Apr. 2007.

[262] A. T. Watson, P. Werler, and A. M. Carr, "Regulation of gene expression at the fission yeast Schizosaccharomyces pombe urg1 locus.," *Gene*, vol. 484, pp. 75–85, Sept. 2011.

[263] P. Annibale, S. Vanni, M. Scarselli, U. Rothlisberger, and A. Radenovic, "Quantitative photo activated localization microscopy: unraveling the effects of photoblinking.," *PloS one*, vol. 6, p. e22678, Jan. 2011.

[264] C. Coltharp, R. P. Kessler, and J. Xiao, "Accurate construction of photoactivated localization microscopy (PALM) images for quantitative measurements.," *PloS one*, vol. 7, p. e51725, Jan. 2012.

[265] B. Chance, B. Schoener, R. Oshino, F. Itshak, and Y. Nakase, "Oxidation-reduction ratio studies of mitochondria in freeze-trapped samples. NADH and flavoprotein fluorescence signals.," *The Journal of biological chemistry*, vol. 254, pp. 4764–71, June 1979.

[266] S. Huang, A. A. Heikal, and W. W. Webb, "Two-photon fluorescence spectroscopy and microscopy of NAD(P)H and flavoprotein.," *Biophysical journal*, vol. 82, pp. 2811–25, May 2002.

[267] K. A. K. Tanaka, K. G. N. Suzuki, Y. M. Shirai, S. T. Shibutani, M. S. H. Miyahara, H. Tsuboi, M. Yahara, A. Yoshimura, S. Mayor, T. K. Fujiwara, and A. Kusumi, "Membrane molecules mobile even after chemical fixation.," *Nature methods*, vol. 7, pp. 865–6, Nov. 2010.

[268] V. Vogel and M. Sheetz, "Local force and geometry sensing regulate cell functions.," *Nature reviews. Molecular cell biology*, vol. 7, pp. 265–75, Apr. 2006.

[269] R. S. O'Connor, X. Hao, K. Shen, K. Bashour, T. Akimova, W. W. Hancock, L. C. Kam, and M. C. Milone, "Substrate rigidity regulates human T cell activation and proliferation.," *Journal of immunology (Baltimore, Md. : 1950)*, vol. 189, pp. 1330–9, Aug. 2012.

[270] H. H. Chang, M. Hemberg, M. Barahona, D. E. Ingber, and S. Huang, "Transcriptome-wide noise controls lineage choice in mammalian progenitor cells.," *Nature*, vol. 453, pp. 544–7, May 2008.

[271] L. Cai, N. Friedman, and X. S. Xie, "Stochastic protein expression in individual cells at the single molecule level.," *Nature*, vol. 440, pp. 358–62, Mar. 2006.

[272] A. Raj and A. van Oudenaarden, "Nature, nurture, or chance: stochastic gene expression and its consequences.," *Cell*, vol. 135, pp. 216–26, Oct. 2008.

[273] G. C. Rollins, J. Y. Shin, C. Bustamante, and S. Pressé, "Stochastic approach to the molecular counting problem in superresolution microscopy.," *Proceedings of the National Academy of Sciences of the United States of America*, vol. 112, pp. E110–8, Dec. 2014.

[274] R. Iinuma, Y. Ke, R. Jungmann, T. Schlichthaerle, J. B. Woehrstein, and P. Yin, "Polyhedra self-assembled from DNA tripods and characterized with 3D DNA-PAINT.," *Science (New York, N.Y.)*, vol. 344, pp. 65–9, Apr. 2014.

[275] K. Zimmermann, T. Liechti, A. Haas, M. Rehr, A. Trkola, H. F. Gunthard, and A. Oxenius, "The Orientation of HIV-1 gp120 Binding to the CD4 Receptor Differentially Modulates CD4+ T Cell Activation," *The Journal of Immunology*, vol. 194, pp. 637–649, Dec. 2014.

[276] B. M. Carreno and M. Collins, "The B7 family of ligands and its receptors: new pathways for costimulation and inhibition of immune responses.," *Annual review of immunology*, vol. 20, pp. 29–53, Jan. 2002.

[277] A. V. Collins, D. W. Brodie, R. J. Gilbert, A. Iaboni, R. Manso-Sancho, B. Walse, D. I. Stuart, P. van der Merwe, and S. J. Davis, "The Interaction Properties of Costimulatory Molecules Revisited," *Immunity*, vol. 17, pp. 201–210, Aug. 2002.

[278] M. Tacke, G. Hanke, T. Hanke, and T. Hünig, "CD28-mediated induction of proliferation in resting T cells in vitro and in vivo without engagement of the T cell receptor: evidence for functionally distinct forms of CD28.," *European journal of immunology*, vol. 27, pp. 239–47, Jan. 1997.

[279] M. Tacke, G. J. Clark, M. J. Dallman, and T. Hünig, "Cellular distribution and costimulatory function of rat CD28. Regulated expression during thymocyte maturation and induction of cyclosporin A sensitivity of costimulated T cell responses by phorbol ester.," *Journal of immunology (Baltimore, Md. : 1950)*, vol. 154, pp. 5121–7, May 1995.

[280] R. Siefken, R. Kurrle, and R. Schwinzer, "CD28-mediated activation of resting human T cells without costimulation of the CD3/TCR complex.," *Cellular immunology*, vol. 176, pp. 59–65, Feb. 1997.

[281] J. P. Van Wauwe, J. R. De Mey, and J. G. Goossens, "OKT3: a monoclonal anti-human T lymphocyte antibody with potent mitogenic properties.," *Journal of immunology (Baltimore, Md. : 1950)*, vol. 124, pp. 2708–2713, 1980.

[282] C. Ball, B. Fox, S. Hufton, G. Sharp, S. Poole, R. Stebbings, D. Eastwood, L. Findlay, P. W. H. I. Parren, R. Thorpe, A. Bristow, and S. J. Thorpe, "Antibody C region influences TGN1412-like functional activity in vitro.," *Journal of immunology (Baltimore, Md. : 1950)*, vol. 189, pp. 5831–40, Dec. 2012.

[283] G. Suntharalingam, M. R. Perry, S. Ward, S. J. Brett, A. Castello-Cortes, M. D. Brunner, and N. Panoskaltsis, "Cytokine storm in a phase 1 trial of the anti-CD28 monoclonal antibody TGN1412.," Tech. Rep. 10, Sept. 2006.

[284] F. Lühder, Y. Huang, K. M. Dennehy, C. Guntermann, I. Müller, E. Winkler, T. Kerkau, S. Ikemizu, S. J. Davis, T. Hanke, and T. Hünig, "Topological requirements and signaling properties of T cell-activating, anti-CD28 antibody superagonists.," *The Journal of experimental medicine*, vol. 197, pp. 955–66, Apr. 2003.

[285] E. J. Evans, R. M. Esnouf, R. Manso-Sancho, R. J. C. Gilbert, J. R. James, C. Yu, J. A. Fennelly, C. Vowles, T. Hanke, B. Walse, T. Hünig, P. Sø rensen, D. I. Stuart, and S. J. Davis, "Crystal structure of a soluble CD28-Fab complex.," *Nature immunology*, vol. 6, pp. 271–279, 2005.

[286] D. R. Davies and G. H. Cohen, "Interactions of protein antigens with antibodies.," *Proceedings of the National Academy of Sciences of the United States of America*, vol. 93, pp. 7–12, Jan. 1996.

[287] C. Yu, A. F.-P. Sonnen, R. George, B. H. Dessailly, L. J. Stagg, E. J. Evans, C. A. Orengo, D. I. Stuart, J. E. Ladbury, S. Ikemizu, R. J. C. Gilbert, and S. J. Davis, "Rigid-body ligand recognition drives cytotoxic T-lymphocyte antigen 4 (CTLA-4) receptor triggering.," *The Journal of biological chemistry*, vol. 286, pp. 6685–96, Feb. 2011.

[288] S. J. Davis, G. A. Schockmel, C. Somoza, D. W. Buck, D. G. Healey, E. P. Rieber, C. Reiter, and A. F. Williams, "Antibody and HIV-1 gp120 recognition of CD4 undermines the concept of mimicry between antibodies and receptors.," *Nature*, vol. 358, pp. 76–9, July 1992.

[289] K. M. Ottemann, W. Xiao, Y. K. Shin, and D. E. Koshland, "A piston model for transmembrane signaling of the aspartate receptor.," *Science (New York, N.Y.)*, vol. 285, pp. 1751–4, Sept. 1999.

[290] D. H. Margulies, "CD28, costimulator or agonist receptor?," *The Journal of experimental medicine*, vol. 197, pp. 949–53, Apr. 2003.

[291] L. S. Barak and W. W. Webb, "Diffusion of low density lipoprotein-receptor complex on human fibroblasts.," *The Journal of cell biology*, vol. 95, pp. 846–52, Dec. 1982.

[292] A. Kusumi, Y. Sako, and M. Yamamoto, "Confined lateral diffusion of membrane receptors as studied by single particle tracking (nanovid microscopy). Effects of calcium-induced differentiation in cultured epithelial cells.," *Biophysical journal*, vol. 65, pp. 2021–40, Nov. 1993.

[293] L. Weimann, K. A. Ganzinger, J. McColl, K. L. Irvine, S. J. Davis, N. J. Gay, C. E. Bryant, and D. Klenerman, "A quantitative comparison of single-dye tracking analysis tools using Monte Carlo simulations.," *PloS one*, vol. 8, p. e64287, Jan. 2013.

[294] G. J. Schütz, H. Schindler, and T. Schmidt, "Single-molecule microscopy on model membranes reveals anomalous diffusion.," *Biophysical journal*, vol. 73, pp. 1073–80, Aug. 1997.

[295] G. Guigas and M. Weiss, "Size-dependent diffusion of membrane inclusions.," *Biophysical journal*, vol. 91, pp. 2393–8, Oct. 2006.

[296] D. Grünwald, R. M. Martin, V. Buschmann, D. P. Bazett-Jones, H. Leonhardt, U. Kubitscheck, and M. C. Cardoso, "Probing intranuclear environments at the single-molecule level.," *Biophysical journal*, vol. 94, pp. 2847–58, Apr. 2008.

[297] C. Tardin, L. Cognet, C. Bats, B. Lounis, and D. Choquet, "Direct imaging of lateral movements of AMPA receptors inside synapses.," *The EMBO journal*, vol. 22, pp. 4656–65, Sept. 2003.

[298] S. Wieser, M. Moertelmaier, E. Fuertbauer, H. Stockinger, and G. J. Schütz, "(Un)confined diffusion of CD59 in the plasma membrane determined by high-resolution single molecule microscopy.," *Biophysical journal*, vol. 92, pp. 3719–28, May 2007.

[299] X. Michalet, "Mean square displacement analysis of single-particle trajectories with localization error: Brownian motion in an isotropic medium.," *Physical review. E, Statistical, nonlinear, and soft matter physics*, vol. 82, p. 041914, Oct. 2010.

[300] B. Wang, J. Kuo, S. C. Bae, and S. Granick, "When Brownian diffusion is not Gaussian.," *Nature materials*, vol. 11, pp. 481–5, June 2012.

[301] K. L. Angus and G. M. Griffiths, "Cell polarisation and the immunological synapse.," *Current opinion in cell biology*, vol. 25, pp. 85–91, Feb. 2013.

[302] A. Einstein, "Über die von der molekularkinetischen Theorie der Wärme geforderte Bewegung von in ruhenden Flüssigkeiten suspendierten Teilchen," *Annalen der Physik*, vol. 322, no. 8, pp. 549–560, 1905.

[303] J. Charles A Janeway, P. Travers, M. Walport, and M. J. Shlomchik, "The structure of a typical antibody molecule," Garland Science, 2001.

[304] R. Wombacher, M. Heidbreder, S. van de Linde, M. P. Sheetz, M. Heilemann, V. W. Cornish, and M. Sauer, "Live-cell super-resolution imaging with trimethoprim conjugates.," *Nature methods*, vol. 7, pp. 717–9, Sept. 2010.

[305] P.-G. de Gennes, *Scaling Concepts in Polymer Physics*. Cornell University Press, 1979.

[306] J. Marrack, *The chemistry of antigens and antibodies,*. London: H.M. Stationery Off., 1938.

[307] M. Dembo and B. Goldstein, "Theory of equilibrium binding of symmetric bivalent haptens to cell surface antibody: application to histamine release from basophils.," *Journal of immunology (Baltimore, Md. : 1950)*, vol. 121, pp. 345–53, July 1978.

[308] C. Mary, F. Coulon, N. Poirier, N. Dilek, B. Martinet, G. Blancho, and B. Vanhove, "Antagonist properties of monoclonal antibodies targeting human CD28," *mAbs*, vol. 5, no. 1, pp. 47–55, 2013.

[309] B. Vanhove, G. Laflamme, F. Coulon, M. Mougin, P. Vusio, F. Haspot, J. Tiollier, and J.-P. Soulillou, "Selective blockade of CD28 and not CTLA-4 with a single-chain Fv-alpha1-antitrypsin fusion antibody.," *Blood*, vol. 102, pp. 564–70, July 2003.

[310] A. Larsson, "Divalent binding of monoclonal antibody to a cell surface antigen. Modelling of equilibrium data.," *Molecular immunology*, vol. 26, pp. 735–9, Aug. 1989.

[311] R. C. Valentine and N. Green, "Electron microscopy of an antibody-hapten complex," *Journal of Molecular Biology*, vol. 27, pp. 615–617, Aug. 1967.

[312] N. Wrigley, E. Brown, and J. Skehel, "Electron microscopic evidence for the axial rotation and inter-domain flexibility of the fab regions of immunoglobulin G," *Journal of Molecular Biology*, vol. 169, pp. 771–774, Sept. 1983.

[313] L. Gregory, K. G. Davis, B. Sheth, J. Boyd, R. Jefferis, C. Nave, and D. R. Burton, "The solution conformations of the subclasses of human IgG deduced from sedimentation and small angle X-ray scattering studies.," *Molecular immunology*, vol. 24, pp. 821–9, Aug. 1987.

[314] K. Ritchie, R. Iino, T. Fujiwara, K. Murase, and A. Kusumi, "The fence and picket structure of the plasma membrane of live cells as revealed by single molecule techniques (Review).," *Molecular membrane biology*, vol. 20, no. 1, pp. 13–18, 2003.

[315] S. L. Shiao, J. M. McNiff, T. Masunaga, K. Tamura, K. Kubo, and J. S. Pober, "Immunomodulatory properties of FK734, a humanized anti-CD28 monoclonal antibody with agonistic and antagonistic activities.," *Transplantation*, vol. 83, pp. 304–13, Feb. 2007.

[316] S. R. Hubbard, "Structural analysis of receptor tyrosine kinases," *Progress in Biophysics and Molecular Biology*, vol. 71, pp. 343–358, Apr. 1999.

[317] S.-P. Cordoba, K. Choudhuri, H. Zhang, M. Bridge, A. B. Basat, M. L. Dustin, and P. A. van der Merwe, "The large ectodomains of CD45 and CD148 regulate their segregation from and inhibition of ligated T-cell receptor.," *Blood*, vol. 121, pp. 4295–302, May 2013.

[318] D. J. Irvine and J. Doh, "Synthetic surfaces as artificial antigen presenting cells in the study of T cell receptor triggering and immunological synapse formation.," *Seminars in immunology*, vol. 19, pp. 245–54, Aug. 2007.

[319] M. D. Lew, A. R. S. von Diezmann, and W. E. Moerner, "Easy-DHPSF open-source software for three-dimensional localization of single molecules with precision beyond the optical diffraction limit.," *Protocol exchange*, vol. 2013, Feb. 2013.

[320] C. Fang, R. R. Frontiera, R. Tran, and R. A. Mathies, "Mapping GFP structure evolution during proton transfer with femtosecond Raman spectroscopy.," *Nature*, vol. 462, pp. 200–4, Nov. 2009.

[321] J. Bähler, J. Q. Wu, M. S. Longtine, N. G. Shah, A. McKenzie, A. B. Steever, A. Wach, P. Philippsen, and J. R. Pringle, "Heterologous modules for efficient and versatile PCR-based gene targeting in Schizosaccharomyces pombe.," *Yeast (Chichester, England)*, vol. 14, pp. 943–51, July 1998.

[322] R. L. Strack, B. Hein, D. Bhattacharyya, S. W. Hell, R. J. Keenan, and B. S. Glick, "A rapidly maturing far-red derivative of DsRed-Express2 for whole-cell labeling," *Biochemistry*, vol. 48, pp. 8279–8281, 2009.

[323] K. Kaji, I. M. Caballero, R. MacLeod, J. Nichols, V. A. Wilson, and B. Hendrich, "The NuRD component Mbd3 is required for pluripotency of embryonic stem cells.," *Nature cell biology*, vol. 8, pp. 285–92, Mar. 2006.

[324] J. Nichols, J. Silva, M. Roode, and A. Smith, "Suppression of Erk signalling promotes ground state pluripotency in the mouse embryo.," *Development (Cambridge, England)*, vol. 136, pp. 3215–3222, 2009.

[325] Y. Harigaya, H. Tanaka, S. Yamanaka, K. Tanaka, Y. Watanabe, C. Tsutsumi, Y. Chikashige, Y. Hiraoka, A. Yamashita, and M. Yamamoto, "Selective elimination of messenger RNA prevents an incidence of untimely meiosis.," *Nature*, vol. 442, pp. 45–50, July 2006.

[326] A. T. Watson, V. Garcia, N. Bone, A. M. Carr, and J. Armstrong, "Gene tagging and gene replacement using recombinase-mediated cassette exchange in Schizosaccharomyces pombe.," *Gene*, vol. 407, pp. 63–74, Jan. 2008.

[327] A. Weiss and J. D. Stobo, "Requirement for the coexpression of T3 and the T cell antigen receptor on a malignant human T cell line.," *The Journal of experimental medicine*, vol. 160, pp. 1284–99, Nov. 1984.

[328] C. Demaison, K. Parsley, G. Brouns, M. Scherr, K. Battmer, C. Kinnon, M. Grez, and A. J. Thrasher, "High-level transduction and gene expression in hematopoietic repopulating cells using a human immunodeficiency [correction of imunodeficiency] virus type 1-based lentiviral vector containing an internal spleen focus forming virus promoter.," *Human gene therapy*, vol. 13, pp. 803–13, May 2002.

[329] F. L. Graham, J. Smiley, W. C. Russell, and R. Nairn, "Characteristics of a human cell line transformed by DNA from human adenovirus type 5.," *The Journal of general virology*, vol. 36, pp. 59–74, July 1977.

[330] S. M. Watt, D. J. Gilmore, J. M. Davis, M. R. Clark, and H. Waldmann, "Cell-surface markers on haemopoietic precursors. Reagents for the isolation and analysis of progenitor cell subpopulations.," *Molecular and cellular probes*, vol. 1, pp. 297–326, Dec. 1987.

[331] Y. M. Kong, H. Waldmann, S. Cobbold, A. A. Giraldo, B. E. Fuller, and L. L. Simon, "Pathogenic mechanisms in murine autoimmune thyroiditis: short- and long-term effects of in vivo depletion of CD4+ and CD8+ cells.," *Clinical and experimental immunology*, vol. 77, pp. 428–33, Sept. 1989.

# Appendix A

# Supplementary Figures and Tables

Table A.1 *Models of mEos photo-bleaching (Fitted amplitude).* (Values of the fitted amplitudes are given ± one standard deviation of the mean for two fields of view and two biological repeats. A.U.: arbitrary units.)

| | **mEos2** | | **mEos3.1** | |
|---|---|---|---|---|
| No 405 nm illumination<br>$f(t) = A\,e^{-\frac{t}{\tau_1}} + B\,e^{-\frac{t}{\tau_2}}$ | $A = 390$<br>$B = 360$ | ± 240 A.U.<br>± 230 A.U. | $A = 500$<br>$B = 440$ | ± 140 A.U.<br>± 110 A.U. |
| Continuous 405 nm illumination<br>$f(t) = A\,e^{-\frac{t}{\tau_1}} + B\,e^{-\frac{t}{\tau_2}} + C\,e^{-\frac{t}{\tau_3}}$ | $A = 340$<br>$B = 280$<br>$C = 220$ | ± 110 A.U.<br>± 100 A.U.<br>± 75 A.U. | $A = 470$<br>$B = 250$<br>$C = 330$ | ± 85 A.U.<br>± 80 A.U.<br>± 120 A.U. |

Table A.2 *Models of mEos photo-physics (Fitted amplitude).* Amplitudes $A$ and $B$ of the exponential decays fitted to the distributions of 'on' and 'off' times as described in Figure 3.9 under different 405 nm activation powers. Values are given for the fit of a single exponential decay for $t_{ON}$, and a linear combination of two exponential decays for $t_{OFF}$.

| **mEos2** | | | **mEos3.1** | | |
|---|---|---|---|---|---|
| 405 nm | $t_{ON}$ | $t_{OFF}$ | 405 nm | $t_{ON}$ | $t_{OFF}$ |
| 7 µW | $A = 6.98$ | $A = 1.86$<br>$B = 0.16$ | 162 µW | $A = 4.50$ | $A = 3.26$<br>$B = 0.16$ |
| 31 µW | $A = 6.12$ | $A = 2.05$<br>$B = 0.19$ | | | |
| 86 µW | $A = 5.62$ | $A = 2.13$<br>$B = 0.21$ | | | |
| 910 µW | $A = 4.38$ | $A = 3.18$<br>$B = 0.18$ | | | |

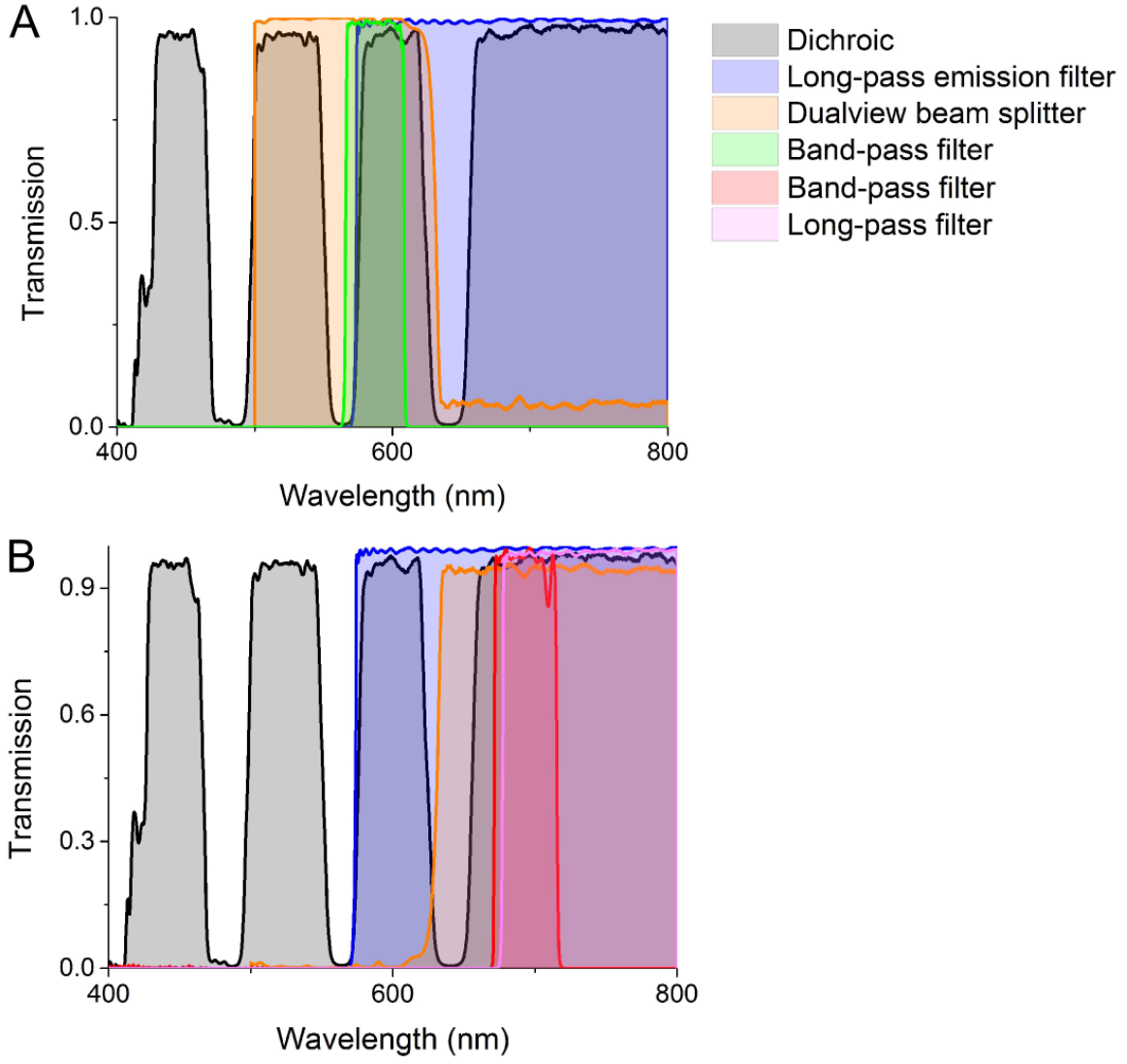


Figure A.1 *Spectra of the dichroic mirrors and filters used in both imaging channels of the dualview.* **Black**: Transmission of the quad-band dichroic mirror separating the illumination beams from the the fluorescent signal. **Blue**: Transmission of the long-pass emission filter inserted before the dualview. **Orange**: Reflection (**A**) and transmission (**B**) of the beam splitter of the dualview. **Green**: Transmission of the band-pass filter inserted in the short-pass channel of the dualview. **Red and Pink**: Transmission of the band-pass and long-pass filters (resp.) inserted in the long-pass channel of the dualview..

Table A.3 *Parameters values used in Peak Fit.* Table summarising the parameters used in the ImageJ plug-in Peak Fit [149] integrated in the bespoke pieces of Software B.4 ('General') and B.5 ('vls') to detect and fit PSFs.

| Name | Value (General) | Value (vls) |
|---|---|---|
| Calibration | 110 nm /pix | |
| Gain | EM Gain / Camera Gain | |
| Exposure time | 50 ms | |
| Initial StdDev0 | Theoretical $\sigma_{PSF}$ (Eqn 2.1) | |
| Initial StdDev1 | Theoretical $\sigma_{PSF}$ (Eqn 2.1) | |
| Initial Angle | 0 | |
| Smoothing | 0.5 | |
| Smoothing2 | 3 | 8 |
| Search Width | 3 | 8 |
| Fitting Width | 3 | |
| Fit Solver | LVM | |
| Fit Function | Free | |
| Fit Criteria | Least squared error | |
| Significant Digits | 5 | |
| Lambda | 10 | |
| Max Iterations | 20 | |
| Fail Limit | 10 | |
| Include Neighbours | true | |
| Neighbour Height | 0.3 | |
| Residual Threshold | 1 | |
| Duplicate Distance | 0.5 | |
| Shift Factor | 1.5 | 3 |
| Signal Strength | 20 | |
| Width Factor | 5 | 30 |
| Precision | 0 | |

# Appendix B

# Supplementary Movies and Software

All movies and software listed here can be found on the accompanying CD.

Movie B.1 *Example of sptPALM analysis.* An example of the single-particle tracking analysis used in this thesis is shown for data from one representative experiment (from Chapter 7). T cell expressing CD28-mEos3.2 at their membrane and decorated with anti-CD28 mAbs are dropped on a glass coverslip coated with secondary antibodies. The live cell forms a contact with the coated surface and is imaged under TIRF 561 nm illumination. A low-power constant TIRF 405 nm illumination is additional applied to activate a sub-population of mEos3.2 fluorophores. For the representative cell shown in this movie, 1,555 frames were acquired and analysed as described in Section 7.2.1 (the single-particle tracking algorithm is developed in Section 3.4.2). The trajectories of all localisations detected in the frame are plotted (one colour per trajectory). Trajectories are shown up to the frame shown and with a maximum of 10 frames of history. The video is played back at real-time (20 frames per second). The scale bar is 1.5 μm and data was acquired at 37°C.

Movie B.2 *Real-time demonstration of the automation algorithm.* Some yeast cells were trapped in the microfluidic device introduced in Section 3.5 and imaged using the automation algorithm without its autofocusing step (Software B.3). First, the different steps of a cycle of the algorithm (Figure 3.16) are presented and described. Then, a real-time movie of the computer screen during four cycles of the algorithm follows.

Software B.3 *Automation μManager plug-in.* The automation of the microscope was operated through the control of various elements (lasers, shutters, $(xy)$ stage, focus and EMCCD) with μManager [173]. A bespoke library ('MicroManager_MP.jar') was designed to operate the microscope with easy-to-use lines of command adapted to the experiments. However, this means that the source code is adapted to the configuration of the instrument in μManager and has to be modified for each new instrument. Nevertheless, it is designed to work on four instruments, so its implementation can be easily generalised to other microscope set-ups. Both the source code and its compiled jar file are provided.
This library was used in both μManager plugins (*e.g.* to calibrate the double-helix in Section 3.2.2) or macros written for specific imaging protocols in the Beanshell script feature of μManager. A few examples of macros are given, such as the one used for 'smart' automation imaging of live fission yeast in micro-fluidic devices ('MicroFluidicDeviceAutomation.bsh'; Section 3.5) or the Fermi 405 nm activation protocol described in Section 3.3.4 and used in Chapter 6 ('Fermi405Activation.bsh').

Software B.4 *vlsSMLM ImageJ plug-in.* An ImageJ plug-in to implement the vlsSMLM optical sectioning method described in Chapter 4 was designed. The plug-in is divided in two consecutive steps: (1) the calibration of the vls by analysing a $z$-scan of immobilised and separated sub-diffraction fluorescent beads. (2) This enables the determination of width and amplitude thresholds that can be applied to SMLM data imaged under similar conditions. A 'ReadMe' text file provides the information to install the plug-in. An example of calibration file and the SMLM data analysed in Figure 4.8 are also provided. Both the source code and its compiled jar file are provided.

Software B.5 *ImageJ plug-ins for SMLM data analysis.* All analysis methods presented in this thesis were implemented as a coherent ImageJ library ('SMLM_.jar') that evolved during the course of this thesis. It is organised in sub-packages and and various plug-ins implementing different analyses (*e.g.* batch analyses, registration of two channels (Section 3.2.3), CBC analysis (Section 3.4.2), single-particle tracking (Section 3.4.2), pair-correlation analysis (Section 6.2.1), clustering (Section 3.4.2)). Although a simple interface asks for the most frequently used parameters in most plug-ins, some plug-ins were slightly modified from one analysis to the other ((un)commenting a few lines) directly in the source code. A 'ReadMe' text file provides the information to install the plug-in. Both the source code and its compiled jar file are provided.